Dynamical Aspects of Exoplanetary Systems

Giammarco Campanella

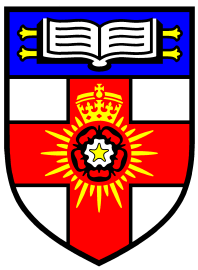

Thesis submitted for the degree of
Doctor of Philosophy (PhD)
of the University of London

June 2013

Abstract

The detection of more than 130 multiple planet systems makes it necessary to interpret a broader range of properties than are shown by our Solar system. This thesis covers aspects linked to the proliferation in recent years of multiple extrasolar planet systems.

A narrow observational window, only partially covering the longest orbital period, can lead to solutions representing unrealistic scenarios. The best-fit solution for the three-planet extrasolar system of HD 181433 describes a highly unstable configuration. Taking into account the *dynamical stability* as an additional observable while interpreting the RV data, I have analysed the phase space in the neighbourhood of the statistical best-fit. The two giant companions are found to be locked in the 5:2 MMR in the stable best-fit model.

I have analysed the dynamics of the system HD 181433 by assessing different scenarios that may explain the origin of these eccentric orbits, with particular focus on the innermost body. A scenario is considered in which the system previously contained an additional giant planet that was ejected during a period of dynamical instability among the planets. Also considered is a scenario in which the spin-down of the central star causes the system to pass through secular resonance. In its simplest form this latter scenario fails to produce the system observed. If additional short-period low mass planets are present in the system, I find that mutual scattering can release planet b from the secular resonance, leading to a system with orbital parameters similar to those observed today.

Finally, I have studied the evolution of low mass planets interacting with a gas-giant planet embedded in a gaseous disc. The transit timing method allows the detection of non-transiting planets through their gravitational perturbations. I have investigated the detectability of low mass planets neighbouring short-period giants after protoplanetary disc dispersal.

Contents

List of Figures

List of Tables

To my family

Acknowledgements

I am infinitely grateful to those who have accompanied me during my PhD studies.

I shell start with a big thank you to my supervisor Richard Nelson for his guidance and support. Thanks to QMUL for having given me the opportunity to undertake these studies and to attend exciting conferences in the UK and abroad. I am grateful to my examiners Hugh Jones and David Waltham for taking the time to so carefully read this work and for their valuable comments.

I offer a special thanks to Stefano Meschiari for valuable discussions when dealing with the observational modelling of both RV and TTV signals. I thank all my fellow PhD students who have shared many glad moments with me over these years and in particular Stephen for his inputs during my last project. Thank you also to the many friends in the campus and in London.

Un immenso grazie a tutti i miei familiari a cui devo semplicemente tutto: Emilio, Wilma, Cristiana, tutti gli zii e cugini. Il mio caro ricordo va alle nonne. In particolare, grazie alla mia famiglia a Londra: Mara, Nino, James, Franco, Graziella, Angelica per avermi fatto assaporare sempre l'aria della nostra unica ed insuperabile terra.

Spasibo Nataliya for having obliged me to have a break from my planets from time to time, for your support, smile and happy moments we have been sharing together.

This work was funded by a PhD scholarship from Queen Mary, University of London.

Declaration/List of Publications

I hereby certify that this thesis has been written by me; that it is the record of the work carried out by me at the Astronomy Unit, Queen Mary, University of London, and that it has not been submitted in any previous application for a higher degree. Where information has been derived from other sources, I confirm that this has been indicated in the thesis. Parts of this work are published in the following papers:

- Campanella, G. "Treating dynamical stability as an observable: a 5:2 mean motion resonance configuration for the extrasolar system HD 181433", 2011, MNRAS, 418, 1028.
- Campanella, G., Nelson, R.P., Agnor, C.B., "Possible scenarios for eccentricity evolution in the extrasolar planetary system HD 181433", 2013, MNRAS, accepted (doi: 10.1093/mnras/stt959, arXiv:1305.7508).

I have made a major contribution to all the original research presented in this thesis.

Giammarco Campanella

"L'amor che move il sole e l'altre stelle"

Dante Alighieri, Divina Commedia,
Paradiso Canto XXXIII (14th century)

CHAPTER 1

Introduction

1.1 From Planets to Exoplanets

The profound question concerning the existence of other worlds has always been part of our culture and history. Planets have long captured the imagination of human minds, seven bodies the Sun, the Moon, Mercury, Venus, Mars, Jupiter and Saturn were known to many cultures across the world and were viewed as abnormal heavenly objects. Greek astronomers employed the term asteres planetai, "wandering stars", for these objects which apparently move over the sky.

It was only with the 16^{th} century, with the heliocentric model of Copernicus, Kepler and Galileo's telescope that theories started to be based on experimental and observational evidences rather than philosophical and theological tradition. Galileo was the first to truly see the planets and moons in our Solar system as other worlds and paved the way for the future discovery of Uranus, Neptune and Pluto. The remarkable Newtonian theory introducing the force of gravity and Einstein's theory of Relativity made possible to finally completely understand the observed motions of the planetary bodies by the early twentieth century. Yet it took until the end of the 20^{th} Century before telescopes and spacecraft were developed to have close-up views of planets, their moons, and the persistent debris from which they have formed.

Astronomers have long suspected that planetary systems are abundant, and perhaps an inevitable by-product of star formation, but proof of this has been difficult to obtain. van de Kamp [1963] claimed to have detected an exoplanet orbiting a nearby M-dwarf known as "Barnard's star". However, the signal was soon identified as spurious, an artefact of maintenance and upgrade work on the telescope. Only in 1988 some first results were recorded: some observations by Campbell et al. [1988] suggested the presence of planetary masses around some near stars. However, Walker et al. [1992] were extremely cautious as planets in orbit was just one of the possible interpretations of the data. Not many took in consideration their studies until the confirmation of γ Cephei b made many years later [Hatzes et al., 2003].

Moving on, Latham et al. [1989] found strong evidence of what could have been a planet around a star, called HD 114762. Since Latham's planet had a mass at least 10 times that of Jupiter, it was hypothesized that actually it was a brown dwarf, so also this news did not have a big impact.

Finally, Wolszczan and Frail [1992] used a very precise timing method and discovered planets in orbit around PSR 1257+12. This is recognised as the first unambiguous detection of planets orbiting another star. What made the discovery even more remarkable was that the planets detected were in the terrestrial mass regime at $2.8m_{\oplus}$ and $3.4m_{\oplus}$ and what would be considered "long-period" from a modern perspective, with respective orbital periods of 98.2 d and 66.6 d. As pulsar planets, they were surprising as it was expected to find planets only around main sequence stars. Not many believed that a Solar system planet-like was discovered; anyway this was the first clue suggesting that planetary formation is a widespread process and yet the real prize of a planet around a Sun-like star remained undiscovered.

Planetary formation models of the Solar system affirmed that gas giants originated beyond the snow-line where the equilibrium temperature is less than 150K, typically at 2-3 AU [Pollack et al., 1996]. Inward migration was expected, but the locations of the Solar system gas giants suggested that this mechanism was not very effective. Thus, even after the findings by Wolszczan and Frail [1992], little resource was devoted to looking for exoplanets, in particular with the Radial Velocity method which was ideal to detect short-period companions. However, some groups continued to work and thus eventually paid off for Mayor and Queloz [1995]. 51 Peg is a G-class star which was part of a exploratory survey being conducted by a Swiss group based in Geneva, led by Michel Mayor looking at 142 bright K and G dwarfs for radial velocity variations with a sensitivity of $\sim$ 13 m/s. 51 Peg b orbits its star in 4.2 days, and is much closer to it than Mercury is to our Sun, yet has a minimum mass about half that of Jupiter. Computational models of this "hot Jupiter" suggested that it is sufficiently massive that its thick atmosphere is not blown away by the star's solar wind [Guillot et al., 1996].

The discovery of this strange and unpredicted object gave a boost to this revolutionary astronomical branch: the study of planetary systems beyond our own. Just six days after the announcement by Mayor and Queloz [1995], two new discoveries were reported: 70 Virginis [Marcy and Butler, 1996] and 47 *Ursæ* Majoris [Butler and Marcy, 1996]. And so began the time of exoplanets with new discoveries released on a regular basis from here on (see Figure 1.1).

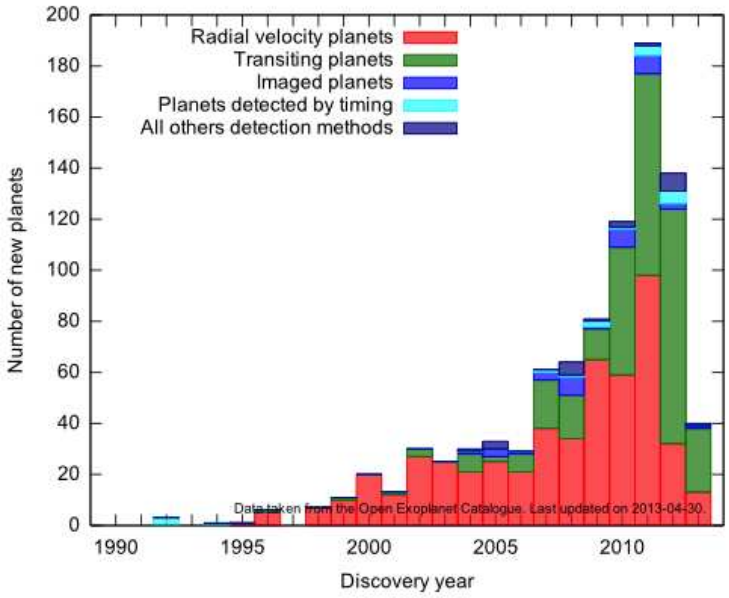

Figure 1.1: Exoplanet discoveries by year, colours indicate the discovery method. Data is from the Open Exoplanet Catalogue `https://github.com/hannorein/open_exoplanet_catalogue`.

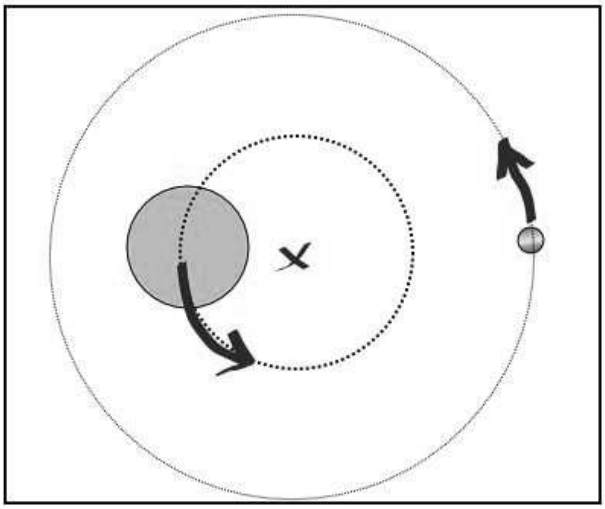

Figure 1.2: The reflex motion of a star in the inertial frame of the barycentre. The planet's presence gives rise to variations in the position (used for astrometry and pulsar timing) and the velocity (considered for radial velocity) of the host star, which can be used to detect an exoplanet.

1.2 Detection Methods

To date, more than 850 candidates have been detected[1] using a variety of techniques including: Doppler radial velocity [e.g., Mayor and Queloz, 1995, Udry et al., 2007], transit photometry [e.g., Charbonneau et al., 2000, Ballard et al., 2011], astrometry [e.g., Benedict et al., 2002], microlensing [e.g., Beaulieu et al., 2006], pulsar timing [Wolszczan and Frail, 1992] and direct imaging [e.g., Chauvin et al., 2005, Marois et al., 2008]. I will now introduce the radial velocity and transit detection methods which are object of this thesis.

1.2.1 Radial Velocity

The Radial Velocity (RV) method detects planets by measuring the parent star's periodic line of sight velocity change due to its orbit around a common centre of mass. Since a planet, and thus the star's corresponding reflex motion, orbit with a higher speed when in tighter orbits, RV favours planets on very short orbital periods. The RV method requires measurements of a star's velocity along the line-of-sight, which can be achieved by measuring the Doppler shifts of said star's spectral lines. This certainly requires a very stable spectrograph, with highly sensitive calibration and a rich pool of lines to measure.

[1] "The Extrasolar Planets Encyclopaedia" `http://www.exoplanet.eu`

It is possible to write down a simple expression for the reflex velocity semi-amplitude in the case of a circular orbit. In fact, the stellar motion and the planetary motion must balance out in the inertial frame:

$$\begin{aligned} m_p v_p &= M_* v_* \\ K \simeq v_* \sin i_p &= \frac{m_p \sin i_p}{M_*} \frac{2\pi a_p}{P} \\ &= m_p (2\pi G)^{1/3} M_*^{-2/3} P^{-1/3} \\ &= (28.4\,\mathrm{m/s}) \sin i_p \Big(\frac{m_p}{m_{Jup}}\Big) \Big(\frac{M_*}{M_\odot}\Big)^{-2/3} \Big(\frac{P}{\mathrm{years}}\Big)^{-1/3} \end{aligned} \tag{1.2.1}$$

where m_p indicates the planetary mass, M the stellar mass, K denotes the RV semi-amplitude and P the orbital period of the planet. Newton's version of Kepler's Third Law has been used to remove the dependency on the planetary semi-major axis a_p. By 1995, typical RV errors could reach $20m/s$ so equation (1.2.1) indicates that for giant planets on an orbit of a year or less, RV would be a feasible detection technique. In fact, for 51 Peg the velocity semi-amplitude is $K = 59m/s$ which was significantly larger than the Swiss group velocity measurement precision. In contrast, the radial velocity signal of the Sun due to Jupiter's orbit is only about $13m/s$. Due to the bias of RV surveys to high mass, short-period planets, a large fraction of these bodies are previously unanticipated "hot-Jupiters". The fact that hot-Jupiters exist was of great help for RV surveys in the early years, but present high-resolution spectroscopy can measure stellar velocities to better than $1m/s$ meaning planets down to a few Earth-masses at long periods can be detected [e.g. Vogt et al., 2010a]. It is important to underline that the radial velocity technique is sensitive to $m_p \sin i$ and not m_p only. Thus, RV measurements allow only to estimate a lower limit to the mass of a planet, unless the inclination i can be determined by some independent means (e.g. the transit method).

1.2.2 Transits

Transit surveys look for photometric variations consistent with planets eclipsing their parent star. The star has a nominal flux level which momentarily decreases due the planet passing in front of a portion of the stellar disk along its orbit. The geometric depth of the transit is given by the ratio of the sky-projected area of the planet and the sky-projected area of the star:

$$\begin{aligned} \Delta F &= \frac{\pi R_p^2}{\pi R_*^2} \\ &= 1.03 \Big(\frac{R_p}{R_{Jup}}\Big) \Big(\frac{R_\odot}{R_*}\Big) \,\% \end{aligned} \tag{1.2.2}$$

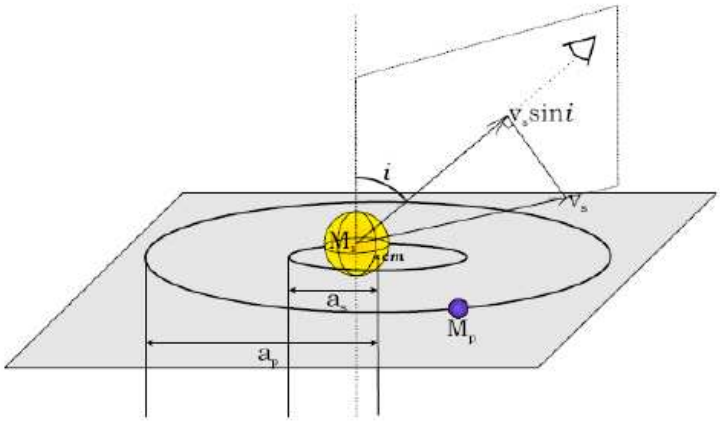

Figure 1.3: Observing a planet-star system. The star s and the planet p are in circular orbit around the centre of mass cm of the system. The orbital radii are a_s and a_p, the angle i between the normal to the orbital plane and the line of sight determines the orbital inclination angle. $v_s \sin i$ is the component along the line of sight of the radial velocity v_s.

The photometric precision of even small telescopes (e.g. 20 cm in diameter) was better than 1% when the first exoplanets were announced, this was due to the development of CCDs during the last decades. The problem was how likely was it that a transit would happen, given the almost perfect alignment required between the observer, the planet and the star? Assuming a planet is on a nearly circular orbit and the inclination angle is uniformly distributed in space, the probability is $P_{tr} \sim R_*/a$. For 51 Peg b, the transit probability is about 10% and transit events recur every ~ 4 days. Applying this equation to the solar system, it follows that for a distant observer the Earth has a $1/214$ probability to produce a transit in front of the Sun; for Jupiter the value is $1/1100$. With the discovery of the "hot Jupiter"-class of planets, the prospects of detecting exoplanets by looking for transits improved dramatically.

The transit method met its first success in 1999 with the observation of the transiting planet HD 209458b [Charbonneau et al., 2000, Henry et al., 2000], a fairly typical hot-Jupiter around a bright star (see Figure 1.4 Left). The light curve showed a depth of around 1.5% lasting for about 3 hours. The observation allowed for a determination of the orbital inclination angle and thus the true planetary mass from the RV determined $m_p \sin i_p$. Also, given that the transit depth is essentially $(R_p/R)^2$, the planetary radius could be estimated and therefore the average density of HD 209458b was calculated. In 2001, the first space-based observation of a transit was made for HD 209458b using HST and demonstrating the excellent precision achievable [see Figure 1.4 Right, Brown et al., 2001].

When several transits are observed, the period, impact parameter and inclination are precisely determined by the flux loss, timing and duration of the eclipses. When is

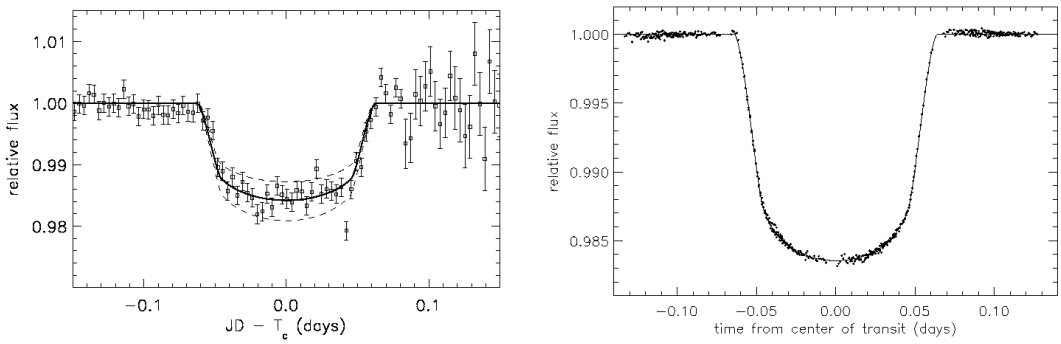

Figure 1.4: Transit light curve for HD 209458b. Left: The solid line shows the best-fit model and the dotted line shows the extrema of a planet which is 10% smaller or larger in radius [Charbonneau et al., 2000]. Right: Using the Hubble Space Telescope (HST/STIS) [Brown et al., 2001].

possible to detect the secondary transit (i.e. when the planet is hidden by the parent star), tight constraints on a combination of eccentricity and argument of pericentre can be placed as well [Deming et al., 2007]. In addition to the planet's size, mass and orbital distance, also other details such as the surface gravity, temperature and albedo can be estimated for transiting planets. Finally, detecting transits at different wavelengths makes possible to infer the planet atmospheric composition and ultimately its habitability.

The transit method has acquired an increasingly instrumental role in the advancement of exoplanetary science. After the first successes, ground-based transit surveys such as HATNet [Hartman et al., 2004] and WASP [Pollacco et al., 2006] were commenced. These campaigns surveyed a large number of stars looking for photometric variations and foreran the dedicated space missions: CoRoT [Léger et al., 2009] and Kepler [Borucki et al., 2003] which are detecting a large number of new planets. These new discoveries have extended the planetary sample into mass regimes and system architectures previously unexplored [e.g. Lissauer et al., 2011a, Gautier et al., 2012].

For a planet following precisely a Keplerian orbit, the timing, spacing and other properties of the transit light curve should be unvarying in time. The existence of additional planets in the system (which themselves may or may not transit the star) can account for gravitational perturbations on the orbit of the transiting planet, inducing detectable transit timing variations (TTVs) of the known transiting planet [Miralda-Escudé, 2002, Holman and Murray, 2005, Agol et al., 2005]. Other works have extended the TTV method to evidence the feasibility of detecting Trojan companions in extra-solar planetary systems [Ford and Holman, 2007]. Considering the TTV along with transit duration variations (TDVs), may also lead to the identification of planetary moons [Kipping, 2009a,b, Kipping et al., 2009].

1.3 An Explosion of Discoveries

Driven by increasingly prolific detection methods, the observational envelope is pushed toward long-period giants, super-Earths in the habitable zone and terrestrial-mass habitable planets, the "holy grail" of exoplanets. An increasing sample of found planets improves our knowledge of their distribution in the mass-period diagram and allows comparison with theoretical predictions [e.g. Wright et al., 2009]. In fact, dynamical analysis of planetary systems can both precisely determine their orbital architectures and constrain their evolutionary histories providing a test bed for planetary formation and evolution theories. Improved observational techniques are providing detailed insights into the physics of planet formation in regimes very different than those of our own Solar system. Also, observations of protoplanetary discs are offering new constraints for theories of planet formation.

In Figure 1.5 are presented the known exoplanets with the semi-major axis on the X-axis and mass on the Y-axis. Astrometry and radial velocity can detect long-period planets better than transits and direct imaging is most sensitive to massive, bright objects at even larger distances. A number of characteristics can be understood from the family of detected exoplanets, for instance:

1. Hot Jupiters cluster around a period of a few days while other massive planets have a period $>$ 200 d. Outside a few AUs, the limited time span of RV surveys inhibit the discovery of longer-period planets.

2. Super-Earths $2m_{\oplus} < m_p < 10m_{\oplus}$, uncommon in our System, have been discovered using the RV [e.g. Rivera et al., 2005, Vogt et al., 2010b] and transit method [e.g. Queloz et al., 2009].

1.3.1 The exoplanetary systems

In 1999, the first multiple-planet exosystem was announced. *υAndromed*æ is a binary system consisting of a yellow-white dwarf star of class F8V younger than the Sun and a M4.5V red dwarf separated by at least 750 AU. Four confirmed extrasolar planets are known in orbit around the primary star, all four are likely to be jovian planets [Butler et al., 1997, 1999, 2006], making *υAndromed*æ both the first multiple-planet planetary system to be discovered around a main sequence star and the first multiple-planet system known in a multiple star system. υ And c and υ And d are in eccentric orbits ($\sim 0.25 - 0.3$), while υ And e was discovered in 2010 and should be in a 3:1 resonance with υ And d [Curiel et al., 2011, Ligi et al., 2012].

More than 130 multi-planet systems are now known[2] and a broad range of planetary

[2] `http://www.exoplanet.eu`

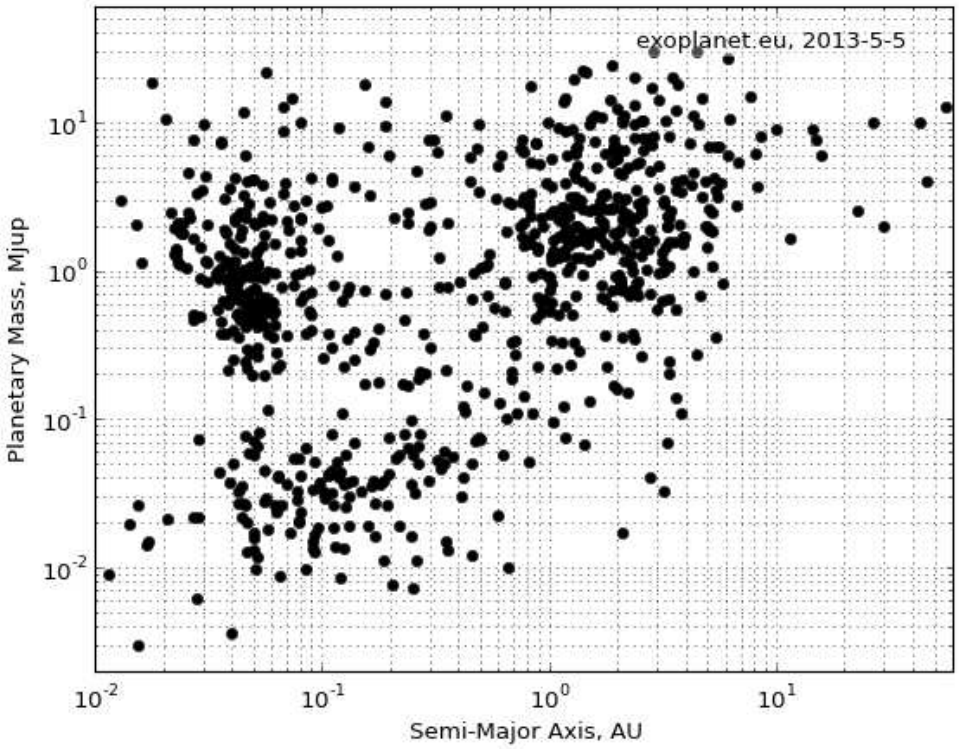

Figure 1.5: Plot of planetary mass vs semi-major axis for the known exoplanets as of May 2013.

system architectures has been sampled. Apart from the increase in instrument precisions, the proliferation of multiple-planet systems is due to thanks to the extension in duration of several planet search programs. This has allowed the detection of longer periods planetary signatures, as well as planetary signatures with lower amplitude.

Some systems such as GJ 876 [Marcy et al., 1998, 2001, Rivera et al., 2005] and HD69830 [Lovis et al., 2006] have been characterised using long term RV measurements. Other systems, for instance ϵ Eridani [Benedict et al., 2006], are studied by means of a variety of observational sources and in some cases have parameters that are significantly uncertain; *dynamical stability* constraints can be very helpful in determining more accurate orbital parameters.

55 Cancri is a binary system consisting of a G8V star and a M4V red dwarf separated by over 1,000 AU. Fischer et al. [2008] report this five-planet extrasolar system to consist of four gas giants ('*b*', '*c*', '*f*' and '*d*') and planet *e*, the first super-Earth discovered around a main sequence star [McArthur et al., 2004].

One of the candidates to be the largest known exoplanetary system is HD 10180, a star of class G1 V with at least six planets confirmed. Lovis et al. [2011] reported six strong RV signatures of low-mass exoplanets in orbits ranging from 5 days to roughly 2000 days and a possible seventh signal at 1.18 days. These planets include five 12 to 25 $m_\oplus$ planets classified as Neptune-like planets, a more massive outer planet with a minimum mass of 65 $m_\oplus$, and a candidate terrestrial planet with a minimum mass of 1.35 $m_\oplus$ orbiting the star in close proximity. Then, Tuomi [2012] found further evidences for two additional super-Earths which would make HD 10180 a very packed system. Furthermore, with as many as nine planets HD 10180 is potentially the largest of all known planetary systems, including the Solar system.

Interesting confirmed planetary systems come especially from the *Kepler* Mission. Kepler-11 is the first discovered case of a star system with six transiting planets: 4 super-Earths, a Neptune-size and a Jupiter-like planet, all within 120-d orbit [Lissauer et al., 2011a]. Kepler-37 hosts three planets and in particular Kepler-37b, the smallest exoplanet so far slightly larger than the Moon [Barclay et al., 2013]. Kepler-62 is a K2V star with five transiting planets, the masses of the planets could not be directly determined using either the radial velocity or the transit timing method, however it is remarkable that both Kepler-62e and Kepler-62f are likely solid planets within the star's habitable zone ($P_e = 122$ d, $P_f = 267$ d) [Borucki et al., 2013]. Much more is expected from Kepler, more than 360 multiple-planet candidate systems (see Figure 1.6) are found in the catalogue of *Kepler* Objects of Interest which are requiring follow-up studies in order to rule out false positives [Fabrycky et al., 2012b].

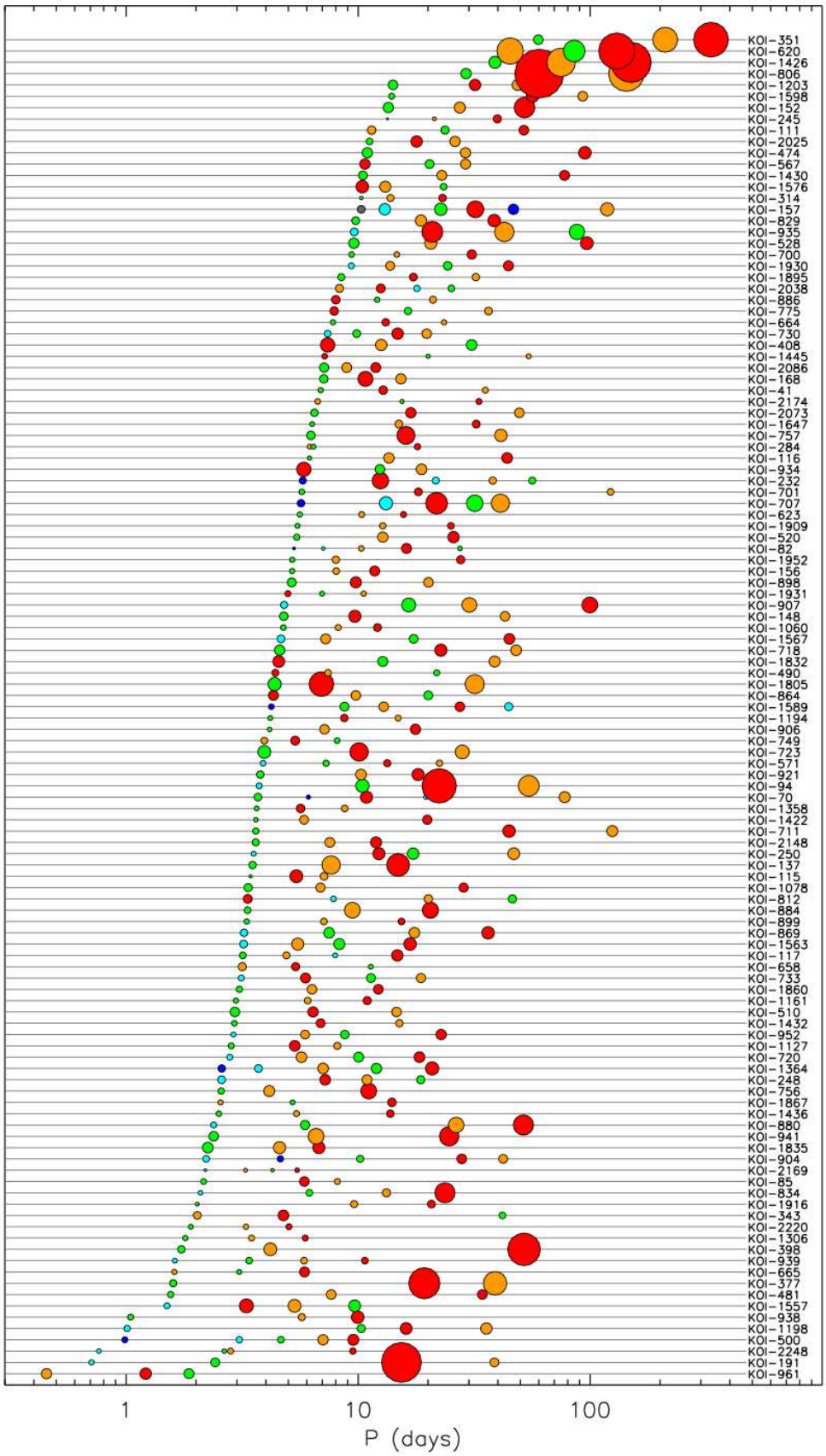

Figure 1.6: Systems from the *Kepler* catalogue. For each system, planet radii are to scale relative to one another and are coloured by decreasing size within each system: red, orange, green, light blue, dark blue, gray [Fabrycky et al., 2012b].

1.3.2 The surprising characteristics

In addition to the large amount of observational work that has gone into the detection of extrasolar planets, there is a parallel effort by theorists to explain the emerging distributions of planets within the context of theories of planetary formation and evolution. In fact, this variegate ensemble of planets offers a wide range of features that are not displayed by our Solar system: giant planets in short period orbits ("hot Jupiters"), the wide eccentricity distribution of exoplanets, the relatively common detection of mean motion resonances (MMRs) in multiple planet systems. All this offers interesting examples against which theories of planetary formation and evolution need to be tested [e.g. Butler et al., 2006].

The physical environment close to stars is not a favourable place for massive planets to form *in situ*. In the innermost regions, temperatures may be too high for solid particles to condense and there may not be enough mass available locally to form a giant planet. It is therefore favourite the hypothesis that hot-Jupiters form in the outer regions of protoplanetary discs. Beyond the ice line, roughly located at $3-5$ AU, the temperature in the nebula is such that ices can begin to form, these ices augment the amount of solid material available and may increase the ability of solids to stick on impact allowing the formation of massive cores within the lifetime of the protostellar discs. So these giants would have arrived at their present locations via inward migration [e.g. Lin et al., 1996, Ida and Lin, 2004].

Typical hot-giants have low eccentricities consistent with tidal circularization of their orbits, whereas planets with $P \gtrsim 10$ d have an eccentricity distribution peaking at $e \approx 0.25$, with a long tail. Such high eccentricities are probably excited by planet-planet scattering [e.g. Jurić and Tremaine, 2008] or Kozai oscillations [Fabrycky and Tremaine, 2007].

In the solar system, Jupiter and Saturn are within 1% of a $5:2$ resonance, Uranus and Neptune are within 2% of a $2:1$ resonance and Pluto is in a $3:2$ resonance with Neptune. One-third of the multi-planet systems studied by radial-velocity measurements contain near-resonant planet pairs, with about half of these near the $2:1$ resonance [Lissauer et al., 2011b], although this result should be biased by the difficulties in detecting low-mass planets in resonance with exterior companions [e.g. Anglada-Escudé et al., 2010]. Near-resonances involving three or more planets are also present in the Kepler data. The four planets of KOI-730 should be in a chain of resonances with period ratios $8:6:4:3$, strong evidence for resonances are also found in the five-planet system KOI-500 [Lissauer et al., 2011b]. Besides, clues for near period commensurabilities are present for the three planets in the systems KOI-720 and in KOI-2086 [Fabrycky et al., 2012b]. It is generally believed that 2:1 resonances can be produced especially through the process of convergent migration, while higher-order resonances can be created through planet-planet gravitational scattering [Raymond et al., 2008].

1.4 Thesis Outline

In this thesis, I aim to discuss some characteristic dynamical aspects of planetary systems following the proliferation in recent years of new extrasolar planetary systems which offer a broader range of properties than are shown by our Solar system. My original results are presented in Chapters 5, 6 and 7. These projects are anticipated by the relevant background material and findings are discussed in context of current knowledge in the field and are tighten up into a unique argumentation.

In particular, in Chapter 2 I will examine the Radial Velocity discovery technique and how it is possible to give constraints on the orbital parameters of those long-period planets, that have not completed a single orbit yet, by applying the criterion of *dynamical stability*. I will implement this method in Chapter 5, where I analyse the phase space in the neighbourhood of the statistical best-fit for the three-planet extrasolar system of HD 181433. I am able to reduce the uncertainty on the location of HD 181433 d to the narrow band where the 5:2 MMR is possible with the other outer giant HD 181433 c.

Moving on, in Chapter 3 I will introduce the secular perturbations theory useful to find analytic approximations of dynamical evolutions and I will apply the secular theory to some extrasolar planetary systems. Moreover, I will present physical processes that can be fundamental in explaining some peculiar orbital characteristics, these are: the sweeping of secular resonances in particular when this is due to stellar spin-down and planet-planet scattering. I will complete the Chapter by showing the code that I have implemented to study these mechanisms by means of numerical simulations. I will apply the complete theory to the stellar system of HD 181433 in Chapter 6. In fact, the three planets hosted by HD 181433 are on eccentric orbits and I will explore plausible scenarios of how the observed large eccentricities may have been generated after depletion of the protoplanetary disc. Analysis of the possible tidal evolution of the innermost planet HD 181433 b will suggest that it should be considered as a hot-Neptune rather than a short-period super-Earth. The planet-planet scattering scenario will be found to be plausible in explaining the present architecture, but it will suggest that it only occurs as a rather rare event in planetary system evolution. When studying the possibility that secular resonance can cause excitation of planet b's eccentricity, I will identify two distinct modes of evolution: for nominal values of the stellar spin-down parameter, planet b is trapped in the resonance temporarily leading to a maximum growth of eccentricity to a not sufficient value of 0.25; for values of the stellar spin-down parameter that are marginally smaller than the nominal value, planet b becomes trapped in the resonance indefinitely with its eccentricity being driven toward unity. I will find that the inclusion of additional short-period low mass planets in the system can perturb planet b out of long-term resonant capture when its eccentricity has reached large values. This would account successfully for the observed orbital properties of planet b requiring a stellar spin period $\lesssim 20$ hours for resonant capture to occur.

The theory of transit timing effects is presented in Chapter 4 along with the predictions made about the strength of the TTV method of discovering, in particular, terrestrial planets which would be outside the grasp of Radial Velocity surveys. However, since no low-mass planet has been detected with the TTV method yet, in Chapter 7 I will study how the outcome of migration processes in protoplanetary discs can depend on planetary masses and disc properties. This will give grounds to investigate the detectability of non-transiting low-mass planets neighbouring short-period giants by showing which formation scenarios are more probable to produce detectable TTV signals. The cases where the companion does not end up in Period Commensurability and the sets where the companion is trapped in MMR, will not produce substantially different RMS TTV if the amplitude of the resonant angle is less than 10-14 degrees. The strongest TTV signals will be generated by planets in resonance with higher-amplitude librations and by smaller planet-planet mass-ratios, so I will deduce that companions to Neptune-like bodies are more probable to be detected as indicated by TTV surveys of *Kepler*'s candidates.

I conclude in Chapter 8 with a summary of the thesis.

CHAPTER 2

Treating Dynamical Stability as an Observable in Radial Velocity Data Analysis

To investigate the orbital architectures of planetary systems and constrain their evolutionary histories, we need measured orbital parameters as accurate as possible. The accuracy of such measurements are limited due to uncertainties and degeneracies inherent to the Radial Velocity (RV) discovery technique. Nevertheless, the RV method is the most efficient technique for detecting extrasolar planets with more than 90% of all currently known planets being either detected or characterized using this method.

2.1 The Orbit of a Planet

2.1.1 The Orbital Elements

A comprehensive understanding of the radial velocity signal due to an exoplanet cannot begin without defining an appropriate coordinate system. It is usually used a Cartesian coordinate system where the planet orbits the star in the $\hat{x}$-$\hat{y}$ plane with the star at one focus, defined to be the origin, and with the x-axis pointing towards the periapse (see Figure 2.1). Defining the *true anomaly* as the angle $f = \theta - \varpi$, where θ is the *true longitude* and ϖ is the *longitude of periastron* of the planet's orbit, the position vector of the planet can be expressed as:

$$\begin{cases} x = r\cos f \\ y = r\sin f \\ z = 0 \end{cases} \tag{2.1.1}$$

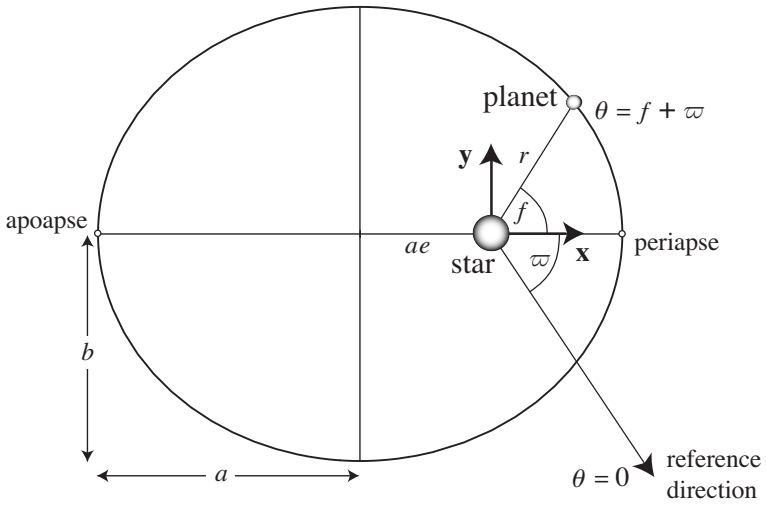

Figure 2.1: The planetary orbit around a star in the simplest reference frame. The orbit follows an elliptical path with the star at one focus, in accordance with Kepler's First Law. a is the semi-major axis of the ellipse, b the semi-minor axis and e the eccentricity. Figure from Murray and Correia [2011].

Where r is the distance between the star and the planet, given by:

$$r = a\frac{1-e^2}{1+e\cos f}. \tag{2.1.2}$$

Defining n as the *mean motion* $n = \frac{2\pi}{P}$, t_0 and the *orbital period* P, the following relations hold:

$$\dot{r} = \frac{na}{\sqrt{1-e^2}}\, e \sin f \tag{2.1.3}$$

and

$$r\dot{f} = \frac{na}{\sqrt{1-e^2}}(1+e\cos f)\,. \tag{2.1.4}$$

In a three-dimensional coordinate system, we need to define three more orientation angles: the *longitude of ascending node*, Ω, the *argument of periapse*, ω, and the *inclination* i. Ω and ω lie in different planes with

$$\varpi = \Omega + \omega \tag{2.1.5}$$

I pass to define the observer frame $\{X, Y, Z\}$ (see Figure 2.2), where the plane of the sky is X-Y and the observer is located far down the Z axis at $\{0, 0, +\infty\}$. One can move from coordinates in the $\{x, y, z\}$ system to the $\{X, Y, Z\}$ system by means of a series of

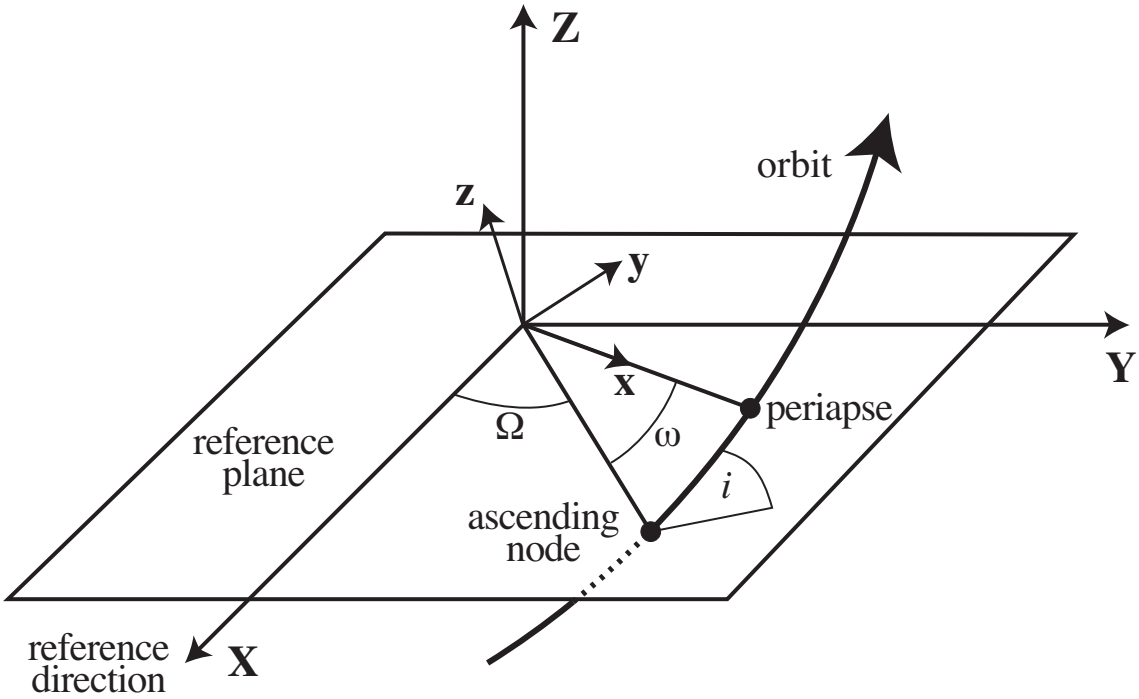

Figure 2.2: Orbital elements of a planet orbiting a star and the coordinate systems $\{x, y, z\}$ and $\{X, Y, Z\}$ (from Murray and Correia [2011]).

three rotations. The transformation can be written as:

$$\begin{pmatrix} X \\ Y \\ Z \end{pmatrix} = \mathbf{P}_z(\Omega)\mathbf{P}_x(i)\mathbf{P}_z(\omega) \begin{pmatrix} x \\ y \\ z \end{pmatrix} \tag{2.1.6}$$

where the rotation matrices about the x-axis and z-axis are respectively:

$$\mathbf{P}_x(\phi) = \begin{pmatrix} 1 & 0 & 0 \\ 0 & \cos\phi & -\sin\phi \\ 0 & \sin\phi & \cos\phi \end{pmatrix} \tag{2.1.7}$$

and

$$\mathbf{P}_z(\phi) = \begin{pmatrix} \cos\phi & -\sin\phi & 0 \\ \sin\phi & \cos\phi & 0 \\ 0 & 0 & 1 \end{pmatrix} . \tag{2.1.8}$$

Simplifying, the final Cartesian coordinates are:

$$\begin{cases} X = r\left(\cos\Omega\cos(\omega+f) - \sin\Omega\sin(\omega+f)\cos i\right) \\ Y = r\left(\sin\Omega\cos(\omega+f) + \cos\Omega\sin(\omega+f)\cos i\right) \\ Z = r\sin(\omega+f)\sin i \end{cases} \tag{2.1.9}$$

2.1.2 The Kepler Problem

Equations (2.1.9) gives the instantaneous position of a planet as seen by the observer in three dimensions. However, that expression is in terms of the true anomaly of the planet, f, rather than time, t. Moving from f to t is the essence of the *Kepler problem*.

In brief, a quantity which scales linearly with time is defined, the *mean anomaly* M:

$$M = n(t - t_0)\,, \tag{2.1.10}$$

where t_0 is the *time of periastron passage*. Introducing the *eccentric anomaly*, E, we can write:

$$M = E - e\sin E\,. \tag{2.1.11}$$

This is *Kepler's equation* and its solution is fundamental to the problem of finding the orbital position at a given time. Solving this transcendental equation is done numerically, starting from $E_1 = M$. For instance, the root can be found using the Newton-Rhapson iteration method [Danby, 1988], given by:

$$E_{i+1} = E_i - \frac{E_i - e\sin E_i - M}{1 - e\cos E_i} \tag{2.1.12}$$

Once E has been found to the desired level of precision, the true anomaly is calculated using:

$$\tan\frac{f}{2} = \sqrt{\frac{1+e}{1-e}}\tan\frac{E}{2}\,. \tag{2.1.13}$$

And the rate of change of f with respect to time is given by:

$$\frac{\mathrm{d}t}{\mathrm{d}f} = \frac{P}{2\pi}\frac{(1-e^2)^{3/2}}{(1+e\cos f)^2} \tag{2.1.14}$$

2.1.3 Kepler's Laws of Planetary Motion

Kepler's laws are fundamental in describing the orbital motion of planets and therefore it is opportune to mention them here as part of the basis of planetary dynamics. The three laws are:

1. The orbit of every planet is an ellipse with the Sun at one of the two foci (i.e. Figure 2.1)
2. A line joining a planet and the Sun sweeps out equal areas during equal intervals of time
3. The square of the orbital period of a planet is directly proportional to the cube of the semi-major axis of its orbit.

As will be seen for instance in §5.2.2, Kepler's third law is particularly significant for exoplanetary dynamics. Originally it was stated as $P^2 \propto a^3$ but Newton's version of Kepler's third law furnishes the constant of proportionality, derived from his Laws of Gravitation. For a star of mass M_* and a planet of mass m_p, in the reference frame of the star's rest frame, Kepler's Third Law states:

$$P^2 = \frac{4\pi^2}{G(M_* + m_p)} a^3 \tag{2.1.15}$$

2.2 The Radial Velocity Signal

As anticipated in §1.2.1, the radial velocity method searches for periodic Doppler shifts in the absorption spectra of stars caused by motion along the line of sight as the star orbits the centre of mass of the system. Therefore, in order to determine this observable, one needs to work in the *barycentric coordinate system*. Given the vector $\mathbf{r}$ which designates the distance between the star and the planet and defining the vectors pointing from the barycentre to the star and to the planet as $\mathbf{r}_*$ and $\mathbf{r}_p$ respectively, I have:

$$M_* \mathbf{r}_* + m_p \mathbf{r}_p = 0 \tag{2.2.1}$$

with

$$\mathbf{r} = \mathbf{r}_* - \mathbf{r}_p \,. \tag{2.2.2}$$

Using Equations (2.2.1) and (2.2.2), it is simple to obtain:

$$\mathbf{r}_* = \Big(\frac{m_p}{M_* + m_p}\Big)\mathbf{r} \tag{2.2.3}$$

Now, in the observer frame $\{X, Y, Z\}$ (Figure 2.2), I can define the position vector of the centre of mass $\mathbf{R}$, and the position vector of the star $\mathbf{R}_*$. The radial velocity of the star, v_r, is simply given by the projection of the velocity vector on the line of sight:

$$v_r = \dot{\mathbf{R}}_* \cdot \hat{\mathbf{Z}} = (\dot{\mathbf{R}} + \dot{\mathbf{r}}_*) \cdot \hat{\mathbf{Z}} = V + \frac{m_p}{M_* + m_p} \dot{Z} \,, \tag{2.2.4}$$

where $V = \mathbf{V} \cdot \hat{\mathbf{Z}}$ is the proper motion of the barycentre (stellar offset velocity) and $\dot{Z}$ can be calculated directly from Equations (2.1.9):

$$\dot{Z} = \dot{r} \sin(\omega + f) \sin i + r\dot{f} \cos(\omega + f) \sin i \,. \tag{2.2.5}$$

Making use of Equations (2.1.3) and (2.1.4), I obtain:

$$\begin{aligned} \dot{Z} &= \frac{na}{\sqrt{1-e^2}} e \sin f \sin(\omega + f) \sin i + \frac{na}{\sqrt{1-e^2}} (1 + e\cos f) \cos(\omega + f) \sin i \\ &= \frac{na \sin i}{\sqrt{1-e^2}} \left(e \sin f \sin(\omega + f) + e \cos f \cos(\omega + f) + \cos(\omega + f) \right) \end{aligned} \tag{2.2.6}$$

Using simple trigonometric identities for the angle $(\omega + f)$ one retrieves:

$$\dot{Z} = \frac{na \sin i}{\sqrt{1-e^2}} \left(\cos(\omega + f) + e \cos \omega \right) \,. \tag{2.2.7}$$

I can now write

$$v_r = V + K \left(\cos(\omega + f) + e \cos \omega \right) \,, \tag{2.2.8}$$

where K is the "radial velocity semi-amplitude":

$$K = \frac{m_p}{M_* + m_p} \frac{na \sin i}{\sqrt{1-e^2}} \,. \tag{2.2.9}$$

Using Kepler's third law (Equation 2.1.15) and the approximation $M_* + m_p \approx M_*$, I obtain:

$$K = \left(\frac{2\pi G}{P} \right)^{1/3} \frac{m_p \sin i}{M_*^{2/3}} \frac{1}{\sqrt{1-e^2}} \,. \tag{2.2.10}$$

It is remarkable that Z does not contain any dependency upon Ω and thus RV measurements cannot constrain this parameter. Moreover, it is important to underline that i here indicates the planetary orbital inclination to the plane of the sky (not the star's equator). In general, mass and inclination cannot be determined independently from the RV signature alone; therefore, we can only infer the minimum mass $m_p \sin i$.

In the case of a multi-planet system, to first approximation, the resulting signal is a

linear superposition of Keplerian orbits. Even if we make the assumption that the system is coplanar and seen edge-on ($\sin i = 1$) and that we know M_* from stellar models, an N-planet configuration is described by some $F_P = 5N + 1$ parameters: the stellar offset velocity V and for each planet ω, e, m_p, P (interchangeable with a) and M. The mean anomaly M is deductible from f and changing with time while the planet moves along its orbit, produces the shape of the Radial Velocity curve.

2.3 Radial Velocity Measurements

The radial velocity signal has to be derived from spectral shifts with huge precision: better than 12 m/s for a Jupiter-like planet at 5.2 AU, 3 m/s for an indicative super-Earth and better than 0.1 m/s for an Earth-like planet in the habitable zone. These indicate that spectral shifts of the order of 10^{-4} to 10^{-6} Å have to be detected.

Radial velocity measurement precision has continually improved from the initial ∼15 m/s regime [Campbell and Walker, 1979] (indicated with CW79 in Figure 2.3) to the current state-of-the-art of 1 m/s or better. This has permitted the detection of weaker signals consenting the discovery of some of the lowest-mass planets identified such as: GJ 876 d [Rivera et al., 2005], HD 40307 b [Mayor et al., 2009b], 61 Vir b [Vogt et al., 2010b], GJ 581 e [Mayor et al., 2009a] and α Centauri B [Dumusque et al., 2012].

Moreover, a naïve exposure taken with the highest-resolution spectrograph available would still be inconclusive due to thermal changes and pressure fluctuations, which alone procure shifts of the order of hundreds of m/s and effectively overwhelm any planetary signal.

The attainment of very high measurement precision has mostly been a matter of controlling systematic measurement errors. Current precision radial velocity bypasses this matter by employing high-resolution echelle spectrographs and taking synchronous reference spectra for continuous calibration of the stellar spectra. The two more suitable approaches to dealing with drifts are the thorium-argon reference (e.g. ELODIE, CORALIE, HARPS; Pepe et al. [2003]) and the iodine absorption cell techniques (e.g. HIRES; Vogt et al. [1994]). The use of a gas absorption cell or the continual illumination with a separate reference spectrum measures intrinsic spectrograph drifts. Enclosing the spectrograph in a vacuum vessel and stabilizing the temperature to mK tolerances can result in the achievement of residuals to planetary orbit fits as low as 30 cm/s. This is the case of the High Accuracy Radial velocity Planet Searcher (HARPS), a high-resolution optical spectrograph installed on the 3.6-m telescope at La Silla Observatory (ESO, Chile) also for follow-up studies of transit candidates from the Kepler mission [Torres et al., 2009].

Nonetheless, a number of intrinsic limitations make reaching the sub-m/s precision, which is required to detect Earth-mass planets around solar-type stars ($K \approx 0.1$ m/s), a

challenge. Intrinsic stellar noise, both on the short term (of the order of tens of minutes; e.g. granulation, atmospheric oscillations and other magnetic activity) and long term (e.g. magnetic activity cycles) can dominate the error budget in the form of "jitter".

In addition to stellar noise, the main factors currently limiting the precision of the RVs are photon noise, the wavelength calibration, telescope guiding, stability in the illumination of the spectrograph, and detector-related effects. The only solution to photon noise is more photons. This may come from either larger telescopes equipped with high-precision spectrographs, or more telescope time on existing facilities permitting longer exposures without compromising the size of the samples of stars surveyed for planets. Indications are that the remedy to the problem of stellar noise may be similar. Longer exposures or binning over suitable time-scales (again implying access to more telescope time) can reduce astrophysical jitter to some extent by averaging out those intrinsic variations (see, e.g., Pepe and Lovis [2008]).

Overall, this technique has been the most prolific in terms of number of planets discovered; at the time of writing, more than 500 planets were first detected through their radial velocity signal. The RV technique is intrinsically biased towards planets that produce a large K (Equation (2.2.10)): short-period, massive planets will be more easily detected, which explains the initial prevalence of hot Jupiters among planet candidates. Long-period and very eccentric orbits, on the other hand, suffer from inadequate phase coverage (e.g. Cumming [2004], Cumming et al. [2008]).

Reaching this level of measurement precision opens up new possibilities for planet detection. While the radial velocity signal of an Earth-mass planet in a 1-AU orbit around a solar-mass star is only 9 cm/s, we do have the measurement precision to detect habitable Earths around low-mass M stars, and to detect Super Earths in short-period orbits around solar-mass stars. For super Earths an extremely wide variety of compositions is possible, with mixtures of various fractions of metals (iron and nickel), silicates, "ices" (water, methane, ammonia, etc.) and H_2-He. The detection of these objects, and the measurement of their mass and radius (for those that undergo transits), can open up new areas of planetary astrophysics.

2.4 Systemic

To perform an analysis of RV data I use the Systemic Console[1] [Meschiari et al., 2009]. Systemic is a software package that provides an intuitive graphical user interface for the fitting of planetary signatures, and an associated suite of dynamical analysis tools. The program is written in Java programming language and it has already been used to derive orbital fits in other works such as Vogt et al. [2010b] and Meschiari et al. [2011]. I give an overview of the computational tools included in the Console and

[1] Available at `http://www.oklo.org`

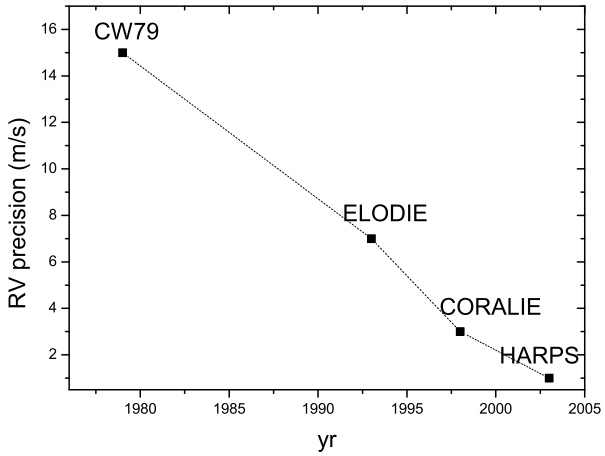

Figure 2.3: Development of Doppler techniques during last decades.

of the algorithms offered for streamlining the characterization of planetary systems: the Lomb-Scargle (LS) periodogram identifies periodicities in the RV dataset, Lomb-Scargle periodogram of residual studies periodicities in the residual RV dataset, simulated annealing is used for global multi-parameter optimization, while for local multidimensional optimization there are the Levenberg-Marquardt (L-M) scheme which ensures a rapid convergence and the Nelder-Mead (sometimes called AMOEBA) algorithm [Press et al., 1992].

2.4.1 Modelling the Radial Velocity Signal

When dynamical interactions among planets are negligible during the time range spanned by observations, as for the majority of cases, an extrasolar planetary systems can be represented as a sum of N Keplerian orbits each described by the osculating orbital elements, with the radial velocity variation of the star being:

$$v_r(t) = V + \sum_{i}^{N} K_i \left(\cos(\omega_i + f_i) + e_i \cos\omega_i\right) , \tag{2.4.1}$$

Summed Keplerians offer a satisfactory model for almost all of the planetary systems that have been detected so far. Kepler's equation is quickly solved using a simple iterative scheme, and hence models can be rapidly assessed.

In some cases, such as HD202206 [Correia et al., 2005], GJ 876 [Rivera et al., 2005] and HD60532 [Laskar and Correia, 2009], a *self-consistent*, or Newtonian fit is required. For instance, in this way a 3:1 MMR was confirmed for the two giant planets orbiting HD 60532. Here, planetary interactions are taken into account in the fit, and the Console

adopts an N-body model of the system with:

$$\frac{\mathrm{d}^2\mathbf{x}_i}{\mathrm{d}t^2} = -\sum_{j\neq i} \frac{Gm_j(\mathbf{x}_i - \mathbf{x}_j)}{|\mathbf{x}_i - \mathbf{x}_j|^3}\,, \tag{2.4.2}$$

whereas the integrations are carried out using either Hermite 4th-order, 4th/5th order Runge-Kutta with adaptive timestep or Gragg-Bulirsch-Stoer integrator [Press et al., 1992, Hut et al., 1995].

The Console performs parameter minimization of the so-called reduced chi-square statistic:

$$\chi^2_{red} = \frac{1}{D - F_P} \sum_{i=1}^{D} \frac{(v_r(i) - \bar{v}_r(i))^2}{\sigma_i^2}\,, \tag{2.4.3}$$

where D is the number of radial velocity data points, F_P is the number of parameters to fit (so $D - F_P$ indicates the number of degrees of freedom), σ_i is the uncertainty on data point $v_r(i)$ and $\bar{v}_r(i)$ is the expected value given by the fitted model. As a rule of thumb, a reduced Chi-square value near unity is denotative of a *good* fit to the data, indicating that the model is a reasonable explanation of the data within the observational errors. Generally, larger values usually signal an insufficient modelling of the data, whereas smaller values denote that the data has been over-fit.

Sometimes, adding a planet to a model can improve the fitting. Therefore, it becomes important to assess the probability that the best model fitted to a set of velocities could have been generated just by noise fluctuations, rather than being originated by a genuine signal. This false alarm diagnostic is particularly appropriate for signals having amplitudes comparable to the noise in the velocity measurements.

The F-test can be used in this sense and it works under the hypothesis that the errors of the measurements have a Gaussian distribution. This test determines the probability that one model built with additional free parameters (e.g. the five parameters describing a new planet) is to be preferred over another model [Bevington and Robinson, 1992, Cumming, 2004]. Although an a priori limit cannot provide an absolute evidence that the orbits are real as fluctuations may produce spurious signals, usually a threshold of *false alarm probability* $FAP < 0.01$ is seen as an useful benchmark for suggesting that a planetary signal exists in the velocity measurements (e.g. Marcy et al. [2005])

Other considerations about the quality of a fitting follow. Given the residuals r_i of the radial velocity data to a model, the root mean square (rms) scatter is defined as:

$$rms = \sqrt{\frac{1}{D}(r_1^2 + ... + r_D^2)}\,. \tag{2.4.4}$$

A genuine model should not have rms scatter less than the median uncertainty of the RV data and the amplitude K of a real planetary signal should be greater than the rms

scatter.

2.4.2 Best-fit Model Estimation

Given the observations and related uncertainties, the aim is to reach a model configuration $\mathbf{z}_{best}$ (a $5N + 1$ vector of parameters) such that $\chi^2(\mathbf{z}_{best}) = min_z\chi^2$; this is the so-called "best-fit". As shown for instance in Cumming et al. [2008], normally, the fitting process begins with analysing the Lomb-Scargle periodogram to search for periodicities in the data; periodicities are selected in order of decreasing semi-amplitude K and optimized employing line-minimization. This process leads to a set of orbital parameters $\mathbf{z}_0$ which is an approximate estimate of the best-fit solution, and can be polished by making a minimization of multi-parameters at the same time.

Periodograms and False Alarm Probabilities Astronomical time-series observations are often characterized by uneven temporal sampling and/or non-uniform coverage (e.g., from day/night cycles). This complicates the search for periodic signals, as a fast Fourier transform (FFT) algorithm cannot be employed.

Systemic incorporates the Lomb-Scargle (LS) periodogram, an algorithm for time series analysis of unevenly spaced data [Lomb, 1976, Scargle, 1982, Press et al., 1992]. The LS periodogram and the subsequent residuals to a given fit are useful to extrapolate the orbital periods from the observed data. This is done without having to fit at first for the other orbital parameters. The Console implements the formula for an error-weighted periodogram $P_x(w)$ given in Gilliland and Baliunas [1987], where the individual weights are given by $w_k = \frac{1}{\sigma_k^2}$.

Each periodic signal is associated with an analytic *false alarm probability*. Normalizing the periodogram by the total variance $p_0(w) = P_x(w)/\sigma^2$, we have that the estimated probability that a peak as high or higher would arise by chance is given by $\mathbb{P}(p_0; N_f) = 1 - [1 - exp(-p_0)]^{N_f}$, with N_f being the effective number of frequencies (a technical discussion is reported in Cumming [2004]).

Lastly, the Console gives also the possibility to show the power spectral window [Deeming, 1975] superimposed on the standard (non-error weighted) periodogram. In fact, the unequal spacing of the data can be a source of spurious periodicities like those associated with yearly observational schedules or the synodic lunar month.

Simulated Annealing (global minimization) The best-fit to the data is searched by utilising simulated annealing (SA, [Press et al., 1992]), a "global" minimization technique which attempts to avoid getting trapped in local minima by adding a degree of randomness at each iteration step, although at a much greater computational cost. SA is an algorithm suitable especially for rugged χ^2 surfaces. Similarly to numerous

thermodynamic processes in nature, simulated annealing designates an "energy" E as the actual function to minimize and permits temperature variations between states at various energies as function of the current temperature T_k; the latter being decreased by a scheduler.

The user can configure the parameters:

1. *generator of trial configurations*: by default the configurations are generated according to a Gaussian function centred around the current configuration. The scale parameter vector σ_μ^2 can be modified by the user and can be chosen independently for each parameter.

2. *temperature scheduler*: by default temperature is lowered according to $T_k = T_0(1 - \frac{k}{A})^\alpha$, where A, T_0 and α indicate the number of steps, initial temperature and cooling rate, respectively.

The trial configuration $\mathbf{z}_{k+1}$ is generated by the current set of parameters using by default a multivariate Gaussian distribution centred on the current step $\mathbf{z}_k$. The function to be minimized is $\chi^2(\mathbf{z})$ in our case. Considered a state $\mathbf{z}_k$, the algorithm selects a new set $\mathbf{z}_{k+1}$; this configuration is accepted if $E_{k+1} < E_k$ (a downhill step), moreover, it is kept with probability $\mathbb{P}(k \to k+1) \sim exp(-\Delta E/T_k)$ if $E_{k+1} > E_k$. Afterwards, following the scheduler, the temperature is refreshed to a new value and the iteration is repeated until the target number of steps A is reached. Since uphill steps may be adopted, the algorithm can explore a larger portion of the phase space. This makes less likely the possibility of getting stuck in a narrow local minimum.

Local minimization The solution from SA can be used as a starting point for a "local" χ^2-minimisation. This avoids missing promising solutions when the SA step size is too large to properly resolve them.

Multidimensional parameter minimization can be performed utilizing the Levenberg-Marquardt algorithm (LM, [Press et al., 1992]). Given the initial guess $\mathbf{z}_k$, the LM routine can converge fast to a local minimum $\mathbf{z}_{lm}$. Good convergence of the LM algorithm depends on a favourable geometry of the $\chi^2(\mathbf{z})$ surface and on the selected initial guess: specifically, the routine is sensitive to rugged χ^2 surfaces and can be prone to converging to non-optimal minima.

The local minimisation can be also performed by invoking the AMOEBA routine [Press et al., 1992]. AMOEBA is a downhill simplex algorithm originally published by Nelder and Mead [1965], it is designed to solve the classical unconstrained optimization problem of minimizing a given non-linear function. As anticipated, the Nelder-Mead method is simplex-based, a simplex S in $\mathbb{R}^n$ is defined as the convex hull of $n+1$ vertices $x_0, ..., x_n \in \mathbb{R}^n$. For example, a simplex in $\mathbb{R}^2$ is a triangle (see some examples in Figure 2.4). Fitting for N planetary orbits means that $n = 5N + 1$.

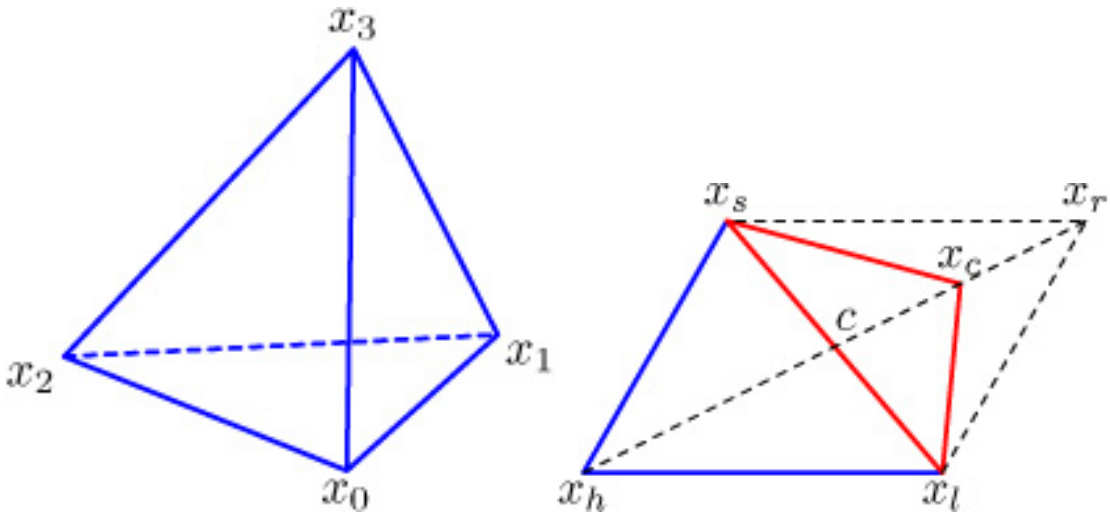

Figure 2.4: Examples of simplexes. Left: A simplex in $\mathbb{R}^3$. Right: The simplex "contract" transformation in $\mathbb{R}^2$, the new simplex is shown in red [Singer and Nelder, 2009].

The method begins with a set of $n+1$ points $x_0, ..., x_n \in \mathbb{R}^n$ that are considered as the vertices of a working simplex S, and the corresponding set of function values at the vertices $f_j := f(x_j)$, for $j = 0, ..., n$.

The method then performs a sequence of transformations of the working simplex S, aimed at decreasing the function values at its vertices. At each step, the transformation is determined by computing one or more test points, together with their function values, and by comparison of these function values with those at the vertices. This process is terminated when the working simplex becomes sufficiently small in some sense, completing the minimization of the function.

2.5 Orbital Resonances

Having introduced the basic theory for the analysis of the Radial Velocity signal, I can now move to describe some dynamical mechanisms among planets that can be relevant when exploring the architecture of a system detected via RV.

Orbital resonances represent special dynamical states for planetary systems. An orbital resonance happens when two orbiting bodies, 1 and 2, exert a regular, periodic gravitational influence on each other. Orbital resonances amplify enormously the mutual gravitational influence of the bodies, i.e., their potential to change or constrain each other's orbits. In some cases, this results in an unstable interaction, in which the bodies exchange momentum and alter orbits until the resonance no longer exists. Under some circumstances, a resonant system can be stable so that the bodies remain in resonance.

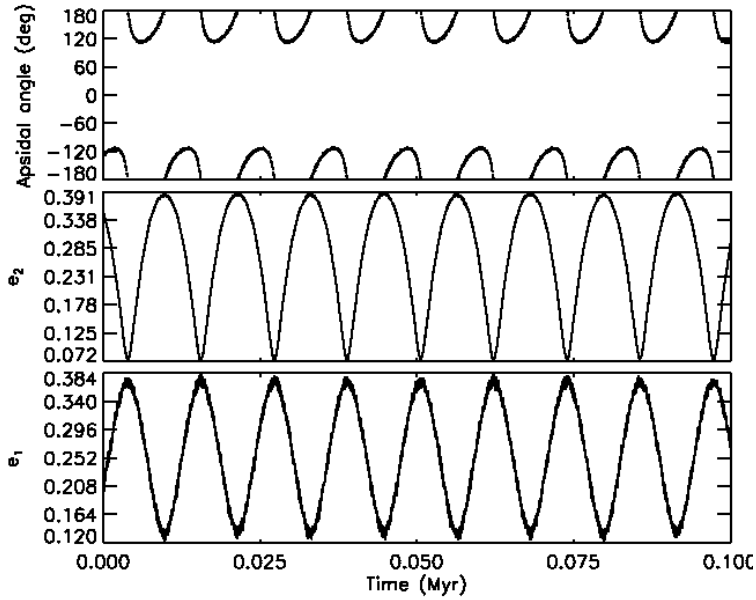

Figure 2.5: Eccentricity and apsidal angle variation from an N-body simulation for the HD 12661 system (from Veras and Armitage [2007]).

2.5.1 Secular Resonances

Secular resonances happen when the precessions of two orbits are synchronised (usually a precession of the periapse or ascending node). Over secular time-scales, the two bodies will exchange angular momentum periodically meaning that the orbital eccentricities and inclinations will vary periodically. A small body in secular resonance with a much larger one will precess at the same rate as the large body. Over relatively short time periods (order of millions of years) a secular resonance will excite the eccentricity and inclination of the small body.

A system of two bodies in apsidal resonance has the critical angle $\phi = \varpi_1 - \varpi_2$ librating. The amplitude of libration, is often used to indicate how "deep" the system is in resonance. As example, Figure 2.5 presents the case of the two planets of the HD 12661 system. The evolution of the eccentricities are shown alongside the apsidal angle librating around 180° with a semi-amplitude of about 60°.

2.5.2 Mean Motion Resonances

Mean Motion Resonances occur when pairs of bodies have orbital periods whose ratio can be approximately expressed as a ratio of two small integers, so we have that "exact" resonance arise when

$$j_1 n_1 + j_2 n_2 \approx 0\,. \tag{2.5.1}$$

Let $j_1 = p + q$ and $j_2 = -p$, where p and q are positive integers and q is the *order of the resonance*. In fact, for planets on nearly circular, coplanar orbits the strength of the resonance potential is proportional to e^q or i^q. Inclination resonances occur only for even q. The case $q = 0$ is the co-orbital resonance; examples in the solar system include the Saturnian satellites Epimetheus and Janus and the Trojan asteroids in $1:1$ resonance with Jupiter, but no extrasolar co-orbital resonances are known. The *nominal resonance location*, a_n, of the $p + q : p$ resonance is defined to be the semi-major axis of the outer body that satisfies the relation

$$a_n = a_1 \Big(\frac{p+q}{p} \Big)^{2/3} . \tag{2.5.2}$$

In a resonant configuration, the longitude of the planets at every qth conjunction librates slowly about a direction determined by the lines of apsides and nodes of the planetary orbits. This geometry is naturally described by the libration of a so-called critical argument which is a linear combination of the angle variables:

$$\phi = j_1\lambda_1 + j_2\lambda_2 + j_3\varpi_1 + j_4\varpi_2 + j_5\Omega_1 + j_6\Omega_2 \, . \tag{2.5.3}$$

where $\lambda = M + \varpi$ is the *mean longitude* and the condition on the coefficients is:

$$\sum_{k=1}^{6} j_k = 0 \, . \tag{2.5.4}$$

The angle ϕ will be seen circulating if the system is not in the considered resonance and librating if it is. To execute this oscillatory behaviour, the resonant angle must reside in a "bound state" within an "effective potential well".

For example, there are ten possible resonant arguments associated with the 2nd order 3:1 commensurability. The time derivatives of the six resonant angles are:

- $\dot{\phi}_1 = 3n_1 - n_2 - 2\dot{\varpi}_1$,
- $\dot{\phi}_2 = 3n_1 - n_2 - \dot{\varpi}_2 - \dot{\varpi}_1$,
- $\dot{\phi}_3 = 3n_1 - n_2 - 2\dot{\varpi}_2$,
- $\dot{\phi}_4 = 3n_1 - n_2 - 2\dot{\Omega}_1$,
- $\dot{\phi}_5 = 3n_1 - n_2 - \dot{\Omega}_2 - \dot{\Omega}_1$,
- $\dot{\phi}_6 = 3n_1 - n_2 - 2\dot{\Omega}_2$,
- $\dot{\phi}_7 = 3n_1 - n_2 - \dot{\varpi}_1 - \dot{\Omega}_1$,
- $\dot{\phi}_8 = 3n_1 - n_2 - \dot{\varpi}_1 - \dot{\Omega}_2$,

- $\dot{\phi}_9 = 3n_1 - n_2 - \dot{\omega}_2 - \dot{\Omega}_1$,
- $\dot{\phi}_{10} = 3n_1 - n_2 - \dot{\omega}_2 - \dot{\Omega}_2$.

Substantial contributions to the precession rates lead to a "splitting" of the basic resonance into subresonances over a range of semi-major axes. If the splitting is much greater than the sum of the subresonaces half-widths, each one can be analysed in isolation. Moreover, when the splitting is exceedingly small compared to the widths, all the subresonances collapse into a single resonance and orbits are non-chaotic. On the other hand, when the separation between neighbouring resonances is comparable to their widths, the interaction between resonances is strong and a strong instability of the motion occurs: most orbits in the vicinity of the resonances are chaotic, with stable resonance possible only in very narrow regions of the phase space [Malhotra, 1998, Murray and Dermott, 1999]. Systems for which the resonance angle librates for several cycles, then circulates for one or more cycles, and then resumes its oscillatory motion (libration) are said to experience the nodding phenomenon. Nodding can be illustrated as complex motion near a separatrix in the phase space of the resonance angle [Ketchum et al., 2012].

The current observational sample of multi-planet systems have orbital period ratios that are close to integer values, these systems are thus candidates for being in MMR (e.g., Fabrycky et al. [2012b]). Because of the special conditions required for a planetary system to reside in mean motion resonance, systems found in such states must have a constrained dynamical history. The relative fraction of planetary systems in mean motion resonance thus provides important information regarding planetary formation and early dynamical evolution.

2.6 The Stability Criterion

I have introduced the basics of planetary motion and given a general idea of the dynamical mechanisms that can characterize planetary systems and make them stable. I can now describe how this knowledge can be used to extrapolate more information from RV signals. In fact, as the time baseline becomes larger, it is possible to distinguish a trend in the RV signals due to long-period outer companions that have not completed a single orbit yet. In this case, it can happen either that the profile of χ^2 is very smooth, or that it does not have a well definite minimum, as a result the confidence levels may comprise large intervals of the parameters fitted.

The *a priori* unspecified number of planets, narrow observational windows, stellar jitter and weakly constrained orbital parameters, can lead to not unique solutions and (quite often) to best-fits representing unrealistic scenarios. In fact, these solutions can present well-constrained minimum masses but also a poorly constrained eccentricity

for the outermost planet; i. e., in the statistically optimal best-fit solutions, the eccentricities can be large and can rapidly (on the time-scale of thousands of years) bring to catastrophic collisional instabilities [Goździewski et al., 2008].

According to the Copernican assumption that we are not observing the universe at a privileged time, the detection of a rapidly unstable system during a few years of RV observations is not likely, then a fit which corresponds to a quickly unstable configuration is also doubtful. Therefore, we can aim to put limits on the masses and orbital elements of the planets by investigating and finding the plausible and stable solutions. In this logic, the *dynamical stability* is an additional observable that must be taken into consideration when interpreting the RV data. It turns into a discriminating element especially when the longest orbital period is only partially covered [Murray and Holman, 2001, Goździewski et al., 2003].

Often, a stability criterion is applied once the best-fit unstable solution is found, subsequently the orbital elements are tuned to get a stable configuration. However this approach does not necessarily provide stable fits that are simultaneously optimal in term of χ^2 or RMS. Most of the times, with the term *stable* is indicated a configuration which does not disrupt or change qualitatively during a period of time of the order of million years. The literature is plenty of studies which take into account stability when modelling the RV data. Here we just mention the work of: Veras and Ford [2010] reporting on the system stability, secular evolution and the extent of the resonant interactions for 5 dynamically active multi-planet systems; Wright et al. [2009] which derive updated orbital parameters for a number of systems considering mutual interactions between planets; Goździewski et al. [2003, 2006, 2008] which directly eliminate unstable solutions during the fitting procedure using GAMP; and Correia et al. [2010] which give constraints on the inclination with respect to the line of sight for some of the planets in the GJ 876 system. In fact, in the GJ 876 system, planets 'd', 'c', and 'b' (in order of increasing semi-major axis) have periods close to the ratio $1 : 2 : 4$; planets 'd' and 'c' are close to a secular resonance. Because of these near-resonances, gravitational interactions between the planets are detectable in the radial-velocity data, and these can be used to constrain the mutual inclinations and determine whether various critical arguments librate or circulate. I also should remind the reader about the directly imaged system HR 8799, where the difficulties in finding regions of stable motion may indicate the system is undergoing a phase of planet-planet scattering [Goździewski and Migaszewski, 2009].

In many situations, the interactions between planets are negligible and can be ignored. So the RV signal is just a linear superposition of different Keplerian RV curves. On the other hand, planetary interactions and resonances can be important and must be taken into account performing numerical integrations. In the short time-scale, these interactions can cause significant variations in the orbital parameters of the planets: an ensemble of constant Keplerian orbital elements cannot be adequate to model the RV

data and an *N*-body Newtonian model should be applied.

However, it can also happen that good Newtonian fits to the data produce planetary orbital parameters that are stable for the period of observations but lead to disruption on time-scales substantially shorter than the age of the planetary system. In this respect, long-term stability is an additional but necessary constraint that must be satisfied by multi-planet fits.

2.7 Studying the dynamical stability with SWIFT

Studying the stability of a planetary system for millions of years using the tools of Systemic is very time consuming. This is because the software plots the orbital elements almost simultaneously making the computation very slow.

For this reason, I have adopted SWIFT [2] for the study of long-term stability [Levison and Duncan, 1994].

The SWIFT subroutine package is designed to integrate a set of mutually gravitationally interacting bodies together with a group of test particles. Four integration techniques are included, for this problem I adopt the Wisdom-Holmam Mapping (WHM), an *N*-body mapping method [Wisdom and Holman, 1991].

I have implemented a code that use the module *orbel_el2xv* to create the initial conditions data file, usually called *pl.in*, to be used by the SWIFT routines. This code needs as input for each planet the mass, semi-major axis, eccentricity, inclination, longitude of ascending node, argument of perihelion and mean anomaly. This information should be listed in *planet_xx.dat* where "xx" indicates the sequence number of the planet included in the computation.

The format of the *pl.in* file is as follows: the first line indicates the number of massive bodies (including the host star), then three lines are dedicated to each body to indicate its mass and its heliocentric position and velocity 3D vectors. Other two input files for SWIFT are usually called *param.in* and *tp.in*. While *tp.in* includes information on the test particles to be included in the simulation, in *param.in* is possible to define the period of integration and the time-step. The output of SWIFT includes the file *energy.out*, to check if energy and angular momentum are conserved during the simulation, and *bin.dat*, a binary file where the orbital information is written.

I have also written another program that takes the information in *bin.dat* and writes the ascii files *follow_xx.dat* reporting for each planet: time, semi-major axis, eccentricity, inclination, longitude of ascending node, argument of perihelion, mean anomaly, periastron and apoastron distance.

I have set with SWIFT a numerical simulation which includes Jupiter and Saturn orbit-

[2] Available at `http://www.boulder.swri.edu/ hal/swift.html`

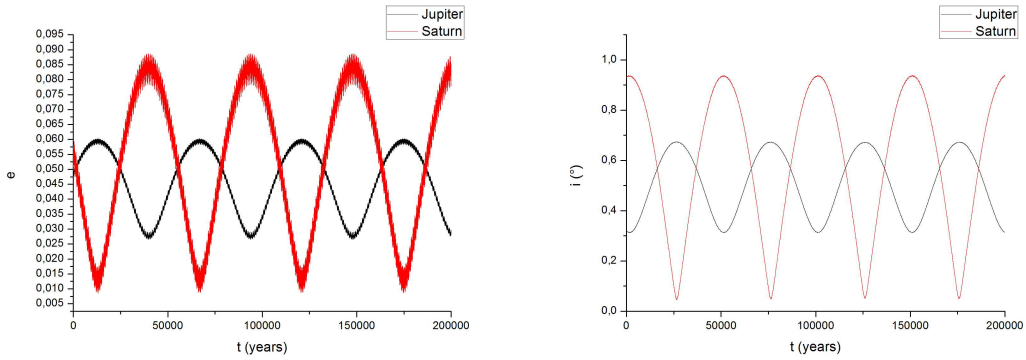

Figure 2.6: Orbital parameters evolution for Jupiter and Saturn derived from numerical simulations. Left: eccentricities. Right: inclinations.

ing the Sun. The computation cover a time span of 200,000 y with a time-step of 0.25 y. Figure 2.6 reports the temporal evolution of the eccentricities and inclinations for Jupiter and Saturn.

CHAPTER 3

Dynamical Mechanisms of Planetary Systems

3.1 Introduction

The number of discovered planets in other systems is rapidly growing, and the observational sample shows an astonishing diversity of architectures. One way to characterize these planetary systems is in terms of their orbital elements, where the semi-major axis a and orbital eccentricity e are most often used. These variables are equivalent to specifying the energy and angular momentum of the orbit. Previous expectations, informed by the structure of our Solar system, predicted planetary orbits with larger values of a and smaller values of e than those found in the current observational sample. A major theoretical effort is now being put forth to provide an explanation of the observed distributions of orbital elements, e.g., the $a - e$ plane. In multiple-planet systems, however, it can be important to keep in mind that the orbital eccentricities can vary dramatically through secular interactions on time-scales that are long compared to observational baselines but short compared to the system ages. Instead of being described by a single value of eccentricity, the orbits of planets in multiple-planet systems should generally be characterized by a complete distribution of eccentricity values (e.g. Takeda and Rasio [2005]).

Considering the multi-planet systems detected by ground-based RV observations and the more than 360 transiting multi-planet systems detected by the Kepler spacecraft, many planets also appear to be close to mean-motion resonances. In particular, Fabrycky et al. [2012b] find that Kepler planet pairs with orbital period ratios within a few percent of $2:1$ or $3:2$ are preferentially found just wide of the resonance (i.e., period ratio slightly larger than 2 or 1.5).

Determining the physical processes that lead to the observed diversity of planetary systems remains an area of active research and debate. The discovery of dynamically quiescent, short-period multiplanet systems by the Kepler mission, such as Kepler 11

[Lissauer et al., 2011a], provides clear evidence for disc-driven type I migration of bodies that probably formed beyond the ice line in their protoplanetary discs [Ward, 1997]. Similarly, giant planet systems in 2:1 mean-motion resonance such as GJ 876 [Marcy et al., 2001] provide evidence for disc-driven type II migration of gap-forming planets because of the slow convergent migration rates required for resonant capture [Snellgrove et al., 2001, Lee and Peale, 2002, Crida et al., 2008], as do giant planets on short to intermediate period orbits that are too remote from their central stars to have undergone significant tidal evolution.

The relatively large eccentricities observed for the extrasolar planet population as a whole, however, indicate that disc-planet interactions do not tell the whole story. A plausible explanation for many of these systems is that they formed on near-circular orbits in the disc, but after disc dispersal dynamical instability led to planet-planet gravitational scattering [Ford and Rasio, 2008]. Evidence is provided by the fact that numerical planet scattering experiments can reproduce the observed eccentricity distribution successfully [Chatterjee et al., 2008, Jurić and Tremaine, 2008], and the observation that a number of short-period transiting planets have orbit planes inclined significantly with respect to the stellar equatorial plane [Winn et al., 2010]. Furthermore, ideas for explaining eccentric orbits include eccentricity driving through disc-driven migration of a resonant pair of planets [Moorhead and Adams, 2005], and sweeping secular resonances caused by the various combinations of protoplanetary disc dispersal, spin-down of an initially rapidly spinning oblate central star, and general relativistic precession [Nagasawa et al., 2005, Adams and Laughlin, 2006a].

3.2 Secular Perturbations Theory

3.2.1 The Laplace–Lagrange Apsidal Precession Model

For the purpose of undertaking a simplified analysis of the dynamical evolution of a planetary system, I have implemented a Laplace-Lagrange secular model. This model can be described using a set of linear first-order differential equations, whose solution is a system of eigenmodes. In fact, with suitable approximations, it is possible to find an analytical solution to the N-body problem. This can be done by considering the effects of the purely secular terms in the disturbing function for a system of N masses orbiting a central body. The disturbing function includes secular terms for the mutual gravitational interaction between all N-1 planets that are second order in the eccentricities and first order in the masses (see e.g. Murray and Dermott [1999]). Therefore, it is possible to construct the equations of motion for the evolution of the planets' eccentricities (e) and longitude of periastra (ϖ): this represents the secular solution for the apsidal precession.

For planet j, Lagrange's equations for the eccentricity vector $(h_j, k_j) = e_j(\sin\varpi_j, \cos\varpi_j)$ are

$$\frac{dh_j}{dt} = \sum_l A_{jl} k_l \tag{3.2.1}$$

$$\frac{dk_j}{dt} = -\sum_l A_{jl} h_l, \tag{3.2.2}$$

where

$$A_{jj} = \frac{n_j a_j}{4} \sum_{l \neq j} \left(\frac{m_l}{M_* + m_j} \right) \frac{\alpha}{a_>} b^1_{3/2} \tag{3.2.3}$$

$$A_{jl} = -\frac{n_j a_j}{4} \left(\frac{m_l}{M_* + m_j} \right) \frac{\alpha}{a_>} b^2_{3/2}, \tag{3.2.4}$$

The standard terms $\alpha = a_</a_>$, $a_> = \max(a_j, a_l)$, $a_< = \min(a_j, a_l)$, and Laplace coefficients (b^s_i) have been used.

Solving these equations for a planetary system is an eigenvalue problem whose eigenfrequencies (g_i) are real and represent the precession frequencies of the modes. The secular frequencies g_i are functions of the planet masses m_j and semi-major axes a_j. The solutions are of the form

$$\begin{aligned} h_j &= \sum_i e_{ji} \sin(g_i t + \beta_i) \\ k_j &= \sum_i e_{ji} \cos(g_i t + \beta_i)\,. \end{aligned} \tag{3.2.5}$$

In fact, with the eigenvalues g_i we retrieve the unscaled eigenvectors with elements of the form $\bar{e}_{ji}$ where $S_i \bar{e}_{ji} = e_{ji}$. The scaling factors S_i are determined from the boundary conditions: one can get the values for h_j and k_j at time $(t = 0)$, substituting $(t = 0)$ in the general solution (3.2.5) and knowing $\bar{e}_{ji}$ it is possible to solve the system of equations to get the unknowns S_i and β_i.

Jupiter and Saturn It is possible to apply the described theory to the case of Jupiter and Saturn orbiting the Sun, in order to obtain the secular solution for the apsidal precession. Using the observed values [1] for the parameters of the system at September 2010, I can retrieve the scaled eigenvectors e_{ji} and phases β_i. From that, I can obtain h and k for Jupiter and Saturn at any time t. The relation $e_j = \sqrt{h_j^2 + k_j^2}$ is used to calculate the eccentricity of planet j. I obtain:

$$e_J(t) = \sqrt{0.00217 + 0.00008\cos(0.00514t) + 0.00136\sin(0.00514t)} \tag{3.2.6}$$

$$e_S(t) = \sqrt{0.00352 - 0.00021\cos(0.00514t) - 0.00337\sin(0.00514t)}\,. \tag{3.2.7}$$

[1] Ephemeris available on JPL HORIZONS `http://ssd.jpl.nasa.gov/?horizons`

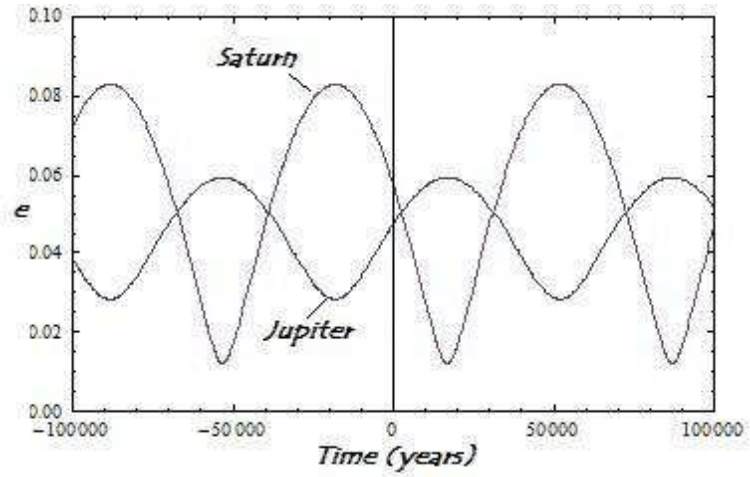

Figure 3.1: The eccentricities of Jupiter and Saturn as derived from the secular theory.

where the frequencies are in degrees per year. This implies a fixed periodicity of $\frac{360}{0.00514} = 70039$ yr in the variation of the eccentricity of each planet. Figure 3.1 shows the evolution of the eccentricities of the two planets over a time span of 200,000 yr derived from my secular solution, the results are in agreement with Murray and Dermott [1999].

These results can be compared with the ones derived in §2.7 from a numerical computation (see Figure 2.6). It is possible to notice that since the orbits of Jupiter and Saturn are close to a 5:2 commensurability, additional perturbations on time-scales that are shorter than those associated with the secular variation are introduced.

The eigenfrequencies of the system are:

$$g_1 = 9.63434x10^{-4}\frac{^\circ}{yr}, g_2 = 6.09908x10^{-3}\frac{^\circ}{yr}\,. \tag{3.2.8}$$

The resulting scaled eigenvectors are:

$$\begin{pmatrix} e_{11} \\ e_{21} \end{pmatrix} = \begin{pmatrix} -0.0438821 \\ -0.0354375 \end{pmatrix} \tag{3.2.9}$$

and

$$\begin{pmatrix} e_{12} \\ e_{22} \end{pmatrix} = \begin{pmatrix} 0.0155788 \\ -0.047581 \end{pmatrix}\,. \tag{3.2.10}$$

Therefore, we have that for mode 1 the pericentres of the orbits of Jupiter and Saturn are oriented in the same direction (aligned mode), while for mode 2 they are oriented in opposite direction (anti-aligned mode); moreover we have that g_2 is one order of

magnitude bigger than g_1.

In general, we can say that if one mode dominates over the other then $\varpi_1 - \varpi_2$ will remain fixed, if the contribution of one mode is not negligible with respect to the other then $\varpi_1 - \varpi_2$ will librate and if the contributions of the two modes are comparable then $\varpi_1 - \varpi_2$ will circulate.

3.2.2 Free and Forced Elements of the Motion of a Test Particle

We have seen that under certain circumstances it is possible to construct a secular solution to the motion of N orbiting bodies moving under their mutual gravitational effects: we can obtain at any given time the eccentricities and longitudes of pericentre of the bodies. We can make use of the secular perturbation solution to study the motion of an additional body, of negligible mass, moving under the influence of the central body and perturbed by planets.

For a test particle, Lagrange's equations for the eccentricity vector $(h, k) = e(\sin\varpi, \cos\varpi)$ are [Murray and Dermott, 1999]:

$$\frac{dh}{dt} = \sum_j A_j k_j + Ak \tag{3.2.11}$$

$$\frac{dk}{dt} = -\sum_j A_j h_j - Ah, \tag{3.2.12}$$

where

$$A = \frac{na}{4} \sum_j \left(\frac{m_j}{M_*}\right) \frac{\alpha}{a_>} b^1_{3/2} \tag{3.2.13}$$

$$A_j = -\frac{na}{4} \left(\frac{m_j}{M_*}\right) \frac{\alpha}{a_>} b^2_{3/2}, \tag{3.2.14}$$

and similarly $\alpha = a_< / a_>$, $a_>$ =max(a_j, a), $a_<$ =min(a_j, a).

The solution to the equations of motion for the test particle are of the form

$$\begin{aligned} h &= e_{free} \sin(At + \beta) + h_0(t) \\ k &= e_{free} \cos(At + \beta) + k_0(t)\,, \end{aligned} \tag{3.2.15}$$

where e_{free} and β are constants determined from the boundary conditions and

$$\begin{aligned} h_0(t) &= -\sum_i \frac{\mu_i}{A - g_i} \sin(g_i t + \beta_i) \\ k_0(t) &= -\sum_i \frac{\mu_i}{A - g_i} \cos(g_i t + \beta_i)\,. \end{aligned} \tag{3.2.16}$$

with

$$\mu_i = \sum_j A_j e_{ji} \,. \tag{3.2.17}$$

The solutions given in Eqs. (3.2.15) have a simple geometrical interpretation: In the h–k plane, the particle's motion can be thought of as motion around a circle with centre (k_0, h_0) at a constant rate A while this point itself moves in the path determined by the secular solution for the perturbing bodies. Defining $e_{forced} = \sqrt{h_0^2 + k_0^2}$, then it is possible to say that the motion of the particle is due to a *forced* part caused by the perturbers and a *free* part proper of the particle.

Jupiter, Saturn and a Test Particle As an example, I show how to apply the previous results to the calculation of the forced orbital elements on a test particle moving under the effects of secular perturbations from Jupiter and Saturn.

The first step is to calculate the value of the precession frequency A, given in Eq. (3.2.13). The value of A depends only on the semi-major axes and masses of the perturbers and the particle. Since all these quantities are constant, the value of A is constant at any given semi-major axis and is time independent.

Figure 3.2 shows the variation of A as a function of the semi-major axis of the test particle in the range $0 - 30$ AU. The singularities in the plot correspond to the orbital semi-major axes of Jupiter and Saturn. On the graph are also denoted by solid horizontal lines the, already calculated, eigenfrequencies of the system g_1 and g_2. The intersection of these lines with the curve identify the locations in semi-major axis where large values of e_{forced} arise. In fact, these are the effects of the small divisors in Eqs. (3.2.16) and are connected with the phenomenon of secular resonance which I had already introduced in §2.5.1.

Using Eqs. (3.2.16) and (3.2.17) is then possible to compute the values of the forced eccentricity and longitude of perihelion as function of semi-major axis for a given time. In Figure 3.3 are shown the variation of e_{forced} and ϖ_{forced} in the range 0 to 30 AU at time $t = 0$, our results are in agreement with Murray and Dermott [1999]. In the vicinity of Jupiter and Saturn the forced values of the eccentricity and longitude of pericentre are equal to the equivalent osculating values of these elements for the two planet at this time. The shape of the curves will vary with the osculating elements for the planets according to the secular solution.

At each of the locations where there is a singularity in the e_{forced} plot, the value of A equals one of the g_i eigenfrequencies of the system, the equivalent effect in the forced longitudes of perihelion is to cause a sudden shift in the longitudes of 180°.

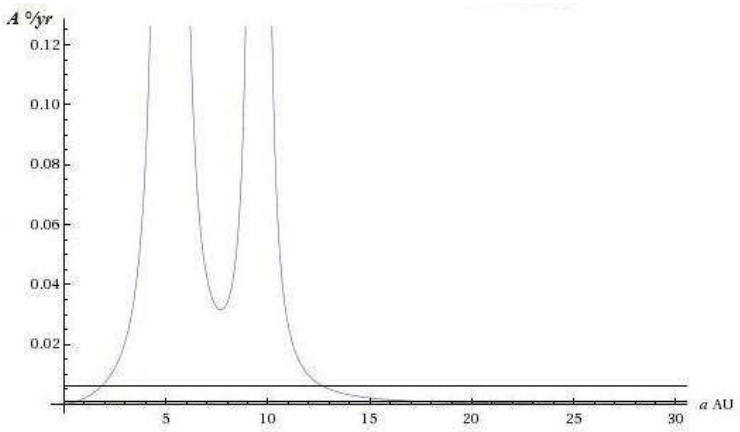

Figure 3.2: The variation of A as a function of semi-major axis for the case of Jupiter, Saturn and a test particle.

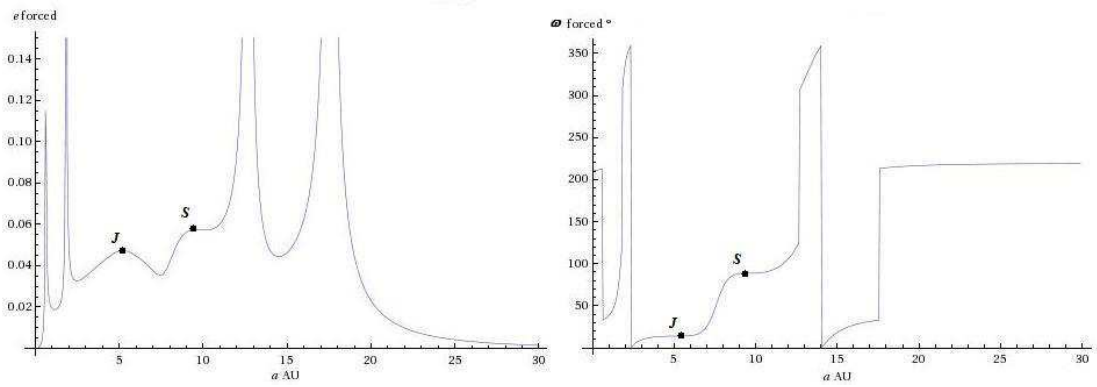

Figure 3.3: The variation in the forced eccentricity and longitude of perihelion as a function of semi-major axis at time $t = 0$ for the case of Jupiter, Saturn and a test particle.

3.2.3 Generalised Secular Perturbations

I have presented the Laplace–Lagrange apsidal precession model to construct analytically the equations of motion for planetary evolution. Then, I have shown how the theory is extended to study the motion of an additional body of negligible mass. Here I consider a more generalised form of the secular theory taking into consideration the effects produced by general relativity and by a non-spherical central mass.

The model is updated by simply amending the diagonal matrix elements, i.e. the terms that do not describe interactions with the other planets [see, e.g., Murray and Dermott, 1999, Adams and Laughlin, 2006b]:

$$A_{jj} = n_j \left[\frac{3GM_*}{c^2 a_j} + \frac{3}{2} J_2 \left(\frac{R_*}{a_j} \right)^2 - \frac{9}{8} J_2^2 \left(\frac{R_*}{a_j} \right)^4 - \frac{15}{4} J_4 \left(\frac{R_*}{a_j} \right)^4 + \right. \\ \left. + \frac{a_j}{4} \sum_{l \neq j} \left(\frac{m_l}{M_* + m_j} \right) \frac{\alpha}{a_>} b^1_{3/2} \right] \tag{3.2.18}$$

where c is the speed of light, R_* is the radius of the parent star and J_2 and J_4 are its first two zonal gravity coefficients.

Post-Newtonian corrections for relativistic precession and oblateness are included similarly in the model for the motion of a test particle by amending the element:

$$A = n \left[\frac{3GM_*}{c^2 a_j} + \frac{3}{2} J_2 \left(\frac{R_*}{a_j} \right)^2 - \frac{9}{8} J_2^2 \left(\frac{R_*}{a_j} \right)^4 - \frac{15}{4} J_4 \left(\frac{R_*}{a_j} \right)^4 + \right. \\ \left. + \frac{a}{4} \sum_{j} \left(\frac{m_j}{M_*} \right) \frac{\alpha}{a_>} b^1_{3/2} \right] \tag{3.2.19}$$

Linear Solution of the Present-day Solar System

As an application of the theory just presented, here I employ the secular model to describe the long-term behaviour of the Solar system.

The oblateness of the Sun has negligible effect on the motion of the planets. I have used the values for J_2 and J_4 of $6.13 * 10^{-7}$ and $-2.8 * 10^{-12}$, respectively [Rozelot et al., 2001].

I have calculated the solution for the eccentricity evolution of the eight-planet system. The system's orthonormal eigenvectors with elements $\bar{e}_{ji}$ are shown in Figure 3.4 with their associated eigenfrequencies (g_i). The retrieved eigenfrequencies are in general agreement with the most widely used secular theory derived by Brouwer and van Woerkom [1950] (which actually use a modified classical theory to take account of a near-resonance between Jupiter and Saturn). As is the convention for the Solar system, the index (i) denotes the mode that is likely to be dominated by planet $j = i$ (i.e., Mercury is likely to be dominant in the $i = 1$ mode and its evolution is strongly governed by

this mode, etc.).

Large components for multiple planets in a single eigenvector suggest significant coupling between those planets in their evolution. The sign of an eigenvector component ($\bar{e}_{ji}$) denotes the relative apsidal orientation within the mode, with like signs denoting alignment and opposite signs anti-alignment.

The eigenvectors of this eight-planet system can be categorised into two groups, those where the terrestrial planets have the largest components ($j = 1$–4) and those where the gaseous planets have the major components ($j = 5$–8). This trend in the architecture of the eigenvectors can be connotative of the weak coupling between the terrestrial and giovian planets in their present configuration.

Using the ephemeris at October 2010 ($t = 0$) available on JPL Horizons, I have computed the initial amplitudes and phases of this system's normal modes. The modal eccentricity amplitudes are listed in Table 3.1. The $i = 1$ and $i = 4$ modes strongly influence the evolution of Mercury and Mars and are responsible for the large eccentricities of these planets. Analogously, the $i = 2, 3$ modes affect the evolution of Venus and Earth. The relatively small amplitudes of these modes are displayed as smaller eccentricities of Venus and Earth [Agnor and Lin, 2012a].

		Mode Index i							
Planet	j	1	2	3	4	5	6	7	8
Mercury	1	–18017	–761	–503	–83	0	0	–1	–1
Venus	2	–2892	1942	1518	270	–1	–1	0	0
Earth	3	153	–1201	1012	2667	–1	–1	0	0
Mars	4	166	–1405	1430	–7400	0	0	–1	–1
Jupiter	5	–2036	–1645	–1655	–1919	–4429	–3506	4025	–130
Saturn	6	10	–40	224	1404	–1500	4640	–164	–12
Uranus	7	44	50	53	72	182	167	2930	–316
Neptune	8	0	1	1	2	7	8	169	1104

Table 3.1: The components (e_{ji}) of the eigenvectors for the e–ϖ solution computed in the eight-planet secular model using the ephemeris at October 2010. All quantities have been multiplied by a factor of 10^5.

The existence of these analytical solutions makes possible the investigation of the long-term variations in the orbital elements of the planets due to their mutual gravitational forces, although it is worth to repeat that these are only approximations to the true behaviour.

Figure 3.5 shows plots of the variation of the orbital eccentricity of Mercury, Venus, Earth, Mars, Jupiter, Saturn, Uranus and Neptune as a function of time. It is shown that there is significant variation in the orbital elements of the inner planets as a result of secular perturbations. To support what was said before, it is possible to notice how in the case of Mercury there is a large-amplitude, long-period variation in its eccentricity. Mars' orbit evolves from near circular to an eccentricity of 0.14 on a time-scale of

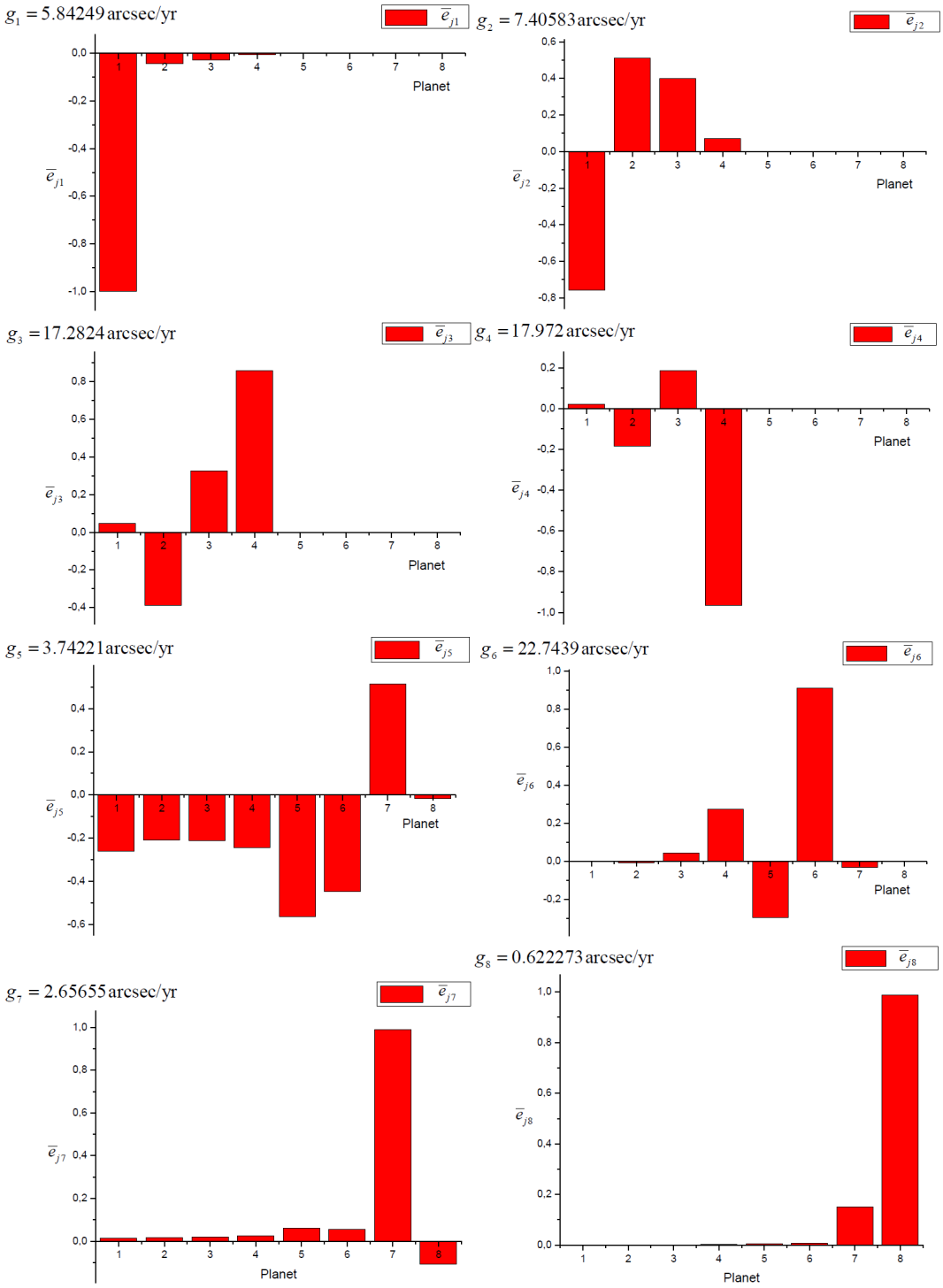

Figure 3.4: Components of the orthonormal eigenvectors of the eight-planet model including Mercury through Neptune. Each eigenvector is labelled with its secular eigenfrequency g_i. Large components for multiple planets indicate strong coupling between those planets in the mode.

around 1 My. Similar variations in the eccentricities of Earth and Venus are also shown, this is evidence of coupling between these two planets.

Another important feature to remark is the high frequency of the variation in e of Jupiter and Saturn. In Section §3.2 was presented the simplified secular theory for the two planets only. Deduced from the eight-planet model, in Figure 3.6 is plotted the variation of e over $200,000$ y which is the same interval shown in Figure 3.1. It is possible to notice how now the eccentricities vary in slightly reduced time-scales.

Figure 3.7 shows, on the left, plots of the proper precession rate of a test particle as a function of semi-major axis from the inner to the outer parts of the Solar system. As discussed in Section 3.2.2, singularities arise at semi-major axes where the value of A matches one of the g_i eigenfrequencies of the system. The effect of small divisors, see eqs. (3.2.16), also applies now when the analysis is extended to include more bodies and the effects of general relativity and oblateness. Superimposed on these plots are horizontal lines denoting the values of the g_i eigenfrequencies (detailed in Figure 3.4). At the points of intersection of the lines and the curves, large values of the forced eccentricity are expected. The forced eccentricity is a function of time and from eqs. (3.2.16), the maximum forced eccentricity is derived to be:

$$e_{\text{forced}-\max} = \sum_i \left| \frac{\mu_i}{A - g_i} \right| . \tag{3.2.20}$$

The right side of Figure 3.7 shows plots of the maximum forced eccentricity as function of semi-major axis. The locations of planets are labelled and the peaks denote the regions of secular resonance.

In particular, the first row is for semi-major axes between 0 and 4 AU. In the region between Mars and Jupiter, where the asteroid belt is located, this model predicts one value of the semi-major axis where a secular resonance occurs: close to 2 AU, the g_6 frequency match the rate A. The extended model by Brouwer and van Woerkom [1950] also presents another resonance near 2.6 AU.

The second row presents a close-in view on distances between 0.06 and 0.23 AU. That is very important to highlight the effects of general relativity: rather than falling, the value of A arises rapidly within 0.2 AU from the star. I detect a very strong resonance near 0.15 AU which does not seem to have been reported in the literature. It would support the theory of a collision between Mercury and a planetesimal early in the Solar system's history [Benz et al., 1988] and it would explain why no vulcanoids have been discovered. In fact, Mercury has a large core and collisions with an eccentric object in the resonance would have stripped away much of the original crust and mantle, leaving the core behind as a relative major component. The fragments could have been cleared by the mentioned resonance. However, another theory that can be used to solve the mentioned problem would be based on the sweeping of the region (see Section 3.4)

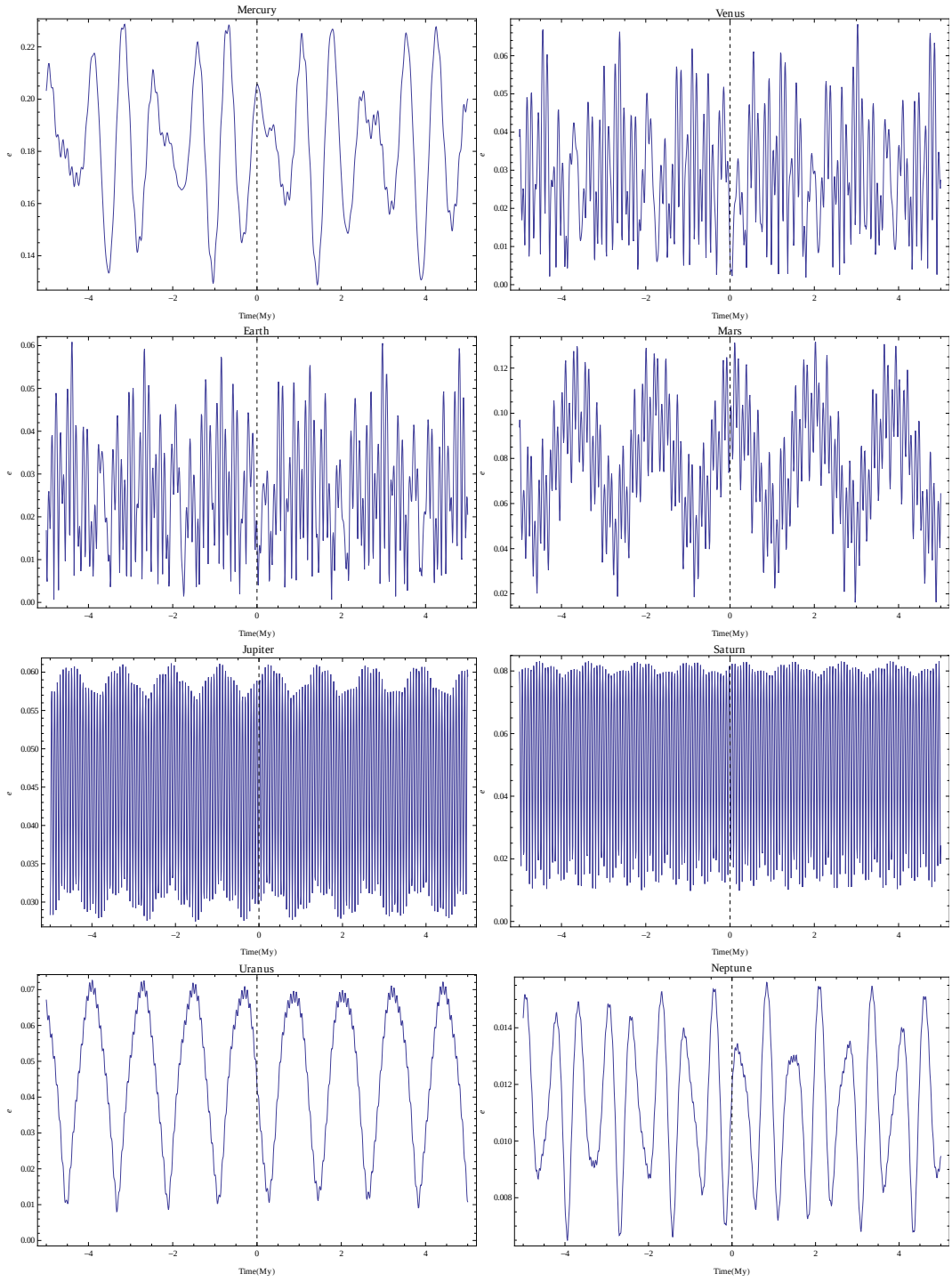

Figure 3.5: The derived evolution of the eccentricity of Mercury, Venus, Earth, Mars, Jupiter, Saturn, Uranus and Neptune over a period of 10 million years centred on October 2010.

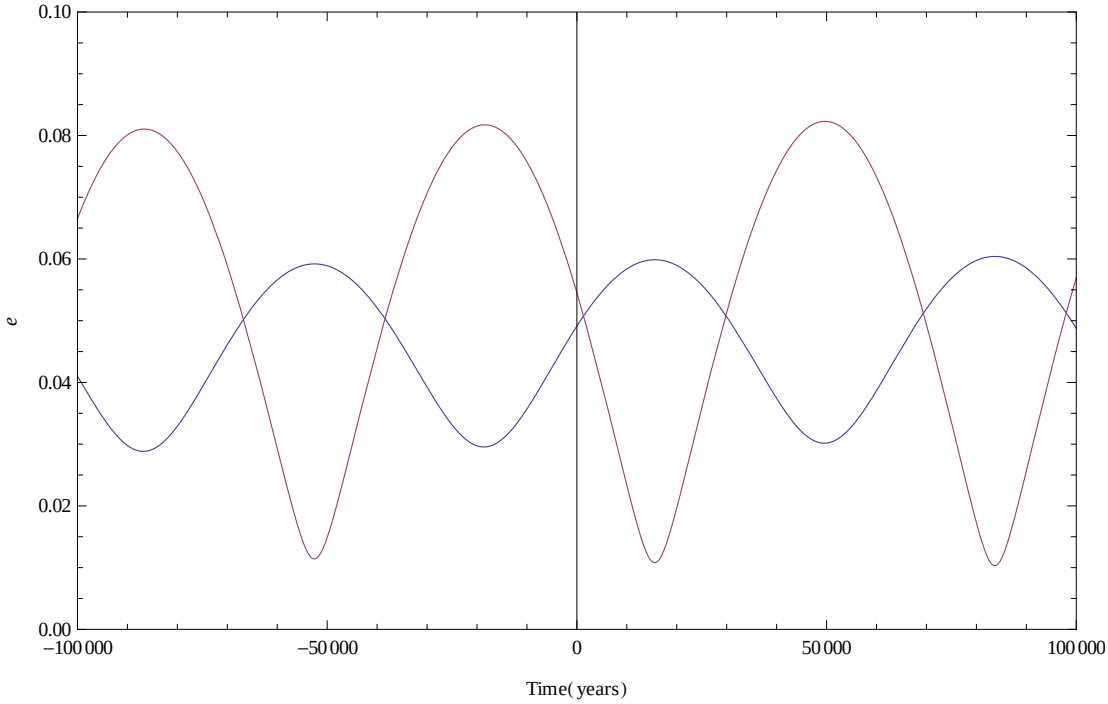

Figure 3.6: The derived evolutions of the eccentricity of Jupiter and Saturn over a period of 200,000 years centred on October 2010, according to the presented eight-planet model. Saturn is in red, Jupiter in blue.

due to the early migration of Jupiter and Saturn.

The region of the outer planets between 4 and 34 AU is object of the third row, while the outer Solar system in the range $34 - 50$ AU is shown in the last row. Here in the Kuiper belt, secular resonances with the g_5, g_7 and g_8 frequencies are found about 34, 35 and 41 AU.

3.3 Secular Interactions in Extrasolar Planetary Systems

In the previous Section I have presented a generalised form of the secular perturbation theory and I have shown a few applications taken from the Solar system. In this Section, I apply the secular theory to some extrasolar planetary systems. These present an inner planet in eccentric orbit and with mass smaller than the outer objects. This follows a large body of previous work. General schemes have been developed for studying secular interactions over the growing collection of planetary systems (see e.g. Adams and Laughlin [2006b], Lee and Peale [2003]).

Note that when using the secular theory, it is not required to define the position of planets along their orbits (given for example by the mean anomaly M or time of peri-astron passage t_0). This is because in this model interactions are averaged on secular time-scales. For simplicity, I assume $\sin i = 1$ during the calculations.

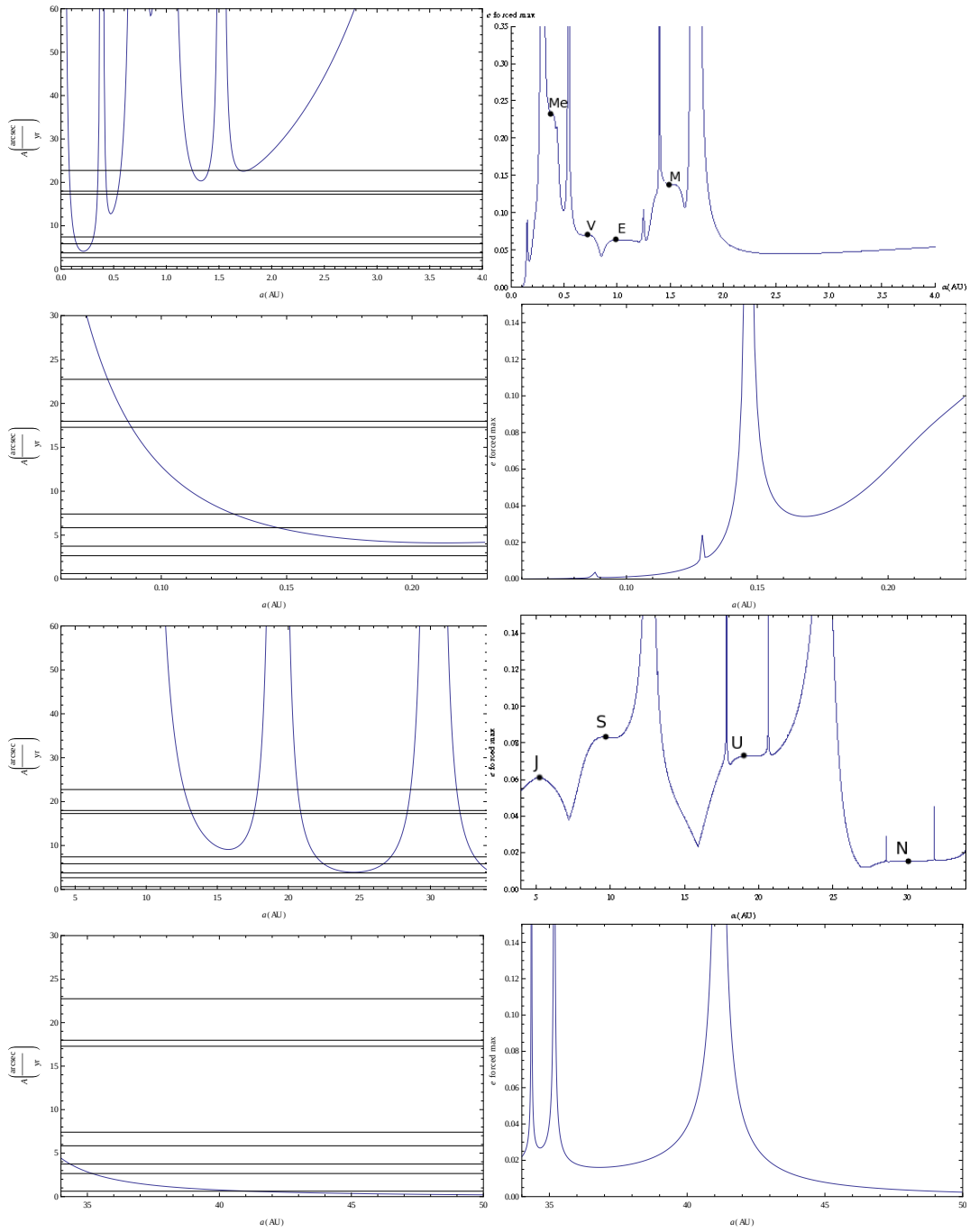

Figure 3.7: Left: The derived precession rate of a test particle as a function of semi-major axis in the inner and outer parts of the Solar system. The solid horizontal lines denote the g_i eigenfrequencies of the system taken from Figure 3.4. Right: the maximum e_{forced} of a test particle as a function of semi-major axis. Letters in the plots denote the locations of the eight planets. The smaller peaks at the locations of secular resonances indicate their tiny areas of influence, smaller than the space-step used in the computation.

Table 3.2: Orbital and physical parameters used for the four planets around μAræ [Pepe et al., 2007].

Parameter	μAr**æ c**	μAr**æ d**	μAr**æ b**	μAr**æ e**
a (AU)	0.09094	0.921	1.5	5.235
$m \sin i$ (m_{JUP})	0.03321	0.5219	1.676	1.814
e	0.172	0.0666	0.128	0.0985
ω ($^\circ$)	212.7	189.6	22.0	57.6

3.3.1 μ Aræ

μAræ is a main sequence G3IV–V star of mass $1.08 M_\odot$. Pepe et al. [2007] report the four-planet extrasolar system μAræ to consist of three outer gas giant planets ('d', 'b' and 'e') on slightly eccentric orbits with periods 310.55 ± 0.83, 643.25 ± 0.90 and 4205.8 ± 758.9 days, and an inner super-Earth ('c') on a 9.6386 ± 0.0015 day orbit with eccentricity $e_c = 0.172 \pm 0.040$. Note planets are labelled according to their discovery date and, as for μ Aræ, that order may not coincide with the increasing distance from the host star. Table 3.2 reports the orbital and physical parameters needed to describe the secular evolution of the system.

The eigenfrequencies of the system are:

$$g_1 = 0.308077 \frac{^\circ}{yr}, g_2 = 0.0332105 \frac{^\circ}{yr},$$
$$g_3 = 0.012911 \frac{^\circ}{yr}, g_4 = 0.00360541 \frac{^\circ}{yr}. \tag{3.3.1}$$

Figure 3.8 shows a plot of the proper precession rate of a test particle as a function of semi-major axis in the range $0 - 12$ AU and a close-in view on distances between 0 and 0.4 AU, this again highlights the effects of general relativity. Superimposed on these plots are horizontal lines denoting the values of the g_i eigenfrequencies (eqs. 3.3.1). The bottom graph in Figure 3.8 shows the maximum forced eccentricity as function of semi-major axis between 0 and 16 AU. The locations of planets are labelled and the peaks denote the regions of secular resonance.

3.3.2 55 Cancri A

I have introduced 55 Cancri in Section 1.3.1, 55 Cancri A has a mass of $0.94 M_\odot$. Here I implement the solution by Fischer et al. [2008] which reports this five-planet extrasolar system to be formed by four gas giants 'b', 'c', 'f' and 'd' with best-fit periods of 14.65, 44.38, 260.67 and 5371.82 days, and planet e, a super-Earth on a 2.80-day orbit with eccentricity $e_e = 0.264$. Table 3.3 reports the orbital and physical parameters used to describe the secular evolution of the system.

Figure 3.9 shows the variation of the orbital eccentricity of the five planets of the system

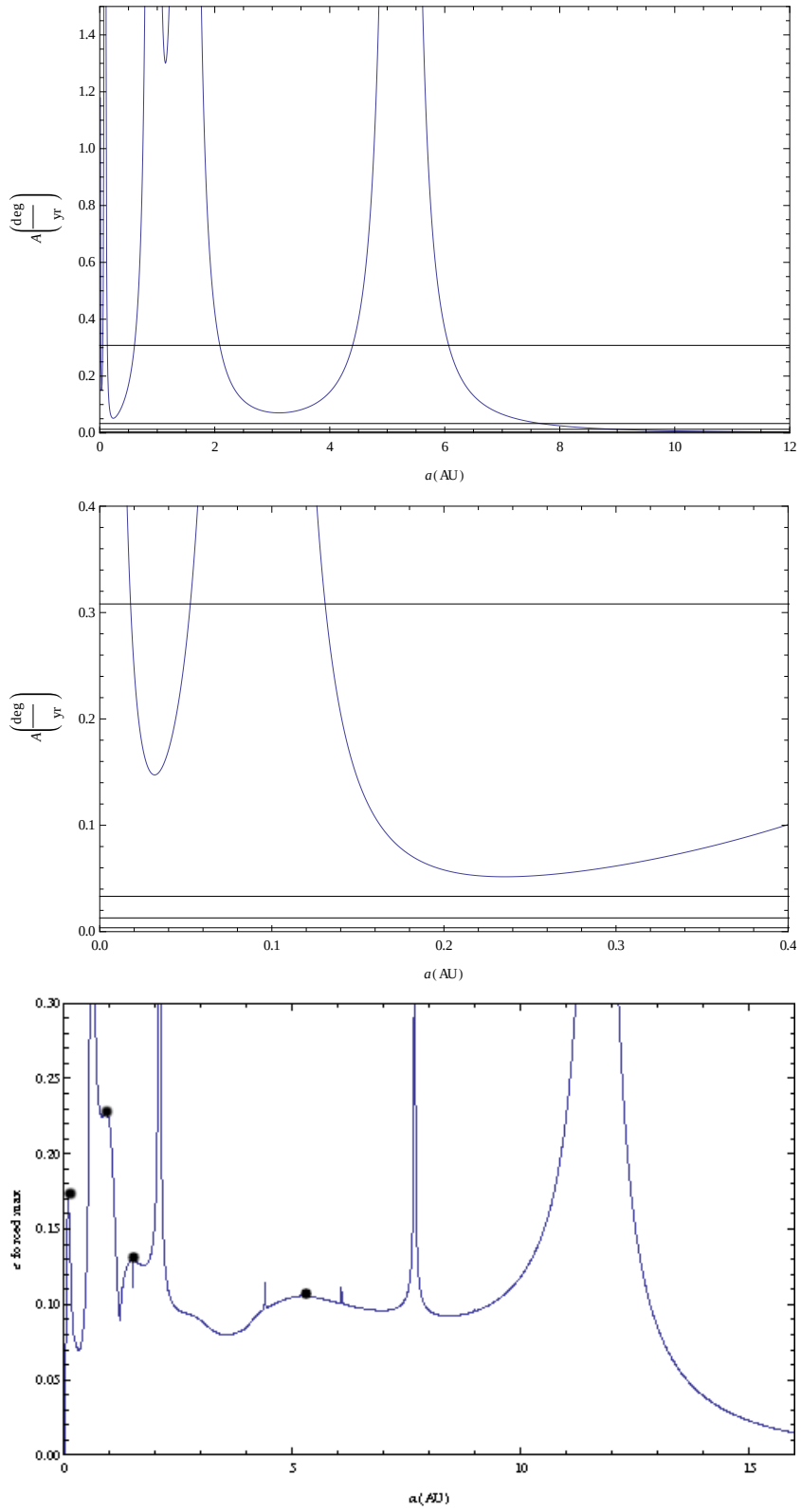

Figure 3.8: The derived precession rate and maximum e_{forced} of a test particle as a function of semi-major axis in the μ Aræ's system. The solid horizontal lines denote the g_i eigenfrequencies of the system. Filled circles denote the locations of the four planets.

Table 3.3: Orbital and physical parameters utilised for the five planets around 55 Cancri A [Fischer et al., 2008].

Parameter	**55 Cnc e**	**55 Cnc b**	**55 Cnc c**	**55 Cnc f**	**55 Cnc d**
a (AU)	0.038	0.115	0.241	0.785	5.901
$m \sin i$ (m_{JUP})	0.0241	0.8358	0.1691	0.1444	3.9231
e	0.2637	0.0159	0.0530	0.0002	0.0633
ω (°)	156.500	164.001	57.405	205.566	162.658

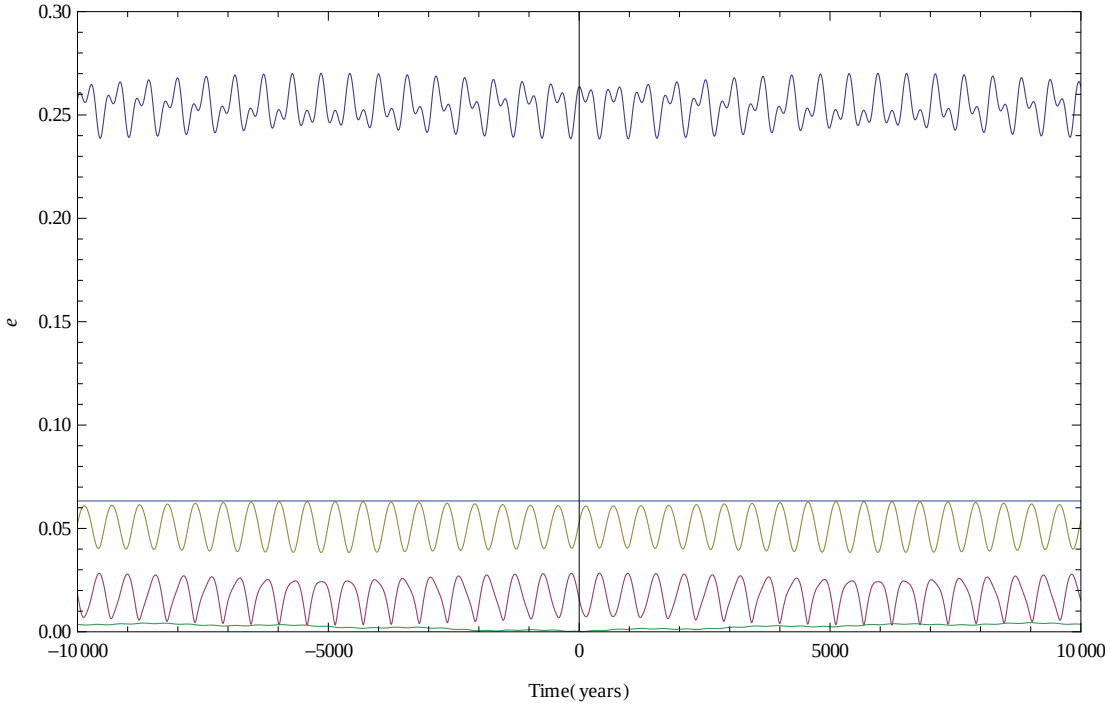

Figure 3.9: The derived evolutions of the eccentricity of the five planets of the 55 Cancri system over a period of 20,000 years. In order of decreasing eccentricity: 55 Cnc *e*, 55 Cnc *d*, 55 Cnc *c*, 55 Cnc *b* and 55 Cnc *f*.

over 20,000 years. These results match what was found by Fischer et al. [2008] (Figure 10 therein).

The eigenfrequencies of the system are:

$$g_1 = 1.40897 \frac{^\circ}{yr}, g_3 = 0.792629 \frac{^\circ}{yr},$$
$$g_2 = 0.143832 \frac{^\circ}{yr}, g_4 = 0.0181169 \frac{^\circ}{yr}, g_5 = 0.00005987 \frac{^\circ}{yr}. \quad (3.3.2)$$

The system's orthonormal eigenvectors with elements $\bar{e}_{ji}$ are shown in Table 3.4. I note how each eigenvector is dominated by a single planet suggesting how these planets are loosely coupled during their evolution.

Figure 3.10 shows, on the left, plots of the proper precession rate of a test particle as a function of semi-major axis in the range $0 - 12$ AU. Superimposed on these plots are

		Mode Index i				
Planet	j	1	2	3	4	5
55 Cnc e	1	99996	–813	–428	–1	–1
55 Cnc b	2	33542	76751	54591	–2004	–1
55 Cnc c	3	–17097	–19973	96482	–313	–1
55 Cnc f	4	–375	–933	–1163	–99988	45
55 Cnc d	5	13	33	43	3352	99944

Table 3.4: The components ($\bar{e}_{ji}$) of the orthonormal eigenvectors for the e–ϖ solution computed for the secular model of the five-planet 55 Cancri′s system. All quantities have been multiplied by a factor of 10^5.

Table 3.5: Orbital and physical parameters utilised for the three planets around HD 125612 [Lo Curto et al., 2010].

Parameter	**HD 125612 c**	**HD 125612 b**	**HD 125612 d**
a (AU)	0.05	1.37	4.2
$m \sin i$ (m_{JUP})	0.058	3.	7.2
e	0.27	0.46	0.28
ω (°)	103	41.5	284

horizontal lines denoting the values of the g_i eigenfrequencies (eqs. 3.3.2). On the right of Figure 3.10 is shown the maximum forced eccentricity as function of semi-major axis between 0 and 12 AU. The locations of planets are labelled and peaks denote the regions of secular resonance. For now, it is just important to mention how 55 Cnc e is found very close to a secular resonance.

3.3.3 HD 125612

HD 125612 is a main sequence G3V star of mass $1.091 M_{\odot}$. Lo Curto et al. [2010] report this three-planet extrasolar system consisting of two outer super-Jupiters (‘*b*’ and ‘*d*’) on eccentric orbits with orbital periods of 559.4 ± 1.3 and 3008 ± 202 days, and a ‘*Neptune*’ planet c on a 4.1547 ± 0.0005-day orbit with eccentricity $e_c = 0.27$. Table 3.5 reports the orbital and physical parameters utilised to describe the secular evolution of the system.

The eigenfrequencies retrieved for the system are:

$$g_2 = 0.0496968 \frac{^{\circ}}{yr}, g_1 = 0.02523 \frac{^{\circ}}{yr}, g_3 = 0.00901853 \frac{^{\circ}}{yr}. \tag{3.3.3}$$

The system′s orthonormal eigenvectors with elements $\bar{e}_{ji}$ are shown in Table 3.6. Also in this case, each eigenvector is dominated by a single planet suggesting how these planets are loosely coupled during their evolution.

Figure 3.11 shows the variation of the orbital eccentricity of the three planets of the system. On the top is shown the secular model, while the plot on the bottom is the result

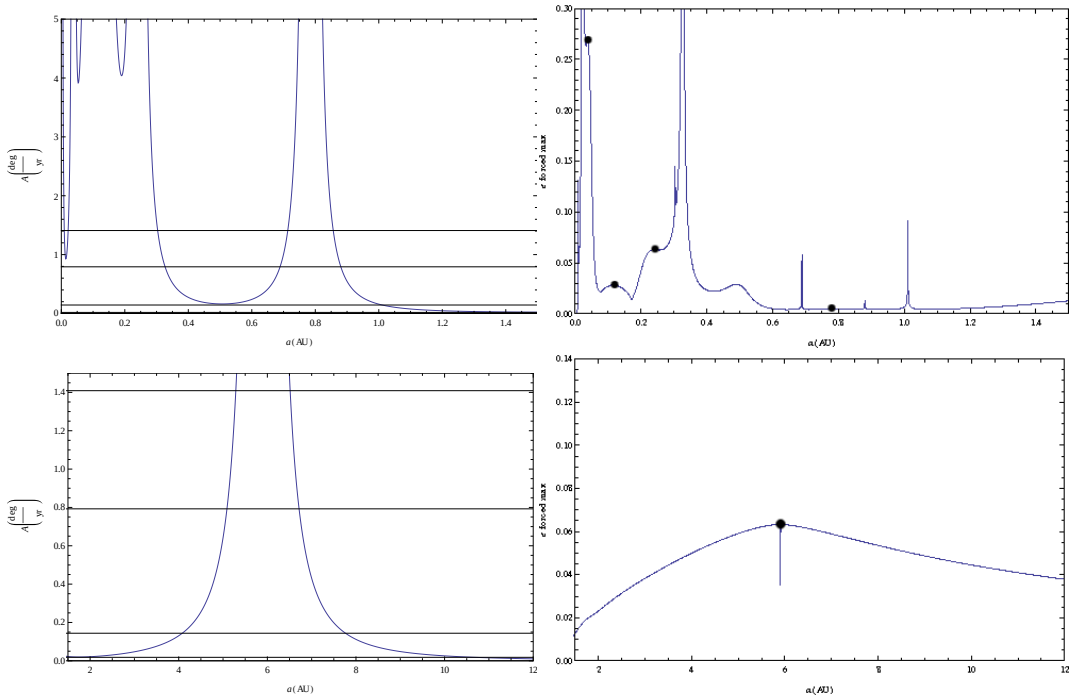

Figure 3.10: The derived precession rate and maximum e_{forced} of a test particle as a function of semi-major axis in the 55 *Cancri's* system. The solid horizontal lines denote the g_i eigenfrequencies of the system. Filled circles denote the locations of the five planets. A sudden deep in the e_{forced} -profile is a spurious result of the computation close to the location of a planet.

		Mode Index i		
Planet	j	1	2	3
HD 125612 c	1	100000	2	–1
HD 125612 b	2	595	–99311	11708
HD 125612 d	3	426	44457	89574

Table 3.6: The components ($\bar{e}_{ji}$) of the orthonormal eigenvectors for the e–ϖ solution computed for the secular model of the three-planet HD 125612's system. All quantities have been multiplied by a factor of 10^5.

of numerical simulations made with *SWIFT*. Focusing on the outer planets, it is possible to notice that, during their evolutions, the eccentricities span a broader range in the numerical model. In fact, the secular model here is an approximation as the implemented secular theory is just second order in the eccentricities. Also, the frequency of the eccentricity signals is faster in the numerics (7.25 cycles every 50, 000 yr rather than the 5.6 cycles predicted by the secular model). This suggests how the eigenfrequencies governing the motion of the outer planets are further apart than what is suggested by the secular theory.

Figure 3.12 shows, on the left, a plot of the proper precession rate of a test particle as a function of semi-major axis in the range $0 - 12$ AU and a close-in view within 0.4 AU from HD 125612. Superimposed on these plots are horizontal lines denoting the values

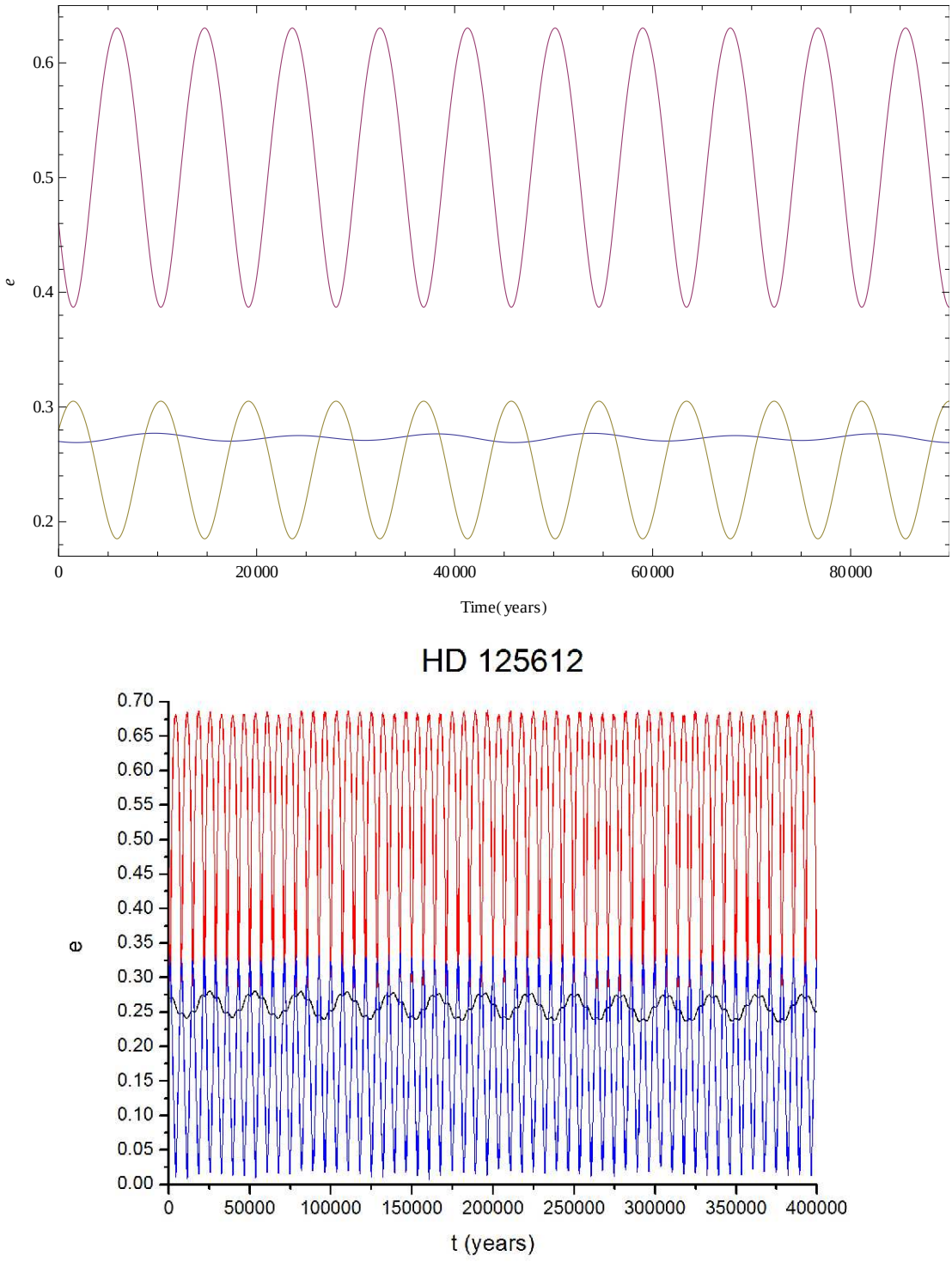

Figure 3.11: Evolution of the eccentricities for the three planets of the HD 125612 system. Top: secular model. $e_c = 0.27$, e_b spans the range $0.39 - 0.63$ and e_d spans the interval $0.19 - 0.31$. Bottom: numerical simulations (not considering GR): e_c moves in the range $0.24 - 0.28$, e_b spans the range $0.28 - 0.68$ and e_d spans the interval $0.01 - 0.33$.

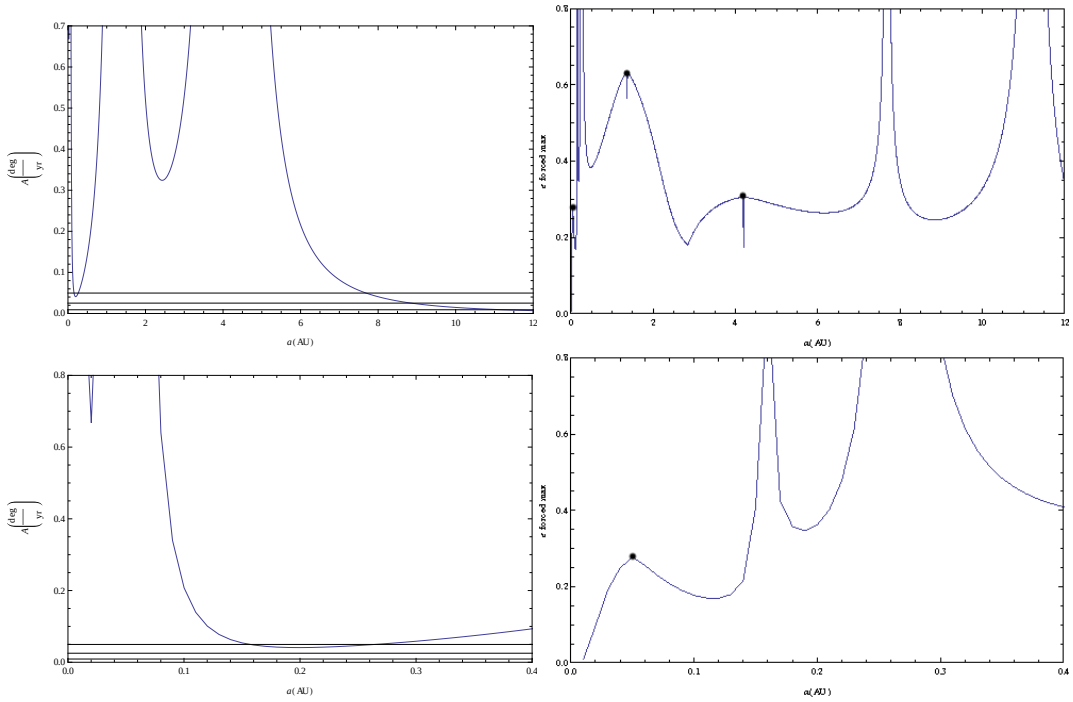

Figure 3.12: The derived precession rate and maximum e_{forced} of a test particle as a function of semi-major axis in the HD 125612$'s$ system. The solid horizontal lines denote the g_i eigenfrequencies of the system. Filled circles denote the locations of the three planets.

of the three g_i eigenfrequencies (eqs. 3.3.3). On the right side of Figure 3.12 is shown the maximum forced eccentricity as function of semi-major axis between 0 and 12 AU. The locations of planets are labelled and peaks denote the regions of secular resonance.

3.4 Sweeping of Secular Resonances

In the previous Sections, I have presented the secular perturbation theory and I have applied the secular model to describe the Solar system and some extrasolar planetary systems. In this Section, I will introduce a dynamical mechanism that can be fundamental in explaining some peculiar orbital characteristics and that can be modelled using the secular theory: the sweeping of secular resonances.

As anticipated in Section 2.5.1, secular resonances are generated when the orbits of two bodies precess synchronously. A small body in secular resonance with a large planet will have its eccentricity and inclination modified over relatively short time periods. As the mass distribution of a planetary system evolves, for example as result of protoplanetary gas disc dispersal, orbital migration or spin-down of an initially rapidly spinning oblate central star, the locations of secular resonances move. Bodies located in regions through which the resonance sweeps are perturbed as the resonance drives the eccentricity and inclination.

		Mode Index i	
Planet	j	1	2
HD 125612 b	2	99312	–11712
HD 125612 d	3	44467	89569

Table 3.7: The components ($\bar{e}_{ji}$) of the orthonormal eigenvectors for the e–ϖ solution computed for the HD 125612's system when the innermost planet is not considered. All quantities have been multiplied by a factor of 10^5.

This process of sweeping of secular resonances has already been demonstrated to be capable of explaining the large mean eccentricity and inclination of Mercury as a consequence of the spin-down and related changes in the oblateness of the Sun [Ward et al., 1976]. They showed that if the primordial gravitational field of the Sun had a larger second-degree harmonic [i.e. $J_2 \gtrsim \mathcal{O}(10^{-3})$], equivalent to a rotation period $\lesssim$ 5.7 hours, then subsequent solar spin-down would drive Mercury's orbit through secular resonances capable of generating its large mean eccentricity and inclination.

The idea that a short-period planet may experience excitation of its eccentricity and inclination, for instance because of stellar spin-down, can be assessed also in the context of extrasolar planetary systems consisting of terrestrial planets perturbed by neighbouring giant planets.

HD 125 612 In §3.3.3, the secular model for HD 125612 was presented. It hosts a '*Neptune*' planet (*c*) in eccentric orbit and two outer super-Jupiters ('*b*' and '*d*'). *HD 125612 c*'s mass is negligible with respect to the super-giants, therefore it can be treated with good approximation as a test particle in order to study the locations of secular resonance.

With this hypothesis, the two eigenfrequencies retrieved are:

$$g_2 = 0.0496856 \frac{^\circ}{yr}, g_3 = 0.00901765 \frac{^\circ}{yr}. \tag{3.4.1}$$

The system's orthonormal eigenvectors with elements $\bar{e}_{ji}$ are shown in Table 3.7. Values for both eigenfrequencies and eigenvectors have not changed substantially confirming the goodness of the approximation.

In Figure 3.13 is presented, on the left, a plot of the proper precession rate of a test particle as a function of semi-major axis in the range $0 - 12$ AU when only planets '*b*' and '*d*' are considered. It follows a close-in view within 0.4 AU from HD 125612. Superimposed on these plots are horizontal lines denoting the values of the two g_i eigenfrequencies (eqs. 3.4.1). On the right side of Figure 3.13 is shown the maximum forced eccentricity as function of semi-major axis between 0 and 12 AU with peaks denoting the regions of secular resonance. In particular, the picture outlining the inner zone shows the two locations of secular resonance with g_2. Recalling that *HD 125612 c*

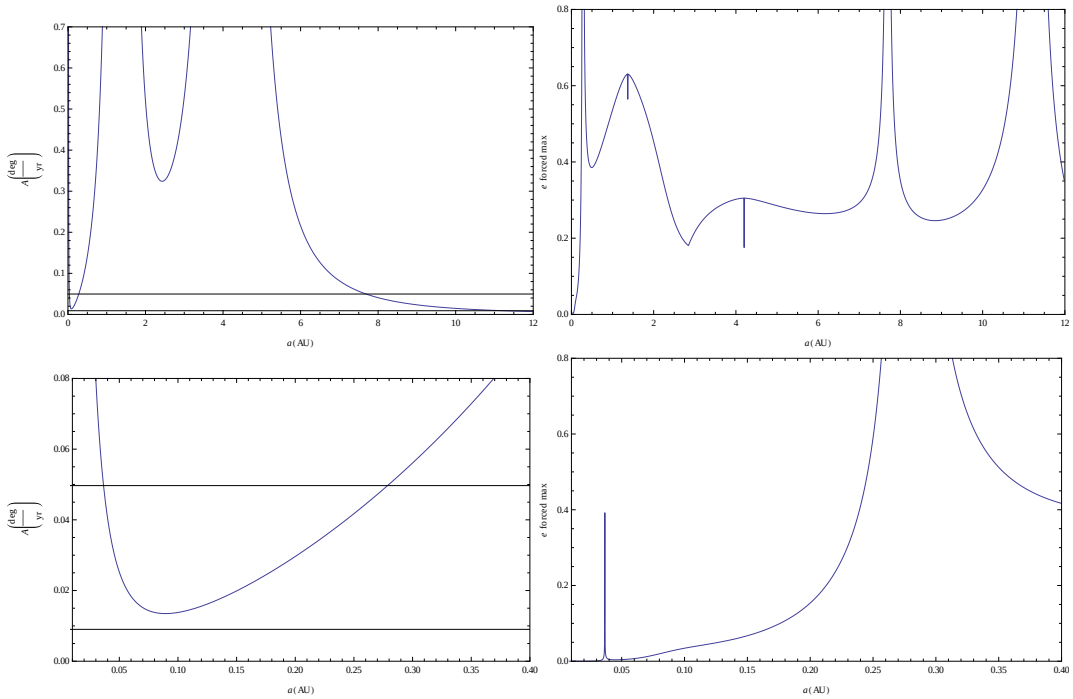

Figure 3.13: The derived precession rate and maximum e_{forced} of a test particle as a function of semi-major axis in the HD 125612$'s$ system when 'c' is not considered. The solid horizontal lines denote the g_i eigenfrequencies of the system. A narrow resonance is located at 0.04 AU, a stronger resonance is found about 0.28 AU

is located at 0.05 AU, a mass redistribution in the planetary system could have caused the resonance now at about 0.04 AU to have swept the location of 'c' generating its observed eccentricity.

It is also important to underline how, without considering GR, the value of A would have faded toward 0 making impossible the secular resonance with g_2 at the considered region.

55 Cancri In §3.3.2, it was introduced the secular model for 55 Cancri. A '$super-Earth$' (e) in eccentric orbit is hosted in the system alongside with four outer gas giants ('b', 'c', 'f' and 'd'). *55 Cnc e*'s mass is not quite negligible with respect to some other planets of the system (see Table 3.3), but it will turn out that the eigenfrequency interested in the sweeping is not particularly affected by e. Therefore, the secular model still produces a good approximation by considering *55 Cnc e* as a test particle in order to study the locations of secular resonance.

In fact, under this assumption, the four eigenfrequencies retrieved are:

$$g_3 = 0.789532\frac{^\circ}{yr}, g_2 = 0.127678\frac{^\circ}{yr}$$
$$g_4 = 0.018091\frac{^\circ}{yr}, g_5 = 0.00005985\frac{^\circ}{yr}. \quad (3.4.2)$$

		Mode Index i			
Planet	j	1	2	3	4
55 Cnc b	2	82170	56941	–2423	–1
55 Cnc c	3	–19888	98002	–320	–1
55 Cnc f	4	–1077	–1249	–99986	45
55 Cnc d	5	38	46	3357	99947

Table 3.8: The components ($\bar{e}_{ji}$) of the orthonormal eigenvectors for the e–ϖ solution computed for the 55 Cancri's system when the innermost planet is not considered. All quantities have been multiplied by a factor of 10^5.

The system's orthonormal eigenvectors with elements $\bar{e}_{ji}$ are shown in Table 3.8. The value for g_3 has changed by 0.4 %, while the value for g_2 has changed by a significant 11.2 %.

In Figure 3.14 is presented, on the left, a plot of the proper precession rate of a test particle as a function of semi-major axis in the range $0 - 1.5$ AU when planet 'e' is considered as massless. It follows a very close-in view within 0.05 AU from 55 Cancri A. Superimposed on these plots are horizontal lines denoting the values of the g_i eigenfrequencies (eqs. 3.4.2). On the right side of Figure 3.14 is shown the maximum forced eccentricity as function of semi-major axis between 0 and 1.5 AU with peaks denoting the regions of secular resonance. In particular, the picture outlining the very inner zone shows the two locations of secular resonance with g_3. The value of g_3 has not been particularly affected by the assumption of considering 'e' massless, therefore the calculated locations of secular resonance remain still a good approximation. Recalling that *HD 125612 c* is located at 0.038 AU, a mass redistribution in the planetary system could have caused the resonance now at about 0.026 AU to have swept the location of 'e' generating its observed eccentricity.

3.4.1 Eccentricity Forcing due to Stellar Spin-down

In the previous part, I have introduced the sweeping of secular resonances as a dynamical mechanism capable of generating large eccentricities. I have also presented the secular model for a couple of extrasolar planetary system where the sweeping of secular resonances may have had a role in producing the large observed eccentricities of inner planets. Here I will introduce how the eccentricity is excited due to the passage of a secular resonance and in particular, I will derive the rate of eccentricity forcing when the passage is due to stellar spin-down and the consequent change of J_2.

The eccentricity excitation due to the passage of a secular resonance is inversely proportional to the square root of the changing rate of the resonant frequency [Nagasawa et al., 2005]. If for a planetary system we assume that the current orbits of the outer planets are established shortly after gas disc dispersal, stellar spin-down can provide the resonant sweeping in the inner part of the system.

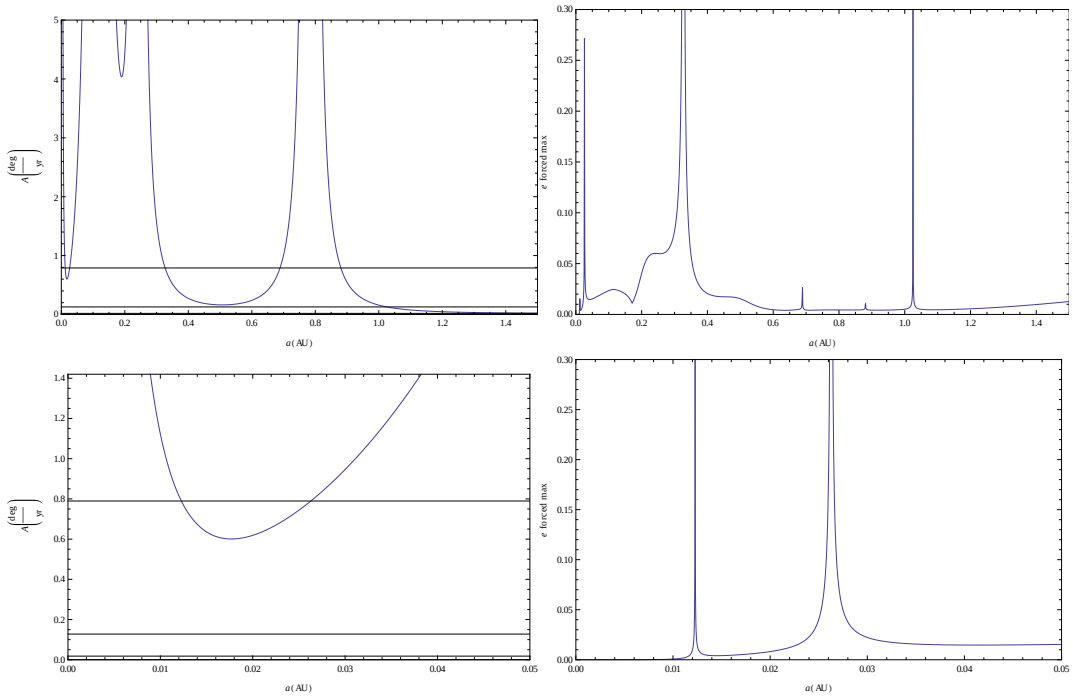

Figure 3.14: The derived precession rate and maximum e_{forced} of a test particle as a function of semi-major axis in the HD 55*Cancri*'*s* system when '*e*' is considered as massless. The solid horizontal lines denote the g_i eigenfrequencies of the system. Two narrow resonances with g_3 are located at 0.012 and 0.038 AU. The latter could have swept the location of '*e*'.

Stars are generally believed to lose their primordial angular momentum through the magnetic braking action of the stellar wind with a mass-loss rate orders of magnitude greater than that on the main sequence [e.g. Skumanich, 1972]. Pre-main sequence stars with masses over $0.25M_{\odot}$ exhibit a bimodal period distribution with observed values clustered around 6–8 days and 2 days. The transition between the two peaks is fairly abrupt. T Tauri stars can have spin periods of the order of hours during their evolution, with a significant fraction of them showing this characteristic [Herbst et al., 2002, Baxter et al., 2008]. In addition to providing a method of exciting the eccentricity of an interior planet through resonant sweeping [Ward et al., 1976], stellar spin-down from an initial rapid state of rotation has also been invoked to explain the low eccentricity of an interior planet. Nagasawa and Lin [2005] have presented a model for the then three planet *υAndromedæ* system which showed that the rotation period of the parent star had to be shorter than 2 days during dispersal of the gas disc so that the passage of the sweeping secular resonance near the orbit of the short-period planet *b* could have been avoided leaving its eccentricity at a low level.

Using the argument that the eccentricity excitation due to the passage of a secular resonance is inversely proportional to the square root of the changing rate of the resonant frequency [Nagasawa et al., 2005], I can estimate the spin-down time $\tau = \Omega/\dot{\Omega}$, where $\Omega = 2\pi/P_*$ is the rotational angular velocity of the star required to excite the present

eccentricity. We have:

$$e \simeq \left(\frac{2\pi}{|\dot{A}|}\right)^{1/2} \mu_x \tag{3.4.3}$$

where, recalling eq. (3.2.17)

$$\mu_x = \sum_{j=1}^{N} A_j e_{jx}. \tag{3.4.4}$$

with μ_x modelling the resonance of interest (due to the eigenfrequency g_x, for a system of N planets), e_{jx} being the components of the scaled eigenvector, A_j defined by equation (3.2.14) and $\dot{A}$ is the rate of change of the resonant precession frequency $A = \dot{\omega}$ at resonance. Stellar rotation enhances the star's oblateness. The effect of rotation on stellar oblateness can be encapsulated in the resulting J_2 coefficient which allows for simple inclusion into secular models and N-body simulations. From Ward et al. [1976], we have:

$$J_2 = \frac{2}{3}\Omega^2 k \frac{R_*^3}{GM_*}, \tag{3.4.5}$$

where for the apsidal constant k I take the value $8.16 \cdot 10^{-3}$ calculated for the Sun [Ward et al., 1976]. Deriving J_2 with respect to time gives:

$$\dot{J}_2 = \frac{4}{3}\Omega\dot{\Omega}k\frac{R_*^3}{GM_*} \tag{3.4.6}$$

Combining equation (3.4.6) with the secular theory for an oblate primary (see Section 3.2.3 and in particular eq. (3.2.19)) gives the following relation between the spin down rate of the star $\dot{\Omega}$ and the rate of change in the precession frequency $\dot{A}$ (ignoring J_4 effects):

$$\dot{A} = n\Big[\left(\frac{R_*}{a}\right)^2 2\Omega\dot{\Omega}k\frac{R_*^3}{GM_*} - 3\left(\frac{R_*}{a}\right)^4 J_2\Omega\dot{\Omega}k\frac{R_*^3}{GM_*}\Big] \tag{3.4.7}$$

where n and a are values calculated at the location of resonance. To summarise, using the secular theory is possible to derive the value of J_2 (or Ω equivalently) necessary to allow the passage of the resonance at the desired location. Then, solving eqs. (3.4.7) and (3.4.3) is possible to estimate τ.

3.5 Stability, Planet-Planet Scattering and Resonant Capture

In the previous Sections I have introduced the secular perturbations theory and the sweeping of secular resonances, a dynamical mechanism that can be fundamental in generating large eccentricities. Also, in Chapter 2 I presented the *dynamical stability* as an additional observable that must be taken into consideration when interpreting RV data. This criterion will be implemented in Chapter 5 to discover the stable best-fit

solution for the HD 181433 planetary system. Here I will tell more about the stability of planetary systems and present another important dynamical mechanism: the planet-planet scattering. In fact, planet-planet scattering is crucial when assessing the physical processes that can lead to the observed assortment of planetary systems. Moreover, in Section 1.3.2 I pointed out the relatively common detection of mean motion resonances, MMRs theory was introduced in Section 2.5.2, while in Chapter 5 the outer pair of giants in HD 181433 will be found to reside in the 5:2 MMR. Here I will outline how planet-planet scattering can also generate MMRs.

In the context of the restricted three-body problem, information about the stability of a test particle interacting with a planet orbiting a star can be provided by the conservation of the Jacobi constant [e.g. Murray and Dermott, 1999]:

$$C_J = 2U - v^2 \tag{3.5.1}$$

where U is given by the centrifugal and gravitational potential and v is the velocity in the rotating frame.

Analytic constraints on dynamical stability of planetary systems began to emerge in the 1980s, when it was shown that the motions of a system of two planets and a star would be bounded in some situations [e.g. Milani and Nobili, 1983, Valsecchi et al., 1984]. This boundary is a direct result of the conservation of angular momentum. For the case of two planets around a much more massive star, the eccentricity exchange (through exchange of orbital angular momentum) is limited, and the planets will never experience a close enough encounter to expel the interior planet from the system (i.e., Hill stability). The Hill stability equation only applies to systems with only two planets in coplanar orbits and that are not in a resonance. It can be described by the following inequality:

$$-\frac{2M_T}{G^2M_X^3}L^2E > 1 + 3^{4/3}\frac{m_1m_2}{M_*^{2/3}(m_1+m_2)^{4/3}} - \frac{m_1m_2(11m_1+7m_2)}{3M_*(m_1+m_2)^2} + ..., \tag{3.5.2}$$

where M_T is the total mass of the system, m_1 is the mass of the more massive planet, m_2 is the mass of the less massive planet, M_* is the mass of the star, G is the gravitational constant, $M_X = m_1m_2 + m_1m_3 + m_2m_3$, L is the total angular momentum of the system, and E is the energy [Marchal and Bozis, 1982]. If a given three-body system satisfies the inequality in Eq. (3.5.2), then the system is Hill stable. If this inequality is not satisfied, then the system may or may not be Hill stable. In this inequality, the left-hand side is a function of the orbits, but the right-hand side is only a function of the masses.

Veras and Armitage [2004] modified the Hill criterion for application to mutually inclined orbits. However, there is no known analytic boundary for systems in a low-order mean motion resonance, or a system with more than two planets. Now, with modern computing power and motivated by exoplanet systems, stability is investigated numer-

ically by performing orbital integrations. From their numerical experiments, Barnes and Greenberg [2007] found that for nearly all known resonant interactions the region of stability is larger than the domain defined by the analytic formula for Hill stability. In fact, also for the case of HD 181433 presented in Chapter 5, we will find that the 5:2 resonance is stable for values well over the collision line (e.g. Fig. 5.7)

To explain the observed large eccentricities a certain dynamical instability is expected for most of the detected planetary system. In fact, it is expected that planetary systems remain stable in nearly circular orbits while planets are embedded in a sufficiently massive disc: after an occasional orbital crossing, the system returns to nearly circular orbits as eccentricities are rapidly damped. Instability may occur due to interaction with a significant disc of debris left over after planet formation. Otherwise, planetary systems may experience instabilities when the gas disc is completely depleted. Initially, several closely spaced planets can be formed, but because of gravitational interactions instabilities resulting in close encounters reduce the number of planets until the stability time-scale exceeds the age of the system.

A range of planetary mass distributions are considered when extensive simulations are set. They are started with planets randomly separated by few mutual Hill radii with:

$$R_{H,m} = 0.5(a_1 + a_2)[(m_1 + m_2)/3M_*]^{1/3} \tag{3.5.3}$$

It is found that strong gravitational scattering between giant planets can naturally create high-eccentricity orbits. For a scattering experiment, Chatterjee et al. [2008] concluded that a wide initial mass distribution can result in remarkable similarity with the observed eccentricity distribution (Figure (3.15).

Results by Raymond et al. [2008] highlight how, through planet-planet scattering, resonant capture in about 5% of cases can be created with these systems having large libration amplitudes. Any stable region of parameter space can be accessed by scattering so that a wide range of low- and high-order MMRs is populated at random.

Another way to evolve into a resonance configuration is, as anticipated, through the process of convergent migration where, for instance, the outer planet migrates inward faster than the inner planet, and the two bodies subsequently move inward together (see the specific analysis in Chapter 7). In this scenario, survival of the resonance can be compromised by turbulent forcing from the disc driving the migration [Ketchum et al., 2011] and/or overly rapid migration [Quillen, 2006].

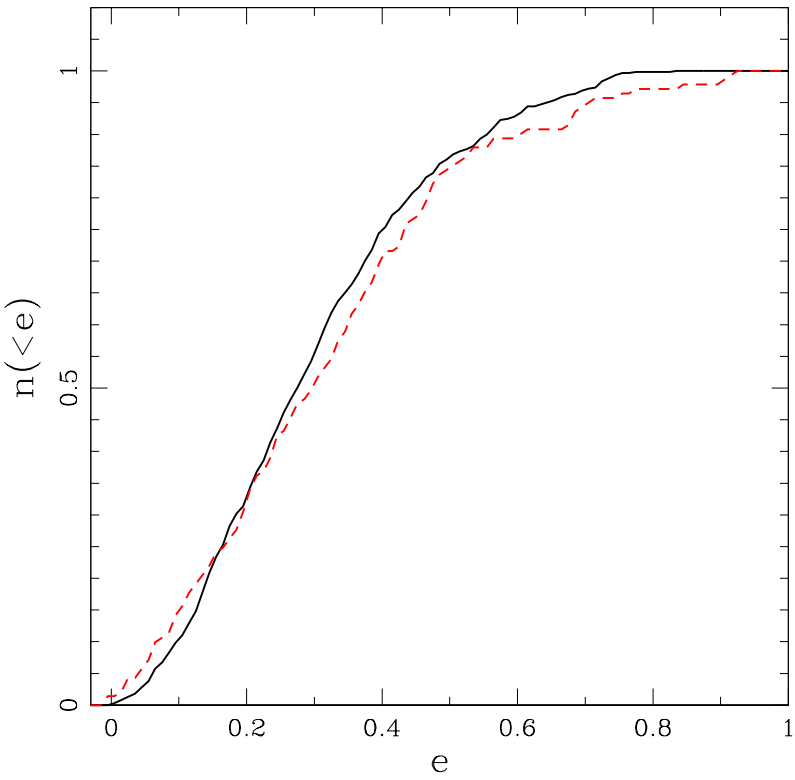

Figure 3.15: Comparison between the observed and simulated exoplanet populations from the scattering experiment by Chatterjee et al. [2008]. The solid black line shows the cumulative distribution of the eccentricities of the remaining planets in their final stable orbits. The dashed red line is that for the observed population. The simulated eccentricities match well the observed.

3.6 *Mercury*: Numerical Integrations including GR and J_2 Effects

I have introduced the secular model augmented for GR and J_2 effects, I have presented the mechanism of sweeping of secular resonances due to stellar spin-down and how planet-planet scattering can generate large eccentricities and pairs in MMRs. In this Section I will present *Mercury-6*, the software package that I have implemented to study these mechanisms by means of numerical simulations.

Mercury-6 [2] is a symplectic N-body code designed to calculate the orbital evolution of objects moving in the gravitational field of a central body [Chambers, 1999]. It is written in Fortran 77 and, among others, includes the following *N*-body algorithms:

1. A second-order mixed-variable symplectic (MVS) algorithm for systems that are not strongly interacting. In fact, it is very fast but it cannot compute close encounters. Here the time-step is constant and is usually set to be 1/20 of the orbital period of the innermost planet to achieve good precision.

2. A Bulirsch-Stoer (BS) integrator, slow but accurate as it is able to deal with approaches between massive bodies.

3. A Hybrid sympletic/Bulirsch-Stoer integrator, it is very fast when implementing the MVS algorithm and switches to BS when a certain minimum separation between objects is reached.

The main reason for switching from the previously used *SWIFT* (see Section 2.7) to *Mercury-6* is because of the need to study planet-planet scattering events. In fact, this is possible with *Mercury-6*: it gives the possibility to set a physical size for the planets and also for the sake of computational efficiency, the hybrid option switches automatically from the fast MVS algorithm to the more precise BS integrator only in case of close encounters, so that energy and angular momentum are conserved along the whole run.

Apart Newtonian gravity, *Mercury-6* gives the chance to implement the effects of other forces by simply modifying a specific subroutine. On the other hand, doing that in *SWIFT* involves modifying several subroutine with the need of precisely reconstructing the sequence of passages followed by the integrator. *Mercury-6* comes also with the possibility of inputting directly the initial Keplerian orbital elements, computing the evolution of test particles and continuing/extending an integration from dump files. Output files include details on close encounters and, for each object, a customisable set of information - i.e. orbital and physical elements in the desired format.

[2] Available at `http://www.arm.ac.uk/~jec/`

3.6.1 General Relativity

To augment the code to include the effects of GR is necessary to simply define the three components of the acceleration vector in the dedicated subroutine. Following Quinn et al. [1991], the additional acceleration for planet i is given by

$$\frac{\mathrm{d}^2\mathbf{r}_i}{\mathrm{d}t^2} = \frac{G(M_* + m_i)}{r_i^3}\left(4\frac{G(M_* + m_i)}{c^2 r_i} - \frac{v_i^2}{c^2}\right)\mathbf{r}_i + 4\frac{G(M_* + m_i)}{c^2 r_i^3}(\mathbf{r}_i \cdot \mathbf{v}_i)\mathbf{v}_i, \tag{3.6.1}$$

where

$$\begin{aligned} r_i &= \sqrt{x_i^2 + y_i^2 + z_i^2}, \\ v_i &= \sqrt{v_{x,i}^2 + v_{y,i}^2 + v_{z,i}^2}, \\ \mathbf{r}_i \cdot \mathbf{v}_i &= x_i * v_{x,i} + y_i * v_{y,i} + z_i * v_{z,i} \end{aligned} \tag{3.6.2}$$

and the speed of light is $c = 299792458$ m/s or 173.1446328 AU/d in the units used by *Mercury-6*.

To test the algorithm, I compare the results of numerical integrations with what is expected from the analytical theory. Rather than using the expression for the orbital precession due to GR in (3.2.18) which is 0-th order in eccentricity, I take the following which is second order in e [e.g., Fabrycky and Tremaine, 2007]:

$$\dot{\omega}_{GR} = \frac{3G^{3/2}(M_* + m)^{3/2}}{a^{5/2}c^2(1 - e^2)}. \tag{3.6.3}$$

I consider a $0.01 M_{Jup}$ planet orbiting a solar-mass star at 0.01 AU. The precession periods obtained are shown in Table (3.9) and demonstrate how the numerical outcomes match with the expectations.

I also set a run to calculate the orbital precession period of Mercury. This is found to be 3,015,300 years which is well in agreement with the analytical expectation (3,013,770 years) and the relativistic perihelion advance of 42.98 arcseconds per century reported for Mercury [e.g. Iorio, 2005].

I now present two planetary systems where GR effects can be relevant as they host planets in very short-period orbits.

υ Andromedæ In the *υAndromed*æ system (Butler et al. [1999], see Section 1.3.1), the forced eccentricity of the inner planet depends sensitively on whether or not the post-Newtonian force is accounted for in secular evolution [Nagasawa and Lin, 2005] because of the proximity of a secular resonance. With my code, the results are replicated: when GR is considered, planet b stays in quasi-circular orbit as indeed it has been observed, otherwise its eccentricity grows to values greater than 0.16 (see Figure 3.16).

Table 3.9: Precession periods due to GR measured for a $0.01 M_{Jup}$ planet orbiting a solar-mass star at 0.01 AU as function of eccentricity. Reported are the analytical expectations and numerical outcomes. Data from the integrations are outputted every 100 years, the relative changes are still negligible.

e	Analytic (yr)	Numerical (yr)	Relative change
0.01	106726	106800	0.000693
0.04	106565	106600	0.000328
0.07	106213	106300	0.000819
0.1	105669	105700	0.000293
0.13	104932	105000	0.000648
0.16	104004	104100	0.000922
0.19	102883	102900	0.000165
0.22	101570	101600	0.000295
0.25	100065	100100	0.000350
0.28	98368.1	98400	0.000324
0.31	96478.9	96500	0.000219
0.34	94397.5	94400	0.000026
0.37	92124	92200	0.000824
0.4	89658.4	89700	0.000464
0.45	85122.1	85200	0.000914
0.5	80052.2	80100	0.000597
0.55	74448.5	74500	0.000691
0.6	68311.2	68300	-0.000164
0.65	61640.2	61700	0.000969
0.7	54435.5	54500	0.001184
0.75	46697.1	46700	0.000062
0.8	38425	38500	0.001948
0.85	29619.3	29600	-0.000652
0.9	20279.9	20300	0.000990

According to Adams and Laughlin [2006b], this represents an evidence of the validity of GR.

However, using the recent information (provided through the astrometric method) on the actual masses of planets *c* and *d* [Barnes et al., 2011] and on a supposed further forth outer planet [Curiel et al., 2011, Ligi et al., 2012], I find the outcome of an integration to indicate instability on small time-scales of the best-fitting solution. Therefore, following the discussion of Section 2.6 and what will be shown in Chapter 5, *υAndromedæ* represents another system where taking into account the *dynamical stability* can add constraints on the orbital elements of the poorly sampled outermost planet.

HD 125612 I have introduced the planetary system of HD 125612 in Sections 3.3.3 and 3.4 along with a secular model for it. The numerical integration conducted with *Mercury-6* shows that the published solution [Lo Curto et al., 2010] is stable, this is shown in the left panel of Figure (3.17). Besides, in the right panel is shown the evolution of the eccentricities for the three planets when GR is considered. The innermost planet *c*, is located at 0.05 AU, so GR effects are relevant and therefore it is possible to compare these results with what was illustrated in Figure 3.11. The eccentricity signal for *c* has a period of about 30,000 years which stretches to 36,000 years when GR is considered. If before e_c could move in the range $0.24 - 0.28$, now e_c can get values between 0.27 and 0.32.

3.6.2 Oblateness of the Central Body

Mercury-6 comes already with the subroutine *mfo_obl* to model the oblateness of a central body. The radius of the star and the factor J_2, J_4 and J_6 can be defined directly into the parameters file and *Mercury-6* calculates directly the extra acceleration vector for each planet.

However, it is beneficial to model the oblateness of a central star as function of its rotation period. This is because that is a measurable quantity and it will be of convenience when there is the necessity to model the stellar spin-down in the simulations. The rotational flattening of the host star can be implemented in the subroutine *mfo_user*, along with GR. I adopt the expression for the acceleration due to the oblate star given by Nagasawa and Lin [2005]:

$$\frac{\mathrm{d}^2\mathbf{r}_i}{\mathrm{d}t^2} = -\frac{R_*^5(1+m_i/M_*)k_*\Omega_*^2}{2r_i^4}\frac{\mathbf{r}_i}{r_i}, \tag{3.6.4}$$

where k_* is the tidal Love number equal to 0.02 for the Sun and the stellar rotation

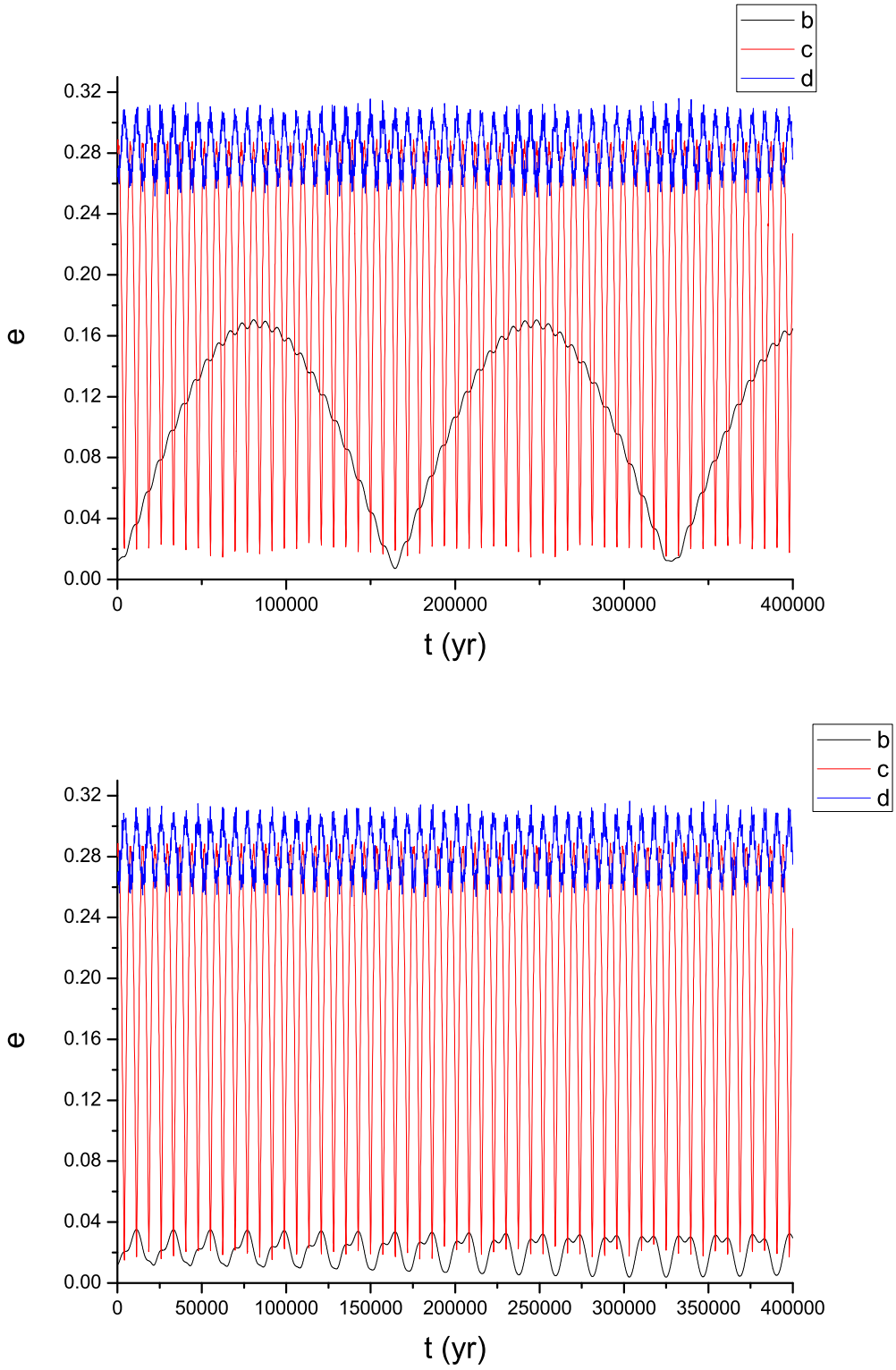

Figure 3.16: Eccentricities evolutions of the three planets around $\upsilon Andromedæ$ [Butler et al., 1999]. Top: with a point-mass potential, e_b can reach a value greater than 0.16. Bottom: including the post-Newtonian effect, this time e_b stays small.

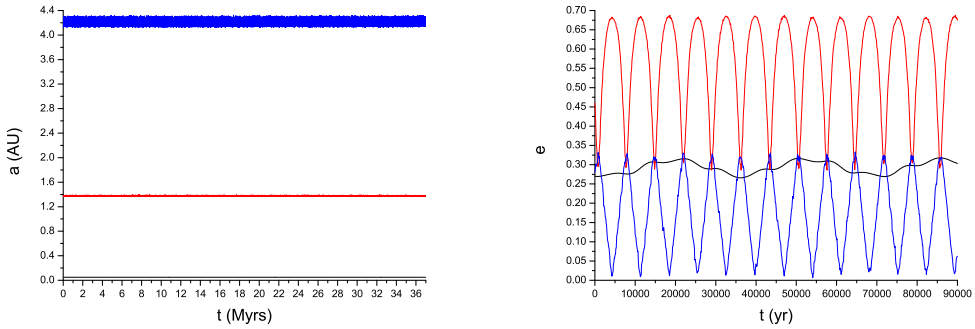

Figure 3.17: Evolution of some orbital elements for the three planets of the HD 125612 system. Left: semi-major axes stay stable for at least 36 Myr. Right: eccentricities when GR effects are considered. As in Figure 3.11, e_b and e_d still span the ranges $0.28 - 0.68$ and $0.01 - 0.33$, respectively. Because of GR, now e_c moves in the range $0.27 - 0.32$.

period S_* in term of its angular velocity Ω_* is

$$S_* = \frac{2\pi}{\Omega_*}. \tag{3.6.5}$$

I run checks to ensure that the precession periods that arise from the simulations agree with the analytical expression. The literature [Iorio, 2005] reports the orbital precession rate due to J_2 as

$$\dot{\omega}_{J_2} = \frac{3}{2}\frac{nJ_2}{(1-e^2)^2}\left(\frac{R_*}{a}\right)^2. \tag{3.6.6}$$

Trying to use eq. (3.4.5) to pass from Ω to J_2 is not successful as gives a difference of $15 - 20$ % for the precession periods calculated. This indicates that eq. (3.4.5) is an approximate expression. Therefore, to check the genuineness of the code I can calculate the precession periods as function of eccentricity for the numerical runs. The ratios of the precession rates will not depend on the particular relation between Ω and J_2 and then those results can be compared with the analytical formulation.

I consider an HD 181433a-like star with rotation period of 1.1 days and a close HD 181433 b with orbital eccentricity equal to 0.1, 0.2, 0.4 and 0.6. The precession periods worked out from the simulations are 50,100; 47,100; 36,100; 21,000 years, respectively. The results shown in Table 3.10 demonstrate the compatibility with what is expected by the analytical model (the difference is never more than 0.32 %).

3.6.3 Modelling the Stellar Spin-down

In Section 3.4.1 I introduced the secular resonance sweeping due to stellar spin-down. Here I present how a stellar spin-down model has been implemented in the BS algorithm of the integrator *MERCURY-6* to account for the time dependent rotational flattening of the host star. The model already includes effects due to GR and (constant)

Table 3.10: Ratios of the precession rates due to stellar oblateness as function of eccentricity measured for HD 181433 b orbiting an HD 181433a-like star with rotation period of 1.1 days. Reported are the analytical expectations and numerical outcomes, subscripts indicate the eccentricity. Data from the integrations are outputted every 100 years, the relative changes are still negligible.

ratio	Analytic	Numerical	Relative change
$\frac{\dot{\omega}_{0.1}}{\dot{\omega}_{0.2}}$	0.94031	0.94012	0.000204
$\frac{\dot{\omega}_{0.1}}{\dot{\omega}_{0.4}}$	0.71993	0.72056	0.000878
$\frac{\dot{\omega}_{0.1}}{\dot{\omega}_{0.6}}$	0.41791	0.41916	0.002971
$\frac{\dot{\omega}_{0.2}}{\dot{\omega}_{0.4}}$	0.76563	0.76645	0.001082
$\frac{\dot{\omega}_{0.2}}{\dot{\omega}_{0.6}}$	0.44444	0.44586	0.003175
$\frac{\dot{\omega}_{0.4}}{\dot{\omega}_{0.6}}$	0.58050	0.58172	0.002095

stellar oblateness in additional to the gravitational interaction between planets. The BS algorithm has been preferred because it gives the chance to study close encounters, something that turns out to be very relevant in this kind of studies.

The stellar spin-down is modelled as a magnetic braking torque based on the empirical Skumanich law [Skumanich, 1972, Barker and Ogilvie, 2009]:

$$\frac{d\mathbf{\Omega}}{dt} = -\alpha\Omega^2\mathbf{\Omega} \tag{3.6.7}$$

where $\mathbf{\Omega}$ is the stellar spin vector and $\alpha = 1.5 \times 10^{-14}$ years for a G or K dwarf. This parameter measures the speed of removal of angular momentum from a rotating star.

The code is adjusted so that the initial rotation period is defined in the parameters file and this variable is passed all the way through the required subroutines. In the BS algorithm is defined the parameter α and is derived the initial spin rate (eq. 3.6.5). The spin rate needs to be updated at each time-step Δt, so in the main loop the new spin rate is defined (following eq. 3.6.7) as:

$$\Omega_{new} = \Omega_{old} - \alpha\Omega^3\Delta t \tag{3.6.8}$$

In BS, Δt is variable and depends on the integration accuracy parameter. I have run checks to find the right compromise between accuracy and time consuming. At time of data dumping, the stellar rotation period is outputted in the information file for the user and is saved in the dump files so that, in case of crash, the computation can be resumed easily.

CHAPTER 4

The Use of Transit Timing for the Detection of Extrasolar Planets

4.1 Introduction

If the orbit of a planet is observed nearly edge-on, the planet may transit over the disk of its host star and periodically block-out a small fraction of the starlight. The existence of the planet is thus revealed by a small and recurrent decrease of the host star's brightness during transits.

With transit photometry it has been possible to observe about 300 extrasolar planets. In addition to the existing ground-based transit surveys and the ESA's CoRoT satellite [Baglin et al., 2002], the NASA's *Kepler* mission [Borucki et al., 2003] continuously monitors 150,000 target stars. This has further accelerated the field, producing more than 130 new, confirmed planets and a large number of candidates "*Kepler* Objects of Interest" (KOI).

A planet following precisely a Keplerian orbit should have transit light curve properties invariable with time. The presence of further planets in the system induces gravitational perturbations on the orbit of the transiting planet, which can generate detectable Transit Timing Variations (TTVs) of the known transiting body.

In this chapter I discuss the geometry of a planetary transit and summarize the present state of transit detections focusing in particular on the *Kepler* Mission. I go on with introducing the TTV method for the detection and characterisation of exoplanets and I introduce the theoretical work and observations made to date. I conclude with presenting how *Mercury-6* is implemented in order to estimate transit timing variations.

4.2 Transiting Planets

As anticipated in Section 1.2.2, the transit method consists in detecting the shallow dip in a stellar light curve due to the passage of a planet in front of its host star during its orbit. The planetary transit geometry can be described by three parameters: depth, duration, shape. Depending on the latitude of the transit on the stellar disk, the transit light curve will be U-shaped (central occultation) or V-shaped (grazing occultation). Quantitatively, the related parameter is the duration of the ingress and egress.

For the purpose of this thesis, it is just necessary to recall the equations for the simplified case of a circular orbit and a stellar disc of uniform brightness [Seager and Mallén-Ornelas, 2003, Moutou and Pont, 2006, Carter et al., 2008], a more general set of equations accounting for eccentric orbits are shown in Tingley and Sackett [2005] and Kipping [2008].

The sketch of a planetary transit is given in Figure 4.1. Ingress is defined as the phase from contact 1 to contact 2, T_{12}. The "flat bottom" corresponds to phases 2 to 3. Egress is the phase from contact 3 to contact 4. Characteristics of the curve are the time of transit minimum τ_{min}, the transit depth ΔF, the total duration t_T and the partial duration T_F.

Transit depth The depth of the transit is related to the star and planet radii:

$$\Delta F \equiv \frac{F_{off} - F_{on}}{F_{off}} = \left(\frac{R_p}{R_*}\right)^2 ; \tag{4.2.1}$$

F_{off} is the observed stellar flux out of transit, and F_{on} is the observed flux during transit. This formula neglects the phenomenon known as limb darkening, i.e. the fact that stars appear slightly brighter in their centre than near the edge. Taking limb darkening into account makes the transits slightly deeper than $(R_p/R_*)^2$, and gives the light curve a more rounded shape.

Transit duration The total duration of the transit, for a circular orbit, is related to the orbital parameters, orbital period P and to the star radius:

$$t_T \approx \frac{PR_*}{\pi a}\sqrt{\left(1+\frac{R_p}{R_*}\right)^2 - \left(\frac{a}{R_*}\cos i\right)^2} \tag{4.2.2}$$

The expression $b = \frac{a}{R_*}\cos i$ is the *impact parameter* and represents the projected distance of the planet's centre to the star's equator.

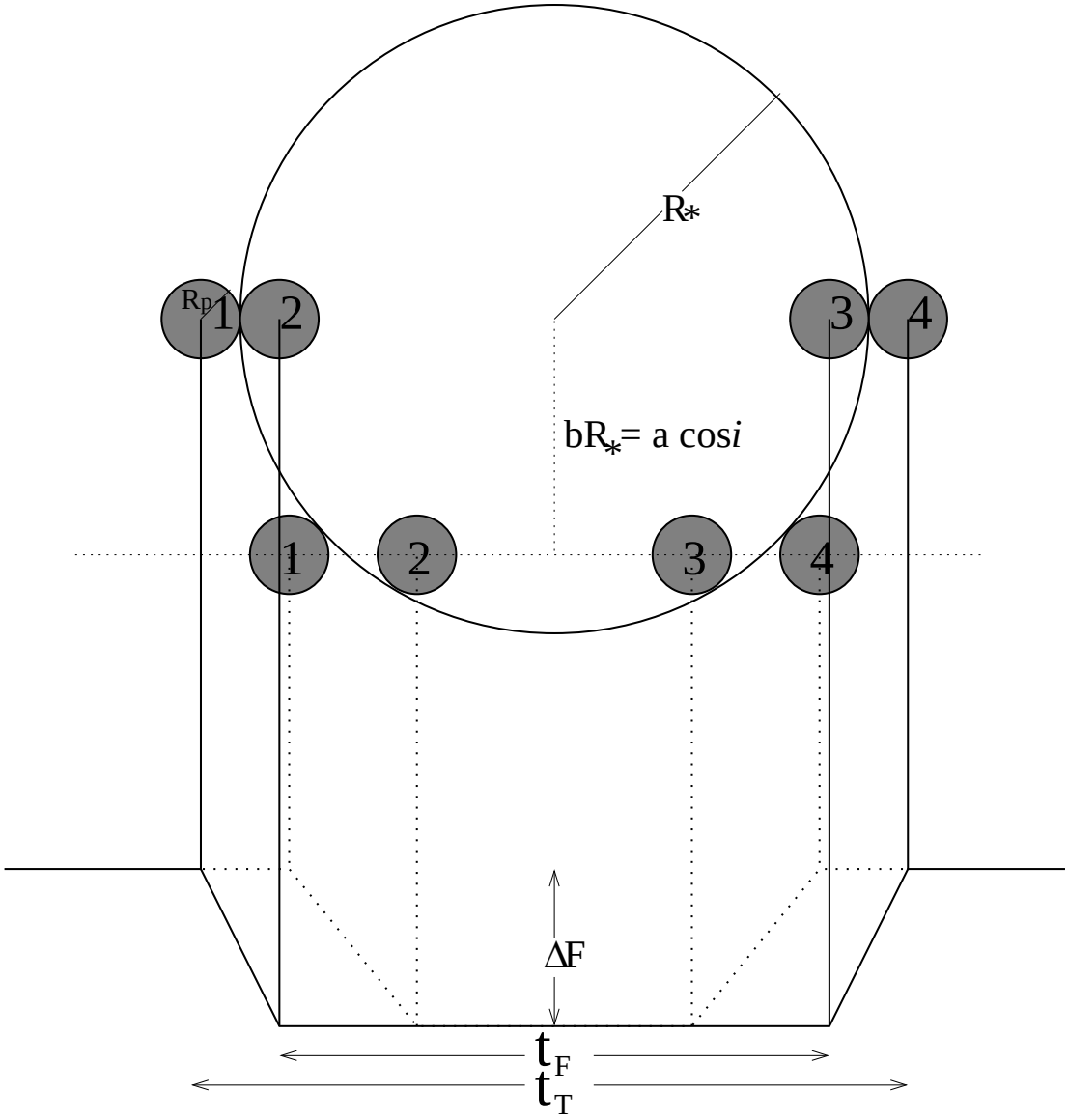

Figure 4.1: Definition of transit light-curve observables. Two schematic light curves are shown on the bottom (solid and dotted lines), and the corresponding geometry of the star and planet is shown on the top. Indicated on the solid light curve are the transit depth ΔF, the total transit duration t_T, and the transit duration between ingress and egress T_F (i.e., the "flat part" of the transit light curve when the planet is fully superimposed on the parent star). The planet is shown from first to fourth contact. Also defined are R_*, R_p, and impact parameter b corresponding to orbital inclination i [Seager and Mallén-Ornelas, 2003].

Ingress duration Another temporal parameter of the transit is the duration of the ingress or egress:

$$T_{12} \approx t_T \frac{R_p}{R_*} \sqrt{1 - b^2} \tag{4.2.3}$$

It is also possible to consider the transit shape by deriving the ratio between the durations of the flat bottom, T_F, and the total transit t_T:

$$\left(\frac{T_F}{t_T}\right)^2 = \frac{\left(1 - \frac{R_p}{R_*}\right)^2 - \left(\frac{a}{R_*}\cos i\right)^2}{\left(1 + \frac{R_p}{R_*}\right)^2 - \left(\frac{a}{R_*}\cos i\right)^2}, \tag{4.2.4}$$

A precise measurement of these three terms (depth, total duration and ingress duration), allows an observer to infer the physical properties of the system, such as the radius ratio $p = \frac{R_p}{R_*}$, transit impact parameter b, and scaled semi-major axis $\frac{a}{R_*}$. The star's radius may be independently constrained by other observations or stellar evolution models, so that it becomes possible to estimate R_p, a and i.

4.3 Transit Measurements

The main requisite of transit measurements is high photometric precision on relatively bright stars. This exigency of precision is determined from the fact that transit measurements are made in the total light of the star and planet. Consequently, the planet signal is greatly attenuated by stellar photons and the measurement precision must be as high as possible. Besides, the time scale of the photometric noise is important. Since transits last generally for a few hours, the precision of single measurements should augment as the inverse square root of the measurement time (Gaussian noise), for observations exceeding several hours. Since a photometric baseline is necessary before and after transit, a reasonable time scale for the required stability is $\sim$ 20 hours for a single transit. Since both IR and visible measurements are relevant for transits, the instrumentation should be projected to attain the fundamental limits generated by the stellar photon noise (important mostly in the visible) and the noise caused by the thermal emission of the telescope, instruments and zodiacal dust (primarily crucial in the IR).

Also, setting up opportune strategies of data analysis is essential to recognise false alarm detections. These can be caused by stellar effects like spots or intrinsic stellar variation, as well as stellar binaries with grazing eclipses or whose image is blended with another background star of constant luminosity. Additionally, atmospheric effects like air mass and seeing are relevant for ground based observations.

Great progress has been made by ground-based photometry which can achieve sub-milli-magnitude precision in some cases [Tregloan-Reed and Southworth, 2013]. How-

ever, exoplanet characterization requires space-borne observations. Heliocentric orbit or placement at a Lagrangian point are the best positions for a space-borne transit mission. Even if important transit science can be done from near-Earth orbit like in the case of CoRoT, those orbits have two main limitations:

1. long uninterrupted observing times are usually not possible from a near-Earth location,

2. contiguity to the Earth leads to time-variable scattered light and thermal radiation that can interfere with attaining the required precision [Lawson et al., 2009].

Kepler Mentioned already several times in this thesis, Kepler is a discovery-class mission designed to explore the structure and diversity of planetary systems by surveying a large sample of stars. Kepler is in an Earth-trailing solar orbit ($a = 1.013$ AU, $P = 371$ d) so that Earth does not occlude the stars which are observed continuously and the photometer is not influenced by stray light from Earth. This orbit allows for a more stable viewing platform as it avoids gravitational perturbations and torques inherent in an Earth orbit. The primary goal of Kepler is to survey our region of the Milky Way galaxy to discover hundreds of Earth-size or larger planets in or near the habitable zone of solar-like stars and get statistical data on the population and distribution of such planets. In fact, Kepler continuously monitors the brightness of more than 10^5 F through M dwarfs (of magnitude from 9^{th} to 15^{th} and of low variability) in our Galaxy. The photometer points to a field in the northern constellations of Cygnus, Lyra and Draco, which is well out of the ecliptic plane, so that sunlight never enters the photometer as the spacecraft orbits the Sun. Cygnus is also a good choice to observe because it will never be obscured by Kuiper belt objects or the asteroid belt. An additional benefit of that choice is that Kepler is pointing in the direction of the Solar system's motion around the centre of the galaxy. Thus, the stars which are observed by Kepler are roughly the same distance from the galaxy centre as the Solar system, and also close to the galactic plane. Data for a subset of target stars can be measured at a cadence of once per minute. This option is exercised for detecting changes in transit timing due to the presence of multiple planets or moons [Borucki et al., 2008]. More than 2,700 planet candidates have been detected with *Kepler*[1]. Recently, a second faulty reaction wheel was announced by NASA. At least three of the four wheels are needed to orient the telescope correctly. If the problem is not fixed, it will be not possible to gather precise data any more. However, the mission has substantial quantities of data on the ground which still need to be fully analysed.

[1] `http://www.nasa.gov/kepler`

4.3.1 Radial Velocity follow-up

Spectroscopic follow up observations become important in order to confirm the real detection of a transiting planet and moreover, they become necessary to obtain the actual mass of a transiting candidate [e.g. Borucki et al., 2010]. In fact, as outlined in Section 4.2, the flux drop observed in transit can only help in determining the planetary radius. Analogously, follow-up of radial velocity observations with transit monitoring can be used to determine real masses rather than estimates of minimum masses. This is because the inclination is determined from b the impact parameter.

As an example, Figures 4.2 and 4.3 show transit timing (from Kepler) and radial velocity (from HIRES spectrometer on the Keck I 10-m telescope) for Kepler-68 system. This is an interesting case as the Mission has revealed two transiting planets orbiting Kepler-68, while follow-up Doppler measurements have established the mass of the innermost planet b through the semi-amplitude K and revealed a third Jovian-mass planet d orbiting beyond the two transiting planets [Gilliland et al., 2013]. Kepler-68d is not expected to transit. The three planets are characterised by $P_b = 5.4$ d, $P_c = 9.6$ d, $P_d = 580$ d, $M_b = 8.3 m_\oplus$, $R_c = 0.95 R_\oplus$, $M_d \sin i = 0.95 m_{Jup}$. This example attests the benefit of using the two methods in synergy, while it reminds as follow-up via RV observations is not always practical, or even feasible. This can be due to faintness of the star [Ford et al., 2012], high stellar activity [Queloz et al., 2009] or the low mass of the planets as for Kepler-68c for which the radius can be estimated precisely but not the mass. In general, this is problematic for Kepler stars because of the faintness and high stellar activity of its sample [Gilliland et al., 2011]. Additionally, the mission aims to detect small, rocky planets in the habitable zone, which are at present outside the reach of Doppler surveys.

4.4 Transit Timing Variations

Transit timing variation is a method for detecting and confirming exoplanets by observing variations in the timing of a transit. These deviations are due to the dynamical perturbation of one or more companions.

Consider a star and a transiting planet on a keplerian orbit, the transit occurs when both the planet and the star are aligned with the line of sight. If the system has only one planet, the time Δt between transit $n-1$ and n is constant and equals the orbital period P, i.e.:

$$\Delta t = t_n - t_{n-1} = P \tag{4.4.1}$$

Including a second planet, intervals between transits vary because of gravitational interactions:

$$\Delta t(n) = t_n - t_{n-1} = P + \delta t(n) \tag{4.4.2}$$

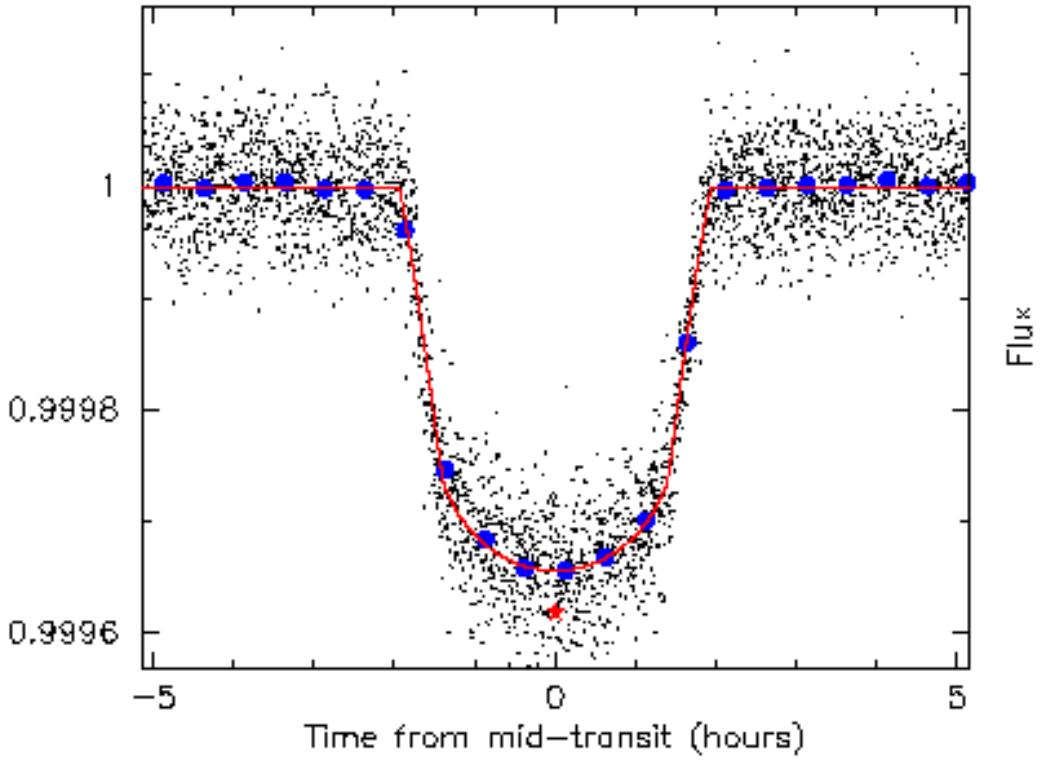

Figure 4.2: The transit of Kepler-68b, the solid line is the best fitting transit light curve fit. The red star marks centre-of-transit time [Gilliland et al., 2013].

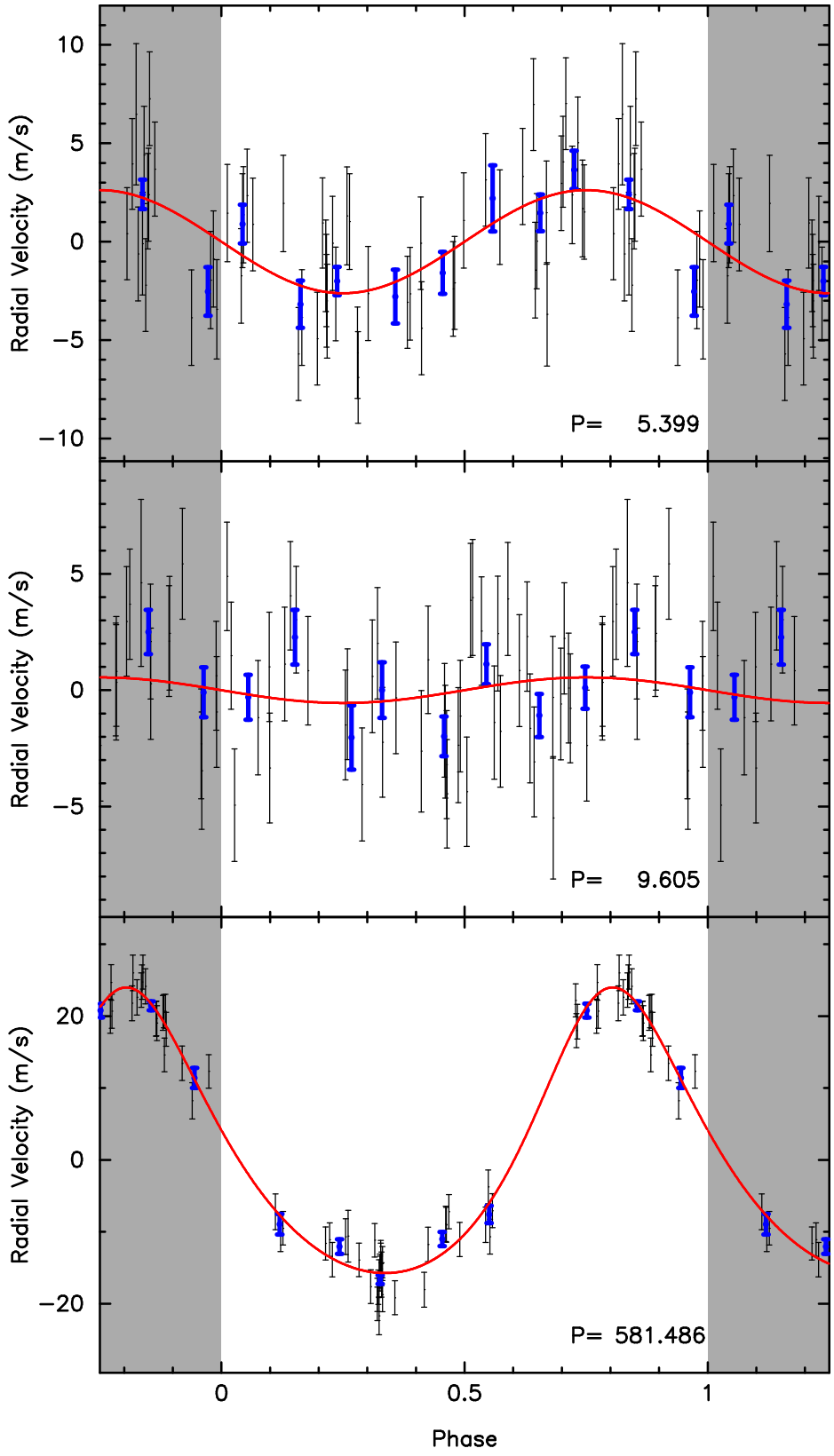

Figure 4.3: The radial velocity measurements and model fits for the planets orbiting Kepler-68. The top panel shows the RV measurements and model phase folded to the orbital period of Kepler-68b. The red line is the best fit Keplerian orbital model. The orbital period is indicated in the lower right portion of the panel. The middle and bottom panels show the RV measurements in similar fashion for Kepler-68c and Kepler-68d respectively [Gilliland et al., 2013].

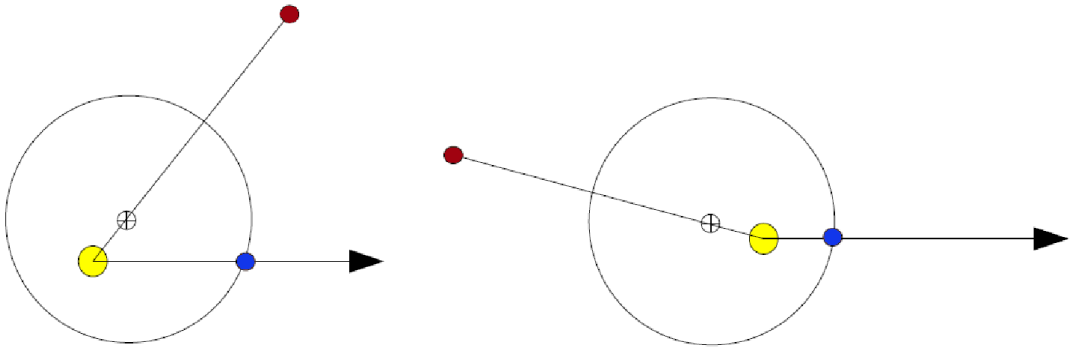

Figure 4.4: Cartoon illustrating the transit timing variation. Left: Transit at $t_0 = 0$. Right: transit at $t_1 = P + \delta t$.

where $\Delta t(n)$ is the timing interval between midtransit times of the n and $n-1$ transits and $\delta t(n)$ is the *transit timing variation*. Figure 4.4 shown motions in a barycentric frame, the wobble of the star due to the interacting planets implies a late (or early) transit.

In general, the observable *transit time variations* which constitute the TTV curve are calculated as

$$\delta t(n) = t_n - n \times \hat{P} - \hat{t}_0 \tag{4.4.3}$$

where the constants $\hat{P}$ and $\hat{t}_0$ are determined by linear least squares minimisation of $\sum_n (\delta t(n))^2$. In fact, P needs to be as accurate as possible to have a precise TTV curve. So it is important to stress that P is estimated directly from timing observations and not deduced through Kepler's equation.

For a series of transits, the strength of TTVs is characterised by the RMS of $\delta t(n)$:

$$\sigma = \sqrt{\frac{1}{N} \sum_{n=1}^{N} (\delta t(n))^2} \tag{4.4.4}$$

where N is the number of observed transits. If the variations are strictly periodic, then the amplitude of the timing deviation is simply $\sqrt{2}$ times larger than RMS.

4.4.1 Predictions

Analytical expressions of the order of magnitude of the amplitude and the period of TTV signals for systems in or near first-order mean-motion resonances have been provided by Agol et al. [2005].

The TTV signal scales roughly linearly with the mass of the perturber [Agol et al., 2005, Holman and Murray, 2005, Nesvorný and Morbidelli, 2008]. Thus, low-mass planets generate weak TTVs except if they are in mean motion resonance or near period commensurability with the transiting planet [Agol et al., 2005, Holman and Murray, 2005].

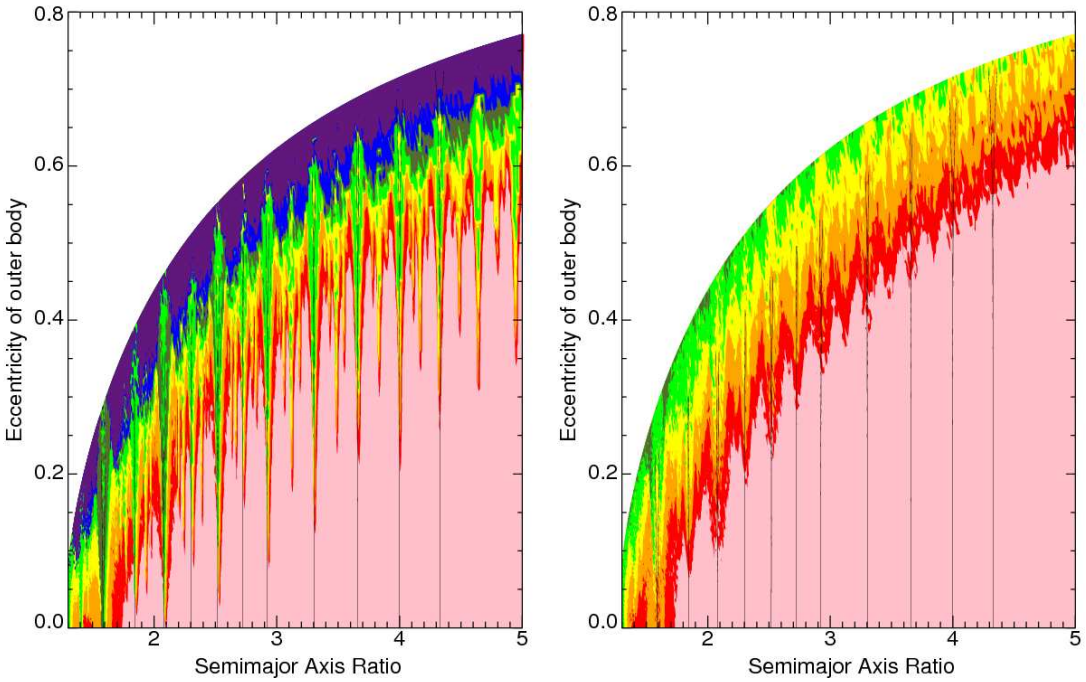

Figure 4.5: The median RMS TTV amplitude for a transiting 1 M_{Jup} on a circular orbit at $a = 0.05$ AU and a $1m_{\oplus}$ external perturber with the orbital parameters indicated on the plots. The contour levels in seconds are: pink (0–1), red (1–3), orange (3–10), yellow (10–30), light green (30–100), olive (100–300), blue (300–1000), and purple (> 1000). Left: $N = 874$ (≈ 10 yr). Right: $N = 30$ (≈ 125 days) [Veras et al., 2011].

Payne et al. [2010] performed numerical calculations of the expected TTVs induced on a hot-Jupiter by an Earth-mass perturber for inclined and retrograde orbits. While Veras et al. [2011] explore the dependence of TTV signals on semi-major axis, eccentricity and orbital angles. Figure 4.5 shows the TTV signals produced from a transiting hot Jupiter ($a = 0.05$ AU, $M_* = 1M_{\odot}$) and an external terrestrial-mass planet monitored for about 10 yr and 125 d, respectively. Taking 10 s as the current detectability threshold for TTV signal, then regions not in white, pink and red should contain a detectable signal. MMR systems that are in or close to a mean motion resonance are seen to produce the most readily detectable TTV amplitudes. In such orbits, the transit timing variation depends on the planet-planet mass-ratio rather than planet-star mass-ratio. Also, planets on eccentric orbits are seen to produce larger signals. As N increases, larger sections of $a - e$ phase space exhibit a reasonable opportunity of characterizing the unseen planet.

Also Boué et al. [2012] consider the strength of TTVs produced by a terrestrial planet ($e = 0.1$) on a Jupiter mass planet in circular orbit with period $P = 3$ days. The TTV RMS shown in Figure 4.6 is computed over 300 transits (2.5 years). The range of typical detection thresholds varying from 10 s to 1 min depends on the instrument and on the depth of the transit. Terrestrial planets of these systems can hardly produce signals at the limit of detection and only in the vicinity of period commensurabilities with $P_2/P_1 \leq 3$.

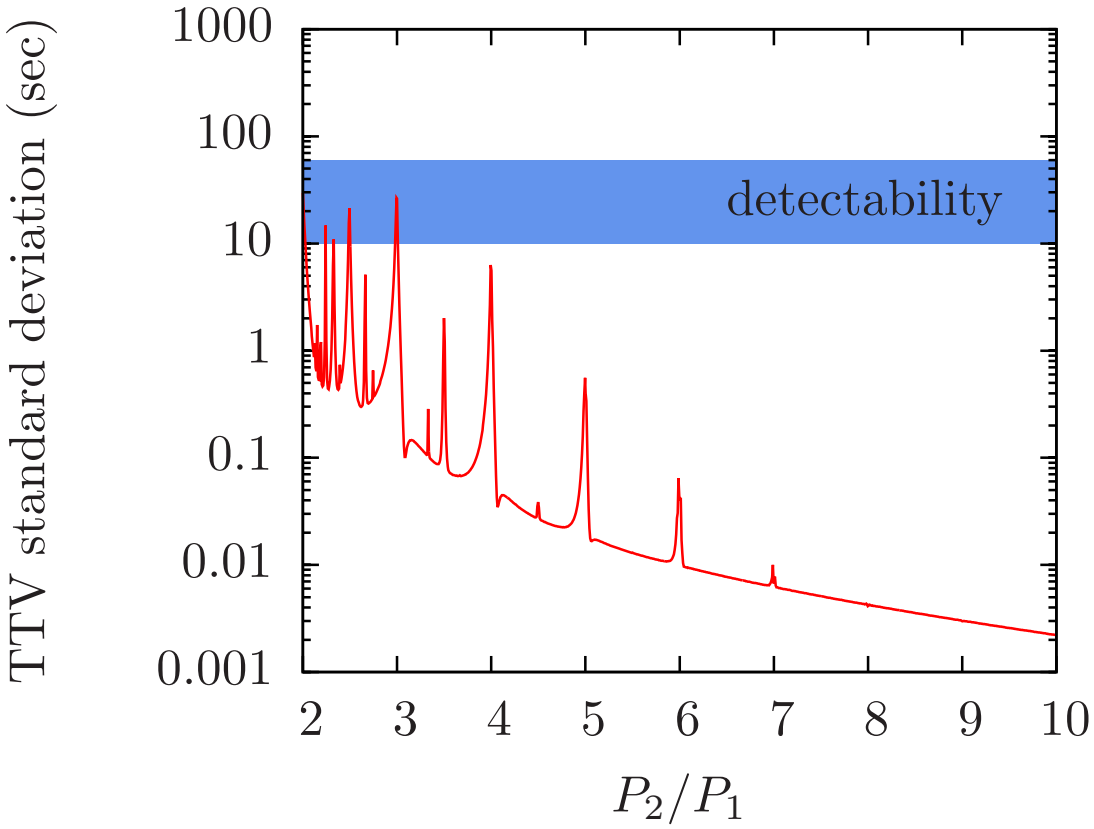

Figure 4.6: TTV RMS produced by an Earth mass planet on a Jovian planet transiting a Solar mass star every three days. The stripe shows the range of typical detectability thresholds [Boué et al., 2012].

Since the amplitude of TTV scales linearly with the period of the transiting planet, the signal produced on a wider orbit, with a period ten times larger for instance, would be easier to detect. However, the period of the TTV signal would be ten times longer too. It may exceed the duration of space surveys like *Kepler*.

The use of TTVs as a detection tool requires the solution of a difficult "inverse problem": given a particular TTV profile, is it possible to reconstruct (or at least restrict) the mass and orbit of the unseen perturber? This problem is non-trivial, as numerous different perturber mass-orbit configurations can lead to degenerate TTV solutions and most of the systems close to MMRs, which produce the most readily detectable TTV amplitudes, generate similar TTVs [Ford and Holman, 2007, Meschiari and Laughlin, 2010, Veras et al., 2011]. Nesvorný and Morbidelli [2008] and Nesvorný [2009] have developed an approximate analytic method to try and tackle the inverse problem that is $\sim 10^4$ times faster than direct N-body simulations. They claim that the timing precision required in order to uniquely characterise the perturbing planet from the TTV signal is a small fraction, $15\% - 30\%$ of the full TTV amplitude (e.g. with a precision of 10 seconds it would be possible to characterise a TTV amplitude of 30-70 seconds) and in general, at least 20 high-precision measurements of at least 20 transits are necessary. Furthermore, Libert and Renner [2013] have studied the possible detection of Laplace-resonant three-planet systems assuming that only the inner planet transits the star. A three-body resonant configuration has a specific TTVs shape which can be uniquely characterised only by means of TTVs long-term observational programs. At the end, the characterisation of non-transiting exoplanet using the TTV method can receive benefits from synergies with RV follow-up.

4.4.2 Observations

Steffen and Agol [2005] have performed one of the first TTV analyses on a particular exosystem when they studied 12 transit observations for TrES-1, demonstrating that the data could have identified a hypothetical perturber in that system that is at the order of an Earth mass or lower. Agol and Steffen [2007] have combined 13 transit observations with 68 radial velocity measurements for HD 209458 in order to constrain the presence of additional planets in that system. Miller-Ricci et al. [2008] have obtained 10 consecutive transits from MOST data sets of HD 189733b and have obtained no TTVs above 45 s. Díaz et al. [2008] analysed just five transit data points for OGLE-TR-111b and detected a TTV signal. They concluded that a satellite cannot explain the variation, and instead suggested an exterior Earth-mass planet could be the source of the variation. Coughlin et al. [2008] analysed 28 transit observations for the Neptune-mass planet Gliese 436 b and were able to rule out the existence of any planets which cause a TTV of over 60 s. Csizmadia et al. [2010] have considered the TTV on 36 transits of CoRoT-1b and did not find any periodic signals, so as to rule out additional planets in

the form of super-Earth, Saturn- and Jupiter-like planets each in particular regions of parameter space observation.

Using transit timing variations has become essential and common for characterizing multiple-transiting systems since the launch of *Kepler*. In fact, a statistical analysis of the Kepler sample demonstrated that at least 11% of systems display deviations suggestive of TTVs [Ford et al., 2011]. Once periods P and initial phases t_0 are calculated for the detected bodies, a TTV dataset coupled with N-body integrations can indicate the planetary masses [e.g. Holman et al., 2010, Lissauer et al., 2011a, Cochran et al., 2011] or at least confirm their planetary status by considering *dynamical stability* [e.g. Fabrycky et al., 2012a, Ford et al., 2012].

Kipping and Bakos [2011] have analysed 18 short-cadence transit light curves of TrES-2b from *Kepler* demonstrating exceptional timing precision at the level of a few seconds. This excluded the previously proposed hypotheses of short-period transit time variation and allowed for very accurate determination of the transit parameters for this system.

Kepler-9 was the first system of multiple planets confirmed by timing variations [Holman et al., 2010]. Kepler-9b and Kepler-9c are two Saturn-size planets which display transit timing variations characteristic of gravitational interaction of two planets near a 2:1 orbital resonance. Also, with radial-velocity observations it was possible to improve the estimates of their masses. The innermost planet, Kepler-9d, is a transiting super-Earth orbiting the star every 1.6 days. Its expected TTV amplitude is only tens of seconds, which is not surprising given the large period ratio (12.1) between it and Kepler-9b. Neither this signal nor the TTVs induced on Kepler-9b or Kepler-9c from Kepler-9d are likely to be measured by Kepler. Kepler-9b and 9c should have formed beyond the "ice line" and have migrated inward due to interactions with the remains of the protoplanetary disc, being captured into orbital resonance during this migration.

Kepler-18 is a system of three transiting planets: a super-Earth, Kepler-18b, and two Neptune-sized planets, Kepler-18c and Kepler-18d, which orbit near a 2:1 MMR [Cochran et al., 2011]. The TTV curves of Kepler-18c and Kepler-18d have amplitudes of roughly 5 minutes.

However, the first significant detection of a non-transiting planet using TTV was presented by Ballard et al. [2011]. The transiting planet Kepler-19b ($P_b = 9.3$ d, $R_b = 2.2R_\oplus$) shows TTV with an amplitude of 5 minutes and a period of 316 days, indicating the presence of a second planet, Kepler-19c. Because of the degeneracy problem, numerous scenarios were considered. The planetary status of c was determined considering dynamical stability (in the case of high eccentricity of the perturber) and constraints from the radial velocity observations. However, the selected set of possibilities spanned many periods near rational multiples of the period of the transiting planet. These included perturbers in period commensurabilities internal and external to Ke-

pler 19-b and co-orbital solutions. The presence of RV data helped in setting upper limits of $P_c \lesssim 160$ days and $m_c \lesssim 6M_{Jup}$, with the small dataset not able to indicate further constraints. Figure 4.7 shows the Kepler transit light curve for Kepler-19b with the best-fit transit light curve overplotted along with the strongly detected nearly sinusoidal variation in the times of transits of planet b.

Nesvorný et al. [2012] have identified a planetary system where the inner, transiting planet, Kepler-46b, displays a TTV signal with large amplitude (2 hours). In this case, the perturber was determined to be a Saturn-mass planet ($m_c \approx 0.37M_{Jup}$), after ruling out other fits yielding a higher χ^2.

Recently, Nesvorny et al. [2013] have identified a 12-hour TTV amplitude (over 14 quarters) for the transiting planet KOI-142b. Along with the related TDVs, this uniquely infers the presence of a non-transiting companion with a mass 0.7 that of Jupiter, KOI-142c. KOI-142b should be a Neptune class planet, with its mass being inferred from the transit variations and transit depth. The orbital period ratio 2.03 ($P_b \approx 10.95$ days and $P_c \approx 22.34$ days) indicates that the two planets are just wide of the 2:1 resonance.

The fundamental issue in characterizing low-mass planets through TTVs comes from the degeneracy of the TTV solution and the unlikelihood of their confirmation from follow-up RV measurements. In fact, no low-mass planet has been detected with the TTV method yet. One of the chief reasons can be the relative scarcity of observed multiple-planet systems where the terrestrial planet is close to a period commensurability with the transiting planets. Continued Kepler observations will dramatically improve the constraints on the planet masses and orbits and provide sensitivity for detecting additional non-transiting planets. Increasing the time span of observations for TTVs provides strong constraints on planet masses and orbits, as expected from N-body integrations of multiple transiting planet candidate systems.

4.5 *Mercury*: Computation of Transit Timings

So far I have introduced the parameters involved in the transit method, I have outlined the state of the transit detections and I have presented the TTV method along with the theoretical work and observations carried out to date. In this Section I will present how *Mercury-6* is implemented in order to study transit timing variations and I will show some applications.

The general assumptions made are:

1. Transit timing is counted at the center of the transit,
2. The perturbing non-transiting planet is an outer planet,
3. There are only two planets and in prograde orbits,

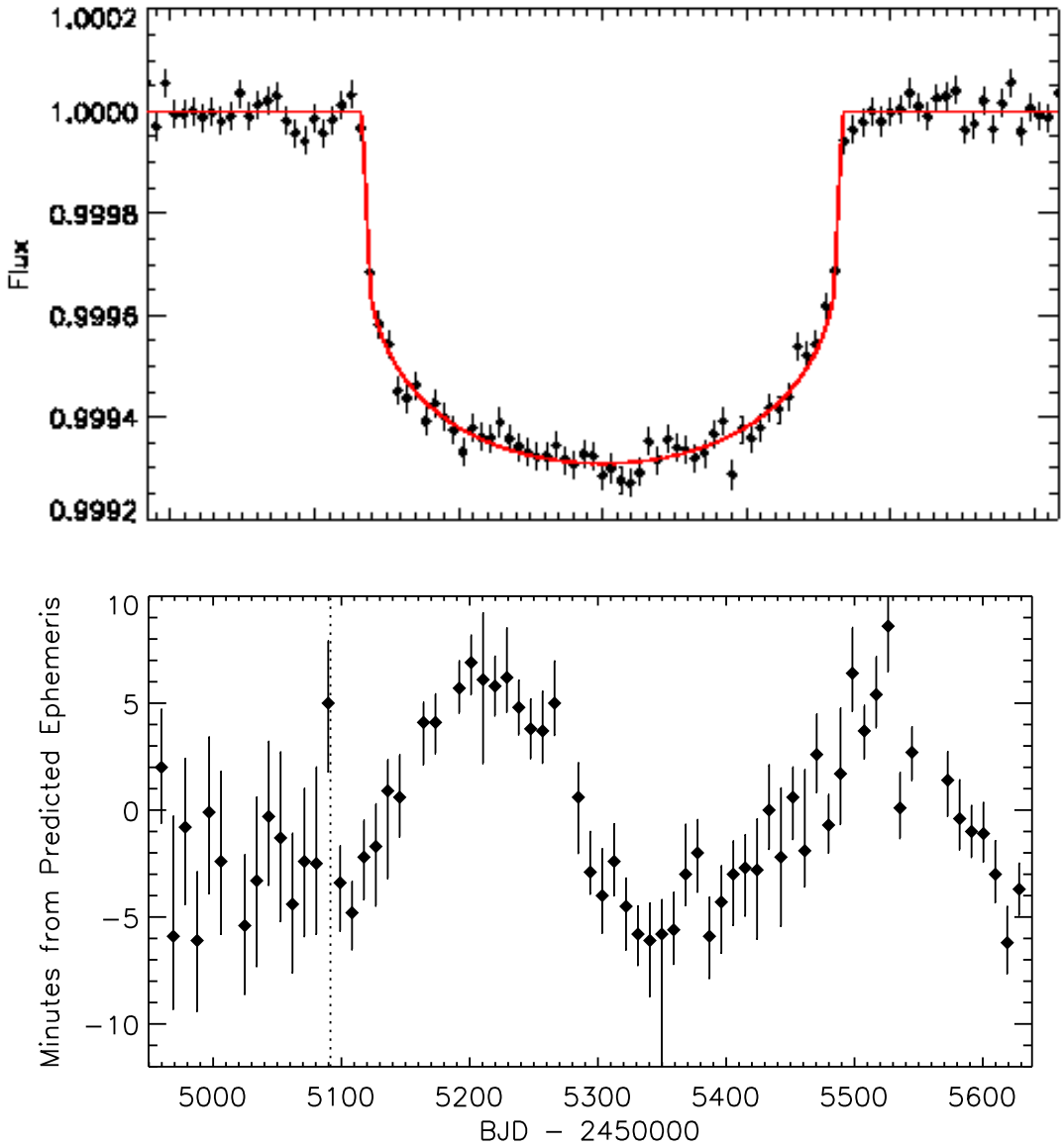

Figure 4.7: Top panel: *Kepler* transit light curve for the short-cadence observations of Kepler-19, centred on time of transit, with transit timing variations removed. Overplotted in red is the best transit model light curve. Bottom panel: *Kepler* transit times for Kepler-19b as compared to the best linear ephemeris model. The demarcation between long cadence and short cadence observations is shown with a dotted line [Ballard et al., 2011].

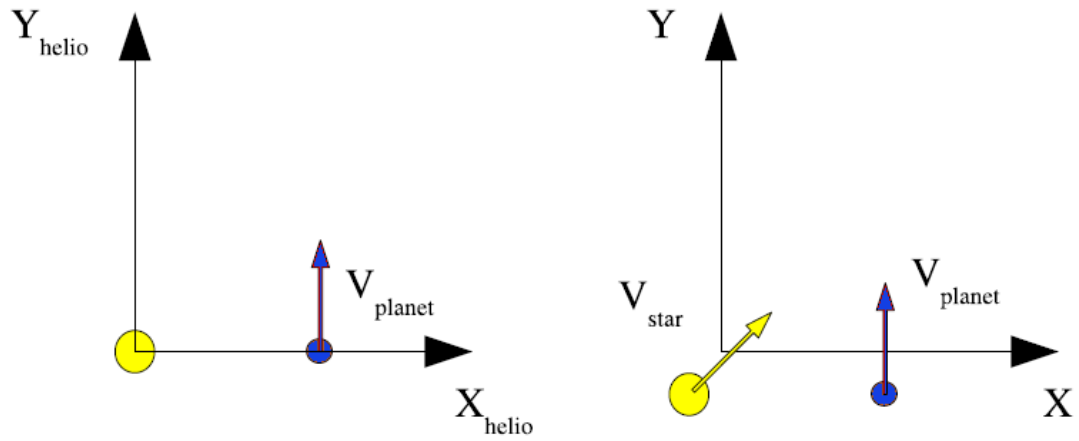

Figure 4.8: The considered two-planet system. Left: Transit computed in an heliocentric frame. Right: In a barycentric frame.

4. An edge-on system with coplanar orbits is considered,

5. Tidal effects are neglected. GR effects are included even if, for instance, Miralda-Escudé [2002] points out that GR induces pericentre change of only 1° over years,

6. Light travel time effects are included.

I use the MVS algorithm derived from that of *Mercury-6* (see Section 3.6) because here the time-step is constant and this makes simple the retrieval of the midtransit times. I look at motions in a barycentric frame, then the condition of transit is when the positions of the star and the inner planet are aligned with a positive X-coordinate (see Figure 4.8):

$$\begin{cases} y_p - y_* = 0 \\ x_p > 0 \end{cases} \tag{4.5.1}$$

The time step Δt is of the order of seconds. After each time step, I test whether the projected star-planet separation (ϵ) has changed sign and the planet in question is closer to the observer than the star. When these conditions are met, I find the nearby time that minimises ϵ via linear interpolation, record the mid-time of the transit t_n and increment the index n:

$$t_n = time - t_{small} = time - \frac{\Delta t}{y_{eg} - y_{ing}} y_{eg} \tag{4.5.2}$$

where *time* corresponds to the post midtransit position y_{eg} and y_{ing} is the position that precedes the transit. A linear interpolation implies a constant speed of the planet during the transit. I find that a Δt of 10 or 1000 seconds give the same results. Observations of transit times are perturbed by the light travel time (LTT) $\delta t_{ltt}(n)$:

$$\delta t_{ltt}(n) \simeq -\frac{\mathbf{r}_p(t_n) \cdot \mathbf{r}_{los}}{c} \tag{4.5.3}$$

where $\mathbf{r}_p(t_n)$ is the barycentric vector of the planet at midtransit time, c is the speed of light and $\mathbf{r}_{los}$ is the unit vector pointing to the observer. Since in my case this equals (1, 0, 0) then

$$\delta t_{ltt}(n) \simeq -\frac{x_p(t_n)}{c} \tag{4.5.4}$$

where $x_p(t_n)$ indicates the position on the X-axis of the planet at midtransit time. That is, again, calculated via linear interpolation:

$$x_p(t_n) = x_{eg} - \frac{x_{eg} - x_{ing}}{\Delta t} t_{small}\,. \tag{4.5.5}$$

The light-time effect [Agol et al., 2005] is due to the varying distance between the star and the observer as the star moves with respect to the centre of mass of the star and planets. I neglect any motion of the stellar centre between the time of light emission and the time of transit.

Therefore, implementing equation (4.4.3), the observable transit time variations are calculated as

$$\delta t(n) = t_n + \delta t_{ltt}(n) - n \times \hat{P} - \hat{t}_0\,. \tag{4.5.6}$$

I estimate $\hat{P}$ first and then $\hat{t}_0$ as arithmetic means considering all the recorded transits:

$$\hat{P} = \frac{1}{N-1} \sum_{n=2}^{N} t_n + \delta t_{ltt}(n) - t_{n-1} - \delta t_{ltt}(n-1) \tag{4.5.7}$$

and

$$\hat{t}_0 = \frac{1}{N} \sum_{n=1}^{N} t_n + \delta t_{ltt}(n) - (n-1) \times \hat{P}\,. \tag{4.5.8}$$

Finally, the RMS TTV (eq. 4.4.4) is calculated and saved along with $\hat{P}$. Also the TTV curve is stored.

LTT's contribution to RMS TTV can be at the few percent level (see Figure 4.9) and it is more relevant for widely separated systems with an eccentric outer planet [Veras et al., 2011].

As an application, I show the case for a Jupiter mass planet transiting a solar-like star at 0.05 AU. This body is perturbed by an Earth-like planet at 0.125 AU (Period ratio equals 2.5) with eccentricity 0.45. Figure 4.10 shows the TTV curve among 10 years of observations. The RMS TTV is of 119 seconds in agreement with the predictions of Veras et al. [2011] (see Figure 4.5).

I replicate the Kepler-18 system introduced in Section 4.4.2. I consider the two Neptune-sized planets, Kepler-18c and Kepler-18d, which are near the 2:1 MMR with $P_c = 7.6$ d and $P_d = 14.9$ d. Figure 4.11 shows the TTV curves of Kepler-18c covering the 750 days of observation (RMS TTV equals 221 s). The signal has a period of about 270 days and an amplitude of about 5 minutes in agreement with Cochran et al. [2011].

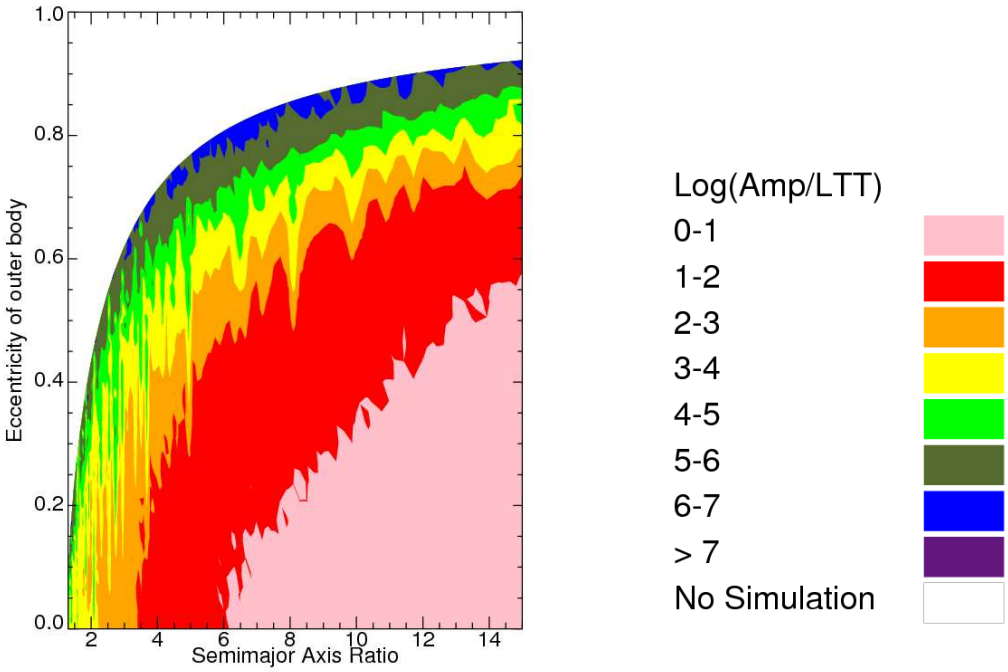

Figure 4.9: Log of the ratio of RMS TTV amplitude to the contribution from LTT alone for 874 consecutive transits and for an outer planet of $10m_{\oplus}$ (a 1 M_{Jup} planet on a circular orbit at $a = 0.05$ AU transiting a sun-like star). LTT makes a contribution of at least few percent in most areas of the studied phase space [Veras et al., 2011].

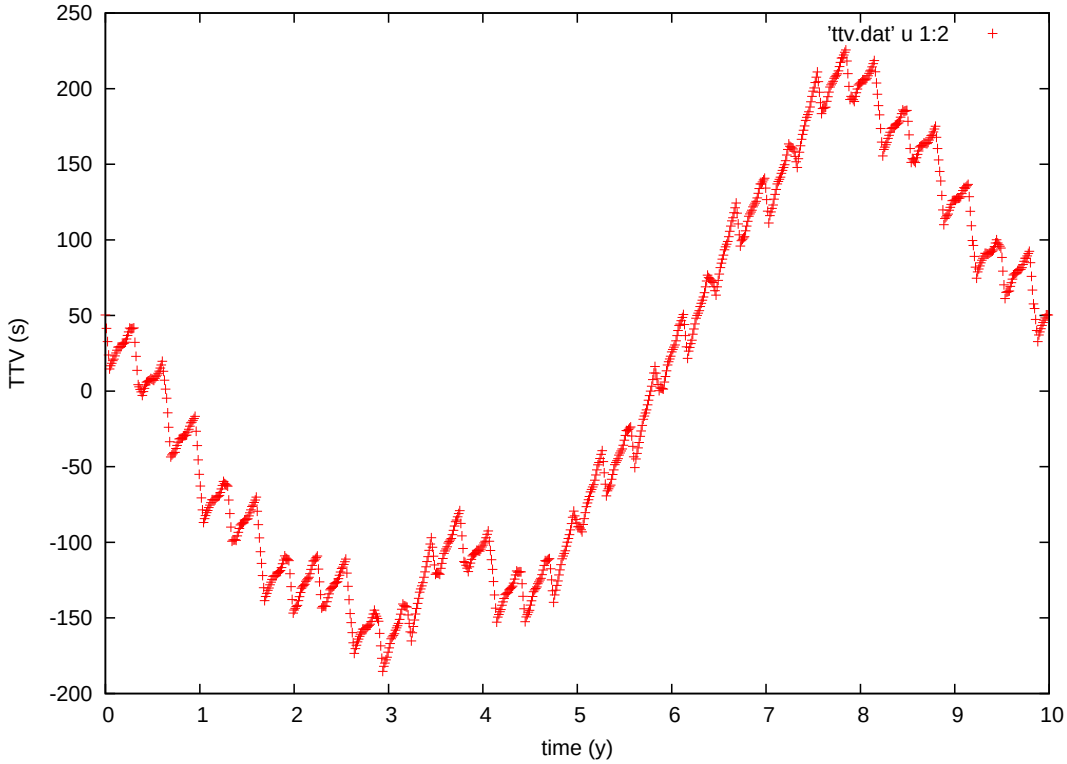

Figure 4.10: TTV curve for a Jupiter mass planet transiting a solar-like star at 0.05 AU perturbed by an Earth-like planet at 0.125 AU, $e = 0.45$. The curve spans 10 years and it has an amplitude of more than 3 minutes.

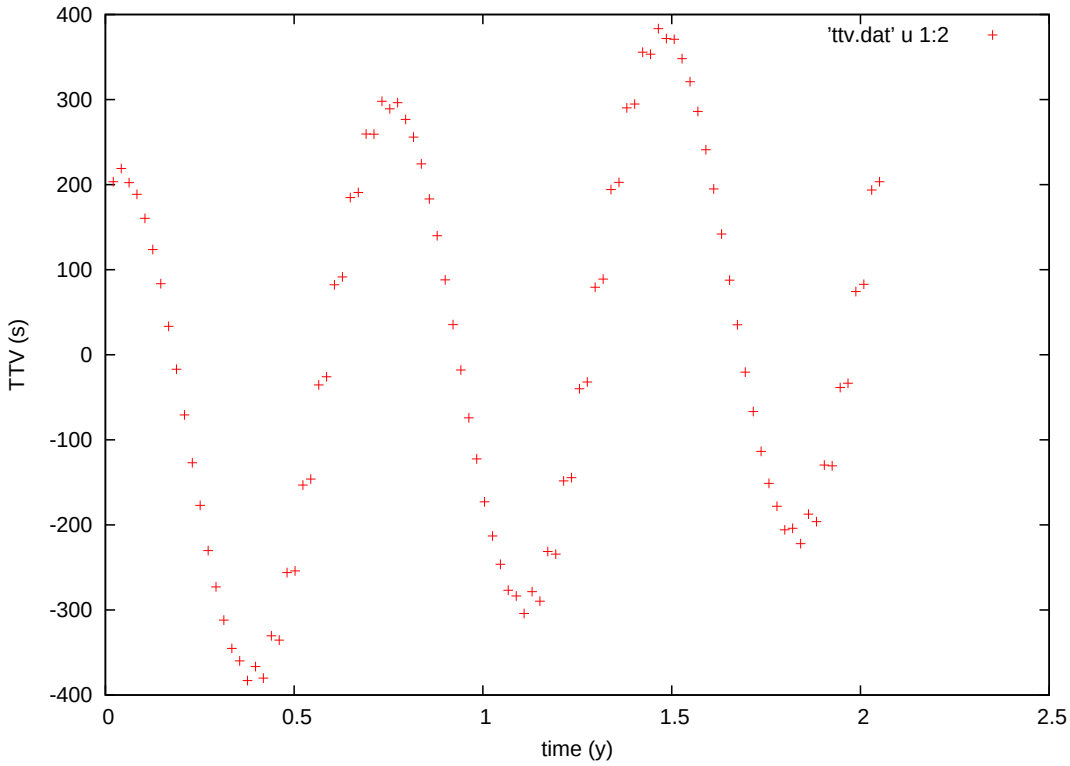

Figure 4.11: TTV curve for the case of Kepler-18c and Kepler-18d. The curve spans 750 days (slightly more than 2 years) and it has an amplitude of roughly 5 minutes.

CHAPTER 5

A 5:2 Mean Motion Resonance Configuration for the Extrasolar System HD 181433

5.1 Introduction

The planetary system of HD 181433 has been discovered with HARPS. It has been reported to contain three planets: two Jupiter-class planets and a Super-Earth of 7.5 $m_{\oplus}$ [Bouchy et al., 2009] (see Table 5.1).

Inspired by the peculiar properties of the system, which includes two giant planets and one rocky planet all in high eccentric orbits, the aim was to study the past and future evolution of the system. Unfortunately, the best fit solution published by the discovery team is unstable[1]. The model in which the initial eccentricities of the planets are reduced by one sigma quickly leads to disruption too. The fate does not change when it is assumed, in addition, a mutual orbital inclination of 20 $^{\circ}$ between planets *c* and *d*. The time evolution of these three cases is shown in the subsequent panels of Figure 5.1.

These attempts evidence the necessity of doing an analysis from scratch in order to get a self-consistent solution compatible with the data.

In this chapter, based upon the paper Campanella [2011], I will examine the available RV data of the HD 181433 system [Bouchy et al., 2009] taking a more general approach, going beyond a formal fit of the Keplerian orbital elements. Even if the RV observations do not span a single period of the outermost planet, it is possible to give reasonable constraints on the orbital elements of the poorly sampled third planet by studying the dynamics of the system. In the Keplerian fit this important information is completely omitted.

[1] See also `http://xsp.astro.washington.edu`

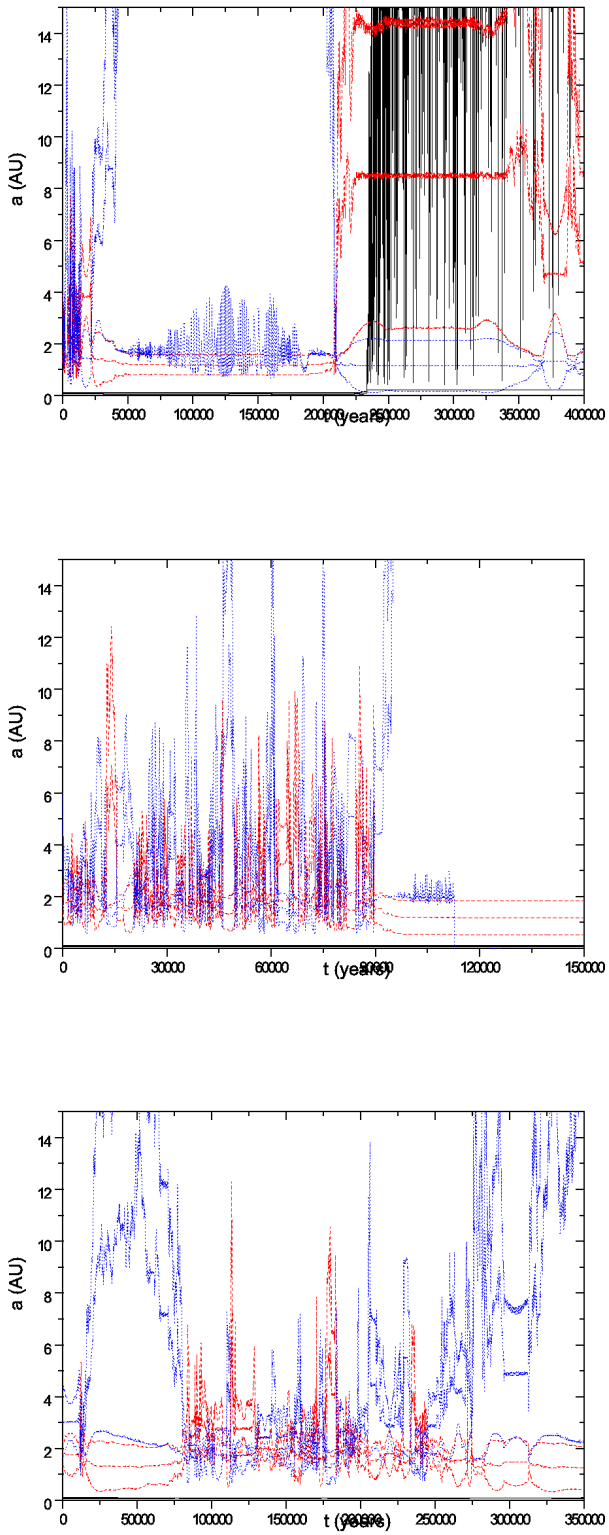

Figure 5.1: Time evolution of the semimajor axes, apocentres and pericentres. The solid line (black) indicates planet *b*, the dashed line (red) denotes planet *c* and the dotted line (blue) represents planet *d*. For each planet, its semimajor axis, apocentre and pericentre are indicated with the same colour. Top: best fit solution. Middle: configuration in which the initial eccentricities are reduced by one sigma. Bottom: a mutual orbital inclination of 20 ° is set in addition between *c* and *d*.

Table 5.1: Orbital and physical parameters of the 3-planet system orbiting HD 181433 as reported by Bouchy et al. [2009].

Parameter	**HD 181433 b**	**HD 181433 c**	**HD 181433 d**
P (days)	9.3743 ± 0.0019	962.0 ± 15	2172 ± 158
T_{peri} (BJD-2400000)	54542.0 ± 0.26	53235.0 ± 7.3	52154 ± 194
e	0.396 ± 0.062	0.28 ± 0.02	0.48 ± 0.05
ω (°)	202 ± 10	21.4 ± 3.2	30 ± 13
K (m/s)	2.94 ± 0.23	16.2 ± 0.4	11.3 ± 0.9
$m \sin i$ (m_{JUP})	0.024	0.64	0.54
$m \sin i$ ($m_{\oplus}$)	7.5	203	171
a (AU)	0.080	1.76	3
V (m/s)		40212.5 ± 0.4	
Data span (days)		1757	
rms (m/s)		1.06	
χ^2_{red}		1.29	

In Section 5.2, I perform an independent analysis of the RV data for HD 181433. I probe the phase space of the orbital parameters looking for likely configurations stable for long timescales, say millions of years. I assume the motion is described by Newtonian interacting orbits. In Section 5.3, I present the dynamical study of the stable best-fit solution and I analyse the behaviour of other plausible stable configurations. In particular, I focus on the description of secular apsidal resonances (SARs) and mean motion resonances (MMRs). In Section 5.4, I briefly summarize my findings, I discuss on the possibility of a terrestrial planet in the habitable zone and I make some predictions about what it may be expected from further observations.

5.2 Radial Velocity Data Analysis

Bouchy et al. [2009] announced the detection of three planets around HD 181433, a K3IV star, considering 107 RV measurements which covered more than 4 years, from June 2003 to March 2008. The median uncertainty for the RV data is 0.53 m/s with most of the uncertainties in the range 0.4-1.0 m/s. The peak-to-peak velocity variation is 48.12 m/s, while the velocity scatter around the mean RV in the measurements is 13.86 m/s.

The data do not completely cover a full period for the third planet. In fact, what is possible to spot it is just an additional long-term trend which is modelled by Bouchy et al. [2009] as being produced by a planet of minimum mass $m \sin i = 0.54\ m_{Jup}$ on a Keplerian orbit with a period of about 6 years and $e = 0.48$. This model is unstable on the order of just thousands of years (see Figure 5.1). The instability arises due to close encounters between planet c and planet d.

I perform a re-analysis of the HARPS data using the Systemic Console (see Section 2.4).

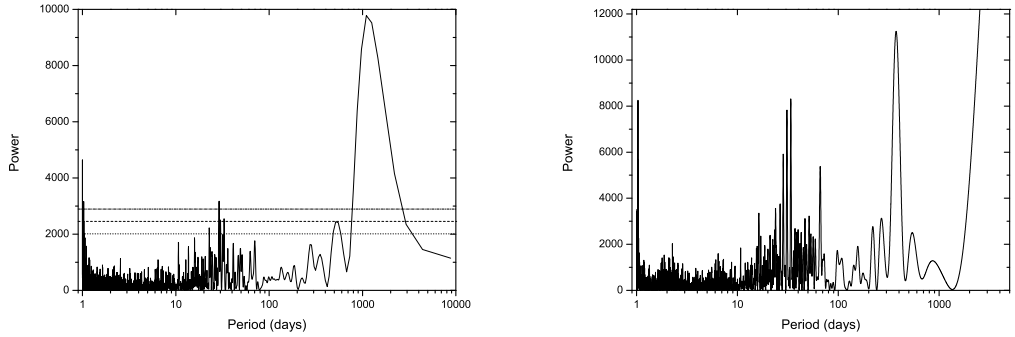

Figure 5.2: Periodograms for HD 181433. Left: LS periodogram of the RV data, a peak at $P = 1171.35$ days is present. The three horizontal lines represent, from top to bottom, the 0.1 %, 1.0 % and 10.0 % FAP levels, respectively. Right: periodogram of sampling showing peaks that are related with periodicities in the cadence of observations.

I held the stellar mass fixed, adopting the value $M_* = 0.781 M_\odot$ [Sousa et al., 2008]. I make the assumption the system is coplanar and viewed edge-on. This conjecture diminishes the quantity of potential orbital configurations greatly, but the plane (a_d, e_d) is dynamically representative for the system in the sense that it crosses all resonances [Robutel and Laskar, 2001]. When long enough time-series of precision data are available, the effects of mutual interactions part of the Newtonian model can potentially help in determining or estimating the masses and inclinations for the planets (see the discussion about this case in Section 5.2.2).

5.2.1 The Keplerian three-planet best-fit

The LS periodogram shows a peak at $P = 1171.35$ days with an estimated false alarm probability (FAP) of $\approx 2 \times 10^{-19}$. Figure 5.2 shows the LS periodogram of the full RV data set and the periodogram of sampling. The latest shows peaks that are related with periodicities in the cadence of observations, for instance these can arise from the solar and sidereal day, the synodic month and the solar year.

The residuals periodogram reveals an additional signal at $P = 9.37$ days with FAP of $\approx 1.1 \times 10^{-4}$. The best two-planet Keplerian fit yields residuals with an rms scatter of 2.44 m/s and reduced chi squared $\chi^2_{red} = 15.7$. The jitter for HD 181433 i.e. the jitter required to have the χ^2_{red} equal to 1.0, is 2.35 m/s. Fig. 5.3 illustrates the LS residuals periodogram evidencing the signal due to planet b and the periodogram of residuals to the solution for planets b and c.

To model the long-term trend in the RV signal, I make the starting guess of a planet in an outer 2:1 resonance with planet c, I adjust the mass to match the amplitude of the signal and set a small eccentricity. At this point, a Keplerian fit using the L-M algorithm naturally evolves to a solution compatible with the one by Bouchy et al. [2009]. The best

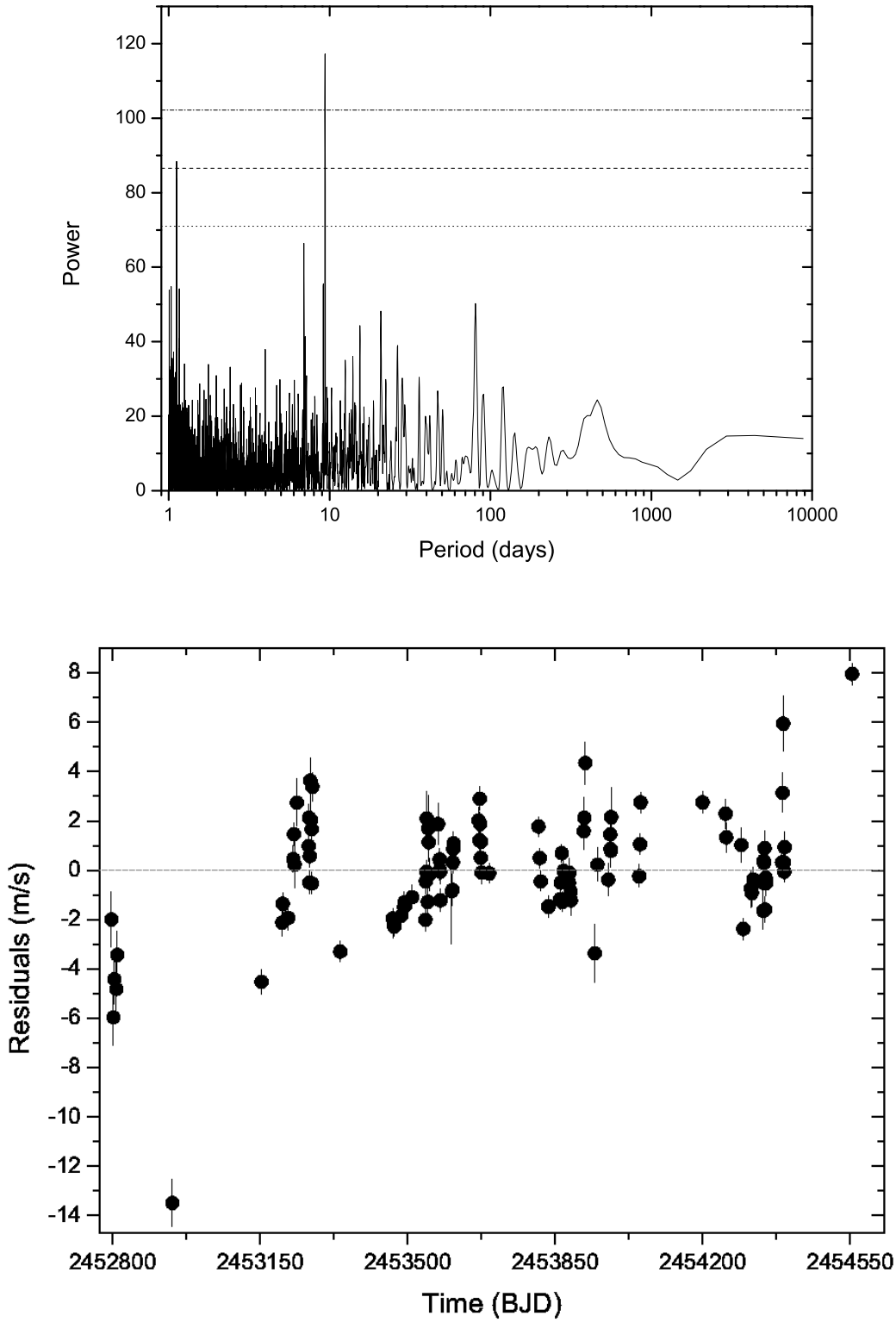

Figure 5.3: Top: LS residuals periodogram which evidences the signal due to planet *b*. Bottom: residuals periodogram to the two-planet Keplerian fit.

three-planet fit achieves a $\chi^2_{red} = 4.6$ with an rms scatter of 1.34 m/s and expected jitter of 1.17 m/s. Figure 5.4 reports the output of the Systemic Console for this case. I am not aware of how Bouchy et al. have obtained a lower χ^2_{red} and a lower value for rms for their solution.

The left panel of Figure 5.5 shows the best-fit orbital configuration at the epoch of the first observation BJD 2452797.87. The orbits of planets *c* and *d* cross each other, collisions/ejections occur due to the strong mutual interactions.

5.2.2 The Newtonian three-planet stable best-fit

Following the argument of Anglada-Escudé et al. [2010] that eccentric orbital solutions can mimic the signal of two planets in 2:1 resonant orbits, I have also tested the hypothesis of a planet in an inner 2:1 resonance with planet *c* but it was not possible to achieve any significant improvement to the goodness of the fit with respect to the two-planet solution.

The problem of exploring a 16-parameter phase space with stability as additional requirement, can get a first simplification by arguing that the elements of the inner planets are well constrained by observations. In fact, even if different starting points for their parameters are set, fits for them converge substantially to the same values. This is because these signals are well sampled. A confirmation to this argument comes from the eccentricity of planet *c*, e_c, which is a very discriminating parameter toward the stability of the system: trying to constrain e_c to lower values the fitting achieved is poor.

Concerning the parameters that describe planet *d*, it is possible to notice how higher values for the eccentricity are preferred by the fitting. Therefore, at the end the problem can be reduced in finding for each reasonable P_d the largest value for e_d for which planets *c* and *d* do not undergo instability. Likewise, it is possible to argue how once a stable solution for a pair (P_d - e_d) is found, then the aim is to investigate if it possible to get a different pair which generates a stable configuration having the same or lower χ^2_{red}. This can described as being an empirical Bayesian approach of inferring the stable best-fit rather than a frequentist approach which involves a time consuming number of simulations. Here the investigation is conducted by evidences like the ones given by the collision line (see later on in this Section) and the outcomes of previous simulations.

The second and third planets reside in regions spanned by a number of strong low-order MMRs (see Figure 5.7 later on). I am aware of the protective role of some MMR. For instance, the 2:1 MMR associated with the SAR consent together stable configurations even for enormously high eccentricities, $\simeq$ 0.95-0.98 [see Goździewski et al., 2003, and references therein]. This could explain a very large eccentricity for planet *d* and still preserve the system stability by keeping the planets away from close encounters. Ac-

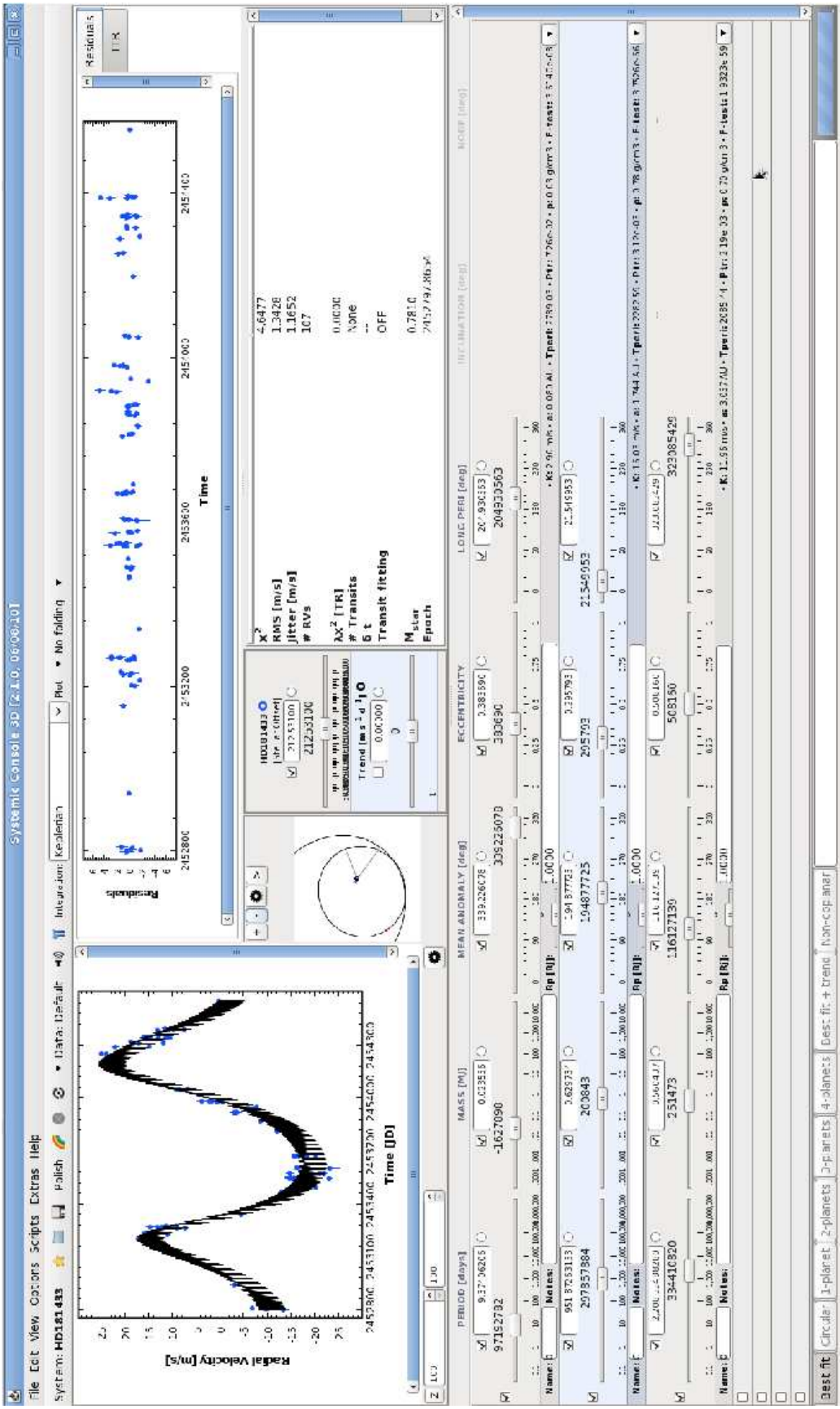

Figure 5.4: The output of the Systemic Console for the best three-planet fit. The residuals periodogram, the orbital and physical characteristics for the three planets, the fitting model and the RV data are shown.

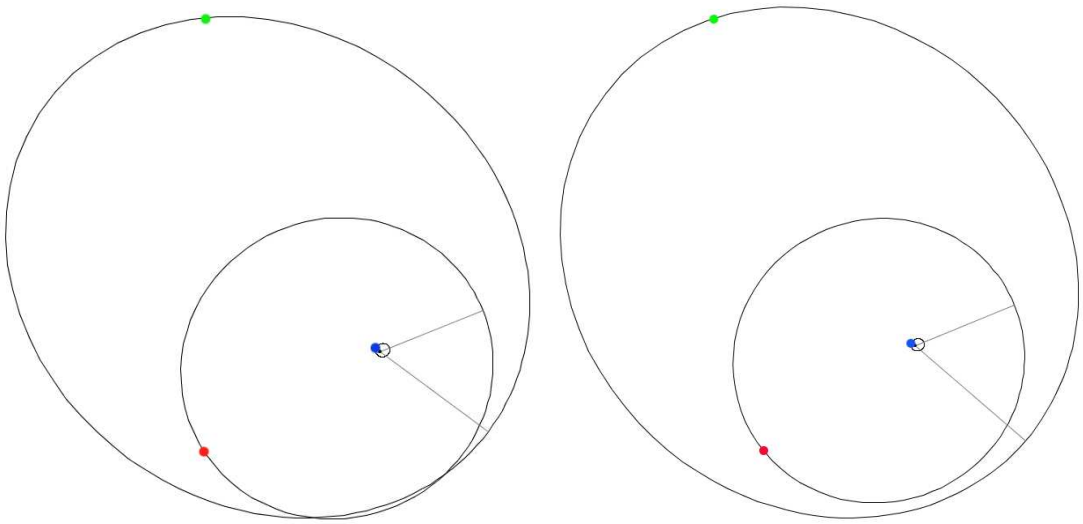

Figure 5.5: Orbital views for the HD 181433 system, the position of the planets along their orbits is the one at the first epoch of observation. The straight lines point toward the pericentres. The osculating elements are valid for the first epoch of observation. Left Panel: best fit solution, the orbits of planets c and d cross each other and collisions/ejections occur. Right Panel: stable best fit solution planets c and d are in 5:2 MMR.

tually, a modification of the relative phase of the planets strongly affects the synthetic RV curve and a *stable* resonance configuration can be far from being consistent with the RV observations. I find that manipulating the values of ω_d and of the mean anomaly, M_d, to get stable configurations is highly unfavourable by the RV data (i.e. poor fits are obtained). Therefore, this supports the argument arisen in the previous paragraph about performing an exploration focused on the (P_d - e_d) space while leaving to the algorithm the task of fitting, without constraints of any sort, the other parameters and in particular m_d, ω_d and M_d.

To perform Newtonian orbital fits, Systemic offers different method such as the Runge-Kutta, Hermite 4^{th} order and Gragg-Bulirsch-Stoer integrators (Section 2.4). Fitting a Newtonian solution takes longer than a Keplerian model but it assures short time-scale interactions, relevant for planets c and d, are considered.

The following step is studying the stability of each distinct fit over a period of time related to the time-scale of unstable behaviours. For these long-term evolution tests, direct N-body integrations are applied to the orbital solutions considered. I integrate the orbits for at least 1 Myrs using the Wisdom-Holman Mapping integrator available in the SWIFT software package (see Section 2.7). A time step approximately equal to a twentieth ($\approx 1/20$) of the orbital period of the innermost planet is used. When studying close encounters, I use the available Bulirsch-Stoer integrator with a tolerance parameter of 10^{-9}. Each configuration is identified to be a stable system if orbits stay well bounded over an arbitrarily long period of time.

The results of my analysis are outlined in Figures 5.6 and 5.7. Here I label as stable

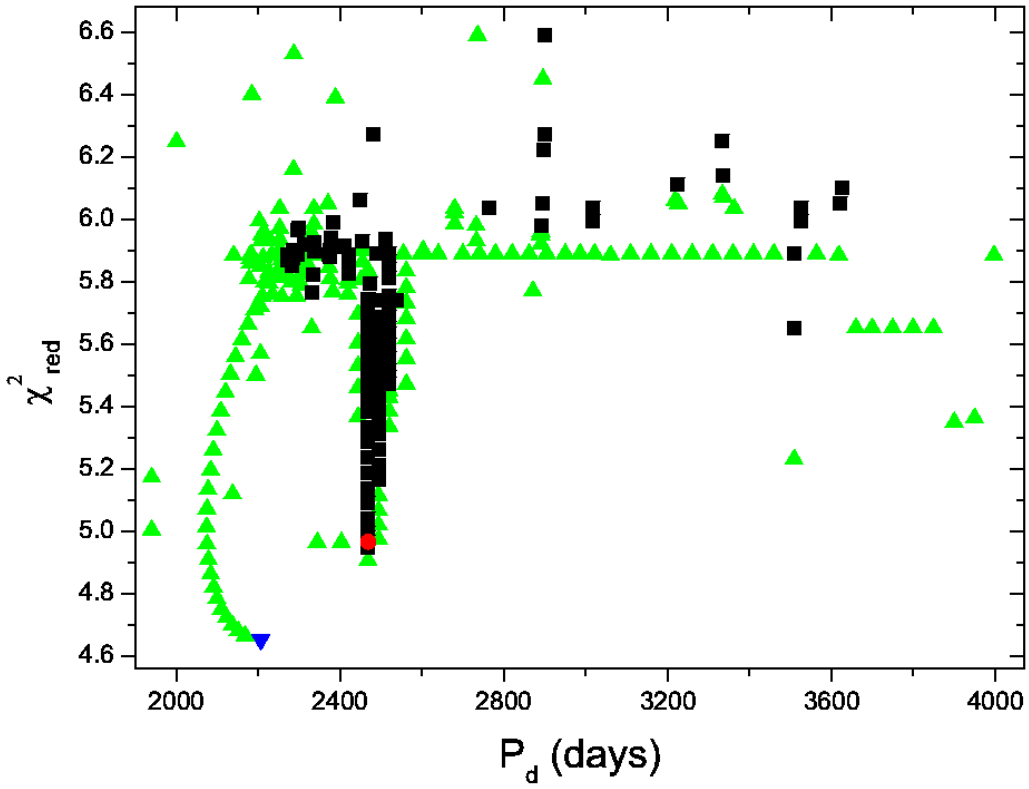

Figure 5.6: The outcome of the simulations for the HD 181433 planetary system in terms of the statistical goodness of the fits and the orbital period of the outermost planet. The statistically best-fit is indicated with an inverted triangle (blue), the stable best-fit is denoted with a circle (red). With triangles (green) I represent unstable configurations while with squares (black) I refer to models stable for at least 1 Myrs. Stable configurations do not exist in the near neighbourhood of the statistically best-fit, the deep minimum with stable models represents the region where a 5:2 MMR configuration is possible.

the solutions that survived at least for 1 Myrs. Once again, I fix (P_d - e_d) and then look for the best fit, initiating the L-M scheme with starting points derived from previously studied configurations. The L-M algorithm and Amoeba offer a clear representation of the parameter space. The dynamical analysis reveals a narrow and long band around 3.3 AU and a small island around 3.2 AU where good fitness is achieved and stability requirements are met. I find a configuration, labelled as stable best-fit, which survives for at least 250 Myrs (see Sect. 5.3 for an in-depth examination). Other models scored a better χ^2_{red} but did not preserve stability for the same amount of time. Therefore, the stable best-fit seems to lie on the border of a chaotic and unstable zone where small changes on the parameters of the outermost planet may push the system into a strongly chaotic state leading, in some scenarios, even to its disruption.

Figure 5.6 illustrates how stable configurations do not exist in the near neighbourhood of the statistically best-fit; smaller quantities for e_d are needed in order for the models to retain stability and that increases the value of χ^2_{red}.

The top panel of Figure 5.7 shows the best fits obtained during my investigation in terms of the mass for planet d, m_d, and the semi-major axis a_d. The picture makes clear how to explain a certain RV amplitude K_d, a bigger mass m_d is required as long as a_d increases.

The bottom panel of Figure 5.7 illustrates the results of my analysis in the semi-major axis-eccentricity plane (a_d - e_d). The parameters represented are the osculating elements at the epoch of the first observation. I show the collision line which is defined in terms of semi-major axes and eccentricities as $a_c(1 + e_c) = a_d(1 + e_d)$. This line denotes the region where the mutual interactions of relatively massive companions can rapidly destabilize the configuration and is calculated for $e_c = 0.269$ and $a_c = 1.773$ AU (the values are from the stable best-fit solution; see Table 5.2 later on). Note how the statistically best-fit is positioned well over the collision line. I also identify the most relevant MMRs between planets c and d, such as the 2:1, 11:5, 9:4, 7:3, 12:5, 5:2, 8:3, 11:4, 3:1, 10:3 and 7:2. The positions of the indicated locations of the mentioned MMRs have been calculated with respect to the values P_c and m_d of the stable best-fit.

I.e., for MMR n:k, we have (recalling Section 2.5.2):

$$\frac{n}{k} = \frac{P_d}{P_c}, \tag{5.2.1}$$

and a_d is calculated employing Kepler's Third Law (eq. 2.1.15):

$$P_d = 2\pi\sqrt{\frac{a_d^3}{G(M_* + m_d)}}, \tag{5.2.2}$$

Planets in some resonant configurations, even if under the collision line, exchange angular momentum rapidly; their eccentricities are quickly pumped and that may lead again to instabilities and self-disruptions. In particular, I have found models that show a stable and bounded evolution for many Myr before the unstable behaviours are manifested. On the contrary, other resonant configurations, such as the 5:2 and 7:2, are observed to retain stability even for values over the collision line.

Table 5.2 reports the determined set of orbital elements for the stable best-fit. For each planet, I list:

- period (P),
- time of periastron passage (T_{peri}),
- eccentricity (e),
- argument of pericentre (ω),
- semi-amplitude (K),

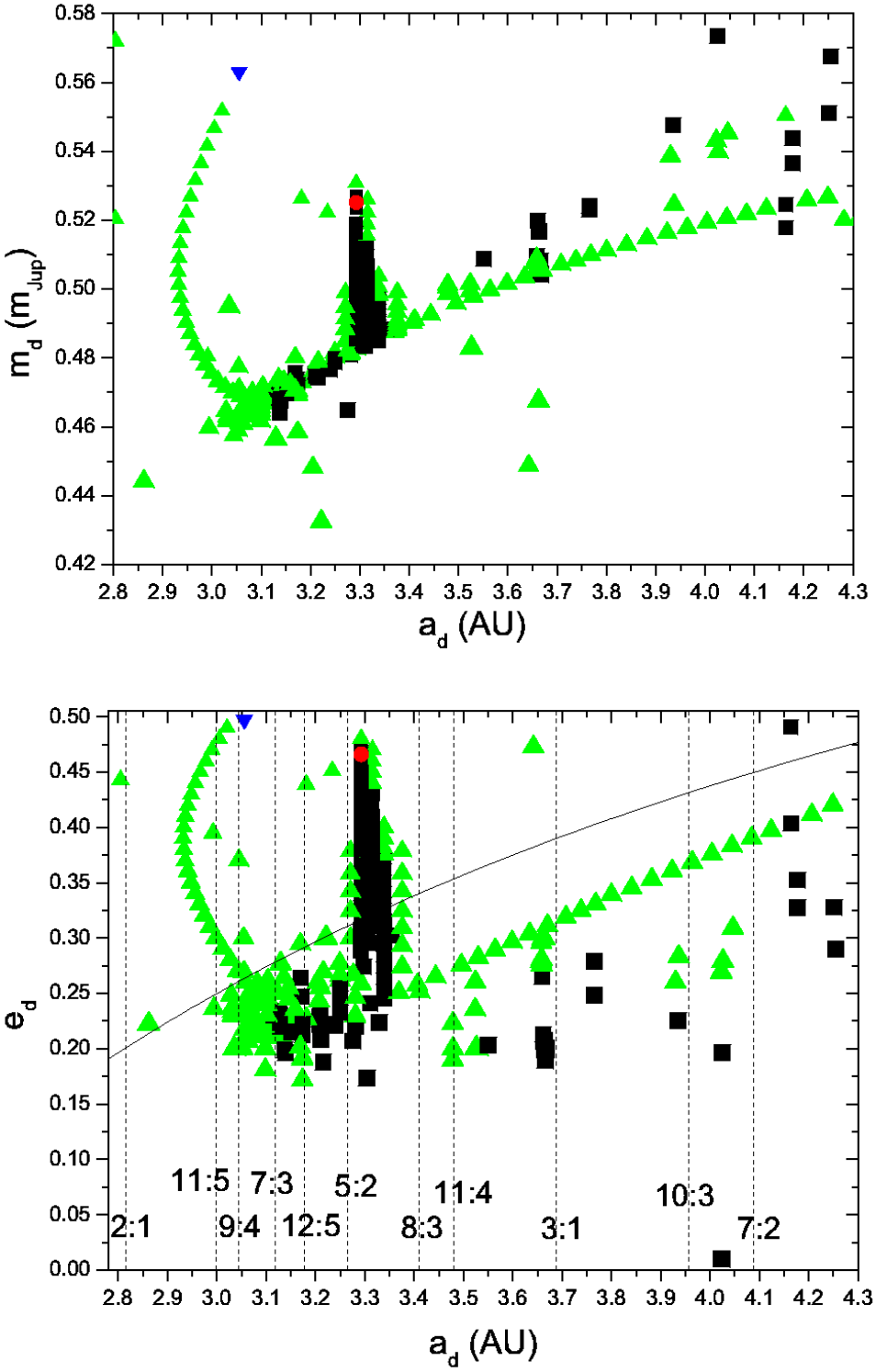

Figure 5.7: The best fits obtained for the HD 181433 planetary system. Top panel: in terms of the mass and semi-major axis of the outermost planet. Bottom panel: in terms of the eccentricity and semi-major axis of planet *d*; the collision line is depicted, the nominal positions of the most relevant MMR are also labelled and marked by dashed lines. The statistically best-fit is indicated with an inverted triangle (blue), the stable best-fit is denoted with a circle (red). With triangles (green) I represent unstable configurations while with squares (black) I refer to models stable for at least 1 Myrs. The size of each symbol is proportional to its χ^2_{red}, i.e. smaller symbols indicate better fits. The 5:2 and 7:2 MMRs retain stability even for values of e_d over the collision line.

- minimum mass ($m \sin i$),
- semi-major axis (a);

I indicate also the stellar offset (V). This model has:

- $\chi^2_{red} = 4.96$,
- an rms scatter of 1.36 m/s,
- expected jitter for HD 181433 being 1.19 m/s.

Figure 5.8 displays the RV data fitted to this model along with the residuals. The right panel of figure 5.5 shows the orbital configuration of the system, this time the orbits of planets c and d do not cross each other.

Since the stable best-fit is found in an active region, rather than estimating an uncertainty on each parameter, I think Figures 5.6 and 5.7 are more useful in visualizing the results of the dynamical study and highlight what is plausible to expect from new observations. Comparing my results with what has already been published for this planetary system[2], I find that the parameters of planet b and c are confirmed to be already well constrained with just K_c not compatible within the 3 σ. For planet d, all the elements are found within the 3 σ from the original conclusion. However, it is worth to underline how to explain the very large eccentricity of the third planet and to retain a good fit to the present data, the uncertainty on the location of planet d reduces dramatically to the narrow band where the 5:2 MMR is possible. Hence, this supports how a dynamical study can be fundamental in interpreting observations, producing a self-consistent model compatible with the data and giving substantial constraints on the orbital parameters.

The data do not offer any possibility of constraining the orbital inclinations. The Newtonian model cannot be particularly improved because, aside from the fact the signal of the outer planet is not well sampled, one needs to wait for secular time-scales before the variations in i can be spotted via the RV method. In fact, I note that for planets GJ 876 b and c which have the strongest mutual gravitational interactions, more than 11 years of observations (corresponding to more than 60 orbits of the outer planet) were used to give a reasonable estimate of the inclinations (as anticipated in 2.6). Figure 5.9 shows original data from [Correia et al., 2010] with inclinations for GJ 876 b and c estimated to be 0.4° and 1.6°, respectively. Planet d, a 6.2 earth mass body in a two-day orbit is not interacting strongly with the outer giants b and c and therefore its inclination is just held at a fixed value with no possibility of being determined at the present time.

[2]Bouchy et al. [2009] do not report directly the uncertainties for the masses and semi-major axes, in this case I considerer what is available on `http://exoplanets.org`

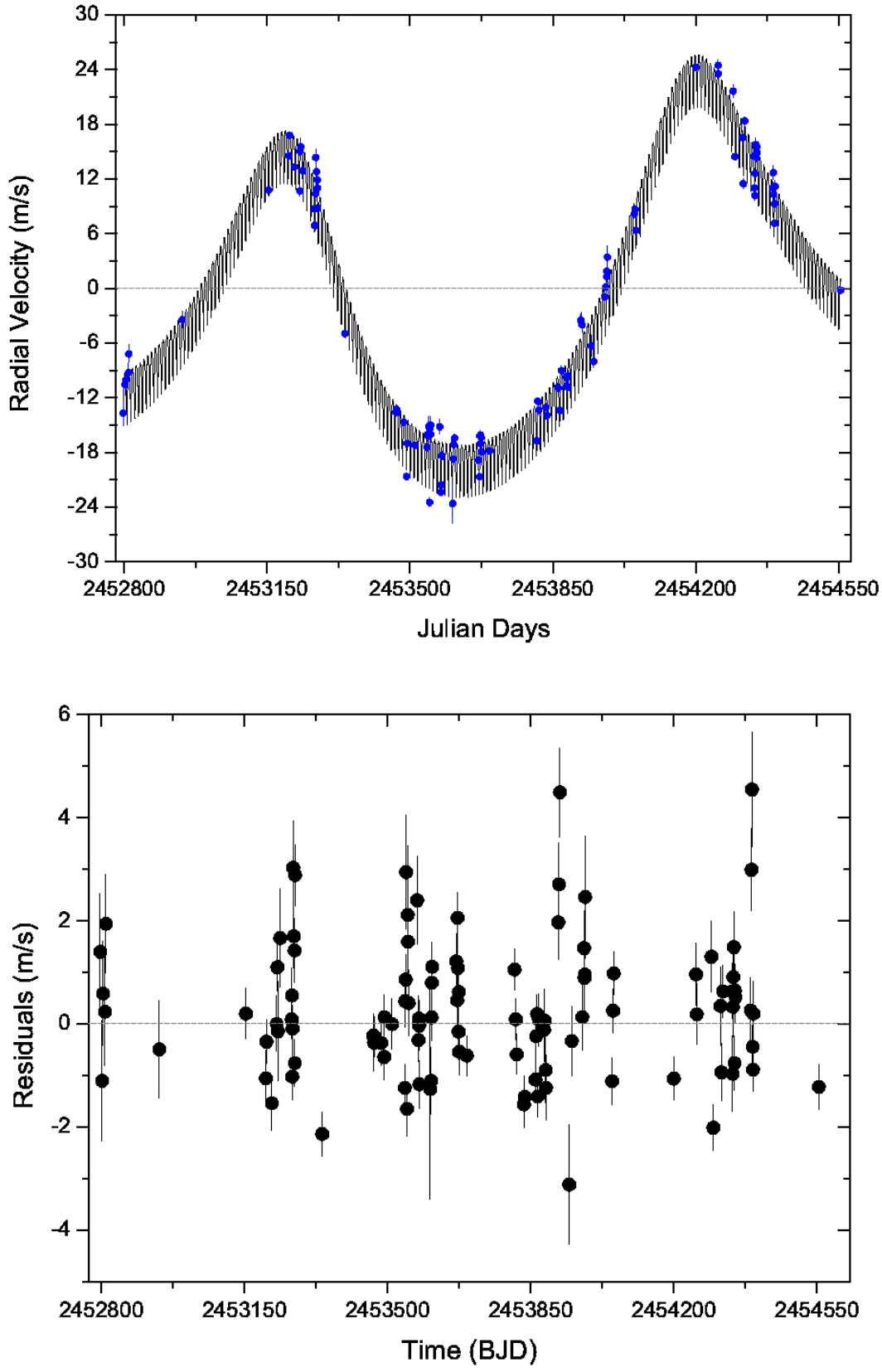

Figure 5.8: The Newtonian three-planet stable best-fit model and residuals periodogram for the HD 181433 RV data.

Table 5.2: Orbital and physical parameters of the stable best-fit found for the HD 181433 planetary system. The osculating elements are given for the epoch of the first observation BJD 2452797.8654.

Parameter	**HD 181433 b**	**HD 181433 c**	**HD 181433 d**
P (days)	9.37459	975.41	2468.46
T_{peri} (BJD-2450000)	2788.9185	2255.6235	1844.4714
e	0.38840	0.26912	0.46626
ω ($^\circ$)	202.039	22.221	319.129
K (m/s)	2.57	14.63	9.41
$m \sin i$ (m_{JUP})	0.02335	0.65282	0.52514
$m \sin i$ ($m_\oplus$)	7.4	207.5	166.9
a (AU)	0.08013	1.77310	3.29347
V (m/s)		40212.846	
rms (m/s)		1.36	
χ^2_{red}		4.96	

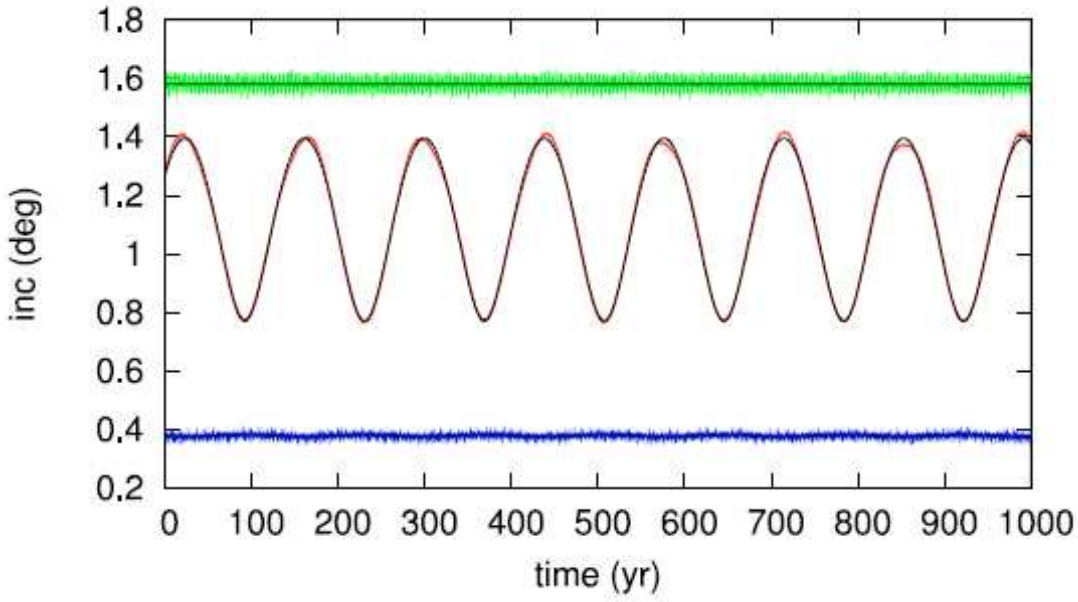

Figure 5.9: Evolution of the GJ 876 inclinations with time as shown by [Correia et al., 2010]. The blue line indicates planet *b*, the green line denotes planet *c* and the red line represents planet *d*. The black curves are the associated values obtained with the linear, secular model.

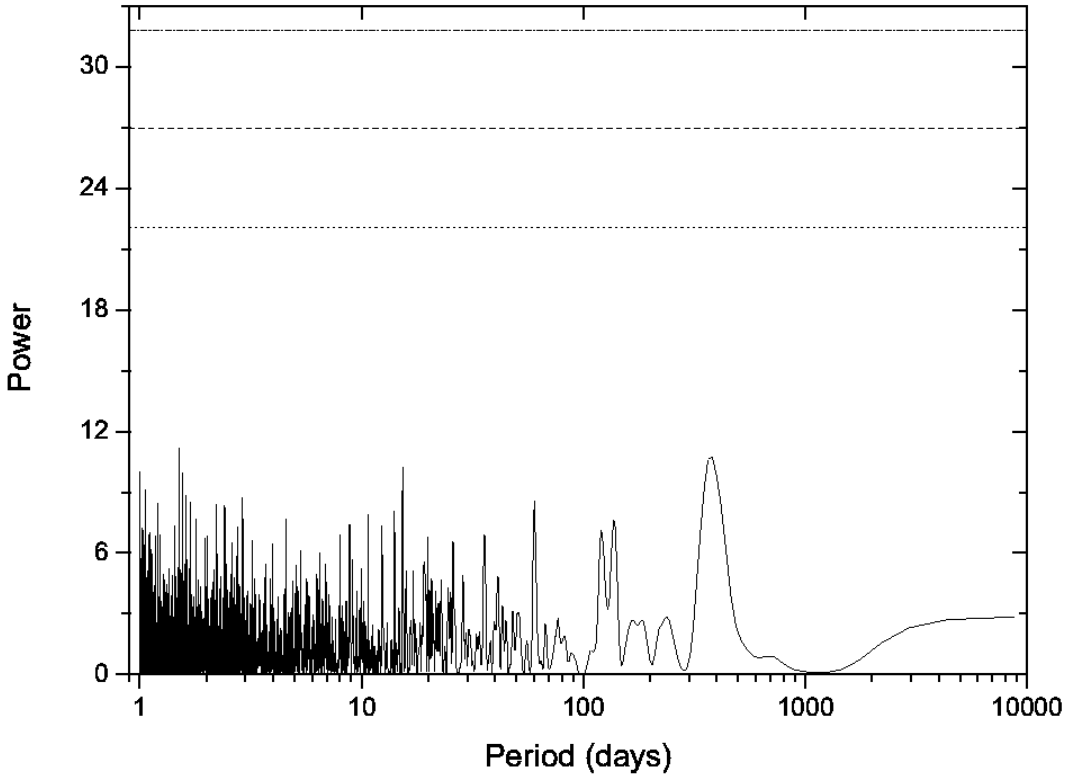

Figure 5.10: Periodogram of the residuals to the three-planet solution for HD 181433. It does not display any strong peak that would support the evidence for additional planets in the system. The three horizontal lines represent, from top to bottom, the 0.1 %, 1.0 % and 10.0 % FAP levels, respectively.

5.2.3 Additional planets?

Finally, following the argument that the proximity of the best fit to the collision line may indicate the presence of further planets [Goździewski et al., 2008], I aim to search for four-planet Newtonian solutions. The periodogram of the residuals to the three-planet solution, in Figure 5.10, displays no strong peaks that would support the evidence for additional planets in the system. Apart from more distant companions, in the inner region of the system a terrestrial planet can only survive if located between planets *b* and *c*. In fact, already planet *b* is found in the proximity of the parent star and the area between planets *c* and *d* is dominated by the strong interactions that interest the two giant planets in eccentric orbits. The existence of this last planet would support the 'packed planetary systems' hypothesis [Barnes and Raymond, 2004].

The present data do not allow making any supposition about possible outer planets (for example an object at 7 AU would have an orbital period of around 7700 d). On the other hand, with a super-Earth in the stable zone between planets *b* and *c* the fit improves. However, this signal would be at the noise level with an *F*-test of the order of 30 per cent. The *F*-test indicates the probability that a planetary model would produce

a signal similar to the one due just to noise fluctuations in the data (see Section 2.4.1), so additional observations are required to investigate on the presence of a super-Earth or less massive planet in this stable region.

5.3 Long-Term Behaviour of the Stable Best-Fitting Configurations

Because of the proximity of the two outermost planets, the system cannot be stable unless a resonant mechanism is present to avoid close encounters. In this Section, I aim to deepen the study of the stable best-fit configuration as well as investigating the evolution of the orbital elements, the secular resonant arguments and critical angles (introduced in Section 2.5) of some particular configurations consistent with the RV observations.

For the stable best-fit, Figure 5.11 shows in the subsequent panels the time evolution of the semi-major axes and of the eccentricities. Moreover, two secular resonant angles and three critical arguments of the 5:2 MMR are illustrated. Specifically, the top-left panel of Figure 5.11 highlights that for the 250 Myr of the numerical integration the apocentre of planet c and the pericentre of planet d share the same region. If we get a close-in view of the situation (top-right panel), it is possible to notice that actually they never cross each other. In particular, the pericentre of d is internal to the apocentre of c. The former approaches the value of a_d around every 50000 years. It is probably a resonance that, protecting the companions from close encounters, allows the stability of the system. The left panel of the third line of Figure 5.11 illustrates the relative large range in which e_c and e_d evolve. The peak-to-peak amplitude is covered in around 2500 years only. e_c moves in the interval 0.17-0.52 while e_d in the range 0.17-0.50. The present eccentricities fall in the middle of these intervals indicating that the system has been snapped in a statistically quite probable state. Also, such a large range reminds that in multiple-planet systems the orbital eccentricities can vary considerably through secular interactions on time-scales that are long compared to observational baselines but short compared to the age of the systems. Therefore, when doing statistical studies on exoplanetary systems the planetary orbits should normally be described by a complete distribution of values for the eccentricities rather than just by the present quantities (see also Adams and Laughlin [2006b]). This model is not observed to be in SAR. The left panel of the second line of Figure 5.11 indicates the time evolution of the secular argument $\omega_c + \omega_d$ which alternates librations with circulations, while the right panel represents the time evolution of the circulating secular argument $\omega_c - \omega_d$. Besides, I find that $5n_d - 2n_c \approx -3.4^\circ/yr$ indicating the proximity of the 5c:2d MMR, therefore here we have a scenario similar to the Jupiter-Saturn case in the Solar system. I have studied the four resonant arguments (coplanar case) of this third-order MMR:

- $5\lambda_d - 2\lambda_c - 3\omega_c$,
- $5\lambda_d - 2\lambda_c - 3\omega_d$,
- $5\lambda_d - 2\lambda_c - 2\omega_c - \omega_d$,
- $5\lambda_d - 2\lambda_c - \omega_c - 2\omega_d$.

The angle $5\lambda_d - 2\lambda_c - 3\omega_d$ librates around 180° with a semi-amplitude of about 110°. Thus, this configuration is seen to be locked in a MMR, the right panel of the third row illustrates how this critical angle evolves with time. Represented in the last line of Figure 5.11 are the evolution of the angles $5\lambda_d - 2\lambda_c - 2\omega_c - \omega_d$ and $5\lambda_d - 2\lambda_c - \omega_c - 2\omega_d$. The former circulates, while the latter experiences the nodding phenomenon (see Section 2.5.2) alternating circulations with librations around 0° and a semi-amplitude of about 45°.

The mass of planet b is negligible with respect to c and d, so I can assume the dynamics of the two giants is not disturbed much by the presence of the rocky planet close by. Then, I study some possible configurations with planets c and d near MMR. I do not find any plausible ($\chi^2_{red} \leq 6.03$) stable solution that would correspond to the 2:1, 11:5, 9:4, 7:3, 8:3, 11:4 and 10:3 MMRs. In particular, the configurations nMMR 11:5, 9:4 and 7:3 seem preferred by the data but the excessive pumping of the eccentricities causes close encounters and planetary scatterings which do not favour stability. On the other hand, outer MMRs are possible because here in particular the planets are more spread and collisions can be avoided.

I compute the evolution of the orbital elements for fits corresponding to MMRs 12:5, 7:3, 3:1 and 7:2 which our simulations have demonstrated to preserve stability for at least 40 Myr. The results are illustrated in Figures 5.12, 5.13, 5.14 and 5.15 and show the complexity of the possible dynamical behaviours of the HD 181433 system that are consistent with the RV observations.

The case I show nMMR 12:5 has $\chi^2_{red} = 5.91$ and rms scatter of 1.46 m/s with $12n_d - 5n_c \approx 1.8^\circ/yr$. This model is in SAR with $\omega_c - \omega_d$ librating around 0° with a semi-amplitude of about 45°. In the planar case this seventh-order resonance has eight critical angles:

- $12\lambda_d - 5\lambda_c - 7\omega_c$,
- $12\lambda_d - 5\lambda_c - 7\omega_d$,
- $12\lambda_d - 5\lambda_c - 6\omega_c - \omega_d$,
- $12\lambda_d - 5\lambda_c - \omega_c - 6\omega_d$,
- $12\lambda_d - 5\lambda_c - 5\omega_c - 2\omega_d$,

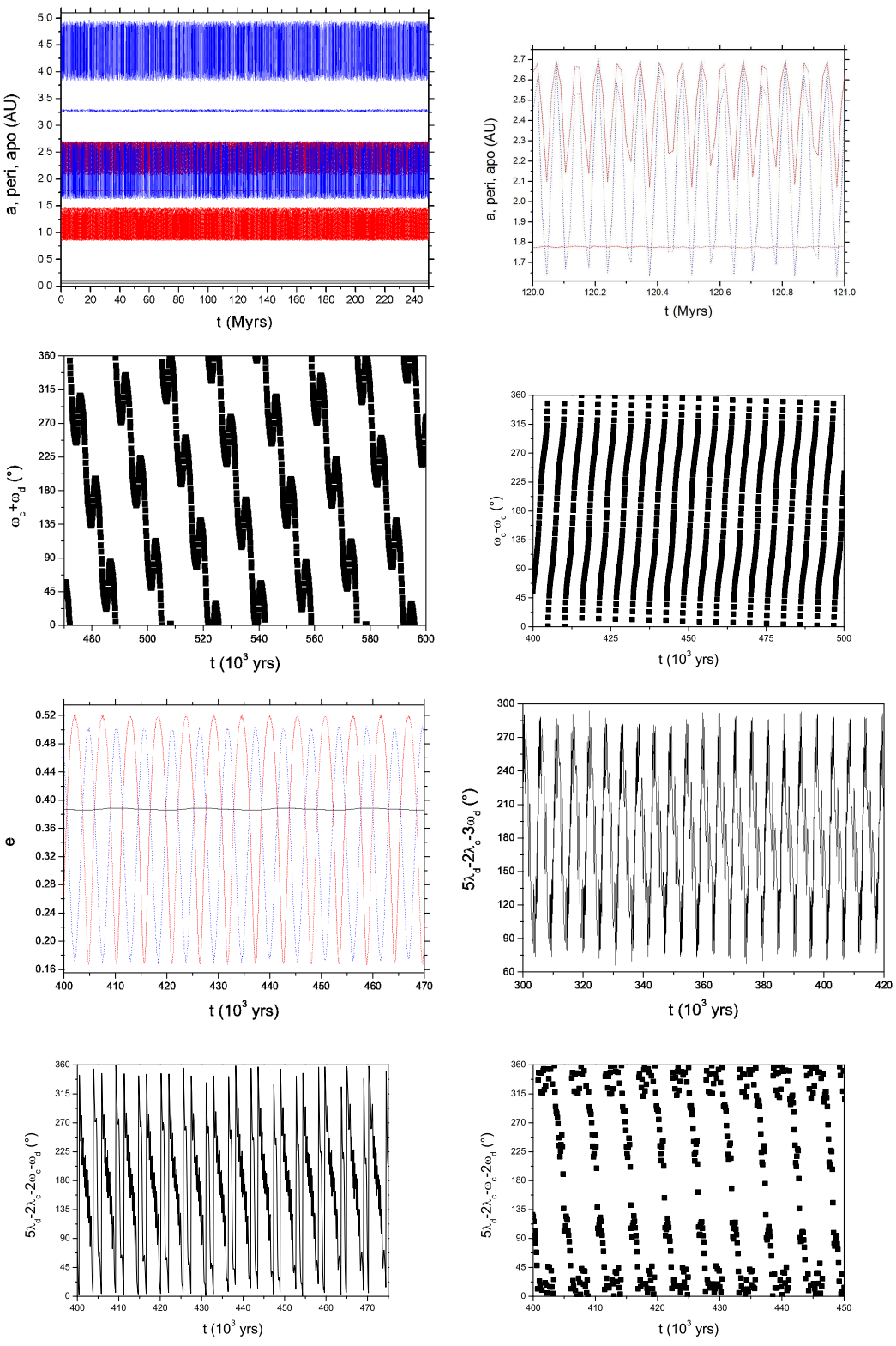

Figure 5.11: Evolution of some orbital elements for the stable best-fit configuration. The solid line (black) indicates planet *b*, the dashed line (red) denotes planet *c* and the dotted line (blue) represents planet *d*.Top: time evolution of the semi-major axes, along with a close-in view on the pericentre of *d* and the apocentre of *c*. Second row: two secular resonant angles. Third row: time evolution of the eccentricities and the librating argument of the 5:2 MMR. e_c moves in the interval 0.17-0.52 while e_d in the range 0.17-0.50. Bottom: evolution of two other critical arguments of the 5:2 MMR.

- $12\lambda_d - 5\lambda_c - 2\omega_c - 5\omega_d$,
- $12\lambda_d - 5\lambda_c - 4\omega_c - 3\omega_d$,
- $12\lambda_d - 5\lambda_c - 3\omega_c - 4\omega_d$.

I have found some critical arguments of the MMR to alternate librations with circulations implying the resonance excites a chaotic configuration. The time evolution of the critical angles $12\lambda_d - 5\lambda_c - 7\omega_d$, $12\lambda_d - 5\lambda_c - 7\omega_c$, $12\lambda_d - 5\lambda_c - \omega_c - 6\omega_d$ and $12\lambda_d - 5\lambda_c - 5\omega_d - 2\omega_c$ are illustrated in Figure 5.12.

The scenario nMMR 7:3 has $\chi^2_{red} = 5.89$ and rms scatter of 1.46 m/s with $7n_d - 3n_c \approx 8.7^\circ/yr$. This model is observed to be in SAR with the critical angle $\omega_c - \omega_d$ librating around 0° with a semi-amplitude of about 40° meaning that their periastrons of planets c and d are maintained aligned. I have studied the resonant arguments of this fourth-order MMR:

- $7\lambda_d - 3\lambda_c - 4\omega_c$,
- $7\lambda_d - 3\lambda_c - 4\omega_d$,
- $7\lambda_d - 3\lambda_c - 3\omega_c - \omega_d$,
- $7\lambda_d - 3\lambda_c - \omega_c - 3\omega_d$,
- $7\lambda_d - 3\lambda_c - 2\omega_c - 2\omega_d$.

It is found that three critical angles i.e. $7\lambda_d - 3\lambda_c - 4\omega_d$, $7\lambda_d - 3\lambda_c - 3\omega_d - \omega_c$ and $7\lambda_d - 3\lambda_c - 2\omega_d - 2\omega_c$, alternate librations with circulations. This indicates that the configuration is close to the resonance separatrices. Figure 5.13 illustrates how the above-mentioned critical angles evolve with time.

The case near the second-order MMR 3:1 has $\chi^2_{red} = 6.03$ and rms scatter of 1.47 m/s with $3n_d - n_c \approx 0.6^\circ/yr$. This model is in SAR with $\omega_c - \omega_d$ librating around 180° with a semi-amplitude of about 110° implying that this time the periastrons of planets c and d are anti-aligned. The data points that diverge from the periodic signal (Figure 5.14, bottom-left panel) represent the instants when e_d gets close to be null and so the argument of pericentre, ω_d, is not well defined. In the planar case this low-order resonance has three critical angles:

- $3\lambda_d - \lambda_c - 2\omega_c$,
- $3\lambda_d - \lambda_c - 2\omega_d$,
- $3\lambda_d - \lambda_c - \omega_c - \omega_d$.

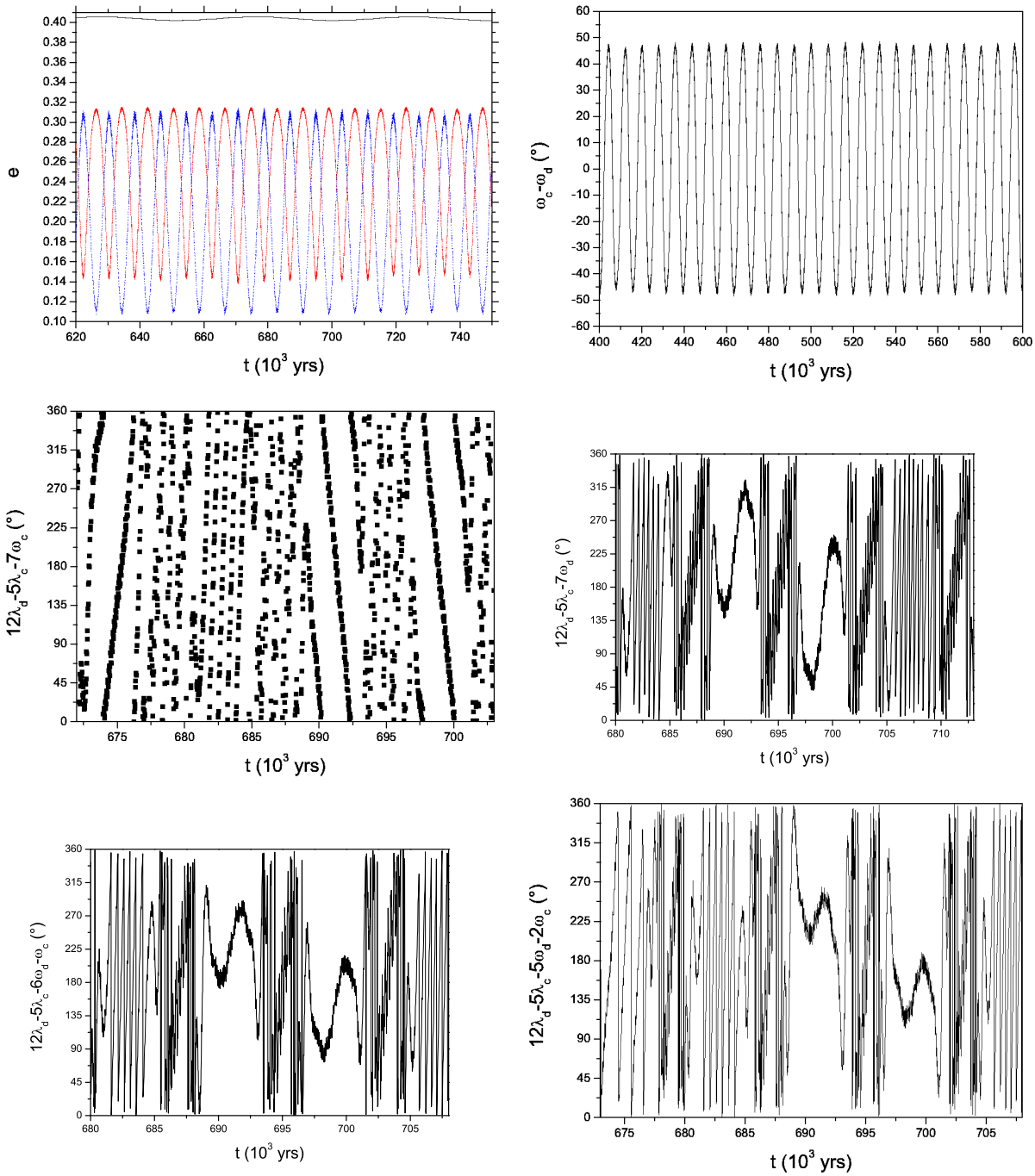

Figure 5.12: Evolution of some orbital elements for the nMMR 12:5 configuration. Top-left panel: the solid line (black) indicates planet b, the dashed line (red) denotes planet c and the dotted line (blue) represents planet d. e_c moves in the interval 0.14-0.31 while e_d in the range 0.11-0.31. Top-right panel: the librating secular angle $\omega_c - \omega_d$. Second and third rows: evolution of some critical angles of the 12:5 MMR which present both ciculation and libration.

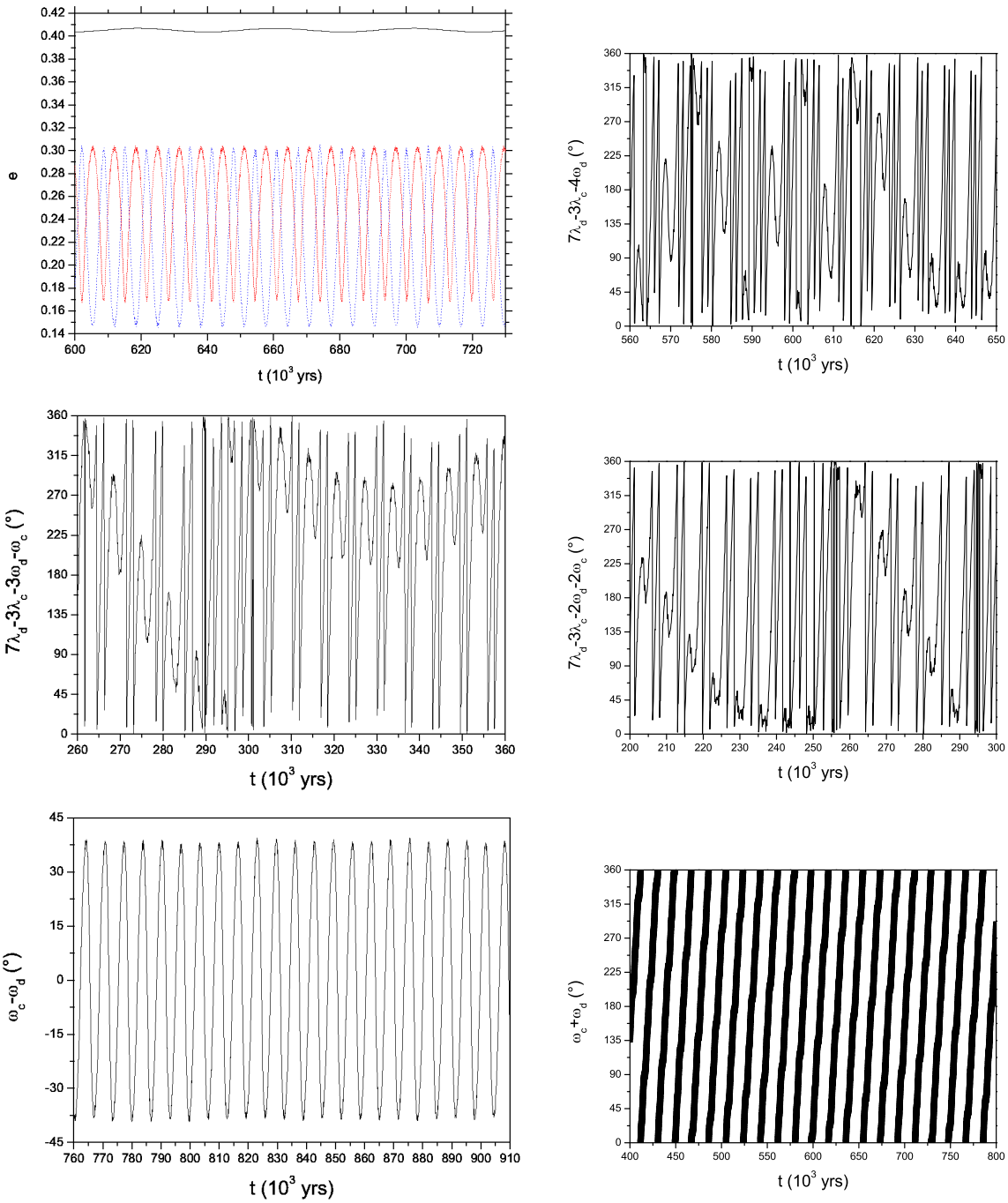

Figure 5.13: Evolution of some orbital elements for the model nMMR 7:3. Top-left panel: the solid line (black) indicates planet b, the dashed line (red) denotes planet c and the dotted line (blue) represents planet d. e_c moves in the interval 0.17-0.30 while e_d in the range 0.15-0.30. Top-right and second row: evolution with time of three critical angles of the 7:3 MMR showing both ciculation and libration. Bottom-left: this model is observed to be in SAR as $\omega_c - \omega_d$ librates. Bottom-right: the circulating SAR critical angle $\omega_c + \omega_d$.

For these arguments I find that librations alternate with circulations with some regions of the phase-space just avoided. This is indication of a chaotic zone spanned by overlapping resonances. The time evolution of the critical angles are also illustrated in Figure 5.14.

The scenario nMMR 7:2, illustrated in Figure 5.15, has $\chi^2_{red} = 5.65$ and rms scatter of 1.45 m/s with $7n_d - 2n_c \approx -1.7^\circ/yr$. This model is not seen to be in SAR. I have studied the six resonant arguments of this fifth-order MMR:

- $7\lambda_d - 2\lambda_c - 5\omega_c$,
- $7\lambda_d - 2\lambda_c - 5\omega_d$,
- $7\lambda_d - 2\lambda_c - 4\omega_c - \omega_d$,
- $7\lambda_d - 2\lambda_c - \omega_c - 4\omega_d$,
- $7\lambda_d - 2\lambda_c - 3\omega_c - 2\omega_d$,
- $7\lambda_d - 2\lambda_c - 2\omega_c - 3\omega_d$.

This configuration is found to be locked in the MMR as the critical argument $7\lambda_d - 2\lambda_c - 5\omega_d$ librates around 180° with a semi-amplitude of about 85°. It is worth noting how this mechanism is capable of pumping e_c from 0.09 to 0.47 in less than 5000 years. This model is located over the collision line; it is the resonance that prevents close encounters and provides long-term orbital stability to the system. The angle $7\lambda_d - 2\lambda_c - \omega_c - 4\omega_d$ is very close to the previous in the phase space and in fact it is seen to experience the nodding phenomenon (Section 2.5.2).

Considering all the the configurations studied, the behaviour of planet b is seen to be unrelated to the two giant companions as, for instance, the amplitude of the eccentricity signal of b appears to be unaffected even in the cases in which c and d are trapped in a resonance. Moreover, it seems unrealistic that planet b can be involved in a p:q:r MMR with the outer two planets: b is too far away from them and, in addition, it is mainly influenced by general relativistic and tidal effects (these mechanisms are discussed in Chapter 6).

The synthetic RV curves for the Keplerian best-fit, stable best-fit and the models nMMRs 12:5, 7:3 and 7:2 are illustrated in Figure 5.16. The period through the year 2017 is covered. It is difficult to distinguish the curves from each other in the time range covered by the observations, but at the time of writing the difference can be spotted. The signal of the Keplerian best fit diverges evidently from the stable best fit only in 2013 February ($\sim$ JD 2,456,340), however no new data have been published by the HARPS team so far.

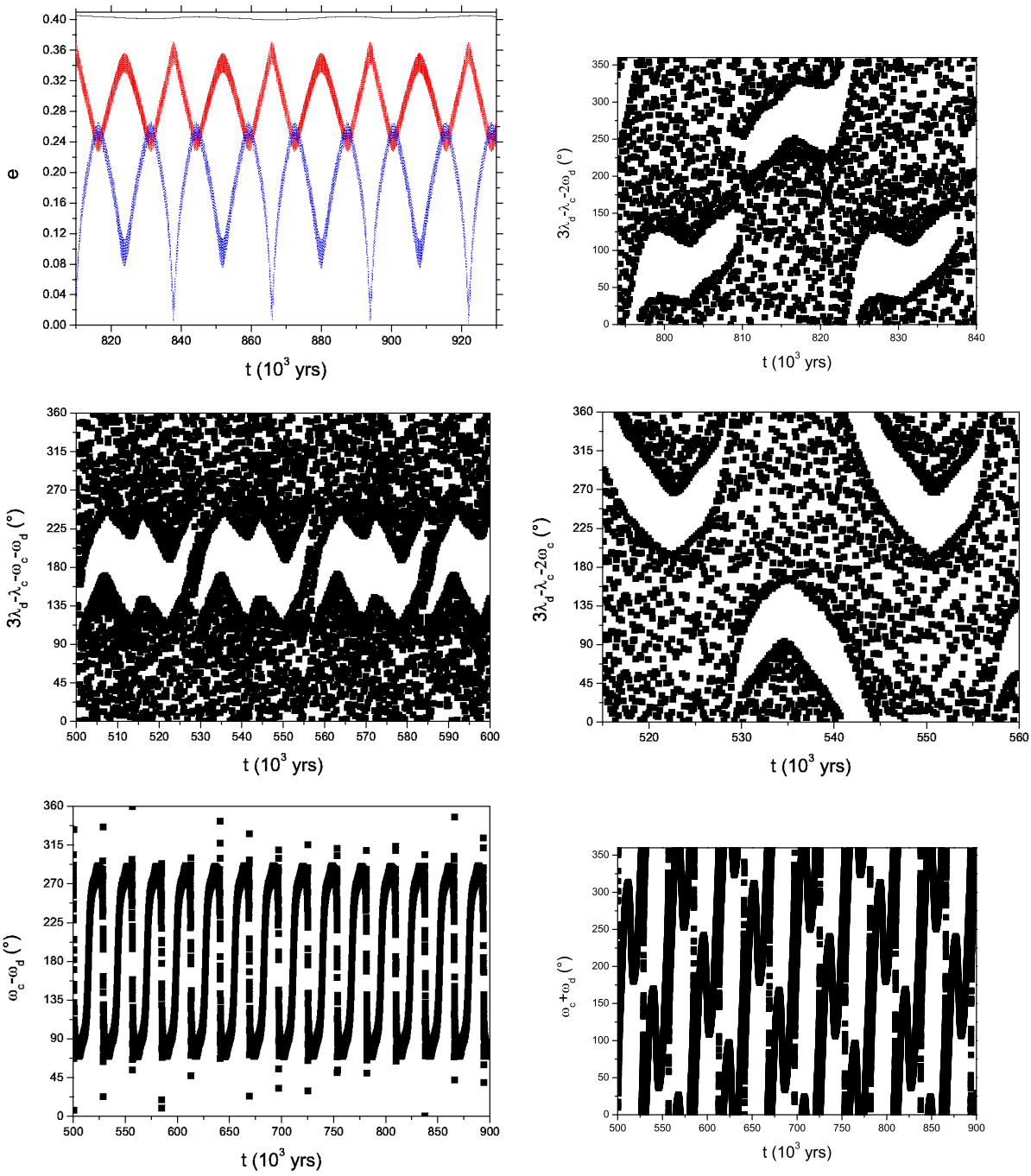

Figure 5.14: Evolution of some orbital elements for the model nMMR 3:1. Top-left panel: the solid line (black) indicates planet *b*, the dashed line (red) denotes planet *c* and the dotted line (blue) represents planet *d*. e_c moves in the interval 0.23-0.37 while e_d in the range 0.0-0.27. Top-right and second row: evolution with time of the three critical angles of the 3:1 MMR displaying both ciculation and libration. Bottom-left: this model is observed to be in SAR as $\omega_c - \omega_d$ librates. Bottom-right: the circulating SAR critical angle $\omega_c + \omega_d$.

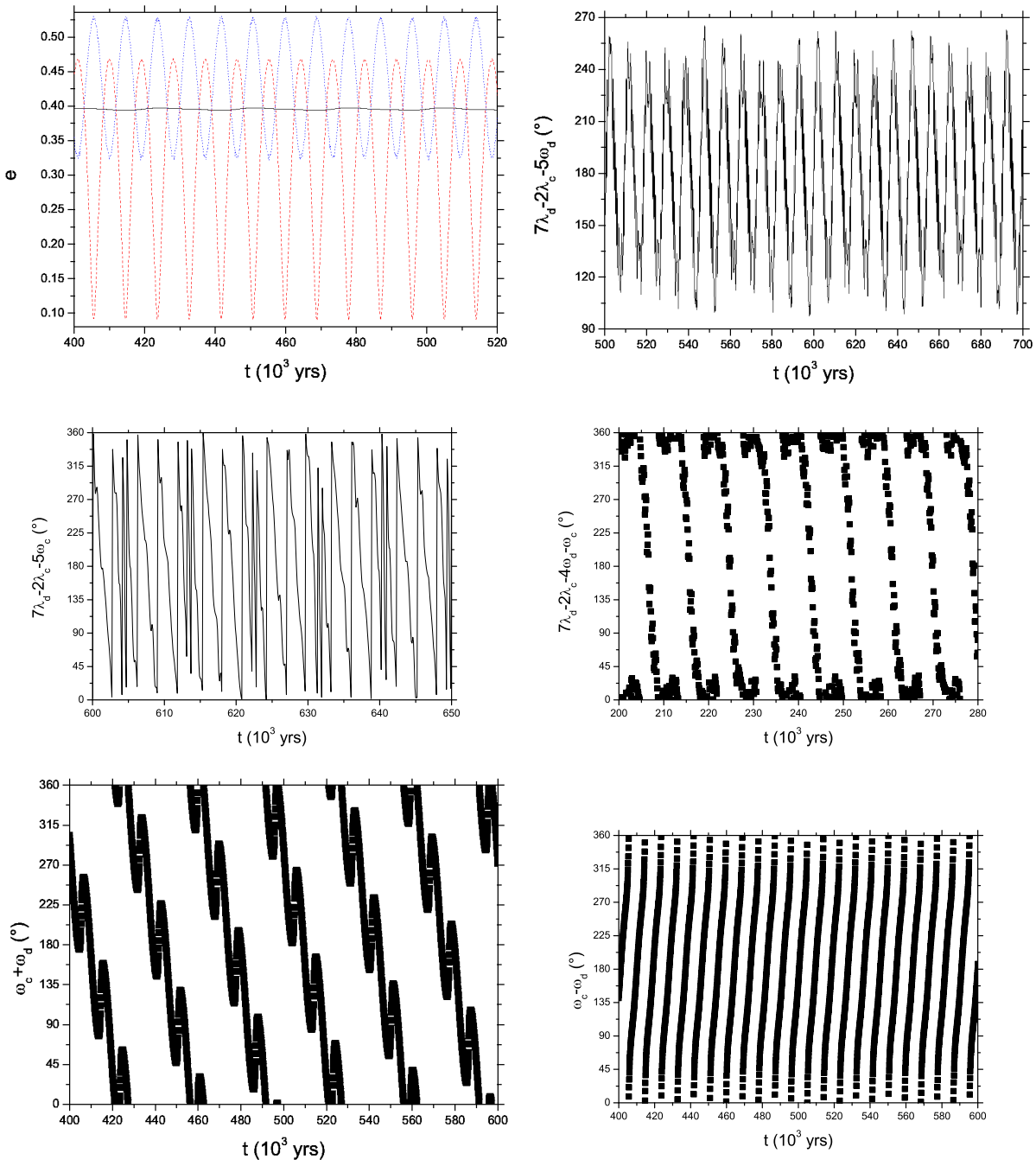

Figure 5.15: Evolution of some orbital elements for the model nMMR 7:2. Top-left panel: the solid line (black) indicates planet b, the dashed line (red) denotes planet c and the dotted line (blue) represents planet d. e_c moves in the interval 0.09-0.47 while e_d in the range 0.32-0.53. Top-right: the resonant argument $7\lambda_d - 2\lambda_c - 5\omega_d$ librates around 180° with a semi-amplitude of about 85°. Second row: critical arguments $7\lambda_d - 2\lambda_c - 5\omega_c$ and $7\lambda_d - 2\lambda_c - \omega_c - 4\omega_d$. The former circulates, while the latter alternates circulations with librations around 0° and a semi-amplitude of about 30°

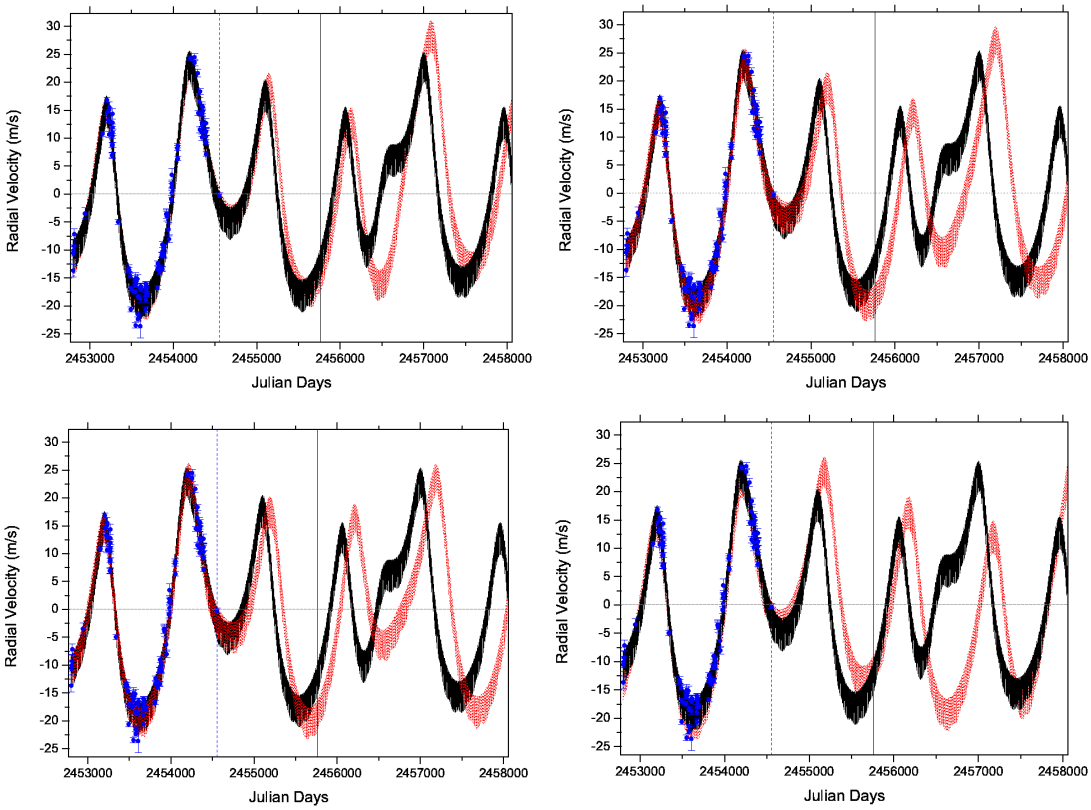

Figure 5.16: Synthetic RV curves for HD 181433. In every panel, the straight line (black) indicates the Keplerian best fit while the dotted line (red) represents (clockwise starting from the top-left panel) the stable best fit, the configuration studied near the MMR 12:5, the model nMMR 7:2 and the scenario nMMR 7:3. Data points (blue) are plotted with error bars (and V_{offset} is the one calculated for the stable best-fit). The dashed (blue) vertical line indicates when the last data point was taken. The straight (black) vertical line at JD 2,455,760 corresponds to the calendar date 2011 July 17 when the difference between most of the curves can be identified.

5.4 Discussion and Conclusion

In this chapter, my efforts have been focused on finding a plausible solution to the available RV data for the planetary system of HD 181433. In my investigation, I have included an analysis of the long-term evolution of the system, and the results support the thesis that the dynamics is an important observable that has to be taken into account with the same priority as the RV observations.

The story with HD 181433 does not differ from the one of many other multi-planet systems found on the edge of long-term dynamical stability. The dynamical modelling of the RV with stability constraints offers precious information on the dynamical architecture of the putative planetary configurations. The stability criterion becomes a fundamental tool which provides limits to the physical and orbital elements of the planets when data do not cover completely the longest orbital period.

My investigation leads to a Newtonian model for HD 181433 stable for at least 250 Myrs. The solution is compatible with what was found by Bouchy et al. [2009], but my analysis strongly diminish the uncertainty on the location of planet d to the exiguous band where the 5:2 MMR is possible and stability is preserved. This seems the only plausible way to explain a very large eccentricity for the outermost planet, a quality which must be met in order to hold a good fit to the present data. In general, it is possible to say that when an unstable high eccentric solution is found for a multiplanet system, the study of resonances may lead to the finding of a reasonable stable solution. By doing so, it is possible to constrain with high confidence the orbital period of the outermost (poorly sampled) planet well before sufficient data, covering several orbital periods, become available.

Apart from the 5:2 MMR, the orbital evolution of the two giant companions is confined to a zone spanned by a number of other low-order two-body MMRs. I have studied different plausible stable configurations for the planetary system and, in particular, I have illustrated the behaviours caused by secular apsidal resonances and mean motion resonances. I have also found that at the time of writing with new data points it is definitely feasible to refine with precision the circle of likely scenarios.

Furthermore, given the strong gravitational interactions between the two giant planets, a self-consistent N-body model for the RV data will help in estimating the inclination of the planetary orbits and of the physical masses (the RV method returns just the minimum masses for the planets, as described in Section 2.2). If it is not possible to use in synergy other methods e.g. astrometry, transits, it may be necessary to observe around 50 full orbits of planet d i.e. 300 years of RV data, to strongly constrain the orbital inclinations. As the large values already observed for the eccentricities may have been trigged by mechanisms which influence also the orbital inclinations [e.g. Libert and Tsiganis, 2009], a considerable value for their mutual inclination cannot be excluded.

It is possible to calculate the orbital distance a_{hab} defined as the distance where a planet would receive the same insolation as the Earth:

$$a_{hab} = \sqrt{\frac{L_*}{L_\odot}} AU. \tag{5.4.1}$$

For HD 181433, it is found $a_{hab} = 0.55$ AU ($P_{hab} \sim 170$ d) which is in the region between planets b and c. Simulations, run for 40 Myr, shows that an Earth-size planet in the HZ (and in eccentric orbit) cannot retain stability. A further theoretical discussion on the existence of a planet between b and c, which would fill the empty gap in the system, is found in Chapter 6. Here it is worth to underline how additional observations are required to investigate on the presence of further terrestrial bodies in the aforementioned zone of HD 181433, as for now the signal would be at the noise level.

The planetary system of HD 181433 offers a wide range of challenges that include the understanding of its real physical architecture, argument that will be discussed in Chapter 6. Further observations can confirm the results illustrated in this Chapter, improve our understanding of the dynamical structure of this system and, in general, give additional insights into the study of the dynamics of planetary systems.

CHAPTER 6

Possible Scenarios for Eccentricity Evolution in the Extrasolar System HD 181433

6.1 Introduction

As anticipated in Chapter 5, the three-planet extrasolar system HD 181433 has an architecture that makes it an interesting test-bed for exploring dynamical processes during and after planetary system formation. Bouchy et al. [2009], as outlined in Table 5.1, report that the system consists of two outer gas giant planets ('*c*' and '*d*') on eccentric orbits with periods 962 ± 15 and 2172 ± 158 days, and an inner super-Earth on a 9.3743 ± 0.0019 day orbit with eccentricity $e_b = 0.396 \pm 0.062$. Dynamical analysis of this system, described in Chapter 5, indicates that the parameters reported by Bouchy et al. [2009] lead to global instability on very short time-scales. Long-term stability requires the two outer planets to be in 5:2 mean motion resonance. Parameters that lead to a minimum χ^2_{red} value of 4.96 for the orbital fits to the data were given in Table 5.2, and these are the parameters of the system that we adopt in this chapter. It is noteworthy that planet *b* is dynamically isolated from the outer planets such that gravitational interaction over secular time-scales is unable to excite the observed eccentricity of this body.

The best-fitting parameters presented in Chapter 5 and reported in brief here in Table 6.1 lead to the 5:2 resonant angles librating with large amplitude. Disc driven migration scenarios for resonant capture of giant planets normally result in capture in low-order resonances with relatively small libration amplitudes [Nelson and Papaloizou, 2002]. Planet-planet scattering, as introduced in Section 3.5, may also result in resonant capture into higher order resonances with large libration amplitudes [Raymond et al., 2008], and this would appear to be a more probable explanation for the currently inferred orbital parameters for the two outer planets *c* and *d*.

Table 6.1: Orbital and physical parameters of HD 181433 planets.

Parameter	HD 181433 b	HD 181433 c	HD 181433 d
P (days)	9.37	975	2468
T_{peri} (BJD-2450000)	2788.92	2255.6	1844
e	0.39	0.27	0.47
ϖ (°)	202.04	22	319
$m \sin i$ ($M_{\rm Jup}$)	0.023	0.65	0.53
$m \sin i$ ($M_{\oplus}$)	7.4	208	167
a (AU)	0.080	1.77	3.29

In this chapter, based upon the paper Campanella et al. [2013], I present a case study of the evolution of the planetary system around HD 181433, and explore plausible scenarios of how the observed large eccentricities may have been generated after depletion of the protoplanetary disc. In particular we have focused on scenarios that can lead to the current observed orbital configuration of planet *b*. In Section 6.2, I discuss the properties of the HD 181433 system, and study the locations of secular resonances and regions of stability. In Section 6.3, I consider how tides may have influenced the evolution of the semi-major axis and eccentricity of planet *b* over the lifetime of the system. In Section 6.4, I explore the planet-planet scattering mechanism as a means of generating large eccentricities. We have simulated the evolution in the presence of an additional giant planet whose role is to destabilize the system. The probability for planets *c* and *d* to be captured into the 5:2 MMR after scattering is estimated, and thus the joint probability for both resonant capture into 5:2 and excitation of the eccentricity of planet *b* is considered. In Section 6.5, I examine an alternative scenario in which sweeping of secular resonances induced by stellar spin-down force the eccentricity of HD 181433*b*. We have studied a range of initial stellar rotation periods and spin-down rates, and examined the effect of including additional terrestrial planets – whose presence we found to be necessary for the model to be successful. In Section 6.6 I briefly discuss and summarize our findings.

6.2 Properties of the HD 181433 System

As quoted in Section 5.2, the mass of the host star is reported to be $M_* = (0.781 \pm 0.10) M_\odot$ [Sousa et al., 2008]. Moreover, its inferred radius is $R_* = (1.01 \pm 0.07) R_\odot$ [Torres et al., 2010], it is a slow rotating star with a rotation period of $P_{rot} = 54$ days (uncertainty is not reported in Bouchy et al. [2009]), while an age of (6.7 ± 1.8) Gyr has been reported [Trevisan et al., 2011]. HD 181433 has a spectral type K3IV and, being a subgiant, it has definitely evolved off the main sequence. The orbital elements of the HD 181433 planets adopted here are shown in Table 6.1. These values are quoted from the best-fitting orbital solution that is dynamically stable which I published in

Campanella [2011].

The orbital period of HD 181433*b* is 9.4 days with an eccentricity of 0.39. The longitude of HD 181433*b*'s periastron advances mostly due to the relativistic correction of the Newtonian potential. Being a close-in planet in eccentric orbit, HD 181433*b* is undergoing tidal circularization. Given the age of the system and the measured $m \sin i$ value, this suggests that planet b has a tidal Q factor substantially larger than inferred for terrestrial planets in the Solar system, for which $Q \sim 100$ [e.g. Murray and Dermott, 1999]. This point is discussed further in Section 6.3.

The orbital parameter values quoted in Table 6.1 are specific to a particular moment in time. In fact, resonant and secular interactions cause e_c and e_d to reach values as large as 0.52 and 0.50, respectively (see Section 5.3). In this Chapter, when discussing the eccentricities acquired by planets during dynamical evolution, I will report the maximum values acquired during numerical computations once final stable systems have been established.

6.2.1 Formation and evolution scenarios

Before embarking on a detailed examination of the HD 181433 system, it is useful to present a qualitative description of the possible formation and evolution history. We have envisaged that the planets formed within a protoplanetary disc exterior to the snow-line. Planet b appears to have characteristics of a Neptune-like planet based on analysis of its tidal evolution (see Section 6.3). It seems likely that this body formed largely from material beyond the snow-line and migrated in by type I migration, arriving at its observed location on a near-circular orbit. It is possible that it accreted during migration, possibly through giant impacts with other large bodies. If these occurred after migration was essentially complete then the body would be close to the star and the impactors would need to be at least as massive as the inferred minimum mass of b to generate significant eccentricity through scattering during the giant impacts phase. Interactions and giant impacts with bodies in the Earth-mass regime at semi-major axes ~ 0.1 AU would lead to $e_b < 0.1$ (see Section 6.4.1). Therefore, it is anticipated that planet b was formed with a small free eccentricity.

The outer giant planets c and d should have formed somewhat later than planet b, but were able to grow larger cores that enabled rapid gas accretion and formation of gas giant planets. Although disc driven migration may have brought the planets into close proximity, it is unlikely that it was responsible for establishing the 5:2 resonance. Disc-driven resonant locking tends to cause the resonant angles to librate with small amplitudes because the planets are pushed deep into the resonance, but planets c and d appear to be weakly embedded in the resonance [Campanella, 2011]. Furthermore, Nelson and Papaloizou [2002] undertook a study of disc-driven resonant capture and only obtained a 5:2 resonance when one of the two planets already had a high eccentric-

ity equal to 0.3. A more plausible explanation for the resonance is capture as a result of planet-planet scattering, possibly involving an additional planet that was ejected during the dynamical instability [Raymond et al., 2008]. Given the stabilization provided by the eccentricity damping influence of the gas disc, this instability most likely occurred during the final stages of the disc lifetime or after it was dispersed altogether.

The rest of this Chapter largely concerns the question of how planet b's eccentricity was excited, and when addressing this I present the following possibilities: scattering by a giant planet during the previously mentioned dynamical instability that created the 5:2 resonance; placing planet b in a secular resonance by invoking the presence of an additional undetected planet in the system; passing planet b through a secular resonance through the process of stellar spin-down from an initially rapidly rotating state.

6.2.2 Secular Evolution

I have presented the mathematical details of the secular theory in Section 3.2 and in Section 3.3 I have applied the secular theory to some extrasolar planetary systems. Here I introduce the secular model for the three planets of HD 18433, assuming that all planets are coplanar. Precession due to GR is also included (Section 3.2.3), but this model does not take account of the 5:2 MMR occupied by the two outer planets. Although techniques have been developed to include first-order MMRs in secular treatments of planetary system evolution [Malhotra et al., 1989, Agnor and Lin, 2012a], this becomes significantly more involved technically for higher order MMRs because of the requirement to include terms that are higher order in the eccentricities. The purpose here is to use the secular theory as a rough guide to the dynamics of the system, and not to accurately predict its long term evolution, so this omission is not crucial here. This point is illustrated later in the Chapter where it is demonstrated, by means of direct numerical simulations, that the eccentricity evolution of the two outer planets maintains highly regular and periodic behaviour, reminiscent of secular evolution (see Figure 6.3 for example). It appears that the effect of the 5:2 MMR is rather weak, with the main influence being a simple increase in the precession frequencies above the values predicted by the secular theory. The secular model, therefore, allows us to identify the existence and approximate locations of secular resonances, in addition to estimating the magnitudes of forced eccentricities experienced by additional low mass planets that may be present in the system today, or which were present in the past. All detailed analyses of the HD 181433 system dynamics undertaken in this Chapter use direct numerical simulations for accurate modelling of the mutual interactions, and all firm conclusions drawn about the past and future evolution are based on those simulations.

The secular model examined is based on the osculating orbital elements listed in Ta-

		Mode Index i		
Planet	j	1	2	3
HD 181433 b	1	–100000	–11	–10
HD 181433 c	2	121	–74725	66454
HD 181433 d	3	–2056	69792	71588

Table 6.2: The components ($\bar{e}_{ji}$) of the orthonormal eigenvectors for the e–ϖ solution computed for the secular model of the three-planet HD 181433′s system. All quantities have been multiplied by a factor of 10^5.

ble 6.1. The eigenfrequencies retrieved for the system are:

$$g_2 = 0.0304015\frac{^\circ}{yr}, g_3 = 0.00651853\frac{^\circ}{yr}, g_1 = 0.00492506\frac{^\circ}{yr}. \quad (6.2.1)$$

The system′s orthonormal eigenvectors with elements $\bar{e}_{ji}$ are shown in Table 6.2. The first eigenvector is dominated by planet b confirming how this planet is not coupled during its evolution with the outers. On the other hand, the second and third eigenvectors are influenced almost equally by planets c and d confirming their coupling.

The top panel of Figure 6.1 shows the variation of the free precession frequency A experienced by a test particle located between 0 and 9 AU. On the same diagram the three eccentricity-pericentre eigenfrequencies of the system are denoted by solid horizontal lines. Note that in the absence of relativistic precession $g_1 = 0.0009^\circ \mathrm{yr}^{-1}$, with the other eigenfrequencies that are largely determined by the outer planets being essentially unaffected. The intersections of the lines with the curve show where the eigenfrequencies g_i equal A, and identify the semi-major axes where large forced eccentricities can be expected. In the bottom-left panel of Figure 6.1, the values of the maximum forced eccentricity (see Section 3.2.3) are shown as a function of the semi-major axis. The singularities close to 0.18, 0.7, 4.7 and 6.3 AU represent locations where the value of A is equal to one of the g_i eigenfrequencies of the secular system, as anticipated above. This plot indicates that the system is more-or-less dynamically packed out to distances of ~ 7 AU, in the sense that additional planets located in the system will experience large forced eccentricities that may be destabilizing. Even in the region between 0.2 and 0.6 AU (focus of the bottom-right panel of Figure 6.1), where a clear minimum exists in the forced eccentricity, a value of $e_{\mathrm{forced-max}} \geq 0.2$ is predicted. It is noteworthy that the habitable zone for this K3IV star is centred at ~ 0.55 AU (Section 5.4).

6.2.3 Full integration of the system

I utilise the symplectic N-body code *Mercury-6* presented in Section 3.6, augmented to include the effects of GR (Section 3.6.1), to perform a direct integration of the system using initial conditions from Table 6.1. Unless stated otherwise, all simulations presented in this chapter adopt the hybrid integrator option which utilises the second-

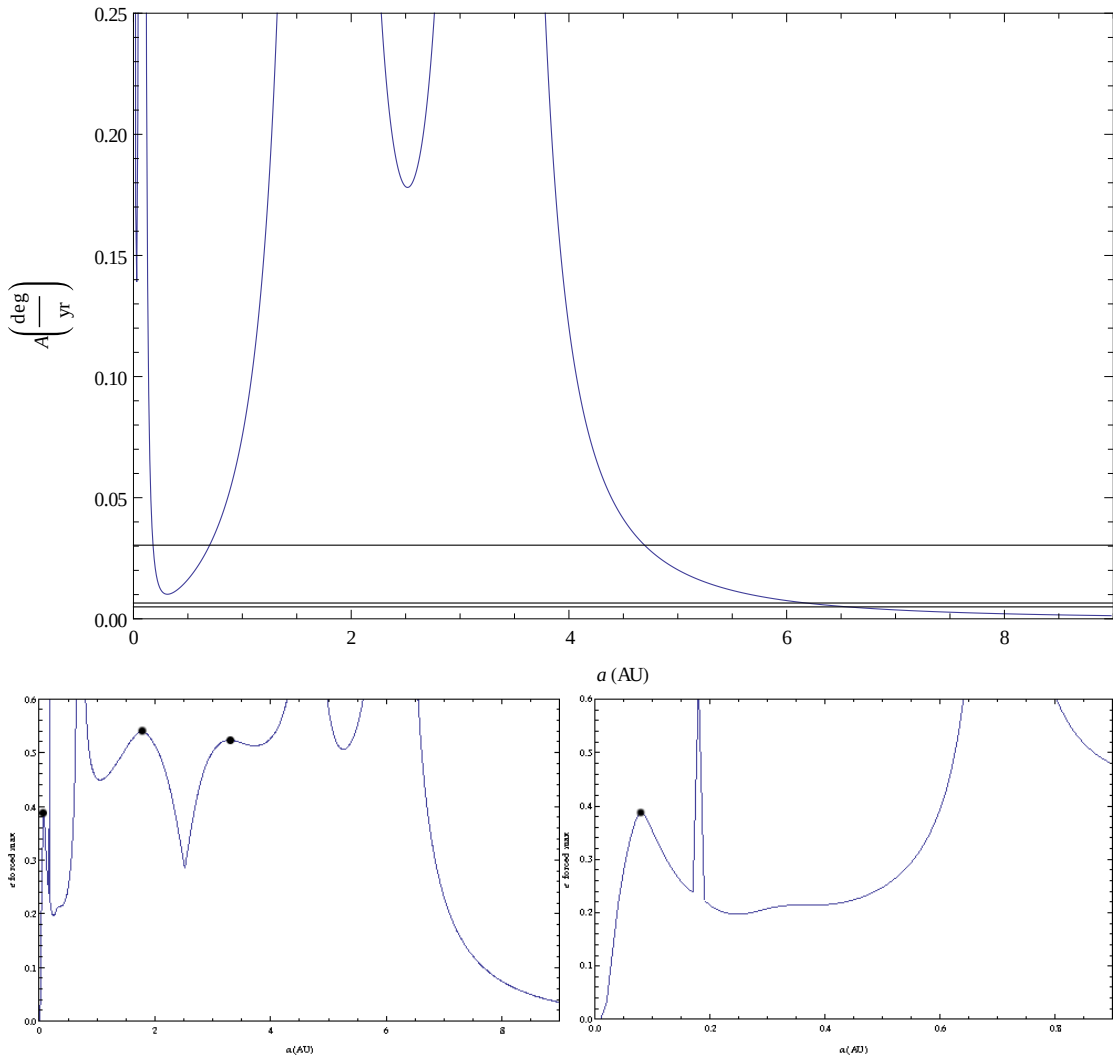

Figure 6.1: Secular model for the planetary system HD 181433. Top: Precession frequency A of a test particle as a function of semi-major axis, derived from perturbations by the planets and considering GR. The horizontal solid lines denote the values of the three eccentricity-pericentre eigenfrequencies. Singularities in the plot correspond to the orbital semi-major axis of the three planets. Bottom-Left: The variation in the maximum forced eccentricity as a function of semi-major axis. The dots indicate the eccentricity for the planets at their semi-major axes. The four singularities indicate regions of secular resonance where A is equal to one of the g_i. Bottom-Right: The maximum forced eccentricity within 0.9 AU.

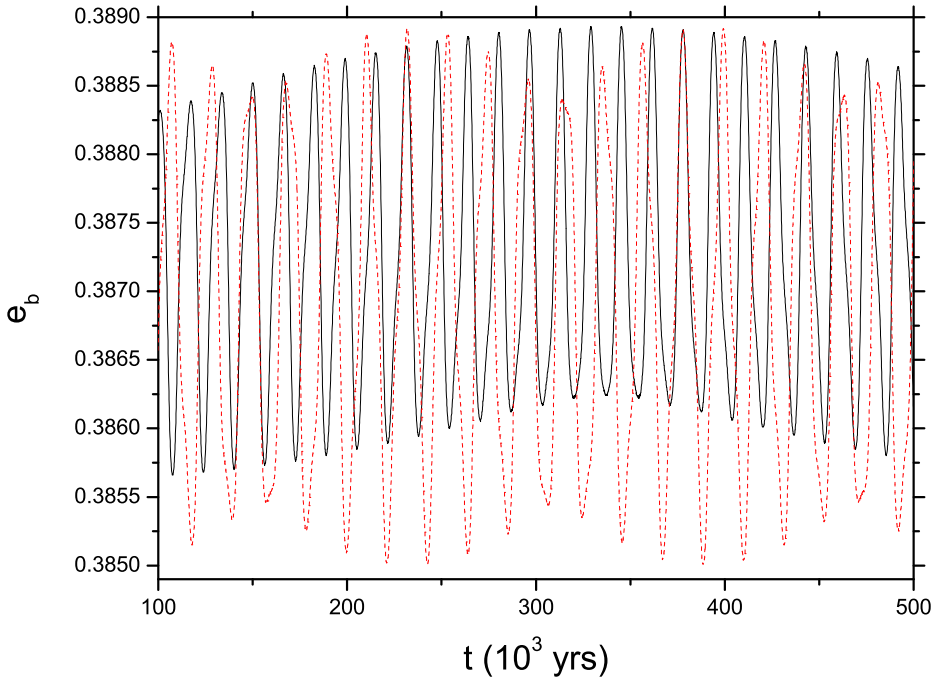

Figure 6.2: Time evolution of the eccentricity of HD 181433 *b*. Solid black line not considering GR, dashed red line including GR.

order mixed-variable symplectic algorithm for systems that are not strongly interacting, but switches to the Bulirsch-Stoer integrator when the minimum separation between objects $\leq$ 4 Hill radii. A time step of 1/20 of the orbital period of the innermost planets is adopted for the MVS integrator, and the Bulirsch-Stoer integrator is employed with an accuracy parameter of 10^{-11}.

GR effects are relevant for planet *b* only, Figure 6.2 displays two integrations of the system: one including the relativistic correction and one without it. Underlined is how the relativistic correction for planet *b* does not produce a major difference with respect to the amplitude of e_b, even if in the previous Section it was noticed how GR is important with regard to the precession period. This differs from the *υAndromedæ* system, where the forced eccentricity of the inner planet depends sensitively on whether or not the post-Newtonian force is accounted for in secular evolution because of the proximity of a secular resonance (see Section 3.6.1 and Figure 3.16).

Table 6.3 presents the precession periods of the pericentres of the three planets of HD 181433 obtained from the numerics and secular calculations. In the full numerical integrations the precession periods for *c* and *d* are not constant, as indicated by the range of values quoted in Table 6.3, and moreover it is found to be considerably shorter for *d* because of the 5:2 MMR. While the loose residence of planets *c* and *d* in the 5:2 mean motion resonances introduces some short-term oscillations, the eccentric-

Table 6.3: Precession periods of the pericentres of HD 181433 planets from secular calculations and numerical integrations.

Period (y)	HD 181433 b	HD 181433 c	HD 181433 d
Secular	73096	11842	55227
Numerics	61000	8000-16000	7700-16000

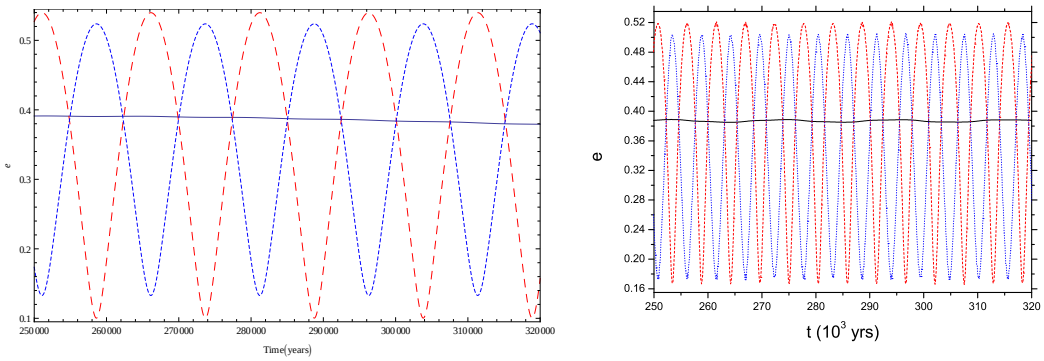

Figure 6.3: Eccentricity evolution of three planets around HD 181433 including the post-Newtonian effect. The solid, dashed and dotted lines show the evolution of planet b, c and d, respectively. Left: Secular model. Right: Numerical simulation.

ity evolution of the system over longer periods appears regular and well-described by a simple three frequency secular model. Fourier analysis of the system's apsidal behaviour indicates that the main effect of the 5:2 resonance is to simply modify the values of the principal precession frequencies that describe the giant planets (i.e., $g_2 = 0.0304^\circ$ /yr $\rightarrow 0.02305^\circ$ /yr and $g_3 = 0.00652^\circ$ /yr $\rightarrow -0.04354^\circ$ /yr making it inaccessible for resonant interaction with g_1). Figure 6.3 shows the evolution of the orbital eccentricities of the HD 181433 planets retrieved from the Laplace-Lagrange secular model (left-hand panel) and the numerical integration (right-hand panel). This time GR effects are considered as opposed to the corresponding plot in Figure 5.11. The amplitudes of the eccentricity variation are very similar, while the periodicity of the eccentricity of c and d is approximately reduced by two-thirds to $\sim$ 5000 years as a result of the 5:2 MMR. This illustrates the accuracy with which the secular model estimates the locations of the secular apsidal resonance, in addition to the strong regularity displayed by the full integration even though the outer two planets are in the 5:2 MMR. It is clear that the effects of the 5:2 MMR in this system are rather weak and make only a modest change to the secular behaviour, namely through shifting the precession frequencies of the outermost planet d.

6.2.4 Stability of an additional low mass planet

In Section 5.2.3, I have investigated whether the RV data were showing signals of a terrestrial planet located between planets b and c and concluded that additional ob-

servations were required. Besides, it is important to examine the consequences for an additional low mass planet in the system arising from the large forced eccentricities predicted in Figure 6.1. I have performed N-body simulations that include an additional planet, placing an Earth-mass object (which would be undetectable in current radial velocity surveys) at different distances between planets b and c to check for the stability of that region. The sampling used was of 0.05 AU for semi-major axes in the range $0.15 - 0.6$ AU and 0.1 AU for semi-major axes in the range $0.7 - 1.7$ AU.

It is found that in full N-body simulations, the secular resonance at 0.18 AU moves inward leaving the region between 0.1 and 0.35 AU stable for a single body, but unstable outside of this region. In particular, for semi-major axes $a > 0.26$ AU the forced eccentricity attains values $e_{\rm forced} \gtrsim 0.2$. Later in the chapter I consider the influence of additional low mass planets, and it is found that inserting two or three extra planets with at least one of them between 0.26 and 0.35 AU makes the system unstable (see Section 6.5.2).

6.3 Tides

The close proximity of planet b to its host star suggests that it should be undergoing tidal evolution. Here I report the main aspects of the tidal theory necessary to evaluate the problem in the context of system HD 181433. The complete standard argumentation describing all the mathematical details can be found in [Murray and Dermott, 1999].

A *tide* is manifested on one body by another as response to the variation of the gravitational force across the body. In fact, the tide experienced by a planet orbiting close to its parent star is due to the fact that the force acting on the side of the planet facing the star is stronger than that acting on the far side of the planet. Tides are a dissipative phenomenon and friction can lead to an orbital evolution of the planet. This can be especially important when the planet's orbit is eccentric. Just as the star raises a tide on the planet, so the planet also raises a tide on the star. Tides raised on a star transfer angular momentum between the star's rotation and the planet's orbit.

Consider the tide raised on a star by a planet moving in a circular, equatorial orbit with mean motion n about a star rotating with angular speed Ω. If $\Omega \neq n$, then the planet experiences tidal oscillations. Tidal oscillations always generate friction and this results in energy loss (dissipated as heat) and a phase shift in the tidal response of the planet. This phase shift can be related to the *specific dissipation function* Q, which is defined by

$$Q = \frac{2\pi E_0}{\Delta E}, \tag{6.3.1}$$

where ΔE is the energy dissipated over one cycle and E_0 is the peak energy stored during the cycle. When the planet is inside the synchronous orbit ($\Omega < n$), the the

semi-major axis of the planet decreases while the rate of rotation of the star increases.

If the orbit of a planet is eccentric, the tidal dissipation in the interior of the planet due to the tide raised on it by the star, apart from heating the planet, can act to circularise its orbit. The eccentricity damping timescale can be estimated from the rate of dissipation of the total energy given by $E = -GM_* m_p/2a$ and, accordingly, it is estimated to be [Goldreich and Soter, 1966]

$$\tau_e = \frac{4}{63} Q \left(\frac{a^3}{GM_*} \right)^{1/2} \frac{m_p}{M_*} \left(\frac{a}{R_p} \right)^5 . \tag{6.3.2}$$

Tidal evolution for extrasolar planets has been studied, for example, to explain the large radii of some transiting giant planets e.g. HD 209458b, WASP-12b, TrES-4, WASP-6b [Ibgui and Burrows, 2009], HAT-P-7, HAT-P-9, WASP-10b XO-4 [Miller et al., 2009], to study the origin of the rocky body CoRoT-7 b [Jackson et al., 2010] and, as anticipated in 1.3.2, to explain the general origin of the eccentricities of close-in planets [Jackson et al., 2008]. In particular, Jackson et al. [2008] have studied for which Q values the distribution of initial e values of planets within 0.2 AU matches that of general population (Figure 6.4).

6.3.1 The tidal evolution for HD 181433 b

The value of Q calculated for rocky objects in the Solar system is of the order of 10^2 [Murray and Dermott, 1999]. Such a value would imply a circularization time-scale of the order of 10^7 years for planet b, much shorter than any reasonable estimate for the age of the system. If we reject the hypothesis that a recent event has generated the observed eccentricity, then the tidal factor Q must be considerably greater than expected for a terrestrial body of mass $\lesssim 10$ $M_\oplus$. If we assume a Q value and density typical of an ice giant such as Neptune ($Q = 10^4$, $\rho_b = \rho_{Nep} = 1.638$ g cm^{-3}), then the circularization time-scale becomes $\tau_e = 8.2$ Gyr, comfortably longer than the estimated system age. This would make HD 181433b a member of the class of low-mass, low-density, close-in planets exemplified by Kepler 11c and Kepler 11e [Lissauer et al., 2011a, 2013]. To uncover the history of planet b and make an estimate for the orbital parameters that existed prior to significant tidal evolution, it is necessary to examine the influence of tides on past orbital evolution and estimate their influence of future evolution.

To study the orbital evolution of planet b, I have integrated the coupled tidal evolution equations for changes in a and e (e.g. Miller et al. [2009]) backward and forward in

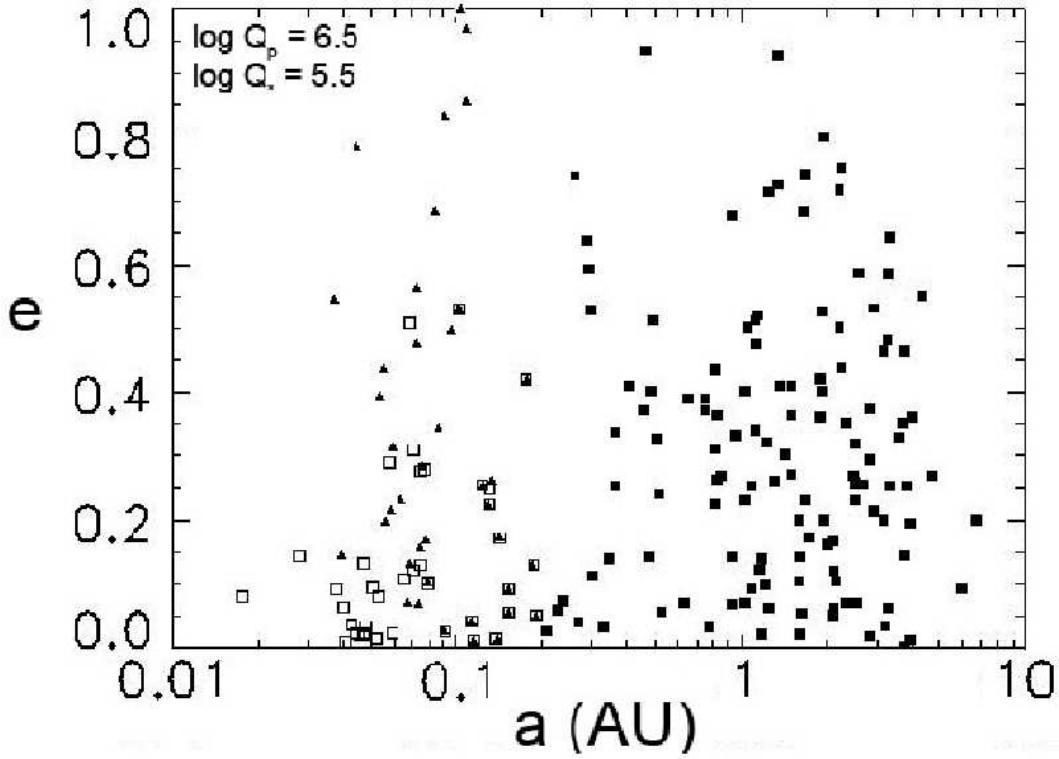

Figure 6.4: Distribution of orbital elements for a population of extrasolar planets. Squares (filled and open) represent the currently observed orbital elements, with the open squares (with $a < 0.2$ AU) being candidates for significant tidal evolution. Triangles represent the initial orbital elements ($e_{initial}$ and $a_{initial}$) determined by integrating the equations of tidal evolution (with $Q_{\rm p} = 10^{6.5}$ and $Q_* = 10^{5.5}$) backward in time to the formation of the planet [Jackson et al., 2008].

time:

$$\frac{1}{a}\frac{da}{dt} = -\left[\frac{63\sqrt{GM_*^3}R_p^5}{2Q_\mathrm{p}m_p}e^2 + \frac{9\sqrt{G/M_*}R_*^5 m_p}{2Q_*}\left(1+\frac{57}{4}e^2\right)\right]a^{-13/2} \quad (6.3.3)$$

$$\frac{1}{e}\frac{de}{dt} = -\left[\frac{63\sqrt{GM_*^3}R_\mathrm{p}^5}{4Q_\mathrm{p}m_p} + \frac{225\sqrt{G/M_*}R_*^5 m_p}{16Q_*}\right]a^{-13/2}. \quad (6.3.4)$$

The effects of the tide raised on the star Q_* as well as on the planet Q_p are both included. The stellar Q value is typically estimated through the observed circularization of binary stars orbits. The rate of tidal effects may be a very strong function of orbital frequency [Ogilvie and Lin, 2004]. If this is the case, the planet may spend a lot of time at certain states where tidal effects are slow and rapidly pass through states where tidal effects are faster. This model assumes that the star is rotating slowly relative to the orbit of the planet (a condition met in this case and more in general when the star has already evolved towards the main sequence) and is second order in eccentricity. It describes tidal evolution associated with orbit circularization, as this operates most rapidly and ignores other sources of tidal interaction which operate on longer time-scales. The intention here is to use this simple tidal theory to develop an approximate picture for the likely orbital history for HD 181433*b*, and its possible future evolution.

I have computed the orbital evolution for various pairs of values of Q_p (ranging between 10^3 and $10^{6.5}$) and Q_* (between 10^4 and 10^7). The chosen Q values span the range that are plausible. The rate of tidal damping may depend on the interior structure of the planet and is likely to be different for different planets. The equations for the age of the star were integrated backward in time (6.7 Gyr) and for 10 Gyr into the future. Results show that only when Q_* falls below 10^4 does the behaviour change in a noticeable manner (Figures 6.5 and 6.6).

A more detailed analysis has been conducted using $Q_* = 10^{5.5}$, which corresponds to the value for which Jackson et al. [2008] have found the distribution of initial e values of close-in planets to match that of the general population (Figure 6.4). The top panel of Figure 6.7 shows the migration of HD 181433*b* for different values of Q_p, while in the bottom panel the evolution in *a*-*e* space is presented (obtained by assuming orbital angular momentum conservation). Since both de/dt and da/dt scale $\propto a^{-13/2}$ (equations (6.3.3) and (6.3.4)), the rate of evolution is slower for larger initial values of a, but speeds up dramatically as a decreases.

A smaller Q_p means a larger range of values is spanned during the evolution for a fixed age of the system. For example, $Q_\mathrm{p} = 10^3$ implies that during the early main-sequence stage planet *b* would have had a semi-major axis of 0.15 AU and an eccentricity almost equal to 0.9. However, assuming a current age of 6.7 Gyr, complete circularization of

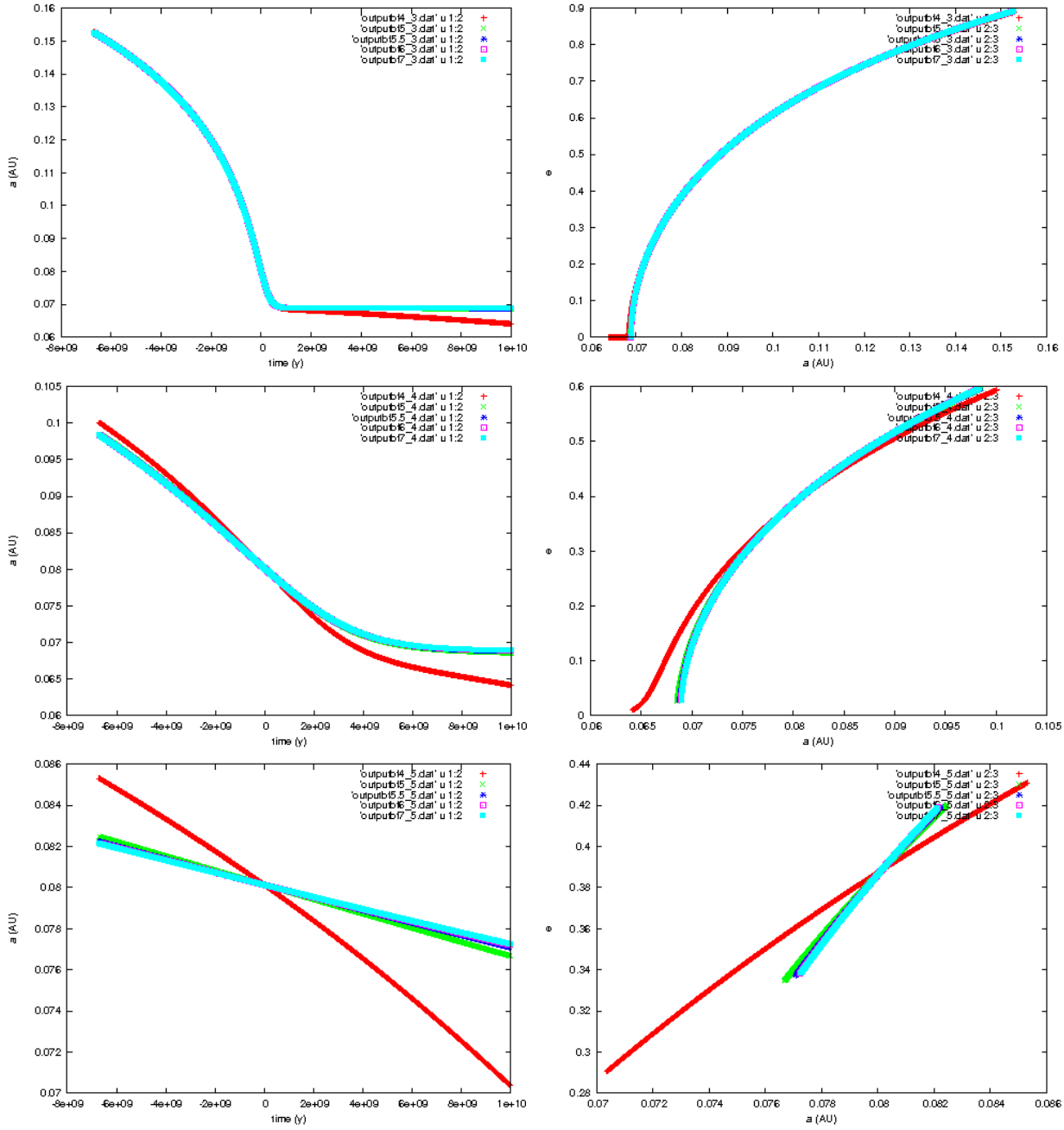

Figure 6.5: Tidal evolution for HD 181433*b* for various pairs of values of Q_p and Q_*. Each row shows for the cases Q_* equal to 10^4, 10^5, $10^{5.5}$, 10^6 and 10^7, on the left the orbital migration and, on the right the evolution of semi-major axis a as function of the eccentricity e. The evolution moves from right to left in $a - e$ space. First row: $Q_p = 10^3$. Complete circularization of the orbit takes much less than one more gigayear to be achieved with the migration terminating at about 0.07 AU. Second row: $Q_p = 10^4$. Circularization is completed within the next 10 Gyr. Third row: $Q_p = 10^5$. Tidal effects are now almost negligible, the point of intersection between all the lines represents the present state. Only when Q_* falls at 10^4 (red line) does the behaviour change in a noticeable manner.

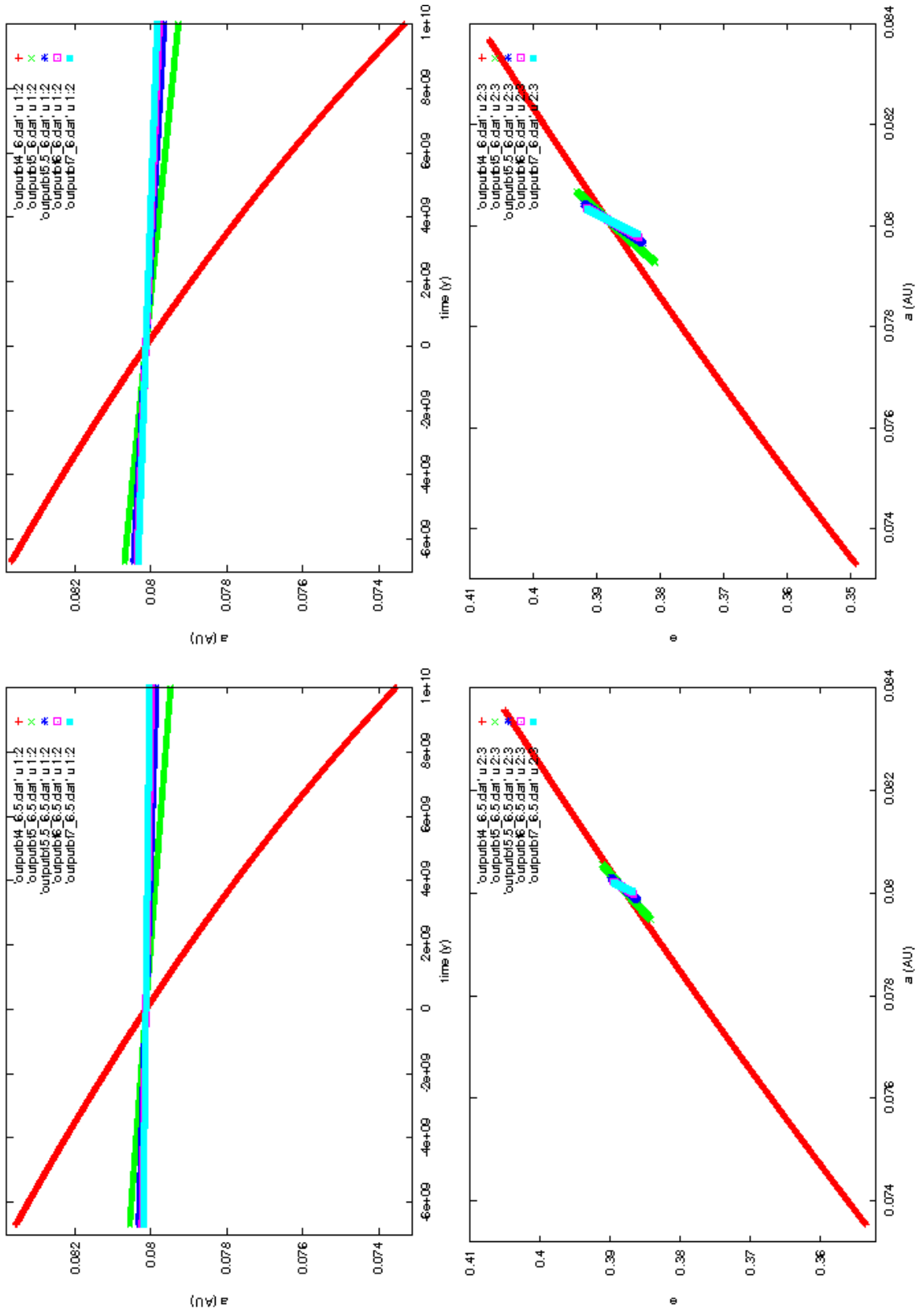

Figure 6.6: Tidal evolution for HD 181433*b* for various pairs of values of Q_p and Q_*. Each row shows for the cases Q_* equal to 10^4, 10^5, $10^{5.5}$, 10^6 and 10^7, on the left the orbital migration and, on the right the evolution of semi-major axis a as function of the eccentricity e. First row: $Q_p = 10^6$. Second row: $Q_p = 10^{6.5}$.

the orbit will take much less than one more gigayear to be achieved (with the migration terminating at about 0.07 AU). Without further detailed information about the system allowing us to constrain its physical nature, this evolutionary track and associated Q_p value is equally probable as any others. Our purpose here is to define a plausible initial state of the system prior to significant tidal evolution, and in doing so we make the assumption that we are observing the system close to the midpoint of its tidal evolution. A value of $Q_{\rm p} = 10^4$ means that planet b would have had initial values $a_b \simeq 0.1$ AU and $e_b \simeq 0.6$, and circularization would be completed within the next 10 Gyr. As noted earlier, $Q_{\rm p} = 10^4$ is similar to the values inferred for Uranus and Neptune [Murray and Dermott, 1999]. We find that a value $Q_p = 10^5$ leads to tidal effects that are almost negligible such that the observed values of a_b and e_b would be very similar to those 6.7 Gyr ago. When considering mechanisms for exciting the eccentricity of planet b, the aim is to achieve values within the range $0.4 \leq e_b \leq 0.6$, implying that modest or essential no tidal evolution has taken place since the excitation occurred.

For completeness, we have also investigated how the tidal evolution may depend on the actual mass of b. A range for $\sin i$ between 0.1 and 1 has been spanned and a density ρ_{Nep} was assumed in all cases. A smaller $\sin i$ implies a more massive planet; when $\sin i = 0.5$, m_b is about the mass of Uranus/Neptune. This is purely a qualitative analysis as a small $\sin i$ would imply a larger mass for planets c and d which could destabilize the system. As expected from equations (6.3.3) and (6.3.4), more massive planets experience significantly more rapid migration than less massive ones. Figure 6.8 displays the case for the instance $Q_{\rm p} = 10^4$. In the extreme case where $\sin i = 0.1$, planet b should have been found initially at around 0.13 AU with an eccentricity of about 0.8; the circularization process speeds up significantly with time and would be fully accomplished in the next billion years for this particular example. Figure 6.9 shows the case for the instance $Q_{\rm p} = 10^5$. Again, here tidal effects are almost negligible. In the extreme case where $\sin i = 0.1$, planet b should have been found initially at around 0.09 AU with an eccentricity of about 0.5 that 10 Gyr into the future would evolve to around 0.1.

I conclude this discussion of tidal evolution by noting that substantial tidal heating of a gaseous planet can in principle cause it to undergo Roche lobe overflow and orbital expansion [Gu et al., 2003, Ibgui and Burrows, 2009, Miller et al., 2009]. As yet calculations have not been performed with parameter sets that would allow to determine whether or not such a scenario is compatible with the current orbital configuration of HD 181433 b.

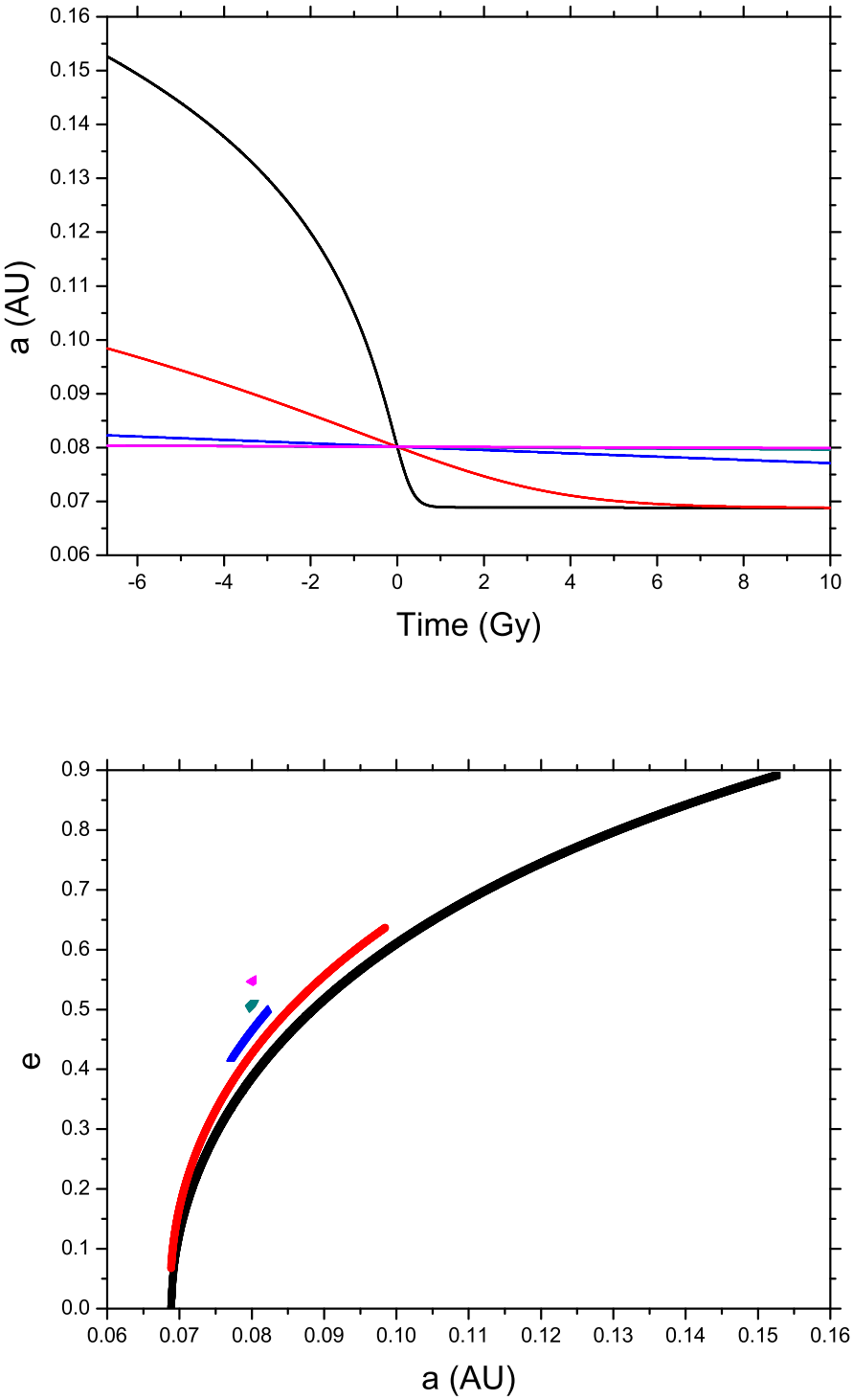

Figure 6.7: Tidal evolution for HD 181433*b* for the case $Q_* = 10^{5.5}$. Top panel: Orbital migration for a range of Q_p. Initially, a greater semi-major axis is expected in the case $Q_p = 10^3$, followed by the values 10^4, 10^5, 10^6 and $10^{6.5}$. The point of intersection between all the lines represents the present state. Bottom: Evolution in $a - e$ space for the cases Q_p equal to 10^3, 10^4, 10^5, 10^6 and $10^{6.5}$. A smaller value of Q_p implies greater fraction of the $a - e$ space has been spanned. The evolution moves from right to left. For clarity, evolutionary trajectories for Q_p equal to 10^4, 10^5, 10^6 and $10^{6.5}$ have been off-setted by $\Delta e = +0.04$ from each previous case.

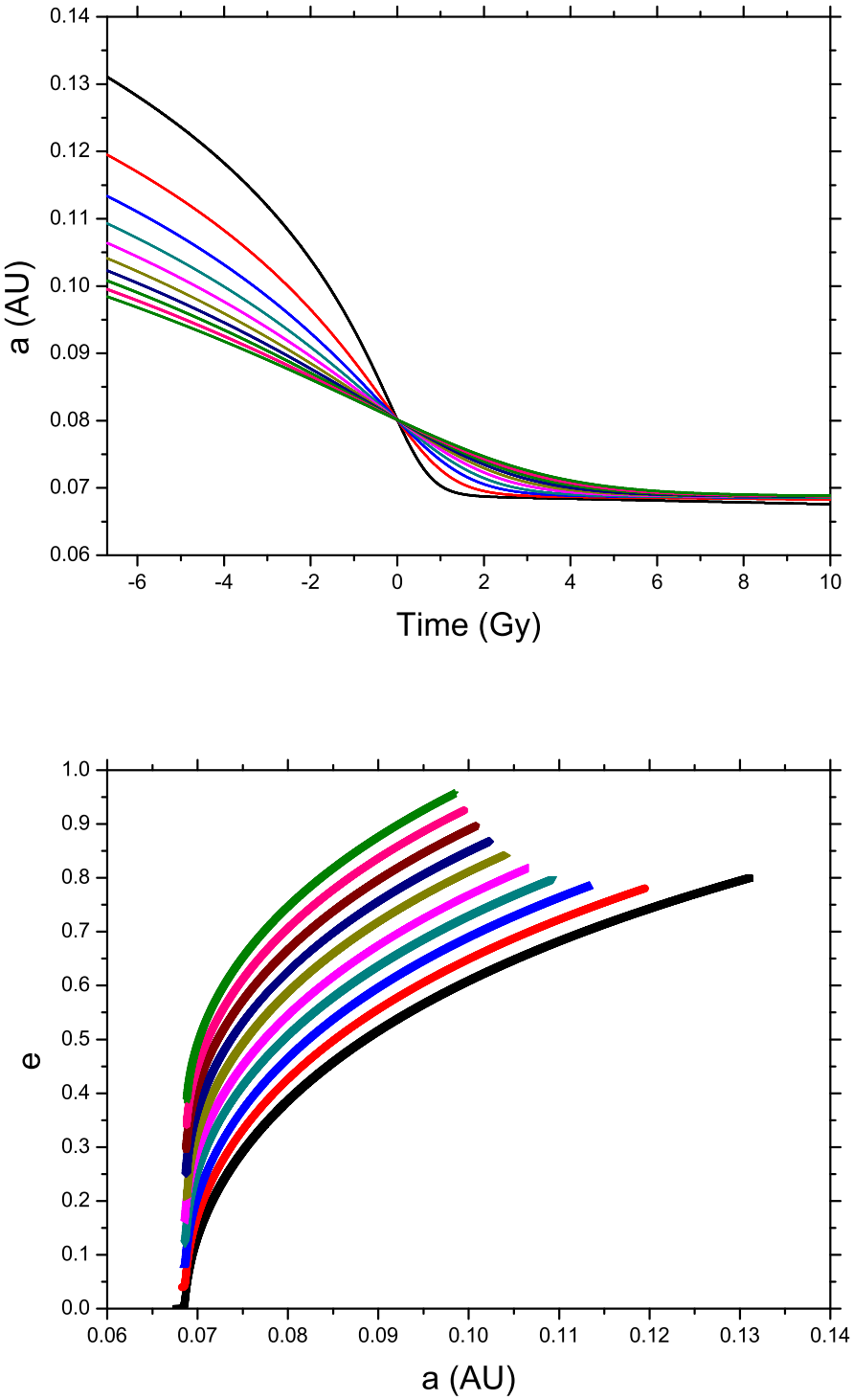

Figure 6.8: Tidal evolution of HD 181433*b* for the range of $\sin i$ between 0.1 and 1 when $Q_* = 10^{5.5}$ and $Q_p = 10^4$. The case $\sin i = 1$ can also be found in Figure 6.7. Top panel: Orbital migration. A smaller $\sin i$ corresponds to a greater initial semi-major axis and a quicker circularization. The point of intersection between all the lines represents the present state. Bottom panel: Evolution in $a - e$ space. A smaller value of $\sin i$ corresponds a greater fraction of spanned space. The evolution goes from right to left. For clarity, evolutionary trajectories for values of $\sin i$ from 0.2 to 1 have been off-setted by $\Delta e = +0.04$ from each previous case.

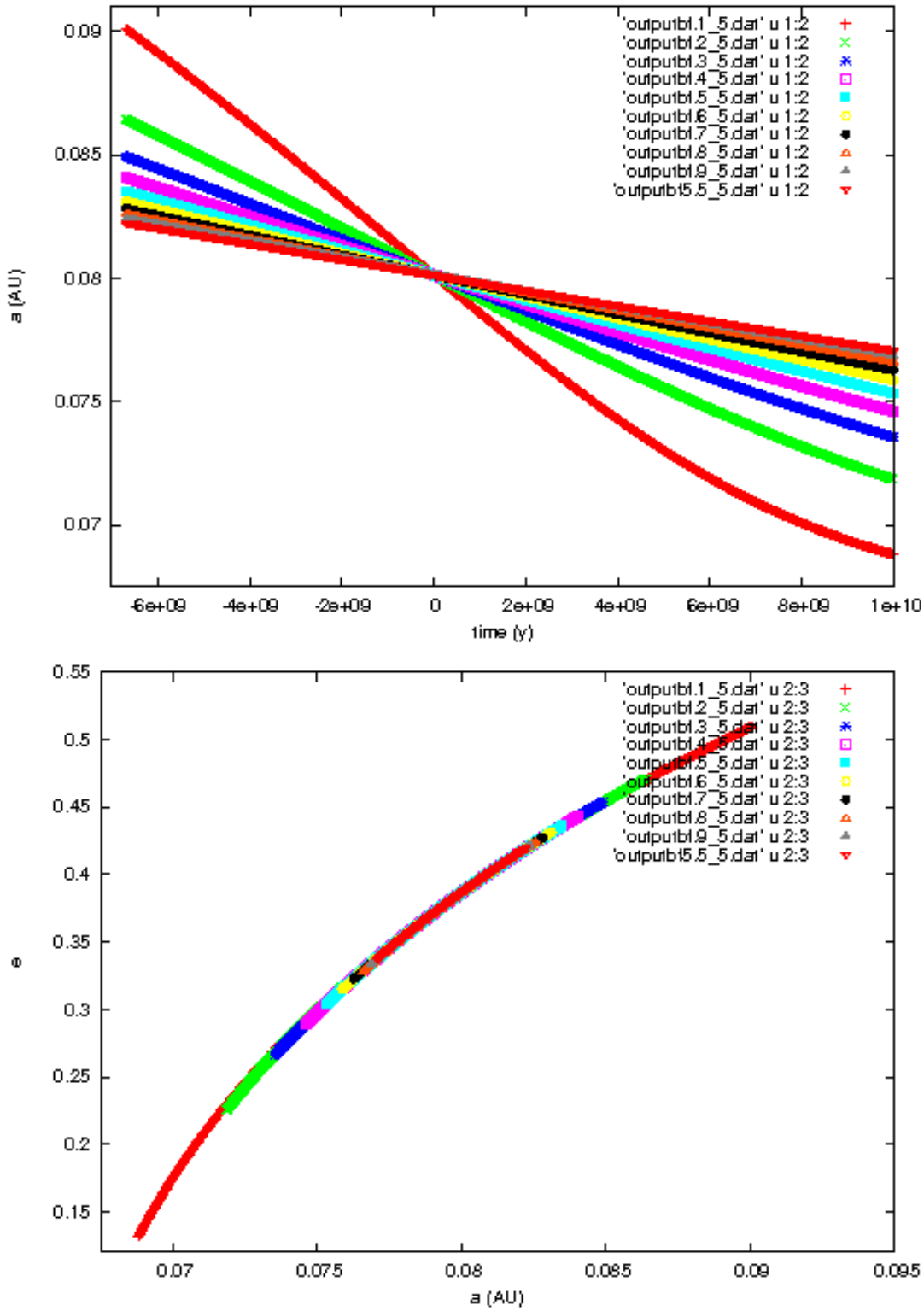

Figure 6.9: Tidal evolution of HD 181433*b* for the range of sin i between 0.1 and 1 when $Q_* = 10^{5.5}$ and $Q_\mathrm{p} = 10^5$. The case sin $i = 1$ can also be found in Figure 6.7. Top panel: Orbital migration. A smaller sin i corresponds to a greater initial semi-major axis and a quicker circularization. The point of intersection between all the lines represents the present state. Bottom panel: Evolution of semi-major axis a as function of the eccentricity e. A smaller value of sin i corresponds a greater fraction of spanned space. The evolution goes from right to left.

6.4 Planet-Planet Scattering

I now consider the origin of the eccentricities of the planets in the HD 181433 system, with the primary focus being the eccentricity of the inner-most body. In Chapter 3 and in particular in Section 3.5 I have introduced planet-planet scattering as a mechanism to create high-eccentricity orbits. In fact, recent work has demonstrated that planet-planet scattering can explain the eccentricity distribution of the extrasolar planet population as a whole [e.g. Chatterjee et al., 2008, Jurić and Tremaine, 2008]. Here I explore a scenario in which an additional giant planet was present in the system originally, orbiting close to the two existing outer giant planets, but shortly after disperal of the proto-planetary disc planet-planet scattering caused this extra planet to be ejected from the system, leaving behind a three-planet system with eccentricities and semi-major axes similar to those observed today. Given the non-linear dynamics involved, the likelihood of producing a system with parameters very close to those of the observed HD 181433 system is exceedingly small. Therefore, we have defined two requirements that must be met for a simulation outcome to be deemed a success: the inner-most planet has a close encounter with one of the giant planets during the period of dynamical instability leading to significant growth of its eccentricity; two giant planets remain at the end of the simulation in 5:2 resonance. We have been able to estimate the probability of each of these separate outcomes from the simulations, and hence the joint probability of both requirements being satisfied.

The N-body code *Mercury-6* has been used to study this problem, and the hybrid integrator with the characteristics described already in Section 6.2.3 has been employed. As introduced in Section 3.6, a physical size for the bodies needs to be set to study close encounters. This is determined by their mean densities. For low mass planets a value equal to 3 g cm^{-3} was adopted, and for giant planets the Jovian value (1.326 g cm^{-3}) was used.

6.4.1 Scattering between three giant planets

In order for one of the giant planets to undergo a close encounter with planet b and scatter it on to an eccentric orbit with $0.4 \leq e_b \leq 0.6$, as required, the perturbing body needs to have a mass large enough to generate the required velocity perturbation. The perturbing body could be the additional planet 'x' or either of the planets c or d. The eccentricity can be approximated as $e \simeq v_r/v_{\rm orb}$, where the v_r is the perturbed radial velocity and $v_{\rm orb} = \sqrt{GM_*/a_b} = 88$ km/s is the Keplerian orbital velocity of b. Assuming that v_r due to an encounter is of the same order as the escape velocity from

the perturbing planet gives $v_r \simeq \sqrt{2Gm_\mathrm{p}/R_\mathrm{p}}$. Therefore:

$$e \simeq \sqrt{\frac{2Gm_\mathrm{p}}{R_\mathrm{p}}}\frac{1}{v_\mathrm{orb}}, \tag{6.4.1}$$

and

$$\begin{aligned} e^2 &\simeq \frac{2Gm_\mathrm{p}}{R_\mathrm{p}v_\mathrm{orb}^2} \\ e^2 &\simeq \frac{2Gm_\mathrm{p}(4\pi\rho_\mathrm{p})^{1/3}}{v_\mathrm{orb}^2 3^{1/3} m_\mathrm{p}^{1/3}} \end{aligned} \tag{6.4.2}$$

where I have rewritten R_p in terms of m_p and ρ_p, the mean density of the perturber which can be set directly into *Mercury-6*.

Rearranging, it is derived

$$m_\mathrm{p} \simeq \frac{e^3 v_\mathrm{orb}^3 3^{1/2}}{G^{3/2}\pi^{1/2}\rho_\mathrm{p}^{1/2}2^{3/2}4^{1/2}}, \tag{6.4.3}$$

and so, the mass required to generate eccentricity e can then be written as

$$m_\mathrm{p} \geq e^3 v_\mathrm{orb}^3 \left(\frac{3}{32\pi G^3\rho_\mathrm{p}}\right)^{1/2}, \tag{6.4.4}$$

Assuming a Jovian mean density gives a required mass for planet x in the range $0.19 \leq m_x \leq 0.64$ $\mathrm{M_{Jup}}$ if it plays the role of planet b's perturber. We have performed simulations with $m_x = 0.3$ $\mathrm{M_{Jup}}$ which is large enough to produce values of $e_b > 0.4$. If planets c or d act as the perturbers then larger values of e_b are possible given their larger masses.

In addition to requiring that the perturbing planet can excite a large enough value of e_b, we have also required that the initial conditions of our simulations at least in principle allow the observed configuration of HD 181433 to be attained once the dynamical stability has caused ejection of the additional planet. The combined specific energy of the two outer planets is given by

$$E_\mathrm{tot} = -\frac{GM_*}{2a_c} - \frac{GM_*}{2a_d}, \tag{6.4.5}$$

and we have noted that ejection of planet x requires a loss of specific energy from the system equal to $E_x = GM_*/(2a_x)$. We therefore have ensured that our initial conditions are such that, if energy E_x is lost from the system of outer giant planets, the remaining energy equals E_tot. We have considered a number of basic initial configurations for our simulations, and each simulation set corresponds to a particular stellocentric ordering of the outer giant planets: *cdx*, *cxd*, *xcd*, *dcx* and *xdc*. The first and last letters in the

labels correspond to the closest and further planets from the star. For each set, planet x is initially placed randomly between 2 and 5 mutual Hill radii (equation (3.5.3)) from its neighbour (for the set *cxd* planet x is initially closest to planet d), and the initial mean longitudes are also set randomly. The planets are initially on circular orbits with mutual inclinations $i \leq 1$ degree. We have noted that with the ice line defined by

$$a_{\rm ice} = 2.7\sqrt{\frac{L_*}{L_\odot}}AU\,, \tag{6.4.6}$$

gives $a_{\rm ice} = 1.50$ AU for HD 181433. Our initial set-up therefore concurs with the general expectation that giant planets emerge from the disc at locations beyond the ice line.

Throughout the integrations, close encounters and collisions between any two bodies were logged, as well as ejections and collisions with the parent star. I ran the simulations for 250 Myr but instabilities usually arise over much shorter time-scales. If dynamical instability resulted in ejection of one or more planet I calculated the orbital elements of the remaining planets. In particular, we were interested in the possibility that the two outer planets are found in 5:2 resonance after the scattering, and also in the value attained for the eccentricity of planet b when the system has stabilized. In all simulations energy was conserved to a level better than one part in 10^4, which is adequate for testing stability [e.g., Barnes and Quinn, 2004]. 300 simulations were performed overall, 50 for each of the sets described above except for set *cdx* where I ran 100 simulations.

The simulation results show that planet x is ejected in almost 50% of cases, but in none of the simulations do I find that planets c and d are in 5:2 mean motion resonance. The dynamical instability often leaves planets c and d more highly separated than in the observed configuration, with planet d in particular orbiting with a significantly larger semi-major axis. Figure 6.10 shows the outcome from sets (*cdx*, *xcd*) that have undergone strong scattering, and we have seen that in each case the currently observed values of e_b, e_c and e_d are at, or close to, the upper limits of the eccentricities generated in the simulations. More importantly, these simulations also demonstrate that the eccentricity of the short-period planet b can also be excited to the required value. Inclinations typically remain small in accordance to what was found by Ford and Rasio [2008].

The left-hand panels of Figure 6.11 show a case from set *cdx* where planet x is ejected after close encounters, and planets c and d land close to their present locations (but are not in resonance). Planets b, c and d achieve maximum eccentricities of 0.09, 0.29 and 0.28, respectively. A case from set *xcd* is presented in the right-hand panels of Figure 6.11. Following close encounters, planet x is ejected with planets c and d landing at 1.6 and 4.4 AU, respectively. Planets b, c and d acquire maximum eccentricities of 0.19, 0.55 and 0.47, and maximum inclinations of 12°, 11° and 9°, respectively. Therefore, in this

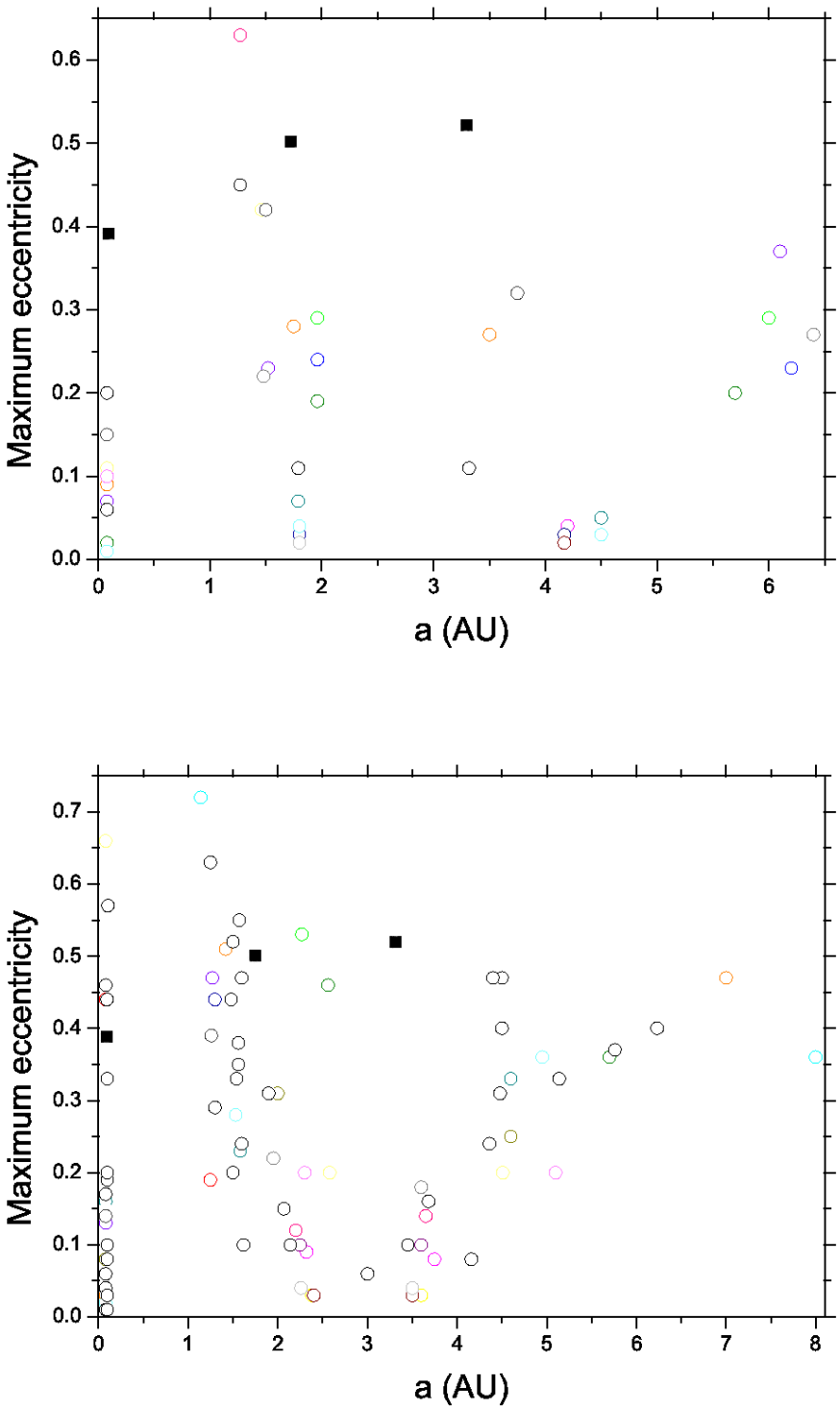

Figure 6.10: Comparison of our synthetic final planetary systems with the HD 181433 system showing maximum eccentricity versus semi-major axis. The values for the real planets are presented with filled black squares. Top panel: Cases from set *cdx*. Bottom: Cases from set *xcd*.

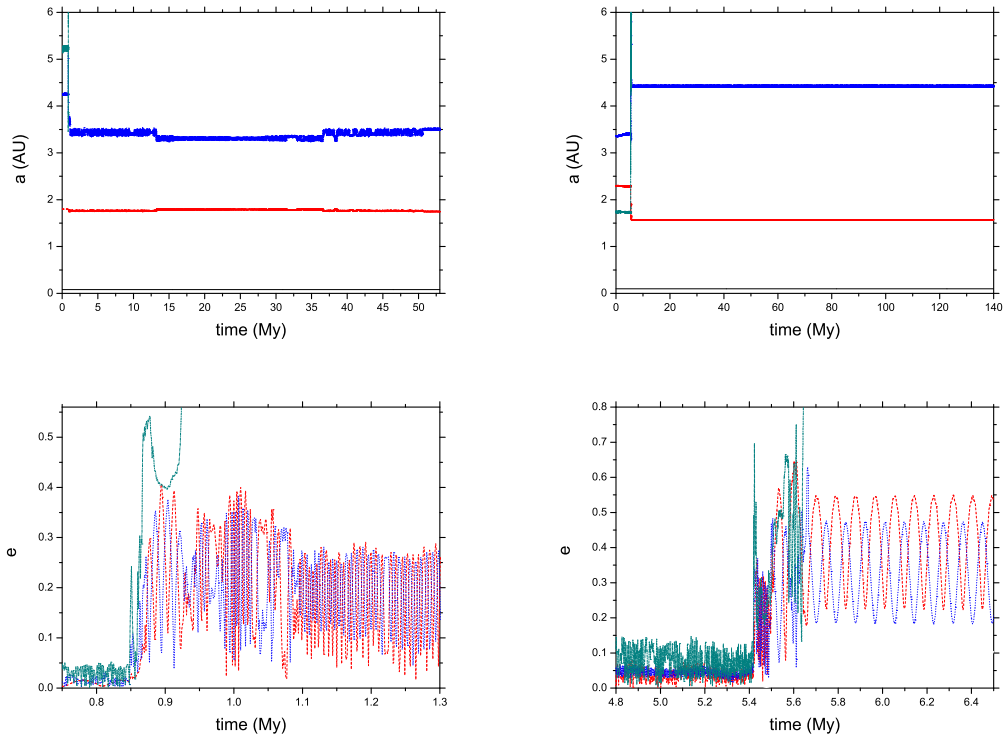

Figure 6.11: Evolution of a and e for two cases of scattering. Top panels: The time evolution of the semi-major axes. Initially, in order of increasing distance, we have planets b, c, d and x (left-hand panel) and planets b, x, c and d (right-hand panel). After ejection, the planets are in long-term stable orbits. Bottom panels: The time evolution of the eccentricities. The dashed line (red) denotes planet c, the dotted line (blue) represents planet d and the dash-dotted line (dark cyan) indicates planet x. After the ejection, the eccentricities oscillate on a secular time-scale. In the first case, e_c moves in the interval 0.03–0.29 and e_d in the range 0.05–0.28. In the second instance, e_c moves in the interval 0.22–0.55 and e_d in the range 0.18–0.47.

case planets c and d reach values for the eccentricities that are similar to the observed one, but planet d orbits at a greater distance.

A case in which e_b grows to the required value is displayed in Figure 6.12 where after many close encounters planet x is ejected and planet b gains a maximum eccentricity of $e_b = 0.65$, which is a value that becomes relevant when considering tidal effects (see Section 6.3.1). The final semi-major axis for planet d, however, is equal to 10.3 AU so the overall final architecture of the system differs considerably from the observed system. This model is also characterized by orbital inclination growth: i_b moves in the interval 25°-83°, i_c in the range 12°-24°, while i_d stays in the range 3°-13°. In this and similar cases, I have checked that the large eccentricity arises because of scattering rather than the Kozai effect which can potentially become active when mutual inclinations exceed a value $\simeq$ 40 degrees [Kozai, 1962]. Summing over all simulations, we find that 11%, 6% and 2% of the runs generate eccentricities for planet b of at least 0.2, 0.4 and 0.6, respectively. These simulations therefore demonstrate the feasibility of dynamical in-

stability of the outer planet system causing all planets in the system to develop large eccentricities.

Probability of resonant capture

Defining a successful outcome for the planet-planet scattering experiments is not straightforward. The non-linear nature of the process clearly means we cannot reasonably expect that a relatively small number of N-body simulations will result in systems that are close analogues to the currently-observed HD 181433 system. Instead, we have used a more restricted definition of success in which planet b experiences an increase in its eccentricity and planets c and d end up in 5:2 resonance. As discussed above, the simulations have demonstrated that the eccentricity of planet b can be raised to the required value, and there are also outcomes in which planets c and d have period ratios that are quite close to 5:2. None of the simulations produce a system in 5:2 resonance, however, so I can now pass to examine the probability of capture in resonance by considering the width of the 5:2 resonance and the relative mean longitudes and longitudes of pericentre required for the planets to orbit stably in resonance.

As anticipated in Section 3.5, Raymond et al. [2008] have shown that planet-planet scattering may result in pairs of planets landing in high order MMRs. The resulting systems tend to have quite high eccentricities and resonant angles that librate with large amplitudes, characteristics that are displayed by the HD 181433 planets as described below and in Campanella [2011]. The simulations presented by Raymond et al. [2008] produced a few 5:2 MMRs for every one thousand simulations. Here, I examine the probability of two planets being scattered into the 5:2 MMR by determining the width of the resonance using N-body simulations that explore the dynamics of two bodies in resonance. Our procedure followed that adopted by Soja et al. [2011] in their study of asteroids in resonance. We have considered the presently inferred orbital elements of planets c and d and we have studied the width of the region inside of which libration occurs by varying the semi-major axis of d in steps of 0.0005 AU. For each case, I have computed the maximum amplitude of the oscillations in semi-major axis by taking the difference between the maximum and minimum values over $50,000$ years of integration, normalized by the initial semi-major axis. The top panel of Figure 6.13 shows how the amplitude of oscillations in semi-major axis varies in the resonant region. Planet d survives only in the range $3.2560 \leq a \leq 3.2995$ AU, and the system is disrupted when d is placed just outside this zone.

In Section 2.5.2, I have introduced mean motion resonances and in particular how subresonaces can be analysed in isolation. In fact, the resonant argument for the 5:2 MMR of the planetary system HD 181433 is [see Section 5.3, Campanella, 2011]

$$\psi = 5\lambda_d - 2\lambda_c - 3\varpi_d \tag{6.4.7}$$

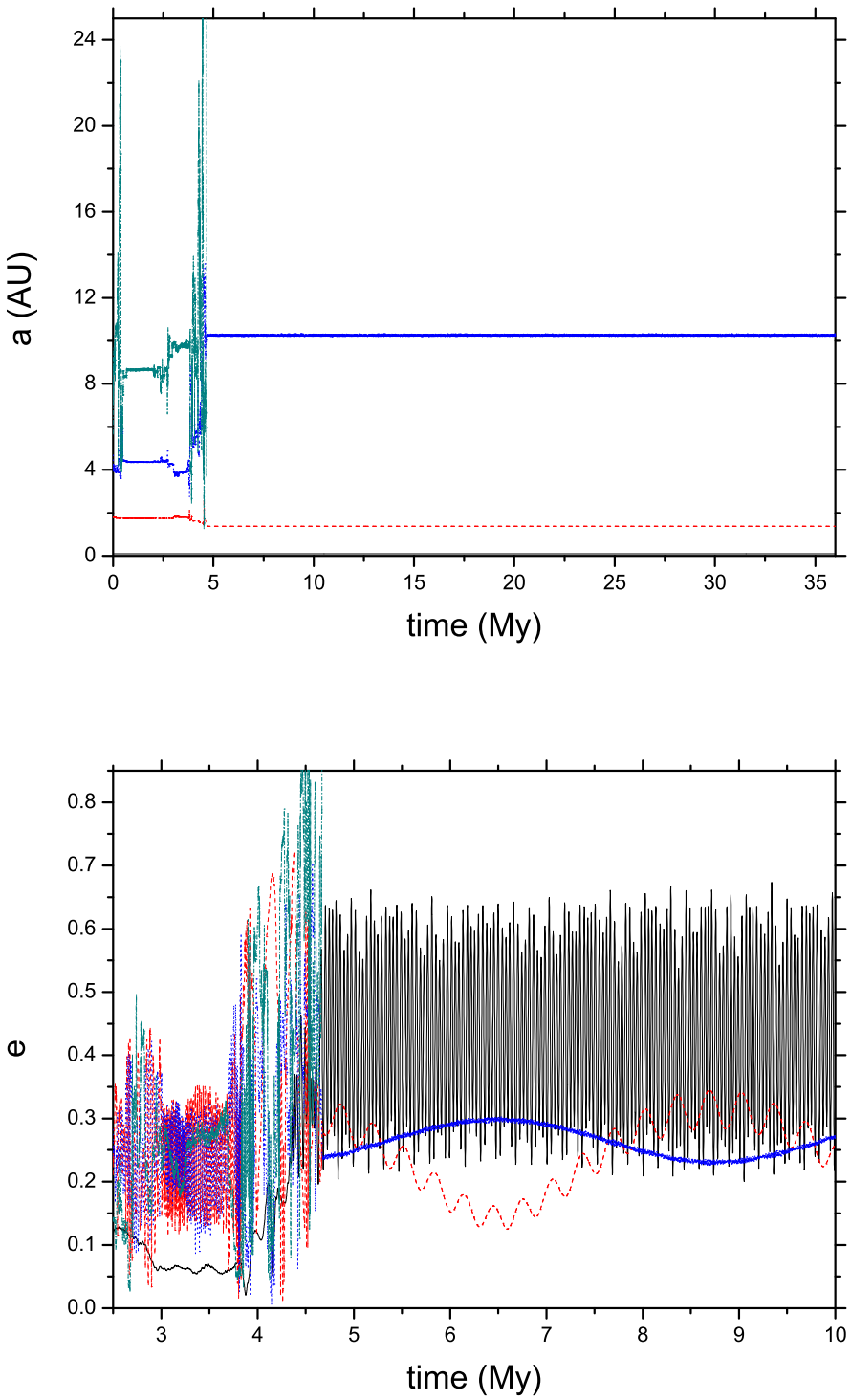

Figure 6.12: Evolution of some orbital elements for a configuration from set *cdx*. Top panel: Time evolutions of the semi-major axes. Initially, in order of increasing distance planets b, c, d and x are located. Bottom: Time evolutions of the eccentricities. The solid (black) line indicates planet b, the dashed line (red) represents planet c, the dotted line (blue) denotes planet d and the dashed-dotted line (dark cyan) is planet x. When x is ejected around 4.5 My, the eccentricities oscillate stably on a secular time-scale. e_b moves in the interval 0.20-0.65, e_c moves in the interval 0.12-0.34, while e_d in the range 0.23-0.30.

where λ is the mean longitude and ϖ is the longitude of pericentre. The bottom panel of Figure 6.13 shows the libration amplitude of this resonant angle as a function of the semi-major axis of planet d. The libration amplitude found at the location of d that corresponds to the best-fitting stable orbital solution presented in Chapter 5 agrees well with the value quoted in the original paper [Campanella, 2011]. The width of the resonance is found to be $\Delta_a = 0.0435$ AU centred at $a = 3.2775$ AU.

A simple estimate for the probability of the planets landing within the resonance after scattering is

$$P(\Delta_a) = \frac{\Delta_a}{\overline{a_d - a_c}} \tag{6.4.8}$$

where $\overline{a_d - a_c}$ is the median value of $a_d - a_c$ at the end of all simulations for which strong plant-planet interactions occurred (we have included only those runs for which final eccentricity of at least one of the planets $e > 0.1$). We have obtained $P(\Delta_a) = 0.0075$. Having planets land within the required Δ_a after scattering, however, does not guarantee that they will be in resonance. It also depends on the angles that define the mutual orientation of their eccentric orbits (the difference between their longitudes of pericentre $\varpi_c - \varpi_d$), and also the values of their mean anomalies at the beginning of their interaction once they land within the resonance width. To quantify this aspect of the problem I ran a set of simulations where the semi-major axis values that lie at the centre of the resonance were taken, and the eccentricity values for the stable best-fitting solution. I have varied $\varpi_c - \varpi_d$ in steps of 90° and the mean anomalies M_c and M_d in steps of 45°, for a total of 256 simulations. I ran the integrations for 30 Myr. 34 pairs of planets survive, all in resonance and in anti-aligned mode. The resonant argument (equation (6.4.7)) librates with amplitudes that vary from a few degrees up to about 240°, as outlined by the lower panel of Figure 6.13. Finally, we have been able to estimate the probability of resonance capture to be $P_{5:2} \sim 0.0075 \times 34/256 \simeq 10^{-3}$, in decent agreement with the larger sample of numerical simulations presented by Raymond et al. [2008].

Probability of scattering generating HD 181433 systems

We have determined that planetary systems with global structure similar to HD 181433, but which originally had an additional gas giant planet orbiting close to the two outer giant planets, can lead to the excitation of the eccentricity of the inner super-Earth up to values $e_b \simeq 0.4$ during approximately 6 % of the time when the system experiences a global dynamical instability. This eccentricity excitation occurs because one or more of the outer planets has a close encounter (or a series of close encounters) with the inner planet during the chaotic phase of evolution. Treating the perturbation of the interior planet b on to an eccentric orbit, and the landing of the two outer planets in the 5:2 mean motion resonance, as being independent processes, the joint probability

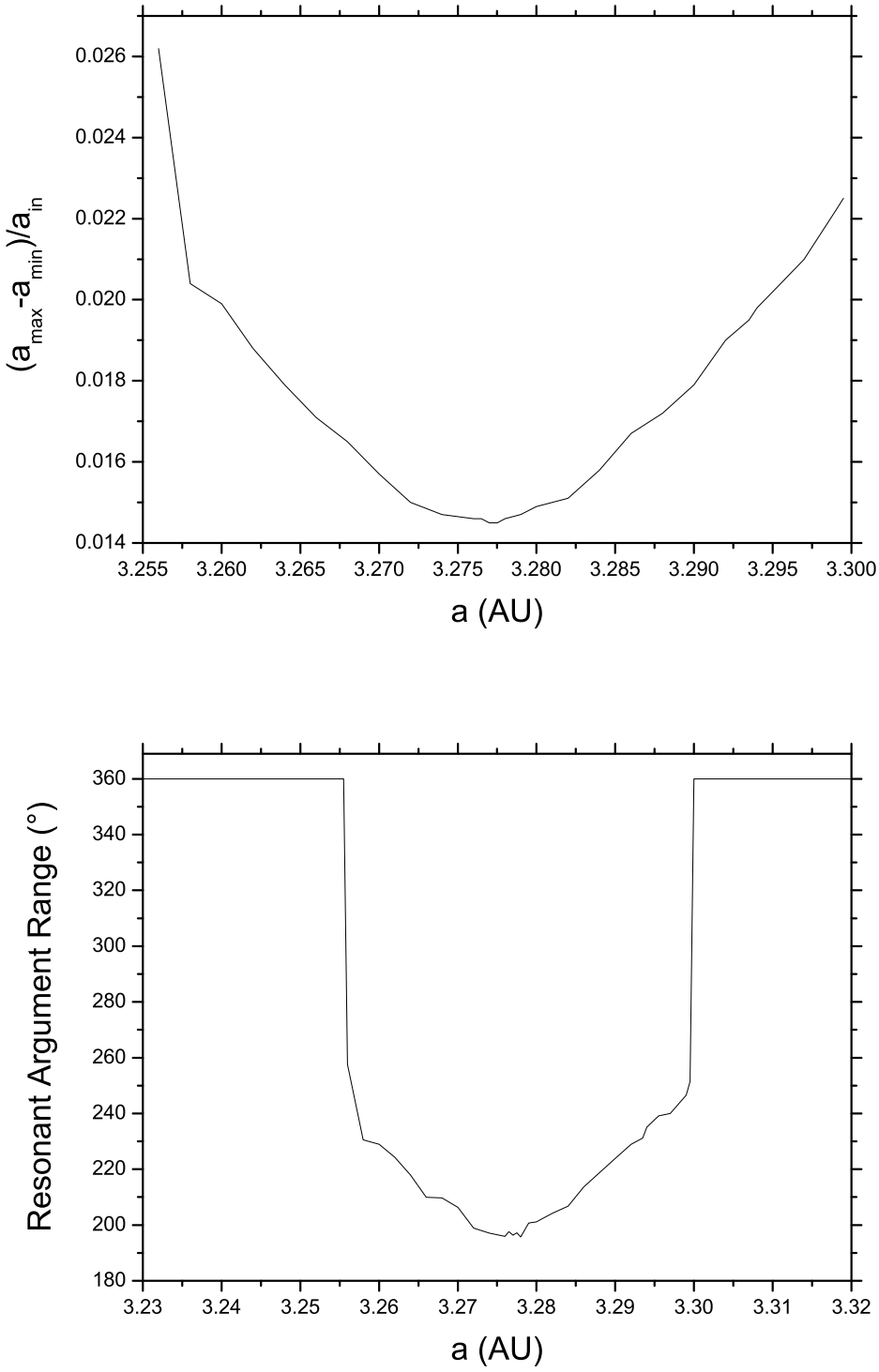

Figure 6.13: The width of the 5:2 MMR. Top panel: The variation in size of resonant semi-major axis oscillations for different locations of planet *d*. Bottom: The variation in the resonant argument. The system is unstable outside this resonant zone.

of eccentricity excitation and resonant capture becomes $P \simeq 6 \times 10^{-5}$. Taken at face value, this result suggests that systems with characteristics similar to HD 181433 occur through planet-planet scattering rather rarely.

6.5 Sweeping Secular Resonances due to Stellar Spin-down

Having determined that the planet-planet scattering hypothesis is a plausible scenario for excitation of the eccentricity of all planets in the HD 181433 system, but that the excitation of e_b combined with resonant capture of planets c and d is likely to be a rare event, I now consider alternative scenarios for exciting planet b's eccentricity. The mechanism of eccentricity forcing due to stellar spin-down was introduced in Sections 3.4 and 3.4.1. Thus, we have considered the hypothesis that the eccentricities and resonant structure for the orbits of the outer planets were established after a period of dynamical instability once gas disc dispersal had occurred, and the eccentricity of planet b was established through the sweeping of a secular resonance with the outer planets caused by the spin-down of the central star from an initial state of very rapid rotation.

In fact, given that we have assumed the current orbits of the outer planets were established shortly after gas disc dispersal, stellar spin-down provides the resonant sweeping in our model. The rate of eccentricity/inclination forcing scales with the square root of the stellar spin-down time (see Section 3.4.1); therefore, in principle it should be possible to tune the spin-down time-scale to obtain the desired eccentricity for planet b. There are other planetary systems with architectures similar to HD 181433 (i.e., a factor of > 10 in orbit period between the inner and outer planets, and an eccentric inner planet), such as HD 125612 and μAræ (introduced in Section 3.3). The same arguments used to constrain the orbital history of the HD 181433 system may apply to these systems too. The more general implications of these evolutionary tuning processes and their application are investigated in Agnor and Lin [2012b].

As introduced in Section 3.4.1, Nagasawa and Lin [2005] presented a model concerning sweeping secular resonances using early system parameters for the then three planet $\upsilon Andromed$æ system. The model presented here differs in that we have assumed the eccentricities of the outer planets to have been established after gas disc removal rather than before or during its occurrence given its role in damping large planetary eccentricities [e.g. Papaloizou et al., 2001].

6.5.1 Secular model including stellar spin-down

I have implemented the Laplace-Lagrange secular model described in Section 3.2 to account for stellar spin-down through inclusion of the J_2 contribution to the eigenfrequencies of the system. As previously remarked, the secular model provides only an

approximate estimate of the locations of secular resonance and can therefore be used to quickly evaluate the hypothesis that a secular resonance may have swept the present-day semi-major axis of planet b at 0.080 AU during stellar spin-down. I have adopted the method described in Section 3.2.3 for including the J_2 terms, and I have used the relation (3.4.5) between the rotational angular velocity of the star Ω_* and J_2, taking the value for the apsidal constant calculated for the Sun.

The mass of planet b is much smaller than the outer two giants so we have treated it as a test particle in the secular model. The top panel of Figure 6.14 presents the free precession period of a test particle induced by planets c and d. It is important to point out the role of GR-induced precession in promoting secular resonances close to the star: neglecting GR, the precession rate would fade to zero very near to the star making it difficult to match any eigenfrequencies of the outer planet secular system (see Section 6.2 for how precession rates change due to GR). The plots in the centre and bottom of Figure 6.14 show the sweeping of two secular resonances as the parent star spins down from a rotation period of 2 days to 30 days (for which the J_2 effects become insignificant). According to this simplified model, when the rotation period of HD 181433 was $P_* \approx 2.1$ days (equivalent to $J_2 \approx 2.2 \times 10^{-5}$), the free precession rate at the present location of planet b matched the one of the eigenfrequencies of the system. Later, the secular resonances move inward towards their present-day locations.

For HD 181433 b, the model presented in Section 3.4.1 suggests that a spin down time-scale of $\tau \approx 1.9 \times 10^7$ years may be capable of accounting for its large observed free eccentricity of 0.39. This time-scale is consistent with estimated mass loss rates from stars in the T-Tauri stage [Ward et al., 1976], suggesting that excitation of planet b's eccentricity through sweeping secular resonances is a realistic hypothesis worthy of further more detailed exploration.

6.5.2 N-body simulations of secular resonance sweeping

As discussed in Section 6.2, the precession period for planet d is shorter than suggested by the secular model because of MMR effects. Therefore, to take into account the time dependent rotational flattening of the host star I use the stellar spin-down model presented in Section 3.6.3. Given the importance of angular momentum in determining the eccentricity evolution of the system, we have confirmed that it is conserved in the numerical simulations at a level better than one part in 10^6.

Evolution during resonant sweeping

As discussed in Section 6.2, the precession rate of the two giant planets in resonance is not constant, with planet c in particular experiencing a precession period in the range $\sim$ 8000-16000 years. According to the secular theory a stellar spin period in the range

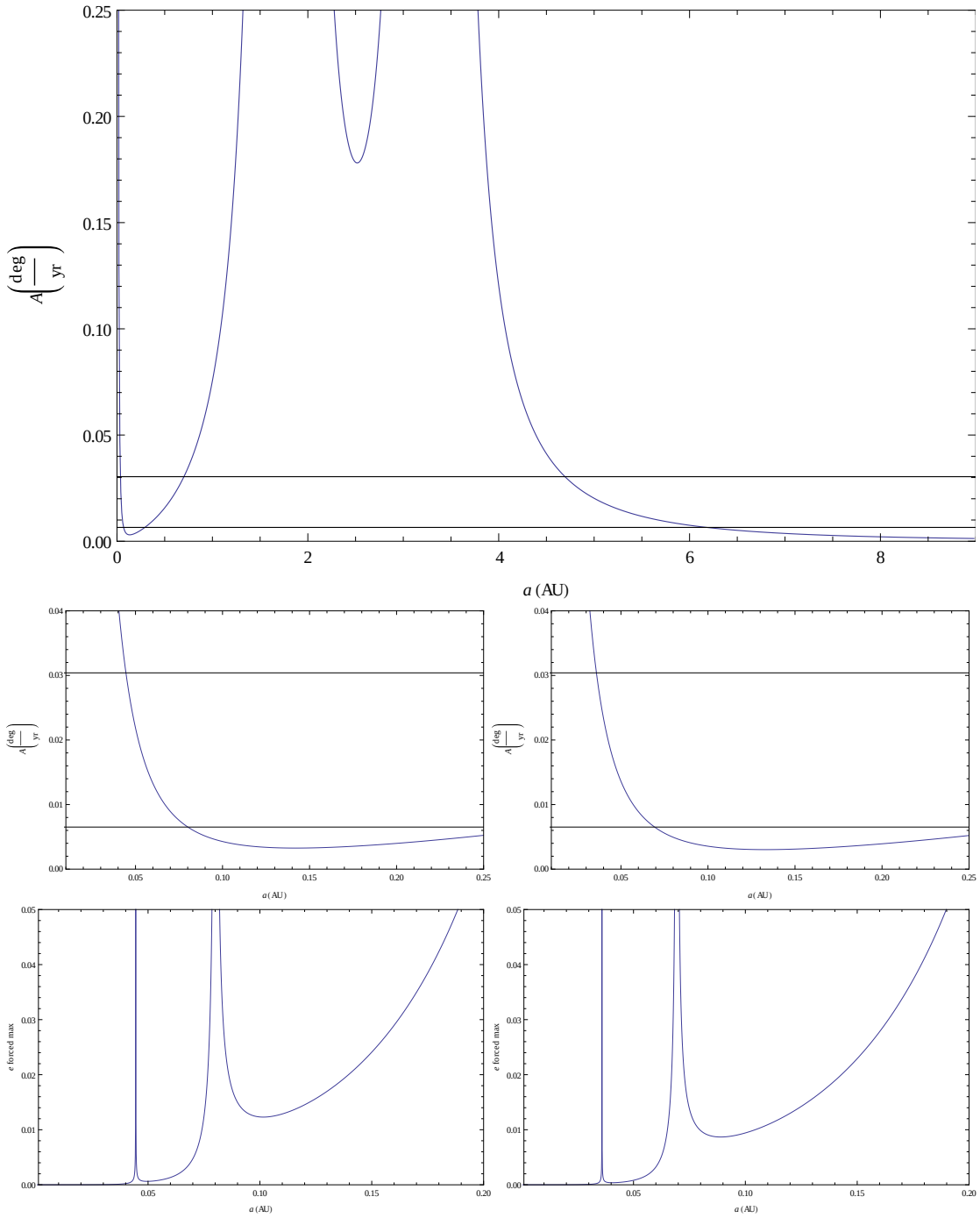

Figure 6.14: The process of sweeping secular resonances for HD 181433. Top: Precession frequency A of a test particle as a function of semi-major axis, derived from perturbations by the two giant planets, considering stellar spin and GR. The horizontal solid lines denote the values of the two eccentricity-pericentre eigenfrequencies. Centre: Precession frequency in the inner region where J_2 effects are relevant. In the left-hand panel the star rotates in 2.1 days while in the right-hand panel the star is slowly rotating. Bottom-Left: The maximum forced eccentricity in the very close region of the parent star which is assumed to rotate in 2.1 days. The secular resonances are located at 0.045 and 0.08 AU. Bottom-Right: The maximum forced eccentricity within 0.2 AU from HD 181433 when it is slowly rotating. The secular resonances have now moved to 0.035 and 0.07 AU, respectively.

11.1–16.7 hours would force planet b to precess with this range of periods, such that secular resonance is established. The break-up rotation period for the star is $P_{cr} = 2\pi\sqrt{R_*^3/GM_*} \approx 3.2$ hours.

I initiate N-body simulations with planets c and d in their inferred present day configuration, and with planet b on a circular orbit close to the star (later on I consider scenarios with differing implications for the long-term tidal evolution of the system discussed in Section 6.3.1, and so place planet b at different semi-major axes). Here, I consider evolution that implies that very little tidal evolution of the system has occurred over its lifetime, consistent with an adopted value of $Q_{\rm p} \gtrsim 10^5$ as discussed in Section 6.3.1. I therefore place planet b with its currently observed semi-major axis $a_b = 0.08$ AU. I initiate simulations with a stellar spin period of 14 hours, and vary the value of the spin-down parameter α, beginning with its nominal value reported in Section 3.6.3.

Results are shown in the top panels of Figure 6.15 for the nominal value of $\alpha = 1.5 \times 10^{-14}$ years. In the right-hand panel it is possible to observe how the relative longitudes of pericentre $\varpi_b - \varpi_c$ evolve during the process: the initial growth of eccentricity begins when the precession rates of planets b and c match ($P_* \approx 16$ hours). The passage of the resonance is anticipated by the orbit of b precessing faster initially and then being overtaken by the precession rate of c. e_b peaks at 0.16 and stabilizes later at a value of $e_b \simeq 0.13$. Setting the initial stellar rotation period to 5 hours instead of 14 hours produces the same result, with the eccentricity peaking when the stellar spin period is 17 hours.

As shown in Section 3.4.1, excitation of orbital eccentricity depends on the mass and eccentricity of the perturber. Bouchy et al. [2009] do not report an uncertainty on the mass of planet c, while the quoted errors on e_c are relatively small with $\sigma_{e_c} = 0.02$. Such a small change in the value of e_c would lead to only small changes in the results here presented. The minimum mass of c is known. However, in Chapter 5 it was noted that the stable best–fit is found in a dynamically active region of phase space, and a value for $\sin i$ noticeably different from 1 would generate instabilities in the system. A slightly increased mass for planet c would lead to only a slightly modified secular resonance.

Also, equation (3.4.3) reports that the expected level of eccentricity excitation depends on the rate of resonant sweeping. A larger value of e_b requires the spin-down rate to be slower, so we have examined how the evolution changes with smaller values of α. Interestingly, I find that the system behaviour can be divided into two distinct modes that depend critically on the value of α. For spin-down rates that exceed the critical value ($\alpha_{\rm crit}$ is 5.75 % smaller than the nominal value) the evolution is similar to that described above and illustrated in the upper panels of Figure 6.15: temporary capture in the resonance and excitation of e_b to values $e_b \lesssim 0.25$. Spin-down parameters equal to or smaller than $\alpha_{\rm crit}$ lead to long-term capture in the secular resonance (apparently

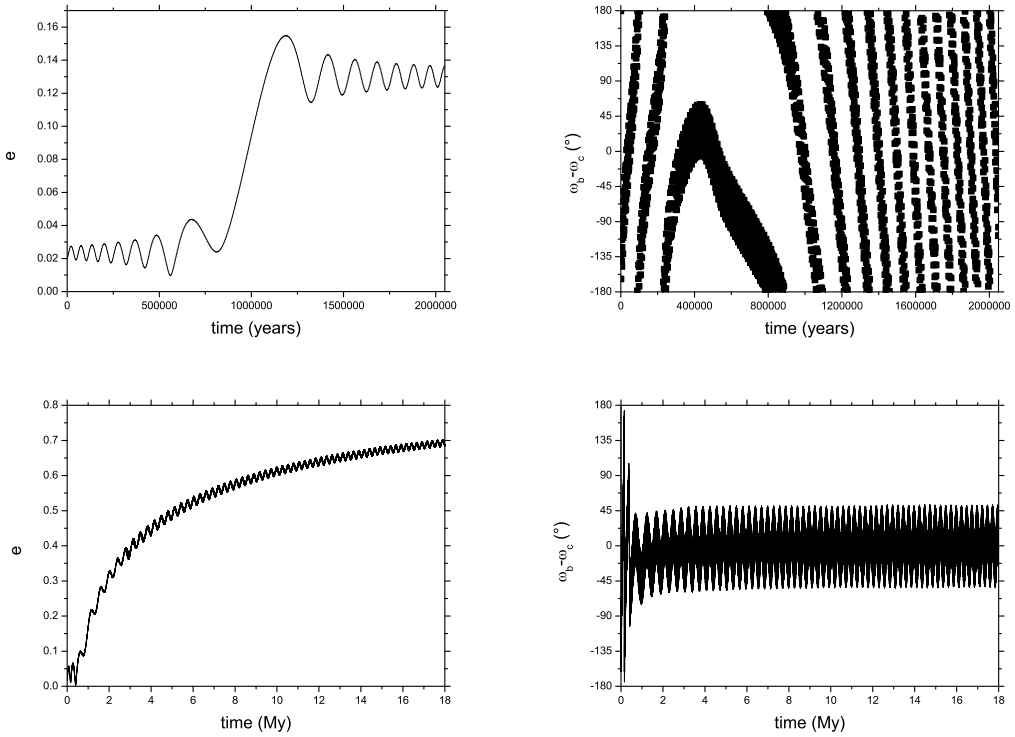

Figure 6.15: The sweeping of secular resonances. Top panels: Evolution of e_b when $\alpha = 1.5 \times 10^{-14}$ years in the left-hand panel, and the related evolution of the secular angle $\varpi_b - \varpi_c$ in the right-hand panel. Note how the angle librates during the passage of the resonance, which corresponds to a sharp increase in the orbital eccentricity of planet b. Bottom panels: Change in e_b when the spin-down parameter is smaller by 5.75% in the left plot, and the evolution of the secular angle $\varpi_b - \varpi_c$ in the right-hand panel. This time, even if the star keeps on spinning down, planet b is locked in the resonance with planet c as a critical value for e_b is reached which generates the precession rate necessary to maintain the resonance. This causes the eccentricity of b to grow indefinitely.

indefinite capture) and growth of e_b towards unity. This mode of evolution is shown in the lower panels of Figure 6.15 for a run with $\alpha = \alpha_{\rm crit}$, where over a run time of 18 Myr e_b reaches a value of 0.7 and $\varpi_b - \varpi_c$ librates around zero with a semi-amplitude of $\sim$ 45 degrees. Apparently a planet caught within this mode of evolution is driven to $e_b = 1$ and collision with the central star unless tides are able to intervene for cases where $Q_{\rm p}$ is small enough to drive sufficiently rapid tidal damping of e_b.

The reason for the existence of these two regimes can be sought in the expressions for the precession rate of the longitude of periastron due to GR and J_2, $\dot{\omega}_{GR}$ and $\dot{\omega}_{J_2}$ introduced already in Sections 3.6.1 and 3.6.2 and here reported for convenience:

$$\dot{\omega}_{\rm GR} = \frac{3GM_*}{ac^2(1-e^2)} n, \dot{\omega}_{J_2} = \frac{3}{2}\frac{nJ_2}{(1-e^2)^2}\left(\frac{R_*}{a}\right)^2 \tag{6.5.1}$$

where both $\dot{\omega}_{GR}$ and $\dot{\omega}_{J_2}$ depend on the eccentricity such that an increase in e leads to an increase in $\dot{\omega}_{GR}$ and $\dot{\omega}_{J_2}$. The condition for the resonance to be maintained during spin-down is given by

$$\frac{\partial \dot{\omega}_{J_2}}{\partial J_2}\frac{dJ_2}{dt} = -\left(\frac{\partial \dot{\omega}_{J_2}}{\partial e} + \frac{\partial \dot{\omega}_{\rm GR}}{\partial e}\right)\frac{de}{dt}. \tag{6.5.2}$$

In other words, the reduction in precession rate due to stellar spin-down needs to be compensated by the increase in precession rate that occurs as eccentricity grows. From equation 6.5.2 is possible to predict that removing the effects of GR will still allow long term secular resonant locking, but for slower values of the spin-down parameter α. I have performed simulations to examine this by omitting the GR term in the equations of motion, and find that a rotation period of $\simeq$ 15 hours is required to enter secular resonance and the spin-down parameter needs to be more than 20 % smaller than the nominal value to maintain long-term resonant capture, in agreement with what was expected. The plots in Figure 6.16 show the growth of e_b for different values of α in cases in which GR effects are included (left-hand panel) and neglected (right-hand panel), demonstrating long-term resonant capture for α below a threshold value in each case.

Resonant sweeping with additional exterior planets

The simulations presented in the previous section indicate two modes of behaviour, but neither of them are able to explain the observed eccentricity of planet b. One results in an eccentricity that is too small, and the other apparently results in either an eccentricity which is too high or collision with the central star. One possibility that I explore here is that there may have been additional planets in the system orbiting relatively close to planet b during sweeping of the secular resonance. If the spin-down is below the critical value required for long-term capture then interactions with the additional planets when the eccentricity becomes large may release planet b from the secular resonance,

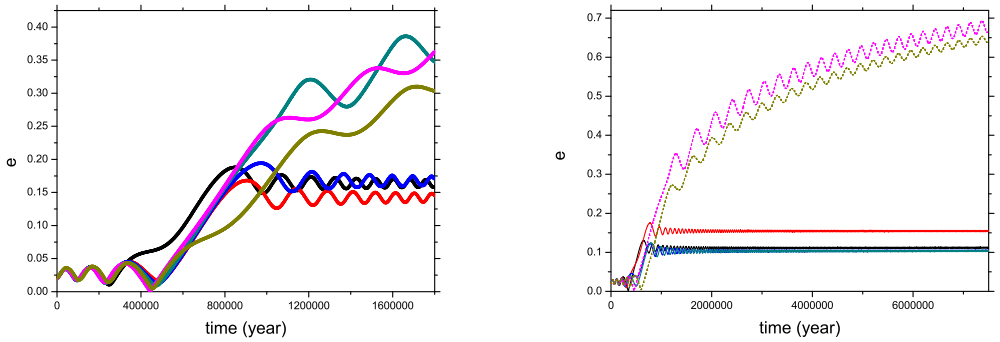

Figure 6.16: The growth of e_b as function of α. Left: Considering both GR and J_2 effects. Values of 10% larger and 3% and 4.5% smaller than the nominal α stabilize around a value for e_b equal to 0.15. For values of 6%, 12% and 50% smaller, e_b grow indefinitely. Right: Considering J_2 effects only. For the nominal α and values 10% larger and 9% and 15% smaller than it, e_b stabilize around 0.15. For values 22% and 50% smaller, e_b grows indefinitely.

Table 6.4: Stellar spin periods necessary to excite a secular resonance at the location of planet b given the semi-major axes of an additional exterior Earth-mass planet.

a_x **(AU)**	0.109	0.111	0.114	0.116	0.142	0.149	0.155	0.162
S_* **(d)**	5.1	2.15	1.63	1.38	0.835	0.797	0.768	0.743

resulting in a final eccentricity of the required magnitude.

I begin by exploring the evolution with one additional Earth-mass planet (so-called planet x) in the system located outside of the orbit of planet b on a circular orbit. I ran a suite of 12 simulations where planet x is located within 2-8 mutual Hill radii from the apocentre of planet b calculated when e_b is in the range 0.3-0.7. The idea here is to induce planet-planet scattering when eccentricity growth is already underway; it is equivalent to placing planet x in the range 0.10-0.16 AU. Including planet x modifies the resonance condition, so for each simulation I have calculated the new spin period required to produce the necessary precession rate for b (see Table 6.4). As illustrated in Table 6.4, the configuration can be such that even a rotation period of 5 days is sufficient for this purpose.

The simulations yield the result that both planets b and x become trapped in the secular resonance with c, and each of them experiences eccentricity growth without limit. Figure 6.17 reports one example with planet x at 0.14 AU, a stellar spin period $\simeq$ 20 hours necessary to generate the resonance, and spin-down parameter α that is 6% smaller than the nominal value. The top-left panel illustrates how the orbits of b and x cross as their eccentricities grow continuously (top-right plot). Collisions are avoided, however, because planet x is trapped in resonance with planet b, as demonstrated by the bottom-left panel. Planets b and c are in a secular apsidal resonance, with $\varpi_b - \varpi_c$ librating around 0° with a semi-amplitude of $\sim$ 45° (bottom-right plot). This behaviour

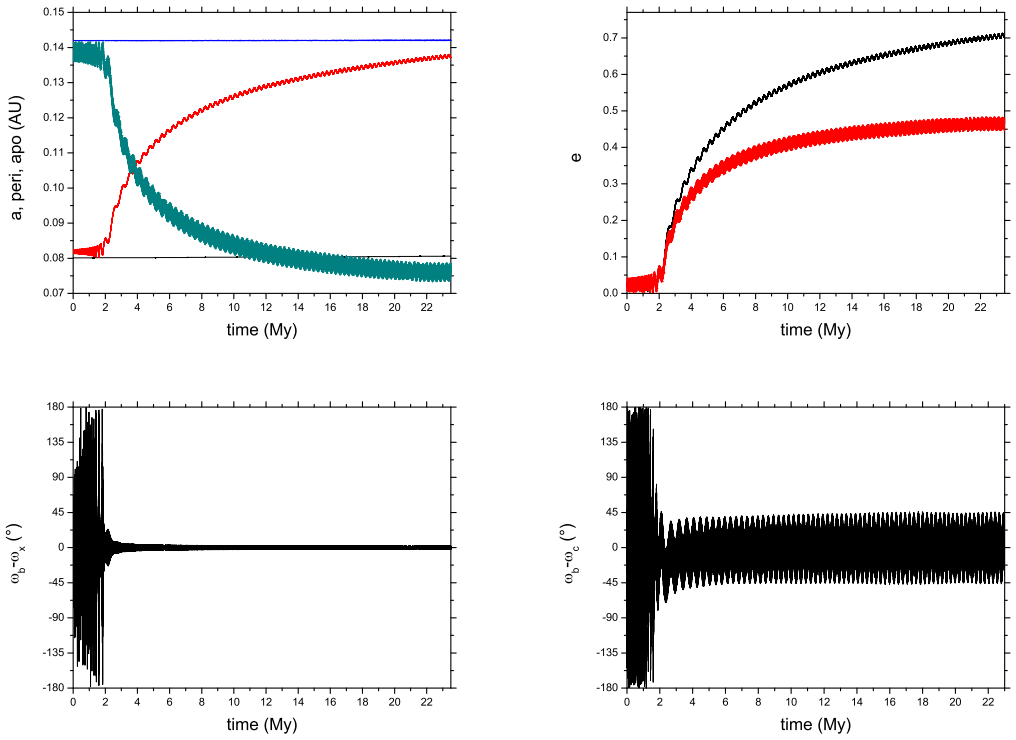

Figure 6.17: The process of sweeping secular resonances for HD 181433 when an Earth-mass planet is added. The spin-down parameter is reduced by 6% with respect to the nominal value. Top-Left: Evolution of semi-major axis and apocentre for planet b, semi-major axis and pericentre for planet x. Top-Right: Evolution of e_b and e_x. Bottom-Left: Evolution of the secular angle $\varpi_b - \varpi_x$, showing the lock into the resonance occurs after $\sim$ 2 My. Bottom-Right: Evolution of the secular angle $\varpi_b - \varpi_c$ which librates around 0°.

is a feature of all runs for which we included one additional Earth-mass planet, and it is important to note that in the absence of stellar spin-down all of the configurations that we considered were dynamically stable over 10^6 years.

For completeness, I consider a model with three additional terrestrial planets to see whether this promotes the sought-after instability when planet b has reached the desired eccentricity $e_b \sim 0.5$. I construct systems consisting of three additional 0.5–1 Earth-mass planets. The inner-most additional body is placed 2–5 mutual Hill radii from the apocentre of the planet, calculated when its eccentricity is in the range 0.3–0.7. The second additional body is placed 2–5 mutual Hill radii from the apocentre of the first additional body, calculated when its eccentricity is in the range 0.3–0.7. The third additional planet is placed 2–5 mutual Hill radii from the apocentre of the second additional body, calculated when its eccentricity is in the range 0.2–0.7. It is important to note that these three bodies are all placed interior 0.26 AU which is a stable zone. In fact, a planet with semi-major axis in the range 0.26 – 0.35 AU obtains a forced eccentricity $e_{\rm forced} \gtrsim 0.2$ (see Section 6.2.4), which will destabilize any planets in the range 0.1 – 0.26 AU before the secular resonance is entered. I consider a spin-down param-

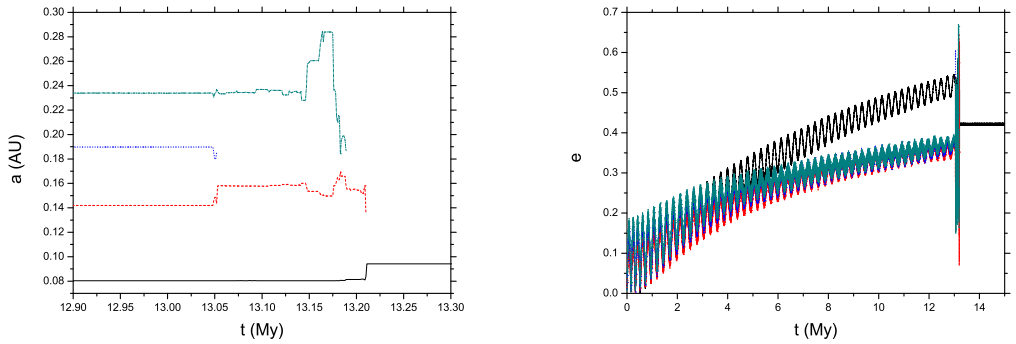

Figure 6.18: The sweeping of secular resonances when three extra Earth-mass planets are included in the inner part of the HD 181433 system. Left: Evolution of the semi-major axes of the four inner planets, with planet b being the innermost. Collisions are observed leading to reduction in the number of planets. Right: Evolution of their eccentricities, e_b is the one growing fastest, achieving a final value of 0.43.

eter 5.75 % smaller than the nominal α and I calculate the necessary spin period for each case to enter resonance. I set a density of 3 g/cm^3 for the additional planets and a Neptune density (1.638 g/cm^3) for b. I ran more than 100 simulations, varying the planetary mutual separations.

From the results of the N-body simulations we have observed that all four inner planets become involved in the resonant trapping, with the eccentricity growing for all of them before instability occurs and strong mutual interactions take place. The outcomes of these simulations include mutual close encounters, collisions between the planets, and collisions with the central star. Occasionally the inner planets can disturb the fragile resonance between the two outer giants causing catastrophic ejections from the system. Out of 100 models I find two models that replicate the present configuration with a value for $e_b \gtrsim 0.4$. When a terrestrial planet survives in the process, the model is still compatible with the detected system because, for example using the Systemic Console (see Section 2.4), a one Earth-mass planet at 0.19 AU would be at the noise level of the radial velocity data with an F-test value of $\approx$ 40%. Figure 6.18 illustrates a successful model for which only planet b survives the instabilities and is able to achieve the required eccentricity. The necessary stellar rotation period to produce the resonance is $\approx$ 22.2 hours. The right-hand panel represents how all the inner planets are increasing their eccentricity during the passage of the resonance, leading eventually to close encounters and collisions which are displayed in the left-hand panel. Orbital inclinations remain small in the system. We have tested the evolution of the systems neglecting the effects of stellar spin-down and found that the eccentricities remain small and the system is stable over runs times of 3.2 Myr.

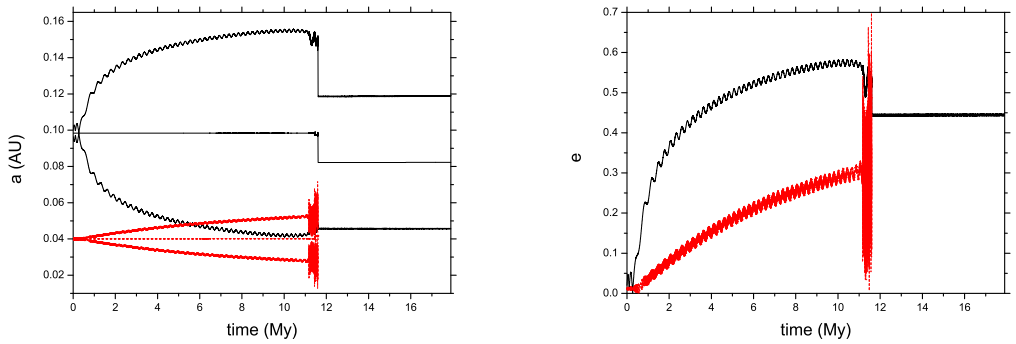

Figure 6.19: The passage of the resonance in the inner part of the HD 181433 system, an Earth-mass planet at 0.04 AU is included. Left: Evolution of the semi-major axes, apocentres and pericentres of the two inner planets, with planet b initially at 0.098 AU. The inner terrestrial planet is destroyed by collision after 11 My. Right: Evolution of the eccentricities. e_b is the one growing faster, achieving a final value of 0.44.

The resonance with an interior planet

To test the generality of the results presented in the previous section, we have evaluated how a hypothetical interior terrestrial planet may have influenced the sweeping of the resonance. We have consider a single Earth-mass planet in circular orbit with semi-major axes in the range 0.03-0.055 AU. We wanted to assess if the additional planet would be trapped long term into the resonance with planet b (as in Section 6.5.2), or if its presence would release b from the resonance with the required eccentricity. I prepare a set of 100 runs with planet b initially located at 0.9-0.11 AU so that close encounters may start when a high eccentricity has already been reached. Each subset has its own stellar spin period for resonance capture. The particular behaviour depends on the individual run, but in general I observe that planets b and x are not quite trapped into a mutual resonance but instead experience differential precession, with the precession periods differing by approximately 2000 years. I find that collisions do occur, but because of the slow differential precession it takes of the order of 10^7 years for them to happen. Figure 6.19 presents a successful case: the eccentricities of the two inner planets grow because of the passage of the resonance, the orbits cross each other, after 11 Myr instability arises leading to a collision, leaving planet b with the required eccentricity. Although planet b is initiated with a semi-major axis of 0.1, the inelastic collision causes the composite planet to effectively migrate to 0.08 AU, which is the observed value. Orbital inclinations stay small in the system. To generate the resonance this simulation required a stellar rotation period $\lesssim$ 13.4 hours. A set of simulations with $a_b = 0.105$ AU demands a stellar spin period of 11.3 hours. In these configurations the eccentricity stops growing and stabilizes around 0.45 as the secular resonance is disrupted.

Resonance passage considering stronger tidal evolution

In the previous section, I showed that sweeping secular resonances due to stellar spin-down, combined with planet-planet scattering, can cause eccentricity excitation of planet b up to $e_b \simeq 0.4$, consistent with present day observations. The HD 181433 system, however, is unusual because of the large eccentricity of the inner planet in spite of the ~ 6.7 Gyr age of the star. The implication is that tidal dissipation inside the planet is weak compared with that measured for terrestrial bodies in the Solar system. If the value $e_b = 0.4$ is primordial then it implies a value of $Q_{\rm p} \geq 10^5$.

A value of $Q_{\rm p} \sim 10^4$ is inferred for Neptune and Uranus [Murray and Dermott, 1999], and I showed in Section 6.3.1 that if such a value is adopted for HD 181433b then the planet is approximately half-way through the process of circularising from an initial eccentricity of $e_b \simeq 0.6$ and semi-major axis $a_b = 0.1$ AU. This raises the question of whether or not the sweeping secular resonance model with additional terrestrial-mass planets can also achieve an eccentricity this large, and we have addressed this issue below using a further batch of N-body simulations.

Here the planet b is placed further out so a shorter stellar spin period is required to generate the resonance. I infer that the star had to rotate in $\lesssim 11.0$ hours in order for the resonance to sweep the location of b. Using the nominal value of α (see equation 3.6.7) in a simulation consisting of planets b, c and d only, e_b peaks at 0.28 and stabilizes later around a value of 0.25. If I reduce the stellar spin-down rate to be equal to or less than the nominal value by just 5.75 %, e_b grows indefinitely as described above.

The original aim was to test the possibility of breaking the secular resonance for planet b by including three additional terrestrial planets orbiting beyond b, but the larger initial semi-major axis and larger final eccentricity required of $e_b = 0.6$ mean that a stable system of three additional planets cannot be set-up because the outer one orbits outside the stable zone located within 0.26 AU (see Section 6.2 and 6.5.2). For this reason I ran a suite of simulations with two Earth-mass planets orbiting outside of planet b. The qualitative evolution is similar to that described in Section 6.5.2. An example of a successful simulation is displayed in Figure 6.20, showing the growth of eccentricity through secular resonance, planet-planet scattering and collision, and two surviving inner planets with planet b orbiting with $e_b \sim 0.6$ and $a_b \sim 0.1$ AU. The necessary stellar rotation period to generate the resonance is 11.6 hours. The rocky planet which survives at 0.16 AU would be in the noise level of the measured radial velocities (F-test value of 84%). Its orbital inclination increases up to 12° for the smaller survivor while it remains much smaller for planet b. Taking account of tides with $Q_{\rm p} = 10^4$, once the initially chaotic phase of evolution has finished the system will evolve to exhibit characteristics very similar to those observed today on a time-scale of ~ 6 Gyr.

Note that I have tested the stability of the system without the resonance and find that it remains stable over a time-scale of 1 Myr.

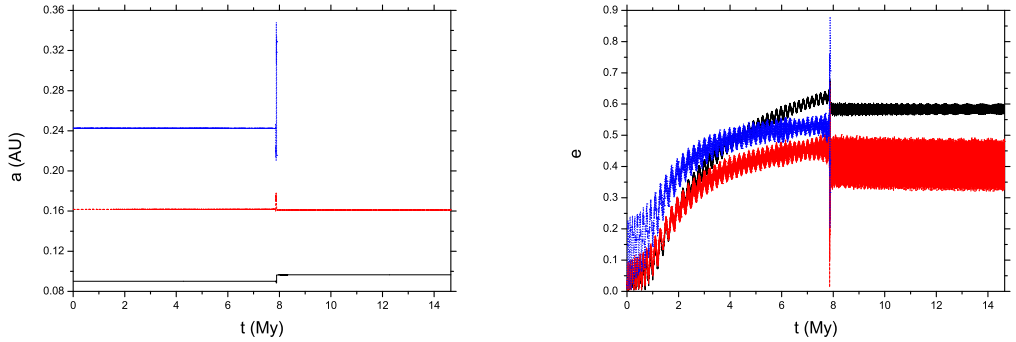

Figure 6.20: The sweeping of secular resonances when two extra Earth-mass planets are introduced in the inner part of the HD 181433 system. Left: Evolution of the semi-major axes of the three inner planets, with planet b being the innermost. The outer terrestrial planet is destroyed through collision after 8 My. Right: Evolution of their eccentricities. The eccentricity of the outer planet is the one growing fastest at the beginning as it is at the outer limit of the stable zone. A final value of 0.6 is achieved for e_b, while the surviving Earth-mass planet acquires an eccentricity of 0.45.

Finally, I report here also an example of evolution when an Earth-mass body is placed on an orbit interior to planet b. This scenario has already been discussed in Section 6.5.2. Figure 6.21 shows the increase of the eccentricities for the two inner planets (b and x). Instabilities arise after 18 My, only planet b survives and it is left with an eccentricity $e_b = 0.56$, close to the required value. To generate the resonance a stellar rotation period $\lesssim 13.4$ hours is required.

6.5.3 Large forced e_b by an additional planet

The spin-down of the central star provides a means of enhancing the eccentricity of planet b. In the absence of a rapidly rotating star an additional undetected planet in the system can also enhance the forced eccentricity of planet b by strengthening coupling with the outer giant planets. By carefully choosing of the mass and location of an additional planet the forced eccentricity of planet b may be enhanced. I focus on the effect of a low mass planet near planet b below.

Exterior low mass planet

Mardling and Lin [2004], for example, have investigated the hypothesis that eccentric short-period planets have eccentricities that are excited by undetected outer companions. I have already discussed in Section 6.2.4 that an additional planet can be stable in the region 0.1 – 0.35 AU. I use the secular model to estimate the planetary mass required in this range in order for the precession period of b to match that of c or of the hypothetical planet. In particular, in Section 6.5.2 it was shown that the eccentricity started to grow for $P_* \approx 16$ hours. The secular model indicates that, with this condition, the

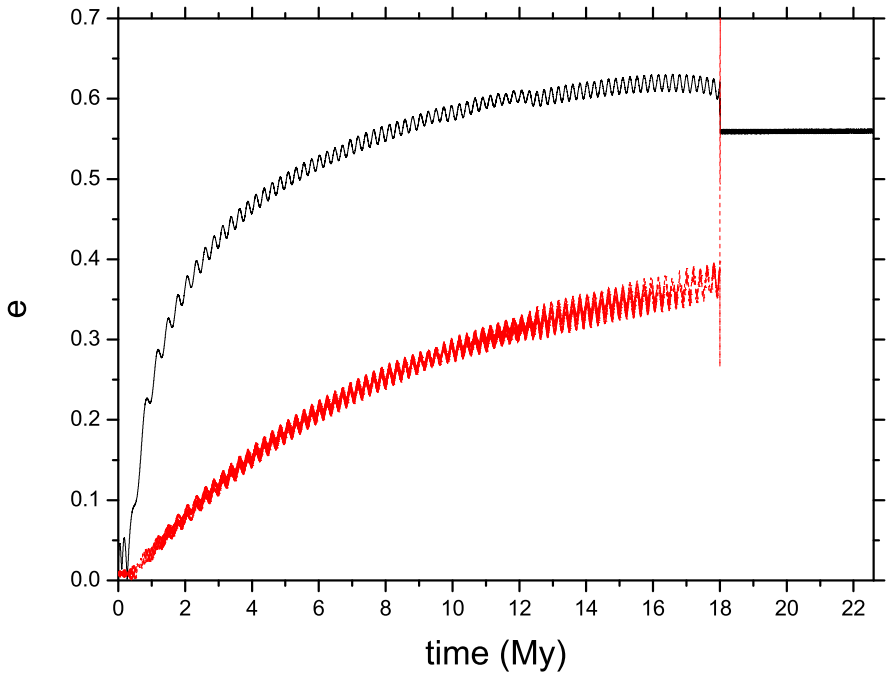

Figure 6.21: The passage of the resonance in the inner part of the HD 181433 system when an Earth-mass planet at 0.04 AU is included. The evolution of the eccentricities is show with e_b growing faster and achieving a final value of about 0.56. The inner terrestrial planet is destroyed after 18 My.

orbital precession period for planet b is $P_{\omega_b} \approx 15200$ years. This value is in compatible with what was found for the precession period of the pericentre of planet c from the numerical integrations (see Table 6.3). Therefore, when the aim is to have a secular resonance with c, I assess for which values of $m_x - a_x$, a test particle placed at a_b has a precession period of $\approx$ 15200 years. I then refine the solution by means of numerical simulations, setting the eccentricities of the extra planet and b to small non-zero values and examining the evolution of 75 configurations for 10 Myr.

The maximum forced eccentricity obtained for these runs was $e_b = 0.28$ for a 12 Earth mass companion orbiting at 0.35 AU or for a 15 Earth mass companion orbiting at 0.3 AU. This latter case is represented in the top panels of Figure 6.22 where the secular angle $\varpi_b - \varpi_x$ is seen to librate about 180 degrees with a semi-amplitude of 120 degrees. All other simulations have resulted in values of $e_b < 0.28$. For example, an 11 Earth mass companion orbiting at 0.25 AU resulted in a peak value of $e_b = 0.27$ with the secular angle $\varpi_b - \varpi_c$ librating about 180 degrees with a semi-amplitude of 90 degrees, while a 3 Earth mass companion orbiting at 0.15 AU resulted in a peak value of $e_b = 0.12$ (see the central and bottom panels of Figure 6.22). This latter configuration is not deeply into a secular resonance as $\varpi_b - \varpi_x$ is seen to circulate while the secular angle $\varpi_b - \varpi_c$ experiences the nodding phenomenon (see Section 2.5.2).

Interior low mass planet

I now consider the evolution when an extra planet is orbiting interior to b. As above, I use the secular theory to estimate the planetary masses required between 0.008 and 0.062 AU for planet b to be in secular resonance.

Results from this secular analysis are shown in the top panel of Figure 6.23. Numerical integration of 40 initial configurations show again that e_b is not forced sufficiently to explain the currently observed value of $e_b = 0.39$. The maximum forced eccentricity obtained was $e_b = 0.21$, this happened in two cases: a 1.5 Earth mass companion orbiting at 0.041 AU and a 0.75 Earth mass companion orbiting at 0.056 AU (central and bottom panels of Figure 6.23). In these two cases the secular angle $\varpi_b - \varpi_x$ is seen to librate while $\varpi_b - \varpi_c$ circulates.

Detectability

I assess the detectability of these hypothetical planets using the simple formula (1.2.1) and assuming a radial velocity precision of 1 m/s [Bouchy et al., 2009]. In the range 0.1 – 0.35 AU planets with mass as small as 4–6 $M_\oplus$ would be detectable. This excludes the possibility of exciting a sufficiently large e_b with an unseen planet in this region. In the inner zone, the detection limit is about 2 Earth-masses. This cannot exclude the generation of a forced eccentricity of 0.21.

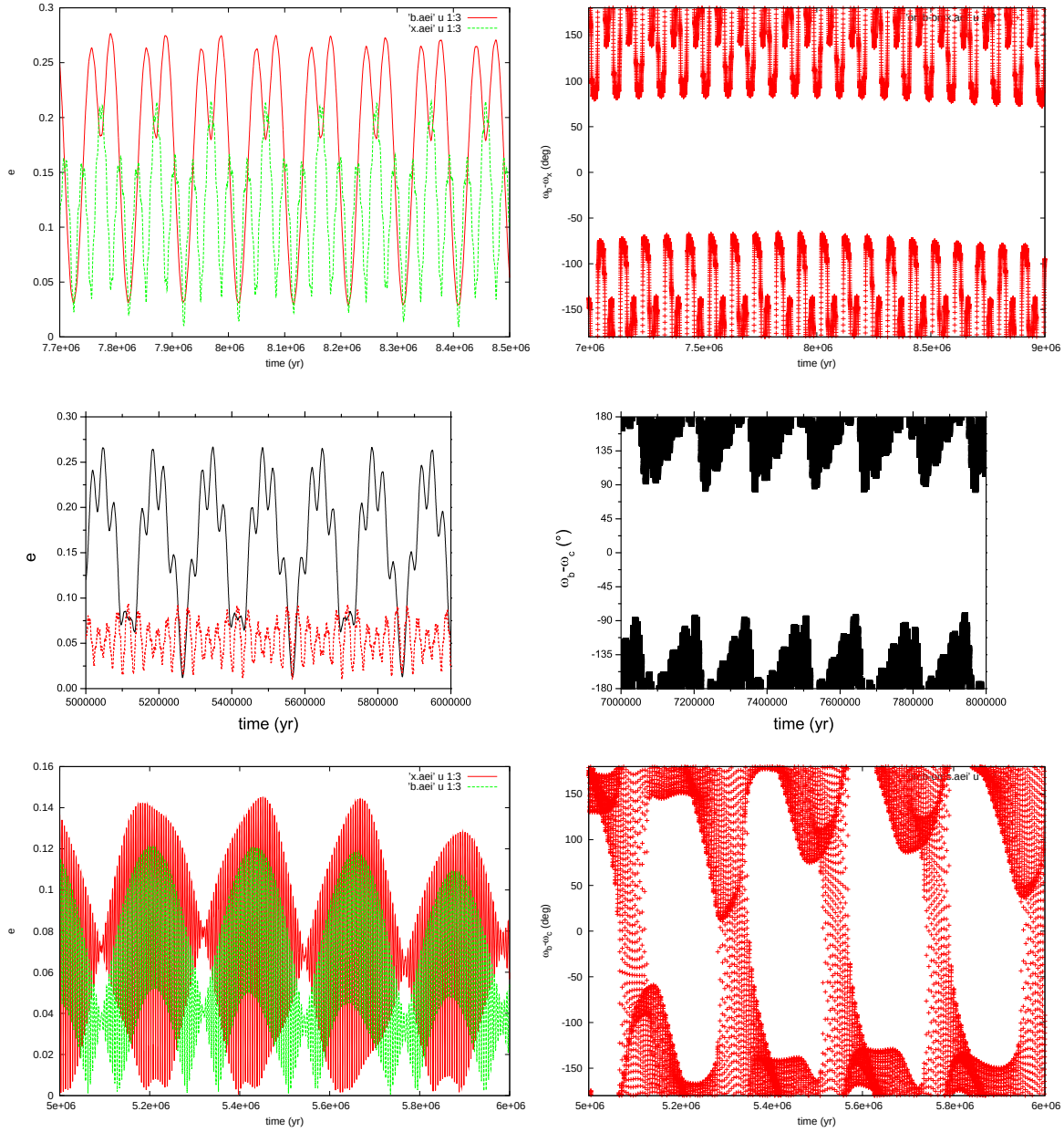

Figure 6.22: Eccentricity excitation due to an exterior low mass planet. Top panels: Evolution of e_b (red) and e_x (green) in the left-hand panel, and the evolution of the secular angle $\varpi_b - \varpi_x$ in the right-hand panel for a case with $a_x = 0.3$ AU and $m_x = 15M_\oplus$. Maximum values for e_b and e_x are 0.28 and 0.22, respectively. The secular angle librates about 180 degrees with a semi-amplitude of 120 degrees. Central panels: Evolution of e_b and e_x in the left-hand panel, and the evolution of the secular angle $\varpi_b - \varpi_c$ in the right-hand panel for a case with $a_x = 0.25$ AU and $m_x = 11M_\oplus$. Maximum values for e_b and e_x are 0.27 and 0.09, respectively. The secular angle librates about 180 degrees with a semi-amplitude of 90 degrees. Bottom panels: Evolution of e_b (green) and e_x (red) in the left-hand panel, and the evolution of the secular angle $\varpi_b - \varpi_c$ in the right-hand panel for a case with $a_x = 0.15$ AU and $m_x = 3M_\oplus$. Maximum values for e_b and e_x are 0.12 and 0.15, respectively. The secular angle experiences the nodding phenomenon.

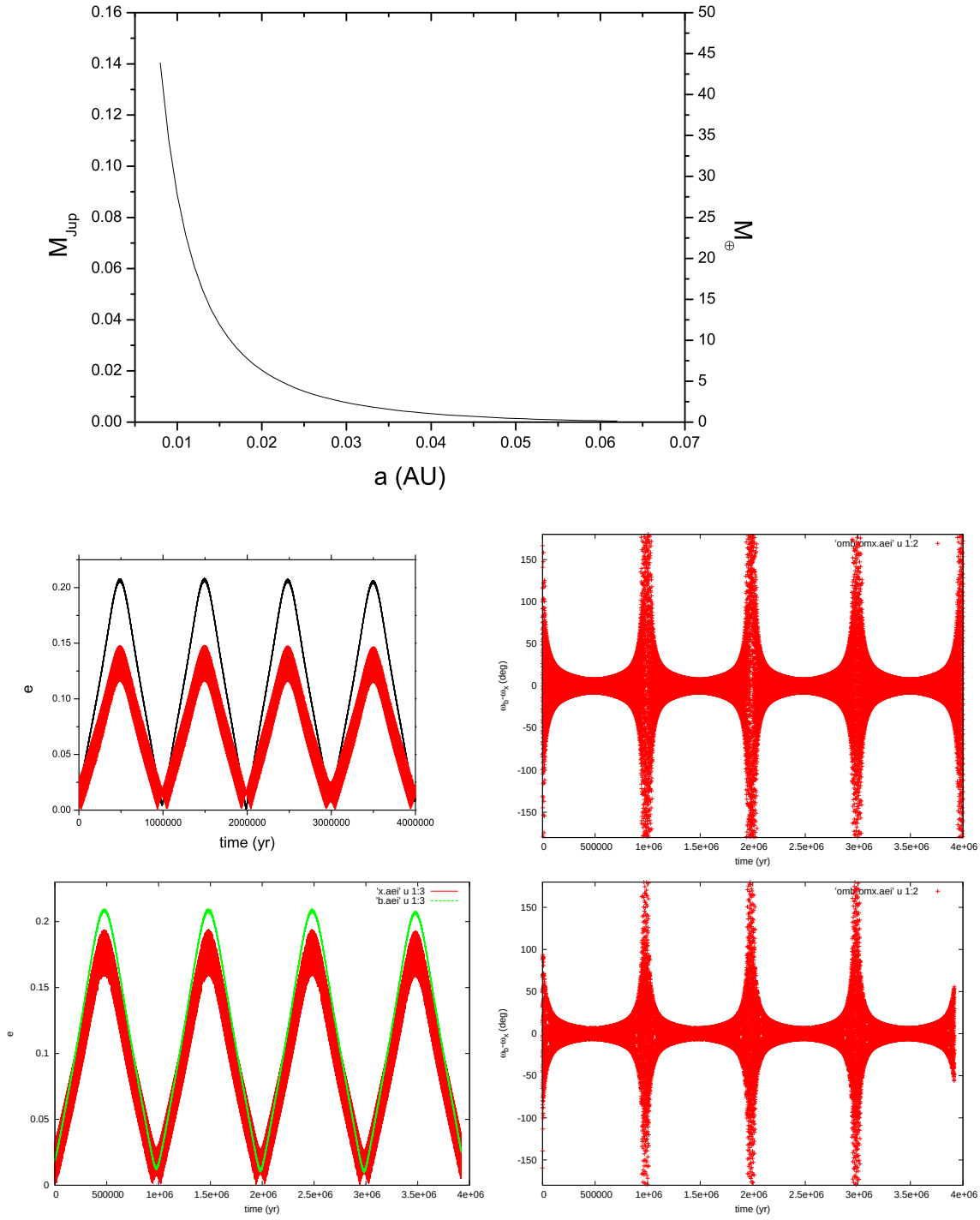

Figure 6.23: Eccentricity excitation due to an interior low mass planet. Top panel: Planetary mass required, as function of semi-major axis, to place planet b in secular resonance. Central panels: Evolution of e_b and e_x in the left-hand panel, and the evolution of the secular angle $\varpi_b - \varpi_x$ in the right-hand panel for a case with $a_x = 0.041$ AU and $m_x = 1.5 M_\oplus$. Maximum values for e_b and e_x are 0.21 and 0.15, respectively. The secular angle librates about 0 degrees but a divergence is noticed when e_b and e_x get close to be null and so the argument of pericentre is not well defined. Bottom panels: Evolution of e_b and e_x in the left-hand panel, and the evolution of the secular angle $\varpi_b - \varpi_x$ in the right-hand panel for a case with $a_x = 0.056$ AU and $m_x = 0.75 M_\oplus$. Maximum values for e_b and e_x are 0.21 and 0.19, respectively. The secular angle librates about 0 degrees but it diverges when e_b and e_x get close to zero.

If planet b had been formed with a free eccentricity of $\simeq 0.18$ then in principle the observed value of $e_b = 0.39$ could have been obtained through excitation of a forced eccentricity equal to 0.21. This value for the free eccentricity, however, is rather large for either of the two most plausible scenarios for the arrival of planet b at its current location. Gas-disc driven orbital migration of a fully formed planet b to its observed location is likely to have left the planet in an essentially circular orbit. Formation *in situ* through a series of giant impacts may have left the planet with a remnant free eccentricity, but a value of $e_b = 0.18$ requires the scattering bodies during the giant impacts phase to be approximately 6 Earth masses (see equation (6.4.4)), which is only slightly smaller than the measured minimum mass of planet b.

6.6 Discussion and Conclusions

I have investigated the dynamical evolution of the three-planet system orbiting the main sequence K-dwarf star HD 181433 [Bouchy et al., 2009]. The system consists of a close-in super-Earth with orbital period 9.37 days, and two sub-Jovian giant planets that orbit at much larger distance from the host star with orbital periods 975 and 2468 days. In order to be dynamically stable these outer giants need to be in a 5:2 mean motion resonance (Chapter 5). The corresponding semi-major axes and eccentricities are $a_b = 0.08$, $a_c = 1.77$ and $a_d = 3.29$ AU. Of particular interest for this study are the large eccentricities displayed by the system: $e_b = 0.39$, $e_c = 0.27$, $e_d = 0.47$. The value for the short-period super-Earth in particular raises interesting questions that I have addressed in this Chapter: given the large separation between the inner super-Earth and outer giants, what are the plausible mechanisms that can lead to excitation of e_b? Given the age of the system (~ 6 Gyr), what are the implications of the observed value of e_b for tidal evolution in the system and the Q-value for the inner body?

We have assumed that the HD 181433 planetary system attained its currently observed configuration shortly after dispersal of the protoplanetary disc. Analysis of the secular dynamics indicates that the eccentricity of the inner body cannot be explained through present day interactions between it and the outer giants. This analysis, however, does point to the existence of a nearby secular resonance that could have caused eccentricity growth during earlier evolution.

The inferred mass of HD 181433b is $m_b \sin i = 7.4$ M$_\oplus$. If $\sin i \sim 1$ then this planet is a super-Earth. We have analysed the tidal evolution and conclude that if the tidal dissipation factor $Q_\mathrm{p} \leq 10^3$ then tidal circularization should be completed easily within the 6.7 Gyr age of the system. This suggests that HD 181433b is not a massive terrestrial-like planet. A value of $Q_\mathrm{p} \geq 10^5$ leads to very little tidal evolution, implying that the system observed now is similar to its primordial state if this Q-value is appropriate. A value of $Q_\mathrm{p} \simeq 10^4$, characteristic of Neptune and Uranus [Murray and Dermott, 1999],

would indicate that the system started out with $a_b \simeq 0.1$ AU and $e_b \simeq 0.6$ such that the system is essentially half-way through the tidal circularization process. This might also indicate that HD 181433*b* should be considered as a hot-Neptune rather than a short-period super-Earth.

Given that all bodies in the system have quite large eccentricities, I began this study by analysing a scenario in which an additional outer giant planet was present originally, leading to global dynamical instability and the ejection of this additional body. This is a natural starting point given the recent work showing that planet-planet scattering can explain the observed eccentricity distribution of the extrasolar planet population [Chatterjee et al., 2008, Jurić and Tremaine, 2008]. The chaotic dynamics involved in such a scenario have precluded us from obtaining a close analogue to the HD 181433 system through N-body simulations, so we have restricted this analysis to addressing the following two issues as a means of estimating the likelihood that the scenario may have operated: can the short-period super-Earth be perturbed on to an eccentric orbit with the required $e_b \geq 0.4$ during the dynamical instability, given that it orbits close to the central star? What is the likelihood of the two outer planets *c* and *d* landing in the 5:2 resonance after scattering? From a suite of 300 N-body simulations we have found that e_b reaches $e_b \simeq 0.4$ in 6% of the runs, and reaches $e_b = 0.6$ in 2% of them, indicating that it is possible to obtain values of e_b that are appropriate for a range of tidal histories. Furthermore, analysis of the width of the 5:2 resonance suggests a probability for landing in resonance of $\sim 10^{-3}$, in good agreement with the more extensive set of N-body simulations of planet-planet scattering reported by Raymond et al. [2008]. A naive estimate of the joint probability of eccentricity excitation for planet *b* and formation of the 5:2 resonance for planets *c* and *d* suggests a value $\sim 6 \times 10^{-5}$, indicating that the hypothetical planet-planet scattering scenario is plausible but only occurs as a rather rare event in planetary system evolution.

Given this conclusion regarding the planet-planet scattering scenario, I also considered the possibility that secular resonance caused excitation of planet *b*'s eccentricity. I examined whether or not an additional undetected planet in the system could have caused planet *b* to be in secular resonance, but this idea was discounted because the forced eccentricity obtained for planet masses below the detectability threshold were too small. During pre-main-sequence evolution most host stars are rapid rotators [e.g. Baxter et al., 2008]. Rotational flattening introduces a J_2 component in the moments of the stellar gravitational potential. Precession caused by this effect can be important in determining the evolutionary fate of short-period planets [e.g. Ward et al., 1976, Nagasawa and Lin, 2005]. The semi-major axis of planet *b* around HD 181433 is $\sim$ 0.08 AU, close to a secular resonance. Using customized N-body simulations that incorporate precession due to GR and stellar oblateness, and the evolution of the stellar spin through magnetic braking, I have tested the hypothesis that the resonance swept past the location of *b*, generating the large eccentricity. We have identified two distinct

modes of evolution: for nominal values of the stellar spin-down parameter planet b is trapped in the resonance temporarily, leading to a maximum growth of eccentricity to $e_b = 0.25$; for the values of the stellar spin-down parameter that are marginally smaller than the nominal value (i.e only 5.75% slower), planet b becomes trapped in the resonance indefinitely with its eccentricity being driven towards unity. The final fate of the system in this latter case appears to be collision with the central star. Neither of these two outcomes leads to a system that looks like HD 181433*b*, but I found that the inclusion of additional short-period low mass planets in the system, orbiting in the vicinity of planet b, can perturb it out of long-term resonant capture when its eccentricity has reached large values. Such a scenario can account successfully for the observed orbital properties of planet b for a range of tidal histories, but in most cases a stellar spin period $\lesssim 20$ hours is required for resonant capture to occur. Given that we have assumed the resonant interaction occurs shortly after protoplanetary disc removal, this scenario requires that HD 181433*a* was a member of the young stellar population that displays rotation periods of less than 2 days. While these stars are in the minority, they are by no means rare [Baxter et al., 2008], suggesting that this scenario provides a plausible explanation for the high eccentricity observed for HD 181433*b*.

CHAPTER 7

On the Detectability of Non-transiting Terrestrial Planets Neighbouring Short-period Giants

7.1 Introduction

In the first place, there was a lot of excitement about the peculiar power of TTVs to discover terrestrial planets which would be outside the grasp of Radial Velocity surveys. In fact, in Chapter 4 and in particular in Section 4.4.1, it was anticipated how it would be possible to detect terrestrial planets located in MMRs with giant planets even if their transits were not observed. This is because of the strong TTV signals with timescales of minutes [Agol et al., 2005, Holman and Murray, 2005, Steffen and Agol, 2007, Veras et al., 2011, Boué et al., 2012].

After several observational efforts and a few interesting hints [e.g. Section 4.4.2, Nascimbeni et al., 2011, Maciejewski et al., 2011], this method indubitably has failed to live up to its promises: the non-transiting Kepler-19c is a gas giant, Kepler-46c is Saturn-size and KOI-142c is $0.7 m_{Jup}$. So far, few companion planets are found in hot Jupiter systems, none in nearby orbits [Wright et al., 2009]. Finding or not terrestrial planets in low-order mean-motion resonances would have implications for theories on evolution and formation of planetary systems. Therefore, because the TTV is most sensitive in these regimes, it should attest itself as a valuable instrument not only for the discovery of additional planets in transiting systems, but also as a tool to identify the prevalent mechanisms of planet formation and the evolution of planetary systems. Reciprocally, by means of numerical simulations it is possible to predict what are the most common configurations of extrasolar system with terrestrial planets and what will be detected by present and future observational programmes.

In particular, [Steffen et al., 2012b] have expressly searched for planetary companions

between the 2:1 interior and exterior mean-motion resonances to hot giant planet candidates identified with *Kepler* during its sixth quarter of science operations [Borucki et al., 2011]. This catalogue contains 997 stars, 1235 planet candidates and measurements have been executed at Short-Cadence level (every 58.85 s) for 137.95 days. They consider stars similar to the Sun and categorise the giant candidates in three samples: 63 hot Jupiters with $2.5R_{Jup} > R_p > 0.6R_{Jup}$ and $0.8d < P_p < 6.3d$ ($a_p \lesssim 0.067$ AU), 222 hot Neptunes $0.126R_{Jup} < R_p < 0.6R_{Jup}$ and $0.8d < P_p < 6.3d$ and 31 warm Jupiters with $2.5R_{Jup} > R_p > 0.6R_{Jup}$ and $15.8d > P_p > 6.3d$. The timing precision of transits is between 0.1 and 15 min with a median of 70 s, this would allow the detection of companions in or near resonant orbits from a few times the Earth to the mass of Mars. They find neither photometric nor TTV evidences for nearby companion planets to hot Jupiters. Their conclusion is that these objects may not exist because such small planets have been ejected through planet-planet scattering (see Section 3.5), otherwise, if these planets exist they must be either very small or not in resonance. On the other hand, roughly one-third of the hot Neptunes sampled have transiting companions and two show significant TTV signals (KOI-244 and KOI-524); specifically, in 38 systems the orbital period ratio is within a factor of 2.3. Furthermore, five of the 31 warm Jupiter systems show evidence of a companion through multiple transiting or TTVs, these would be: Kepler-18, KOI-191, KOI-1241, KOI-190 and KOI-1003. The lack of companions in hot Jupiter systems would favour migration models through planet-planet scattering because eccentricity excitation by planet-planet scattering is mass dependant; the presence of companions to hot Neptunes and hot Earths would suggest that low-mass planets have a different formation history involving disc induced migration.

However, this reasoning does not mention what would be the difference in the formation and evolution history between hot Jupiters and warm Jupiters and what is more important, planets have being categorised according to their radius. Although the transit method gives directly an estimate for the planetary radius, the mass is actually relevant when assessing planetary formation and evolution.

The already introduced Kepler-18d has a mass of only $0.05m_{Jup}$ indeed, for this reason it cannot be defined as a Jupiter-like planet. Regarding KOI-191, KOI-191.01 should have a mass greater than $15m_{Jup}$ and an orbital period of 15.4 days, while KOI-191.02 should have a mass greater than $0.057m_{Jup}$ and a period of 2.4 days. The best fit is unstable and so the pair should reside in a stable resonance, however there is no evidence of TTV nor RV measurements [Ford et al., 2011]. Borucki et al. [2011] flag the signal as probably due to a background variable star. Kepler-56 (KOI-1241) holds a pair of planets in 2:1 MMR: *b* has been confirmed to have an orbital period of 10.5 days and a radius of $0.34R_{Jup}$, while the outer giant has a radius of $0.7R_{Jup}$ and period of 21.4 days [Steffen et al., 2013]. Therefore, Kepler-56b is a Neptune-like body by exact definition of Steffen et al. [2012b]. KOI-190.01 has been rejected thorough RV with *Sophie*: the signal was actually due to a triple system with a low-mass star eclipsing the main component of

a long-period binary. This candidate is therefore a diluted eclipsing binary, likely in a hierarchical triple system [Santerne et al., 2012]. KOI-1003.01 is actually a false positive, a signal due to an eccentric eclipsing binary [Ofir and Dreizler, 2012, NASA Exoplanet Archive[1]]. Therefore, it is demonstrated that in this search companions are excluded for both the so-called hot Jupiters and warm Jupiters (94 cases), while hot Neptune-size candidates exhibit signatures of additional companions via TTVs in three cases (Kepler-18d, KOI-244.02 and KOI-524.01) over a larger sample containing 222 KOIs. It is also worth to point out that Kepler-18c and Kepler-25c [KOI-244.01, Steffen et al., 2012a] are both transiting Neptune-sized planets.

It is believed that the observed architecture of planetary systems might be an outcome of the large-scale orbital migration induced by disc-planet interactions [Nelson et al., 2000]. In this Chapter, I aim to investigate the detectability of non-transiting low-mass planets neighbouring short-period giants looking for differences in the formation and dynamical history among the classes of giant-size bodies. In Section 7.2, I study the effects of orbital and physical parameters of the perturbing planet on the TTV signal produced by a transiting planet. In Section 7.3, I discuss arguments concerning the dynamical evolution and migration of planets embedded in a protoplanetary disc. In Section 7.4, I introduce the model implemented to study the evolution of pairs of planets embedded into a disc. In Section 7.5, I consider a broad range of planetary masses and disc properties and I describe the outcome of the different migration processes. In Section 7.6, I compute the amplitude of TTV signals for all runs considered and I place constraints on which configurations are more probable to produce a detectable TTV signal. In Section 7.7, I discuss findings and indicate future directions for this work.

7.2 The Strength of the TTV Signal

In Section 4.4.1 I have presented an overview of the literature relevant to defining the magnitude of the TTV signal. In this Section I will examine in depth the argument, focusing in particular on the aspects most important to develop the main content of this Chapter.

The effects of eccentricity have already been seen to be strong in Section 4.4.1; however, e is usually damped during evolution in a disc and the planets considered in this Chapter would have generally small eccentricities at time of disc dispersal after migrating through the disc [Tanaka et al., 2002]. The argument of periapse is directly related to the eccentricity, it is possible to find angles for which the variations will be minimum/maximum. Here I present a study showing the effects of mass, semi-major axis and mean anomaly of a perturbing planet on the TTV signal produced by a transiting planet. I consider a Jupiter-mass planet '1' at 0.05 AU on a quasi-circular orbit

[1] http://exoplanetarchive.ipac.caltech.edu

transiting a solar-like star, the perturber '2' is of mass 1, 5, 10, 15, 20, 25, 30 $m_\oplus$ and is located at nearby distances where the period ratio P_2/P_1 spans the range between 1.4 and 3 with step equal to 0.025 (roughly equivalent in this region to a step of 0.001 AU in semi-major axis). The perturber is also in quasi-circular orbit, coplanar and its initial mean anomaly $M_2(0)$ is set to be aligned or anti-aligned with the transiting planet. 910 cases are therefore analysed employing a purpose-built pipeline, computations cover a 10-year timespan using the version of *Mercury6* presented in Section 4.5 (time-step equal to 1000s) and GR effects are included.

Figures 7.1, 7.2, 7.3 and 7.4 show the RMS TTV as function of P_2/P_1 for different m_2. It is deducible that:

1. The bigger the perturbing planet, the bigger the amplitude of the effect; the amplitude of timing variations is an increasing function of the perturbing planet mass.

2. The closer is the second planet, the bigger is the effect. However, resonances tend to increase significantly the effect. The effects of the MMRs 3:2, 5:3 and 7:4 (close to each other at P_2/P_1 equal to 1.66-1.75) and 2:1 are visible. It can be seen that the signal is maximum slightly below resonance at the location of the cusp. This may be understood as follow: the simulations are started with eccentricities very close to zero, after conjunction the eccentricity grows and the outer planet moves outwards, while the inner planet moves inward. This cause the planets to move closer to resonance, causing a longer time between conjunctions, leading to a larger change in eccentricity and semi-major axis. The cusp is the location where the planets reach exact resonance at the turning point of libration, at which point the signal is maximum. To the right of the cusp, the change in eccentricity and semi-major axis is somewhat smaller and hence the amplitude is smaller [Agol et al., 2005].

3. The initial mean anomaly does not change the maximum of the variation as hundred transits are considered during the survey corresponding to several periods of the outer planet. However, differences in the outcome produced by distinct initial conditions are visible near the resonances where the effects are much stronger.

Veras et al. [2011] have performed a high-resolution exploration of the phase space around the 3:1 period commensurability (PC). They found that planets in a PC, and possibly in an MMR, do produce a distinct TTV signature but not necessarily a *high amplitude* signature compared to its near PC surroundings, detecting systems near but not on PC seems more probable. Boué et al. [2012] have calculated analytical approximation of the TTV amplitudes. Inside of MMR, this is a function of the amplitude of libration $\Delta\psi$: the signal is proportional to the amplitude of libration, it is smaller at the exact centre and maximal at the separatrices. The case of a 21.1 $m_\oplus$ planet in the 3:7

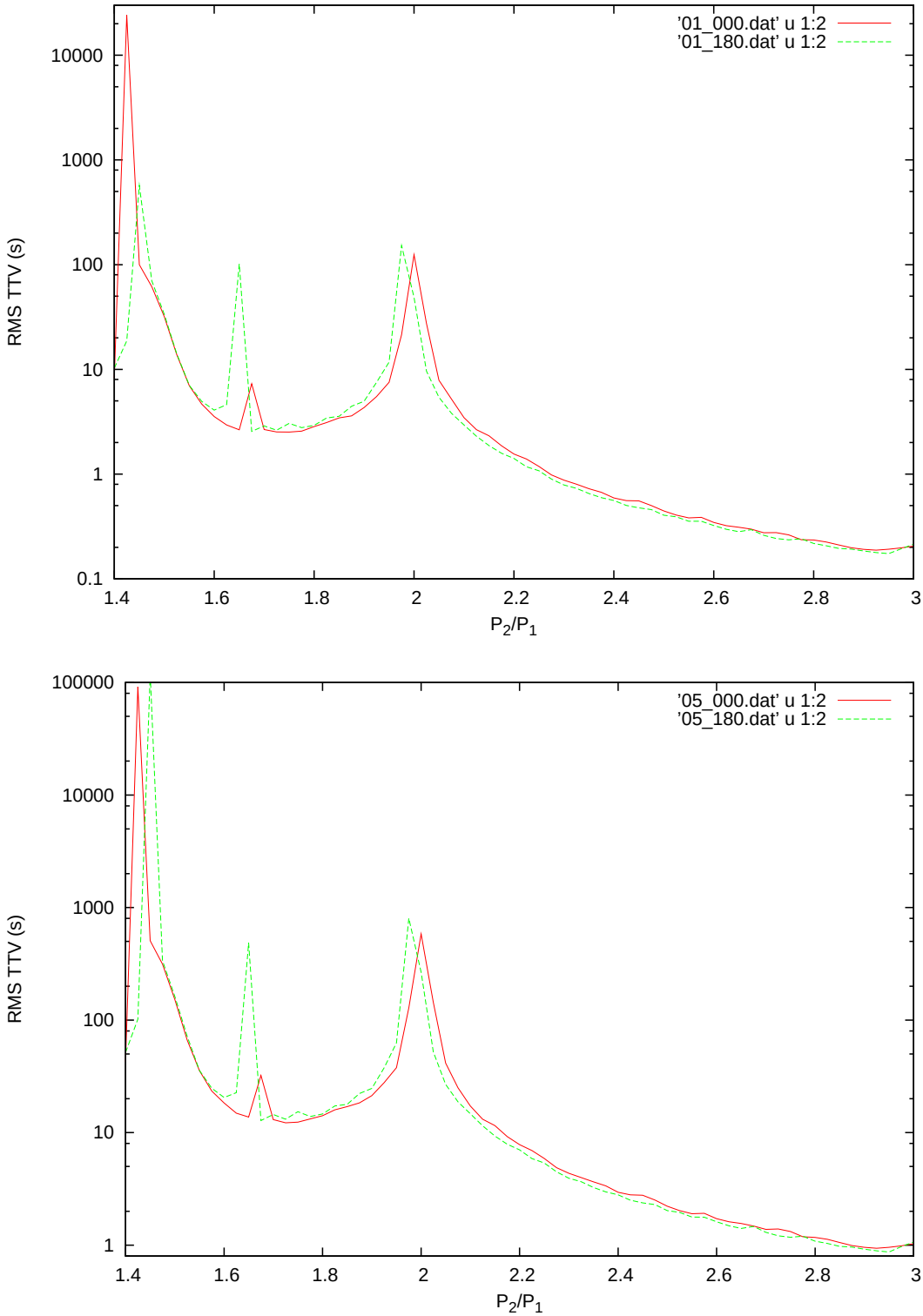

Figure 7.1: The RMS TTV as function of P_2/P_1 for a Jupiter-mass planet at 0.05 AU. The RMS is calculated over a period of 10 years and the perturbing body has a mass of 1 $m_\oplus$ in the top panel and 5 $m_\oplus$ in the bottom. In red $M_2(0) = 0°$ and in green $M_2(0) = 180°$. Note the peaks at the locations of MMR.

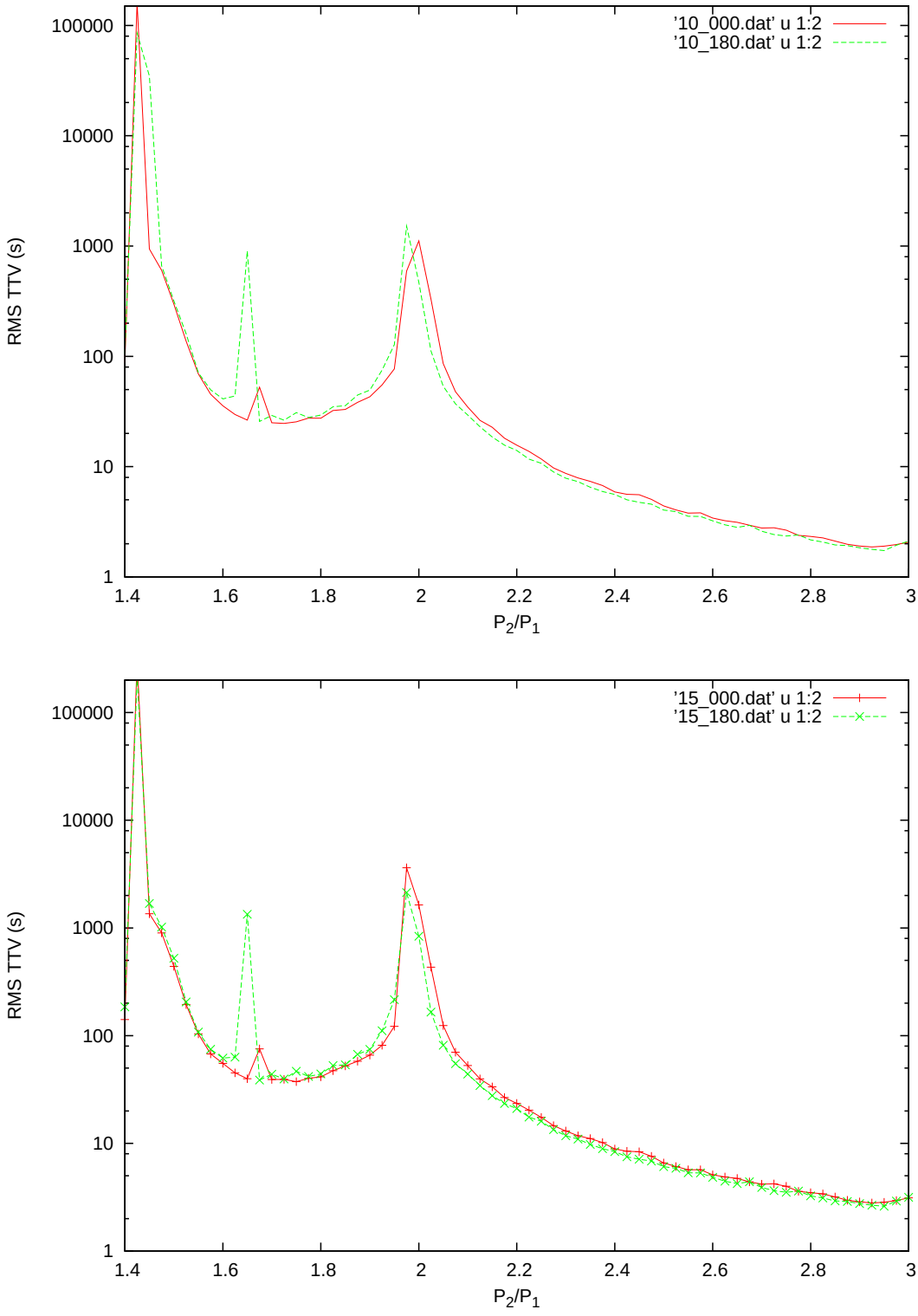

Figure 7.2: The RMS TTV as function of P_2/P_1 for a Jupiter-mass planet at 0.05 AU. The perturbing body has a mass of 10 $m_\oplus$ in the top panel and 15 $m_\oplus$ in the bottom. In red $M_2(0) = 0°$ and in green $M_2(0) = 180°$.

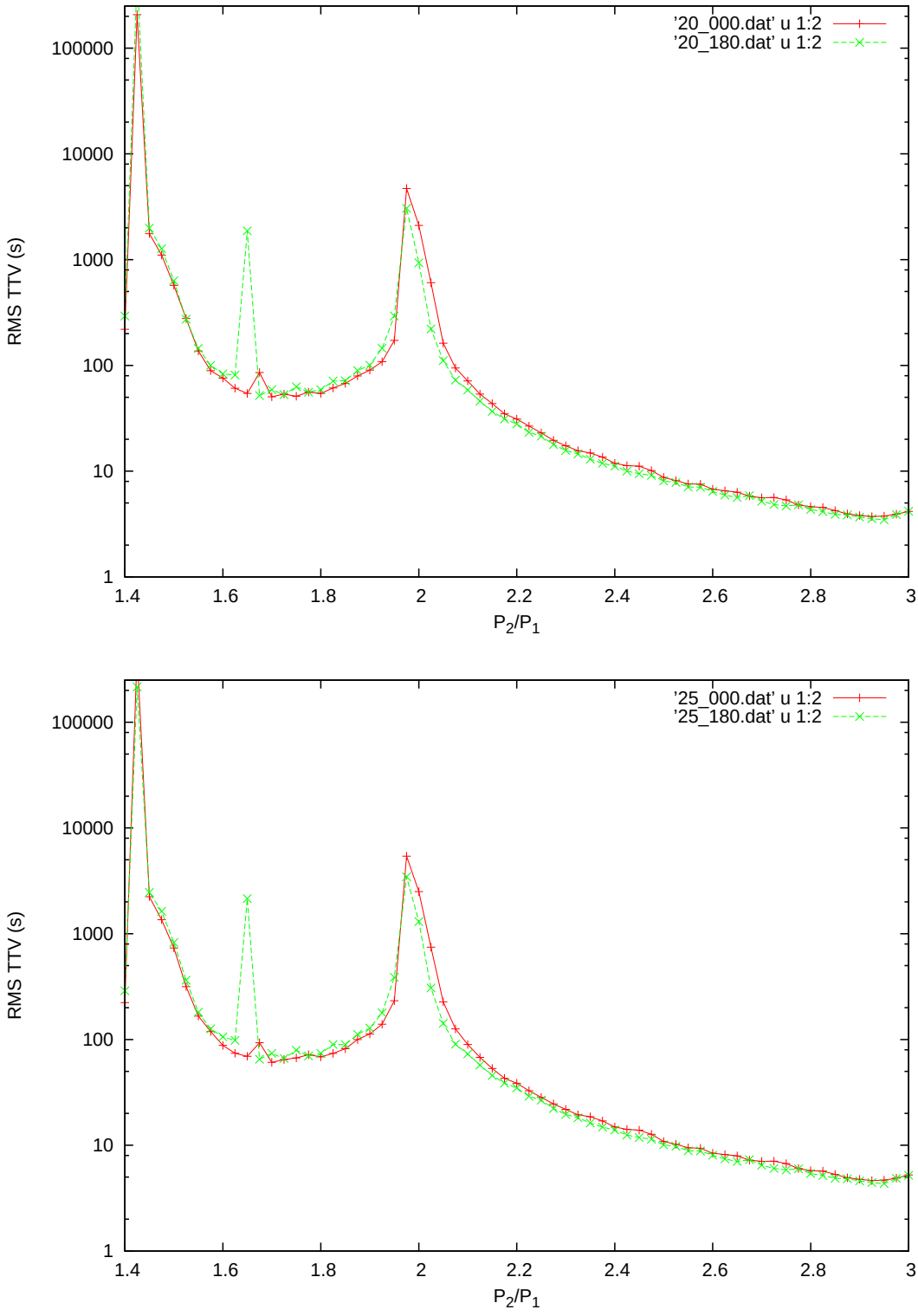

Figure 7.3: The RMS TTV as function of P_2/P_1 for a Jupiter-mass planet at 0.05 AU. The perturbing body has a mass of 20 $m_\oplus$ in the top panel and 25 $m_\oplus$ in the bottom. In red $M_2(0) = 0°$ and in green $M_2(0) = 180°$.

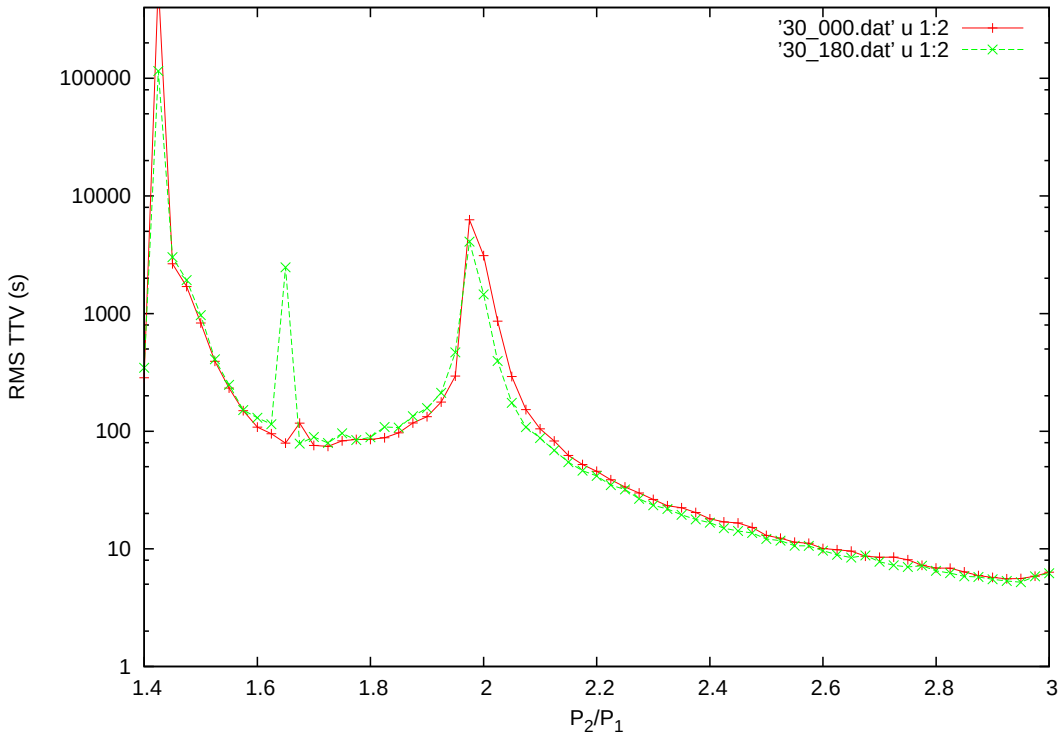

Figure 7.4: The RMS TTV as function of P_2/P_1 for a Jupiter-mass planet at 0.05 AU. The perturbing body has a mass of 30 $m_\oplus$, in red $M_2(0) = 0°$ and in green $M_2(0) = 180°$.

MMR with a Jovian planet transiting a Solar-like star with $P_1 = 3$ d is represented in Figure 7.5.

Table 7.1 shows the cases from my study around the 2:1 MMR for $m_2 = 5m_\oplus$. The resonant angles are $\psi_{ext} = 2\lambda_2 - \lambda_1 - \omega_2$ and $\psi_{int} = 2\lambda_2 - \lambda_1 - \omega_1$. Generally, for the same period ratio, a larger amplitude of the librating angle is seen to correspond to a stronger TTV signal. The signal is stronger for case 178 which is at the separatrix of the resonance caused by ψ_{ext} with a high-amplitude libration. Figure 7.6 presents the TTV curve and librating angle for this case. Figure 7.7 presents case 182 locked into the 2:1 MMR with an RMS TTV of 52 s and the critical angles ψ_{int} and ψ_{ext} both librating. The libration around ψ_{int} is centred on 180° in the inner region of the 2:1 MMR, while it is centred on 0° in the outer region, however weaker signals are produced as in the cases in which ψ_{ext} only is librating.

How does the TTV signal vary with respect to the orbital period of the transiting planet? The strongest signals occur when transiting planets have a long period, this however makes a transit less probable [Agol et al., 2005]. Replications confirm this, for instance, a 20 $m_\oplus$ planet with $P_2/P_1 = 2.3$ from the previous set ($P_1 = 4.08$ d) produces a RMS TTV of 15.7 s. If P_2/P_1 still equals 2.3 but with $a_1 = 0.277$ AU ($P_1 = 53.11$ d) and $a_2 = 0.484$ AU (the other parameters being the same) then $RMSTTV = 192.1$ s, the corresponding TTV curve is shown in Figure 7.8. In both cases, this signal is $\approx 4.3 \cdot 10^{-5}$ of

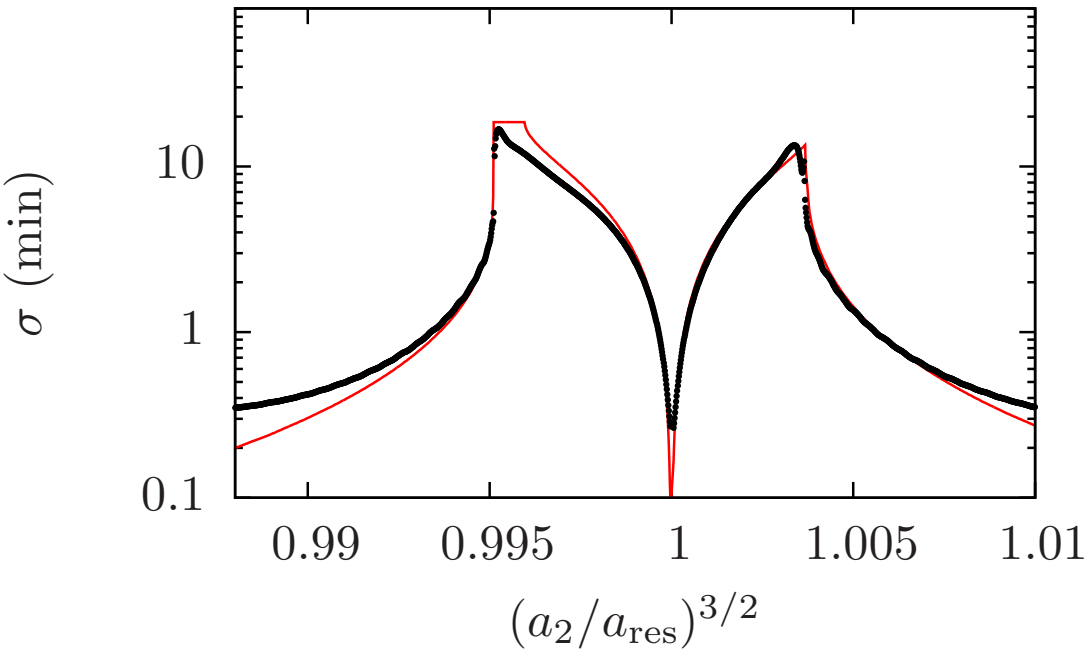

Figure 7.5: The RMS TTV through a 3:7 MMR. The black points correspond to different semi-major axes a_2 of the perturber. The thin solid line corresponds to the analytical approximations, inside of the MMR the signal is larger towards the separatrices [Boué et al., 2012].

Table 7.1: The resonant angles ψ_{ext} and ψ_{int} for cases corresponding to different P_2/P_1 and producing the given RMS TTV over 10 years with $m_2 = 5m_\oplus$.

case	P_2/P_1	**RMS TTV (s)**	ψ_{ext}	ψ_{int}
173	1.925	27	circulation	$180° \pm 175°$
174	1.925	37	circulation	$180° \pm 175°$
175	1.95	37	circulation	$180° \pm 150°$
176	1.95	62	circulation	$180° \pm 165°$
177	1.975	128	circulation	$180° \pm 120°$
178	1.975	802	$180° \pm 135°$	circulation
179	2	582	$180° \pm 120°$	circulation
180	2	266	$180° \pm 90°$	circulation
181	2.025	143	$180° \pm 90°$	circulation
182	2.025	52	$180° \pm 90°$	$0° \pm 60°$
183	2.05	41	$180° \pm 120°$	$0° \pm 60°$
184	2.05	26	$180° \pm 120°$	$0° \pm 50°$
185	2.075	25	$180° \pm 120°$	$0° \pm 53°$
186	2.075	18	$180° \pm 120°$	$0° \pm 40°$
187	2.1	17	$180° \pm 100°$	$0° \pm 45°$
188	2.1	14	$180° \pm 120°$	$0° \pm 35°$
189	2.125	13	$180° \pm 100°$	$0° \pm 35°$
190	2.125	11	$180° \pm 100°$	$0° \pm 25°$

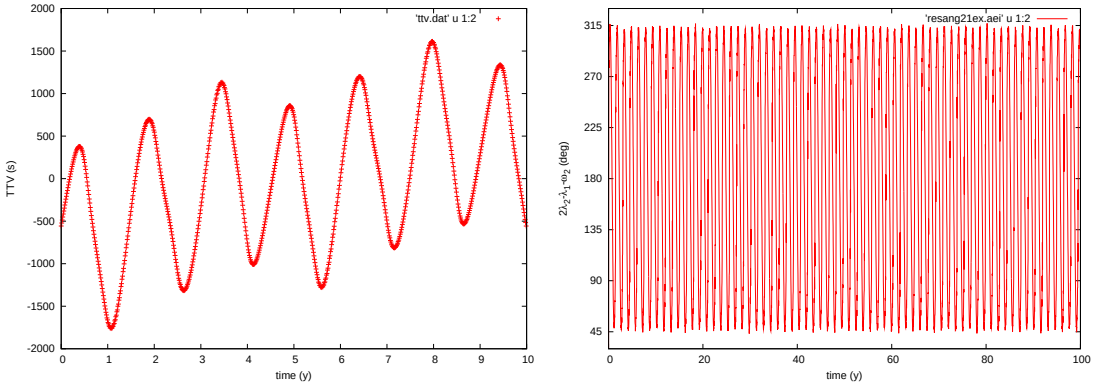

Figure 7.6: Case 178 in 2:1 MMR, $m_2 = 5m_\oplus$. Left: TTV for a period of 10 years. The RMS TTV equals 802 s. Right: The resonant angle ψ_{ext} evolving over 100 years, it librates around 180° with a semi-amplitude of about 135°.

the respective P_1 meaning that the TTV is a fixed fraction of the orbital period; a longer orbital period leads to a larger TTV, in fact as the distance from the star increases by the same fraction as the increase in the mean interplanetary separation, then the fractional change in the orbital period (TTV) produced by the perturbations is more or less fixed.

7.3 Evolution in a Protoplanetary disc

As anticipated in Section 1.3.2, hot giants should have formed in the outer region of a protoplanetary disc where more material is available to form cores within the lifetime of an accretion disc. Dynamical perturbations could have generated large eccentricities in the orbits of giants sufficiently to induce a tidal interaction with the star and the subsequent settling into their close orbits [Rasio and Ford, 1996, Fabrycky and Tremaine, 2007], therefore interior planets would have been scattered during the gas giant's dynamical evolution explaining the lack of discoveries from TTV studies and photometric transit searches. Otherwise, giants could have migrated inward on 10^5-year time scales because of the imbalance of torques generated by the gaseous protoplanetary disc [Goldreich and Tremaine, 1980, Lin and Papaloizou, 1986], stopping close to the host star either by Roche lobe overflow [Trilling et al., 1998], by the planet raising tides on the star which then injects energy into the planetary orbit preventing its further decay [Lin et al., 1996], or by a magnetospheric cavity clearing the disc material, or by disc dispersal through photoevaporation. Hence, low-mass bodies embedded into the disc on orbits exterior to a moving giant would have migrated inward and may have been captured into MMR [Lee and Peale, 2002, Mandell and Sigurdsson, 2003, Narayan et al., 2005]. Small companions near MMRs would induce orbital perturbations which would be detectable as TTV signals. Even in this scenario, survival of the resonance can be compromised by overly rapid migration [Quillen, 2006] and/or by turbulent forcing from the disc driving the migration [Ketchum et al., 2011].

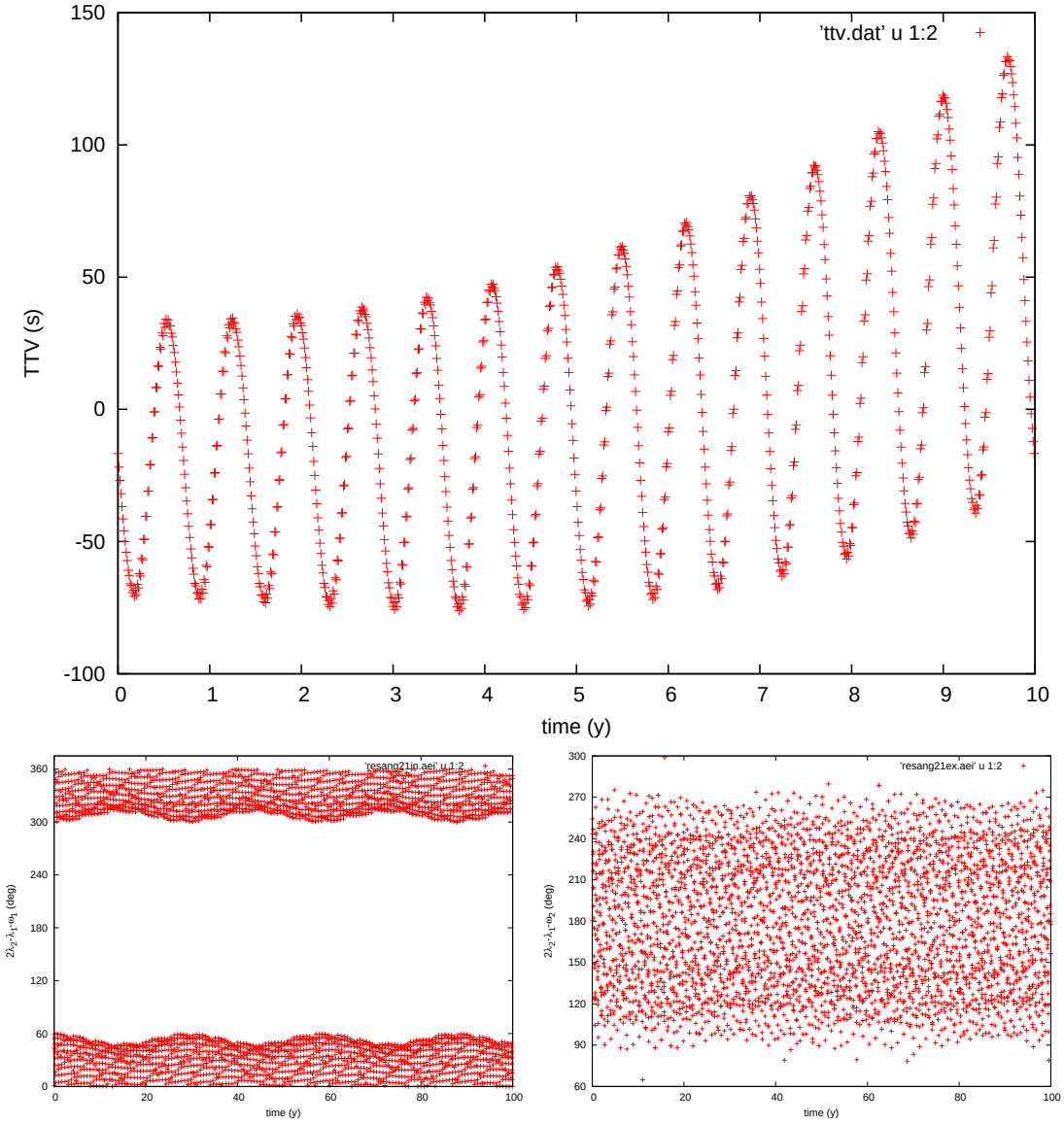

Figure 7.7: Case 182 in 2:1 MMR, $m_2 = 5m_\oplus$. Top: TTV for a period of 10 years. The RMS TTV equals 52 s. The signal seems to be amplified by the end of the observations possibly due to the contributions of the two resonant angles which have different time scales. Bottom-Left: The resonant angle ψ_{int} evolving over 100 years, it librates around 0° with a semi-amplitude of about 60°. Bottom-Right: The resonant angle ψ_{ext} librates around 180° with a semi-amplitude of about 90°. Some outliers are present due to the small eccentricities which cause problems in the definition of the angle ω.

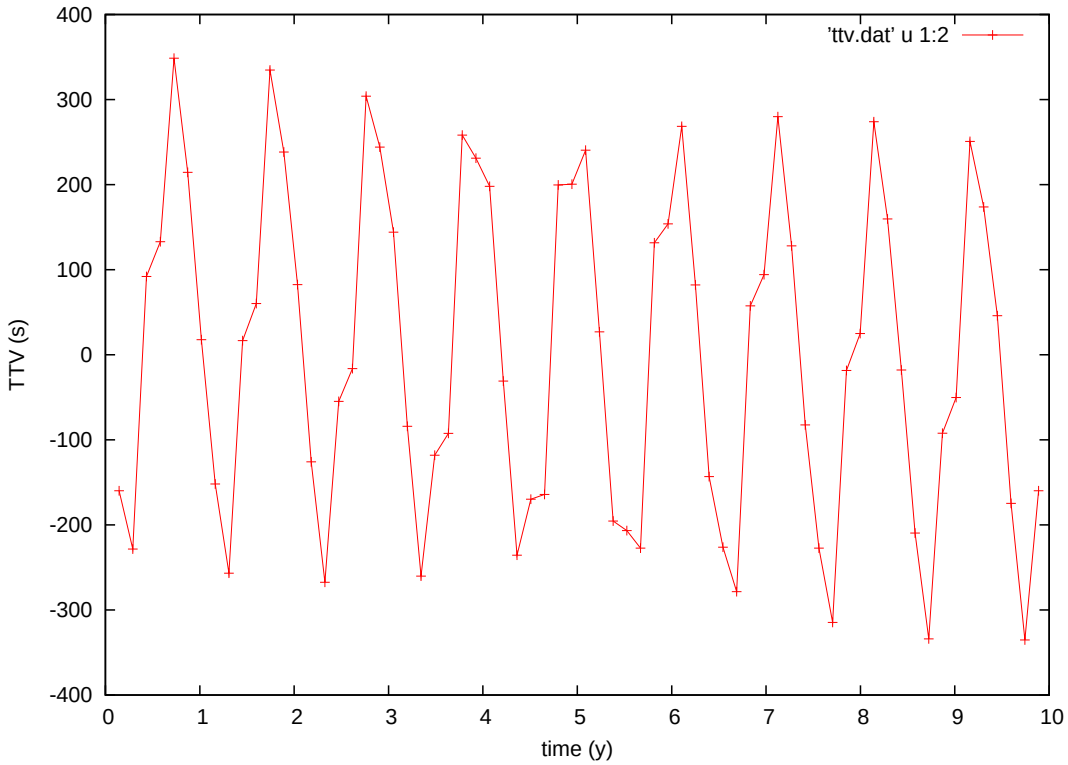

Figure 7.8: TTV curve for a period of 10 years for a Jupiter-mass planet at $a_1 = 0.277$ AU perturbed by a 20 $m_\oplus$ planet at $a_2 = 0.484$ AU. The RMS TTV equals 192.1 s.

In the previous Section I have introduced the dependence of the TTV signal from different parameters showing the strength of this observable according to distinct scenarios. In this Section I will focus on the latter model which was aimed to explain the origin of the hot giant population, I will briefly present the arguments necessary to study the dynamical evolution of two planets embedded into a protoplanetary disc (a more general argumentation of the dynamics of protoplanetary discs can be found in Armitage [2011]).

7.3.1 Planetary Migration

Planets evolving in a geometrically thin disc will perturb adjacent material: faster moving material interior to the planetary orbit loses angular momentum while exterior slower moving particles gain angular momentum. Conservation of angular momentum means that torques are exerted on the planet. If the torques are not symmetrical they can cause the planet's orbital radius to drift. Differential torques are induced by the Lindblad resonances [Ward, 1997] and by contribution from the corotation torque [Tanaka et al., 2002].

1. The planet interacting with the interior Lindblad resonances $(r_L < r_p)$ **gains angular momentum** from the gas disc. This tends to move the planet outward,

while the gas loses angular momentum and is driven inward.

2. The planet interacting with the gas disc at exterior Lindblad resonances ($r_L > r_p$) **loses angular momentum**. This tends to move the planet toward the star, while the gas gains angular momentum and is driven outward.

The gravitational interaction of a planet with a gas disc tends to repel gas from the vicinity of the planet's orbit. Migration can occur in three distinct ways which are now described.

Type I migration For low mass planets, low amplitude density waves are launched into the disc at interior and exterior Lindblad resonances, compensating disc torques are exerted on the planet. The outer resonances are slightly closer to the planet because of pressure support in the disc, therefore the outer disc torques are more powerful: the planet loses angular momentum and spirals inward through the disc [Ward, 1997].

Type II migration High mass planets exert gravitational torques on the neighbouring gas which exceed the intrinsic viscous torques of the gas. This repels gas from the vicinity of the giant planet's orbit, forming a gap in the disc. Hence, the planet migrates with the gas rather than migrating relative to it [Goldreich and Tremaine, 1980, Lin and Papaloizou, 1986, Ward, 1997]. The conditions for a gap to form have been discussed by [Nelson et al., 2000]. These are $R_H > H$ and

$$\frac{m_p}{M_*} > \frac{40}{Re}; \tag{7.3.1}$$

where H is the disc vertical semi-thickness and $Re = \frac{r^2\Omega}{\alpha H^2 \Omega} = \frac{1}{\alpha}\left(\frac{r}{H}\right)^2$ is the Reynolds number (the "alpha" model is discussed in Section 7.4.1). For expected disc viscosities the migration time scale is of the order of 0.5 Myr, an order of magnitude less than a disc lifetime. The planet's orbit will shrink provided that the local disc mass exceeds the planet mass, otherwise migration will be significantly opposed, a scenario that is expected late in the disc's lifetime. Therefore, hot-Jupiters may have formed originally in the outer regions of protoplanetary discs reaching their present locations via type II migration. On the other hand, gaseous giants of the Solar system should have formed later during the disc lifetime, this could have prevented substantial migration.

Type III migration Type III migration may effect planets with masses equal to and above that of Saturn when a partial gap in the disc is opened which creates a local mass deficit roughly equal to the mass of the planet [Masset and Papaloizou, 2003, Lin and Papaloizou, 2010]. In these cases, particles flowing past the planet and making one pass between the interior and exterior disc, would generate an inward co-rotation torque

which can drive a fast migration: the semi-major axis of the planet can be reduced by a large factor in less than 100 orbits. Such "runaway migration" episodes should run out of steam close to the central star and would allow these planets being to attain shorter periods. Potentially, some of the lighter hot giants might be better interpreted by type III migration rather than type II, as their masses may have been too small to have created sufficiently wide gaps in their discs.

Migration halting mechanisms Some mechanism are necessary in order to stop migration of hot giants at their present orbital distances. Migration-halting mechanisms that might be in function when the planet approaches the region close to the central star include: intrusion by the planet into a central cavity in the disc which decouples it from the evolution of the gas [Lin et al., 1996, Papaloizou, 2007] and tidal recession forces due to the star's rotation or Roche lobe overflow and mass loss to the star [Trilling et al., 1998]. Stopping the migration beyond 0.1 AU would require that giant planets form late in the lifetime of the gas disc and so have time only for a partial inward migration before being halted at an intermediate radius when the gas has been completely dissipated [Trilling et al., 1998]. Also fortuitous disc dispersal might explain the presence of the hot-Jupiter population implying that earlier formed giant planets could have fallen into the central star. These halting mechanisms are supported by models which can roughly replicate the exoplanet semi-major axis statistics [e.g. Armitage, 2007].

7.3.2 Do we expect to find terrestrial planets close to gas giants?

Here I discuss some theoretical findings concerning the evolution of terrestrial planets evolving with giants in a gaseous disc. Raymond et al. [2006] have focused on the possible formation of Earth-like planets in the habitable zone which are more difficult to detect. They have simulated terrestrial planet growth and dynamical evolution during and after giant planet migration in a disc. 80 "planetary embryos" which sum up to 17 Earth masses and 1200 "planetesimals" are studied during the migration of a Jupiter planet from 5 AU to 0.25 AU. Earth-mass planets often form in the habitable zone and with low orbital eccentricities and, in general, a large fraction of the sampled systems with a close-in giant are found to harbour hot Earth or Earth-like planets. Also Fogg and Nelson [2007] have predicted that terrestrial planets can grow and be retained in hot-Jupiter systems, both interior and exterior to the gas giant.

Pierens and Nelson [2008] have investigated the evolution of two-planet systems embedded in a protoplanetary disc in order to examine how the long-term evolution of such a system depends on the mass of the outer body. The inner body is a Jupiter-mass planet, the particular disc model considered produces three different evolution pathways according to the mass of the exterior body. The type II migration rate of the giant exceeds the type I migration rate of the outer body when this has a mass $\lesssim 3.5 m_{\oplus}$, so

these configurations experience divergent migration. Exterior planets with masses in the range $3.5m_{\oplus} < m_2 < 20m_{\oplus}$ are trapped at the edge of the gap created by the Jupiter-mass planet. For higher masses the two planets are captured in the 2:1 or 3:2 MMRs. These results suggested that there is a lower limit to the mass of an outer planet that can be captured into resonance with an interior giant planet, this would have implications with what would be observable using the TTV method.

The relative migration rate of the planets varies according to their masses and to the parameters specifying the properties of the disc. Podlewska and Szuszkiewicz [2009] have extended the investigation considering sub-Jupiter mass planets as inner body and different disc parameters. They confirm that Super-Earths are caught in trap at the edge of the gap opened by a Jupiter-mass planet. This mechanism is possible because of the steep and positive surface density gradient in the radial profile of the disc at the location where the corotation torque compensates the differential Lindblad torque [Masset et al., 2006]. It is possible that the migration of the two planets is convergent until the Super-Earth is trapped, then the migration reverses and the outer body moves together with the expanding edge of the gap. Despite not having any MMRs, once the Super-Earth is captured in the trap libration of secular angles are observed. Finally, a $0.5M_{Jup}$ planet is seen to open a narrower gap. For very thin discs and slow migration a Super-Earth is trapped into the 2:1 MMR even if for a short-lasting period only. Here the capture is due to the Super-Earth opening a shallow dip which moves along with the migrating planet, once the dip reaches the outer edge of the gap a trap is created.

7.4 The Hydrodynamical Model

In this Section I will introduced the model implemented to study the evolution of two-planet systems embedded in a protoplanetary disc.

I consider a gas giant orbiting a solar-type star plus a low-mass planet further out in the disc. The aim is to examine how the long-term evolution of such a system depends on the masses of the planets and the disc properties. As anticipated above, a gaseous planet forms beyond the ice line, it can clear the local gaseous material efficiently and open a gap. Due to its interaction with the protoplanetary disc, it experiences type II migration and can reach the very inner region of their system. An outer low-mass planet undergoes type I migration which can eventually be halted at the outer edge of the gap opened by the gas giant. Therefore, the planets cannot get closer and this does not allow the possibility to attain a mean motion resonance. However, if the gap opened is narrower, there will be a chance for attaining the locking into 2:1 resonance. The innovations introduced in this work are:

1. the migration of the inner planet is halted once a location typical for hot giants is reached,

2. a wide selection of disc settings and planetary masses are considered.

These aspects will give the chance to study the final outcome of the process even for those cases for which migration was seen to be divergent and it will help to estimate in which types of discs a sufficiently narrower gap is formed.

7.4.1 Numerical method and initial conditions

We have used a modified version of the Eulerian hydrodynamic code *NIRVANA* [Ziegler, 1998] to solve the hydrodynamic equations for a 2D protoplanetary disc under a gravitational potential, Φ. These are the continuity equation and the momentum equation:

$$\begin{aligned} \partial_t \Sigma + \partial_i(\Sigma v_i) &= 0, \\ \partial_t(\Sigma v_i) + \partial_k(\Sigma v_i v_k) &= -Pr\delta_{ik} - \Sigma\partial_i\Phi, \end{aligned} \tag{7.4.1}$$

where $\vec{v}$ is velocity, Pr is pressure, Σ is density, Φ is the combined gravitational potential of the central star and the planets, i, k are summation indices, ∂_k indicates a partial derivative with respect to k and δ_{ik} is the Kronecker delta. The potential is softened with gravitational softening parameter $\epsilon = 0.6$. More details of the numerical scheme can be found in Nelson et al. [2000].

The computational units adopted are such that the mass of the central star $M_* = 1$ corresponds to one Solar mass, the gravitational constant is $G = 1$ and the radius $r = 1$ in the computational domain corresponds to 1 AU. Recalling that $P = 2\pi\sqrt{\frac{r^3}{GM_*}}$, time is measured so that at $r = 1$ the orbital period is 2π equivalent to 1 year. Therefore in the following, the unit of time (called *orbit* in this Chapter) is $\frac{1}{2\pi}$ times the orbital period of a planet at 1 AU.

The disc is divided into 256 x 380 computational grid cells in the radial and azimuthal directions, respectively. Cylindrical coordinates (R, ϕ) are adopted with the origin located at the position of the central star. The computational domain extends between $r_{in} = 0.025$ AU and $r_{out} = 0.5$ AU in the radial direction, the azimuthal angle ϕ takes values in the interval $[0, 2\pi]$. In order to avoid any wave reflection at the edges of the computational domain, a wave killing zone is employed in the vicinity of the boundaries at 0.045 AU and 0.4 AU. The planets' orbits are evolved using a fifth-order Runge-Kutta scheme.

The disc semi-thickness H (see Figure 7.9) is small in comparison with the distance r from the central star. In the disc model employed in the runs presented here the disc aspect ratio H/R will be set equal to 0.05, 0.03 and 0.02. This remains constant, so that the temperature profile of the disc is $T \propto r^{-1}$. Also adopted is the locally isothermal equation of state of the gas $Pr(R, \phi) = c_s^2(R)\Sigma(R, \phi)$. c_s is the isothermal sound speed

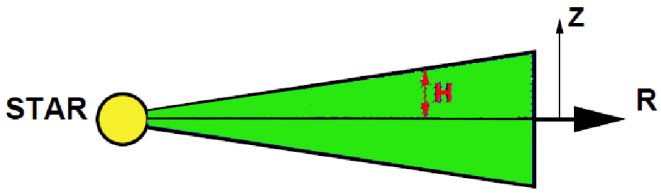

Figure 7.9: Sketch of a protoplanetary disc. The R and z axes are depicted, as well as the semi-thickness H. z represents the third dimension of the disc.

and the initial surface density profile of the disc is chosen to be $\Sigma(R) = \Sigma_0 r^{-1/2}$, Σ_0 can be varied during the runs for computational convenience (see below). The initial disc mass within the computational domain is derivable to be $M_d = \int_{r_{in}}^{r_{out}} \Sigma \cdot 2\pi r dr$. Turbulence in the disc creates an anomalous viscous stress, we have used the standard "alpha" model of disc kinematic viscosity $\nu = \alpha c_s H$ [Shakura and Sunyaev, 1973], where α is set to 10^{-3}.

The inner and outermost planets initially evolve on circular orbits at 0.1 and 0.2 AU, respectively. The mass of the inner planet is considered to be $m_1 = 0.2$, 0.5 and $1 m_{Jup}$, while the outermost bodies studied have masses $m_2 = 3$, 5, 10 and $20 m_\oplus$. After Pierens and Nelson [2008], in order to give the inner planet sufficient time to open a gap, its initial mass is set to $30 m_\oplus$. This body is allowed to accrete gas from the disc on a dynamical time scale until its mass reaches its final value m_1. This method is reasonably consistent with evolutionary models of gas giant planets forming in protoplanetary discs which affirm that rapid gas accretion happens once the body mass is above $30 - 40 m_\oplus$ [Papaloizou and Nelson, 2005]. Once the final mass has been reached, both planets are allowed to interact gravitationally and can migrate under the action of disc torques. The interactions between the inner planet and the disc are stopped once it reaches 0.065 AU, this simulates an unspecified halting migration mechanism (see Section 7.3.1). Then, the computation can continue till the outer planet stops at the physical barrier at the edge of the gap opened by the inner giant, or till it arrives at the location of the 2:1 resonance. After reaching the final stage of the process, the disc is finally depleted.

Placing an already formed giant would corrupt the natural characteristics of the disc, while allowing mass accretion on the protoplanet recreates fairly the process of gap formation typical for high mass planets. Actually, the planet should have formed in the outer region and then migrate to 0.1 AU, however with the present computational power it would be impractical to model such a long process. In fact, the final outcome of this mechanism is not altered if the giant planet is allowed to complete its gap formation. Feeding mass at 0.1 AU would be unrealistic as the mass there present is insufficient. Here the expedient is to set a large disc mass and still it is especially difficult to obtain a $1 m_{Jup}$ planet with aspect ratio $H/R = 0.03$ and 0.02, and a $0.5 m_{Jup}$ with aspect ratio $H/R = 0.02$. The disc mass can be modified gradually during the

runs so that migration is speeded up to complete the process within a reasonable time computational time. Then, it is slowed down once the process has reached its final outcome, i.e. when the outer planet has been caught at the edge of the cavity or when the 2:1 resonance has been created. In fact, the planetary migration rate is proportional to the disk surface density [Goldreich and Tremaine, 1980, Edgar, 2007], however the final outcome of the process depends on the shape of the gap and its surface density profile rather than on the migration speed. Besides, depending on the shape of the gap formed by the giant, the ability of the outer planet to penetrate through the gap of the giant is also influenced by its ability to open a small gap and not on the disc mass; its migration will be stopped at the point where the overall torque is null, i.e. the final result is due to the balance of the torques and not to the relative quantities contributing to the total torque.

7.5 Results

In the description of the results I will focus on the final state of the pairs of planets, rather than on their migration stories. The capacity cluster Apocrita[2] is used to run the simulations. They last from weeks to months using a node of 12 cores with 24GB of RAM each. The migration process is generally slower in thinner discs. The outcome of the studied 36 cases which include different planetary masses and disc parameters is summarised in Table 7.2. As in the final stage the two planets may experience a small variation in their semi-major axis, in the table are reported their average final positions r_{f1}, r_{f2} and period ratio $p = (r_{f1}/r_{f2})^{1.5}$. The cases in period commensurability (PC) are seen to be in MMR. In fact, for all these configurations the resonant angle $\psi_{ext} = 2\lambda_2 - \lambda_1 - \omega_2$ is seen to librate around 0° with a rather small amplitude, while $\psi_{int} = 2\lambda_2 - \lambda_1 - \omega_1$ circulates. For cases in PC, e_2 has moderately grown because of the effects of MMR, Model 14 near-PC has $e_2 = 0.02$; all other cases outside of PC with $p \leq 2.5$ have been checked and it was found $e_2 \leq 0.01$. Low mass planets of Models 23, 31, 35 have been able to reach the location of the 2:1 MMR. Trapping into the 2:1 MMR is seen to be more probable for pairs with a smaller giant and for cases which have evolved into thinner discs.

Usually migration of the outer planet is halted when the Lindblad torque, which in this context tends to push the planet inward, is counterbalanced by the corotation torque produced by a steep and positive surface density gradient in the radial profile of the disc. However, a new mode to stop planetary migration is suggested by some runs with terrestrial low mass planets in thin discs. In fact, the super-Earth in Models 7, 11, 12, 19, 24, 36 is able to create a shallow gap in a thin disc, but the presence of a disc of material trapped between the two planets does not allow it to approach the inner

[2] `https://www.hpc.qmul.ac.uk`

giant. Here the outer Lindblad torque is seen to be balanced by the inner Lindblad torque caused by the trapped material which is denser than the constituents located exterior to the outer planet.

7.5.1 The Evolution with the Jupiter-like Planet

The evolution in a disc with aspect ratio $H/R = 0.05$ of a system consisting of a Jupiter mass planet and a low-mass planet with a mass in the range of $3.5 - 20 m_\oplus$ was predicted to end up with the trapping of the low-mass planet near the outer edge of the gap produced by Jupiter mass planet by Pierens and Nelson [2008]. Podlewska and Szuszkiewicz [2009] confirmed this and found the same outcome in a disc with aspect ratio $H/R = 0.03$ and $m_2 = 5.5 m_\oplus$.

These results are here confirmed as for $m_1 = 1 m_{Jup}$ and $H/R = 0.05$, the outer companion cannot reach the location of the 2:1 MMR for all the m_2 considered. While for $H/R = 0.03$ and $H/R = 0.02$: with $m_2 = 20$ and $10 m_\oplus$ the outer planet is seen to reach PC, while this does not happen for $m_2 = 5$ and $3 m_\oplus$. In particular, with $H/R = 0.02$ the Super-Earths are stopped further out. The migration of the Jupiter-size planet in models 9 and 10 has been difficult to achieve in such a thin disc and it has required the implementation of a particularly heavy disc. Respectively, 18,000 and 28,000 "orbits" have been required, this is much more than the time required by all the other cases.

In Figure 7.10, the evolution for Model 3 ($H/R = 0.05$ and $5 m_\oplus$) is shown. The top plot presents the migration of the two planets. Changing the disc mass corresponds to a change in migration rate. The central plot shows the period ratio, migration is divergent and only when the inner planet has reached is final destination then the low-mass object is able to catch up to its final location. This is also represented in the surface density profile in the bottom panel: the outermost planet reaches the edge of the gap opened by the inner giant. The planet is unable to approach any closer to the giant, but instead remains trapped near the gap edge where its corotation and Lindblad torques counterbalance. The eccentricities achieved during this process are seen to be very small, no more than 0.01.

In Model 5, with aspect ratio $H/R = 0.03$, a 20 Earth-mass planet is now able to form a gap in the disc, so that it is able to penetrate through the gap formed by the giant planet and reach the PC. This is shown in the surface density profile in the top panel of Figure 7.11. Having achieved this final outcome, the disc mass is set to zero to simulate the disc depletion and the orbital elements are calculated for 10 years. The central panel shows the resonant angle ψ_{ext} librating around 0° with a semi-amplitude of about 19°. At 0.065 AU, the orbital period is 6.1 d and the outer body in 2:1 MMR is located at 0.103 AU. Because of the resonance, the outer planet achieves an eccentricity of 0.07 (bottom panel).

Table 7.2: The outcome of the migration process for a pair of planets. All the performed simulations with different planetary masses and disc parameters are here summarised. The first column shows the model number, the second the mass of the gas giant, the third the disc aspect ratio, the fourth the mass of the low-mass planet, the fifth the average final radial distance from the star of the gaseous planet, the sixth the average final radial distance from the star of the low-mass object, the seventh the average final period ratio p, the eighth the librating resonant angle ψ_{ext} for cases in-PC, the ninth the maximum value of e_2 for cases in-PC.

Model	$m_1(m_{Jup})$	H/R	$m_2(m_\oplus)$	r_{f1} (AU)	r_{f2} (AU)	p	ψ_{ext}	e_2
1	1	0.05	20	0.065	0.107	2.11		
2	1	0.05	10	0.065	0.108	2.15		
3	1	0.05	5	0.065	0.108	2.15		
4	1	0.05	3	0.065	0.111	2.23		
5	1	0.03	20	0.065	0.103	2.00	$0^\circ \pm 19^\circ$	0.07
6	1	0.03	10	0.065	0.103	2.00	$0^\circ \pm 10^\circ$	0.05
7	1	0.03	5	0.065	0.109	2.15		
8	1	0.03	3	0.065	0.109	2.16		
9	1	0.02	20	0.065	0.103	2.00	$0^\circ \pm 45^\circ$	0.10
10	1	0.02	10	0.065	0.103	2.00	$0^\circ \pm 110^\circ$	0.12
11	1	0.02	5	0.065	0.117	2.38		
12	1	0.02	3	0.065	0.122	2.56		
13	0.5	0.05	20	0.065	0.103	2.00	$0^\circ \pm 4^\circ$	0.02
14	0.5	0.05	10	0.065	0.106	2.04	$0^\circ \pm 8^\circ$	0.02
15	0.5	0.05	5	0.065	0.103	2.00	$0^\circ \pm 7^\circ$	0.02
16	0.5	0.05	3	0.065	0.103	2.00	$0^\circ \pm 4^\circ$	0.03
17	0.5	0.03	20	0.065	0.103	2.00	$0^\circ \pm 34^\circ$	0.07
18	0.5	0.03	10	0.061	0.098	2.00	$0^\circ \pm 7^\circ$	0.05
19	0.5	0.03	5	0.065	0.106	2.09		
20	0.5	0.03	3	0.065	0.106	2.10		
21	0.5	0.02	20	0.064	0.102	2.00	$0^\circ \pm 43^\circ$	0.08
22	0.5	0.02	10	0.065	0.103	2.00	$0^\circ \pm 75^\circ$	0.08
23	0.5	0.02	5	0.065	0.103	2.00	$0^\circ \pm 39^\circ$	0.06
24	0.5	0.02	3	0.065	0.113	2.32		
25	0.2	0.05	20	0.062	0.099	2.00	$0^\circ \pm 4^\circ$	0.04
26	0.2	0.05	10	0.063	0.102	2.00	$0^\circ \pm 9^\circ$	0.03
27	0.2	0.05	5	0.065	0.103	2.00	$0^\circ \pm 14^\circ$	0.04
28	0.2	0.05	3	0.065	0.103	2.00	$0^\circ \pm 23^\circ$	0.05
29	0.2	0.03	20	0.063	0.100	2.00	$0^\circ \pm 51^\circ$	0.07
30	0.2	0.03	10	0.064	0.100	2.00	$0^\circ \pm 12^\circ$	0.04
31	0.2	0.03	5	0.065	0.103	2.00	$0^\circ \pm 15^\circ$	0.04
32	0.2	0.03	3	0.065	0.103	2.00	$0^\circ \pm 60^\circ$	0.03
33	0.2	0.02	20	0.065	0.201	5.44		
34	0.2	0.02	10	0.064	0.099	2.00	$0^\circ \pm 15^\circ$	0.05
35	0.2	0.02	5	0.065	0.103	2.00	$0^\circ \pm 18^\circ$	0.03
36	0.2	0.02	3	0.065	0.125	2.67		

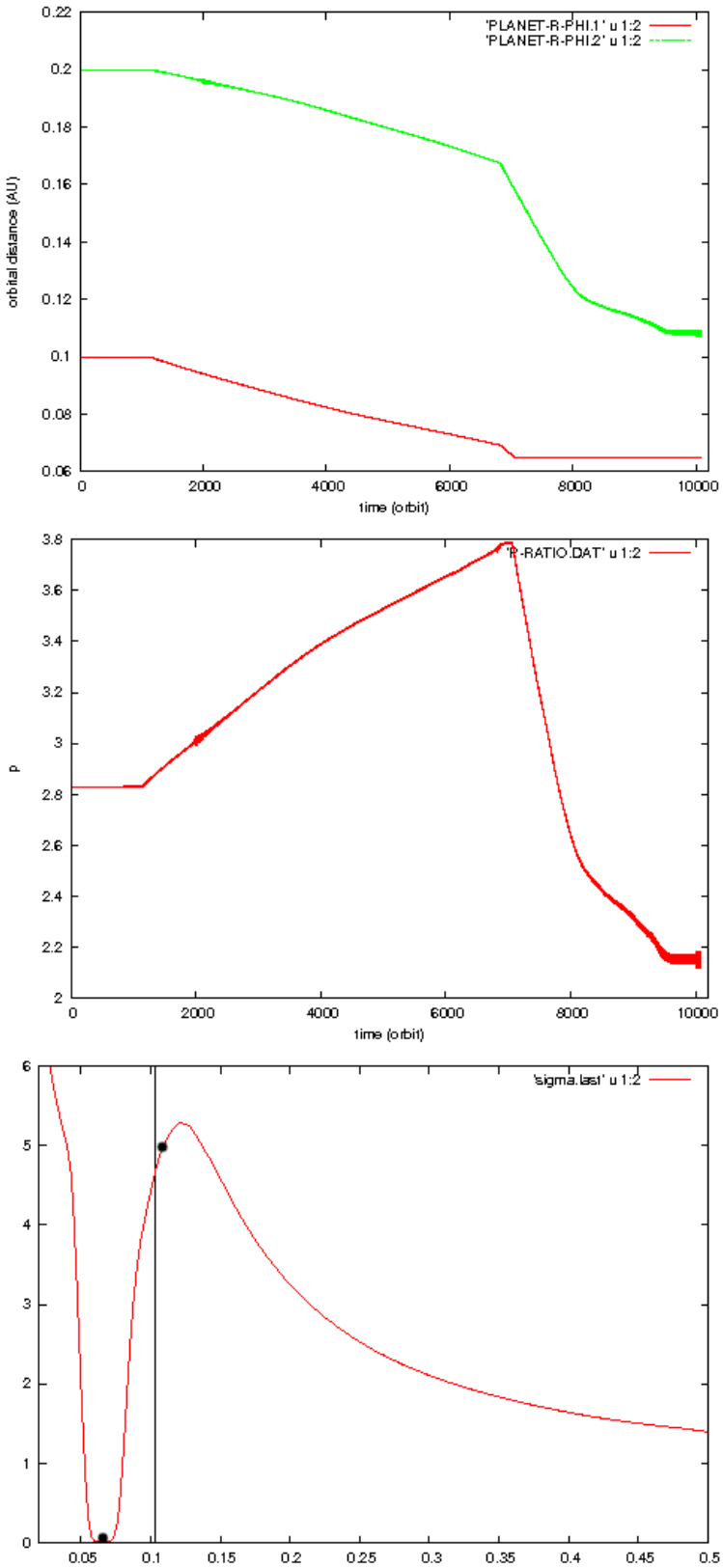

Figure 7.10: The evolution of the system for Model 3. Top: evolution of the orbital distances for both planets. The inner planet stops at 0.065 AU while the outer planet arrives at 0.108 AU. Centre: Evolution of the period ratio, final value is around 2.15. Bottom: Surface density as function of the orbital distance (in AU) at the end of the computation. Here the planets are represented by black circles and the vertical line denotes the location of the PC.

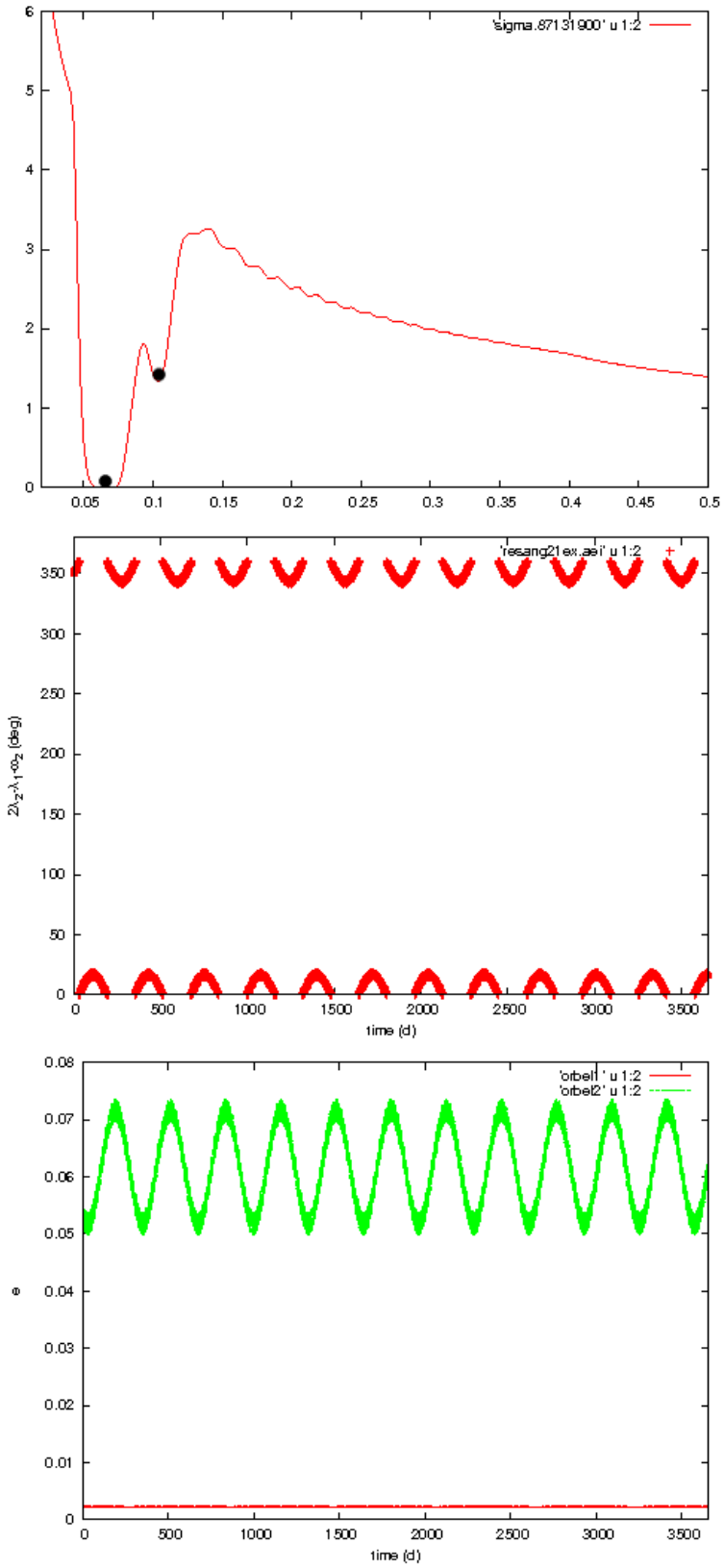

Figure 7.11: The evolution of the system for Model 5. Top: Surface density profile at the end of the computation, the planets are represented by black circles and are located in PC. Centre: evolution of the librating resonant angle ψ_{ext}. Bottom: Evolution of the orbital eccentricities e_1 (red) and e_2 (green).

7.5.2 The Evolution with the 0.5 Jupiter-mass Planet

For $m_1 = 0.5 m_{Jup}$, Podlewska and Szuszkiewicz [2009] found that in a disc with aspect ratio $H/R = 0.03$, a $10 m_\oplus$ body can be trapped into the 2:1 MMR, this result is here confirmed (Model 18). In fact, for $H/R = 0.05$ the outer companion reaches the location of PC in all the four cases because the gap formed by a lower mass 0.5 m_{Jup} planet is narrower than a Jovian mass. For $H/R = 0.03$, with $m_2 = 20$ and $10 m_\oplus$ the outer planet approaches the PC, while for $m_2 = 5$ and $3 m_\oplus$ the planet halts at a larger distance. With $H/R = 0.02$, cases with $m_2 = 20$, 10 and $5 m_\oplus$ are able to approaches the PC, while the 3 Earth-mass planet is inhibited.

Model 18 ($H/R = 0.03$ and $10 m_\oplus$) is represented in Figure 7.12, here the PC is maintained. In fact, the top panel shows the orbital evolution of the two planets: both planets evolve at constant semi-major axis till m_1 reaches its final mass, then migration begins and the outer body is trapped into the 2:1 MMR, then both planets migrate inward as the outer can push the inner ahead of it maintaining the resonance. The migration stops once the disc mass is reduced and the gas depleted. As shown in the central panel, the sub-Jupiter mass planets forms a narrower gap, also m_2 is able to form a small gap and can reach the PC. The bottom panel shows the resonant angle ψ_{ext} librating around 0° with a semi-amplitude of about 7°. e_1 is seen to stay small while e_2 achieves a value of 0.05.

Model 20 ($H/R = 0.03$ and $3 m_\oplus$) is a limiting case and it is shown in Figure 7.13. The top plot presents the orbital evolution of the two planets, a long computational time was required for the inner planet to reach its final mass, then the bodies migrate and the outer planet is stopped close to the PC with $p = 2.10$. In fact, this is represented in the surface density profile in the bottom panel: the gap created by the inner planet is narrower but still includes the location of the 2:1 MMR, the Super-Earth is unable to create a gap in the disc and gets trapped at the edge of the cavity just inside the location where the surface density gradient in the radial profile of the disc becomes steep and positive. In this case, the eccentricities are seen to be very small, no more than 0.01.

7.5.3 The Evolution with the 0.2 Jupiter-mass Planet

A 0.2 Jupiter-mass planet is roughly equivalent to a 4 Neptune-mass body, no previous studies have been made with this m_1. Here, with both $H/R = 0.05$ and $H/R = 0.03$ the low-mass body reaches the PC. With $H/R = 0.02$, the case with $m_2 = 20 m_\oplus$ has experienced no migration of the outer planet. This is probably due to the fact that the pair has comparable masses ($m_2/m_1 = 0.3$) and the disk is very thin. Models with $m_2 = 10$ and $5 m_\oplus$ can reach the PC, while the 3 Earth-mass planet does not. Therefore, with such a sub-giant planet the trapping in 2:1 MMR is substantially predominant.

Model 35 has aspect ratio $H/R = 0.02$ and $m_2 = 5 m_\oplus$. m_2 is able to open a small

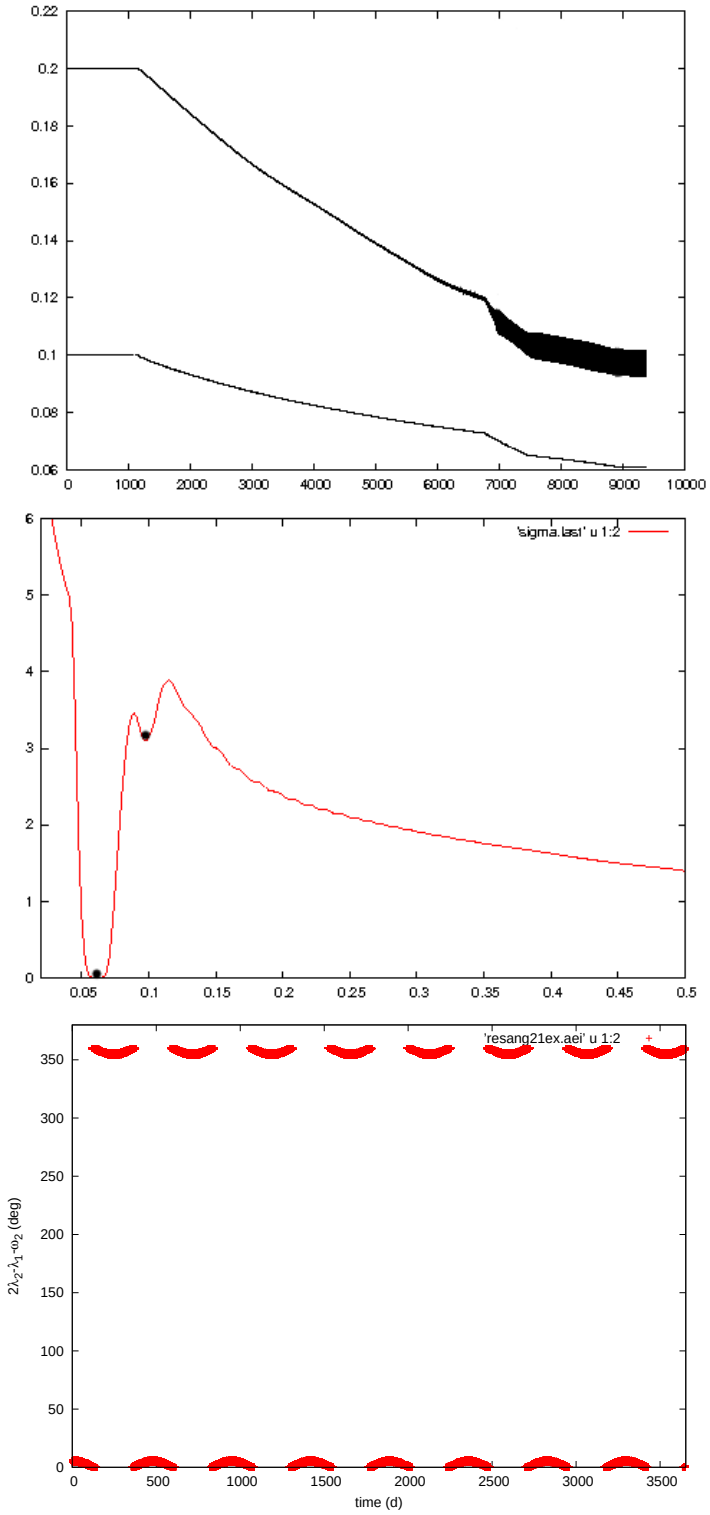

Figure 7.12: The evolution of the system for Model 18. Top: evolution of the orbital distances (in AU) for both planets. Time on the X-axis is in unit of "orbits". Increasing the disc mass the migration rate is seen to speed up. The inner planet is set to stop interacting with the disc once it reaches 0.065 AU, however it keeps migrating pushed by the outer planet in MMR. Migration is stopped reducing the disc mass when the inner body is at 0.061 AU, while the outer planet is at 0.098 AU. Centre: Surface density profile at the end of the computation, the planets are represented by black circles and are located in PC. Bottom: Time evolution of the librating resonant angle ψ_{ext}.

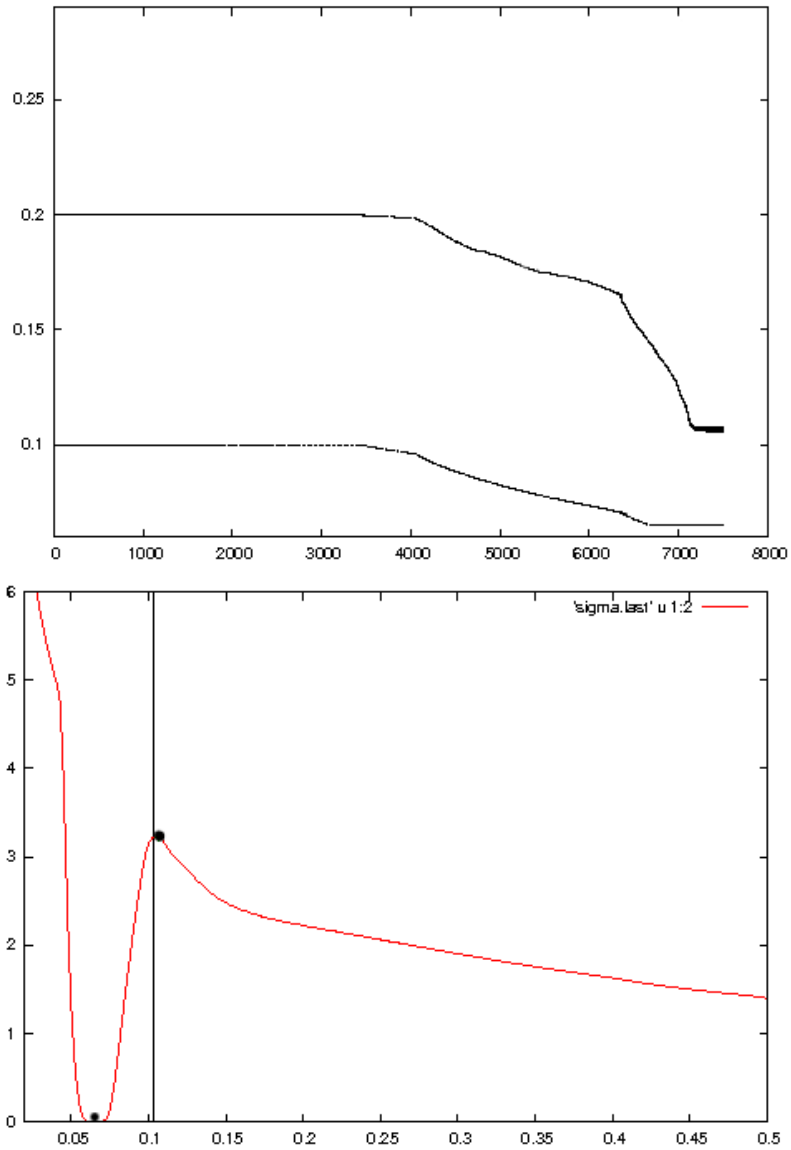

Figure 7.13: The evolution of the system for Model 20. Top: Evolution of the orbital distances (in AU) for both planets. Time on the X-axis is in unit of "orbits". The inner planet stops at 0.065 AU while the outer planet arrives at 0.106 AU. Bottom: Surface density profile at the end of the computation. Here the planets are represented by black circles and the vertical line denotes the location of the PC ($r = 0.103$ AU). The Super-Earth is stopped just outside the PC, at the edge of the gap.

gap in the disc and to reach the PC. This is shown in the surface density profile in the top panel of Figure 7.14. The central panel shows the resonant angle ψ_{ext} librating around 0° with a semi-amplitude of about 18° indicating a deep MMR trapping. The eccentricity obtained by the outer planet is 0.03 (bottom panel).

The dynamical evolution for Model 36 ($H/R = 0.02$ and $3m_\oplus$) is represented in Figure 7.15. The top panel shows the migration of the two planets. The rate of migration is modified by changing the disc mass. The outer body is seen to meet a physical barrier and cannot proceed any further. The two planets are seen to remain in quasi circular orbits. The central plot shows the period ratio: a minimum $p \approx 2.15$ is reached but after the super-Earth is stopped in its approach. The surface density profile in the bottom panel indicates that the sub-Jupiter giant forms such a narrower cavity that the 2:1 resonance is located barely outside the gap. In such a thin disc, also the super-Earth creates a shallow gap but this is not sufficient to move any closer. The density profile indicates the presence of disc of material trapped between the two planets; therefore, here the outer Lindblad torque is balanced by the inner Lindblad torque caused by the trapped material which is denser than the constituents located exteriorly to the outer planet.

7.6 TTV of Non-transiting Planets

So far, I have recalled the inability of identifying terrestrial companions to transiting giants in the *Kepler* catalogue. Small planets located near MMR should produce a strong TTV signal, actually in Section 7.2 this was seen to happen for planets in the surrounding of the exact PC where the amplitude of libration of the resonant angle is higher. I have then presented the theory about the dynamical evolution of two planets embedded into a protoplanetary disc and I have explored the outcome of this process according to the masses of the planets and the disc properties in order to estimate the number of cases which produce pairs in 2:1 MMR. In this Section, I will estimate the amplitude of the TTV signal for all runs considered.

For RV surveys, a 1 m/s precision corresponds to a detection limit of $3.6m_\oplus$ body at 0.105 AU, using equation (1.2.1). However, $5m_\oplus$ planets are detectable by RV only for nearby stars, such a detection is usually more difficult for higher magnitudes. A close companion to a transiting giant is detectable photometrically with *Kepler* only if their mutual orbital inclination is very small [e.g. Nesvorný et al., 2012]. Therefore, if the giant planet is transiting and the low-mass terrestrial planet ($m_2 \lesssim 5m_\oplus$) is non-transiting, then its detection is possible only with the TTV method.

I compute the TTV signal for the cases presented in the previous Section, assuming that the system observed now has not experienced any variations since the gas dispersal of the disc. I set in *NIRVANA* a null disc mass, the Cartesian positions and velocities are

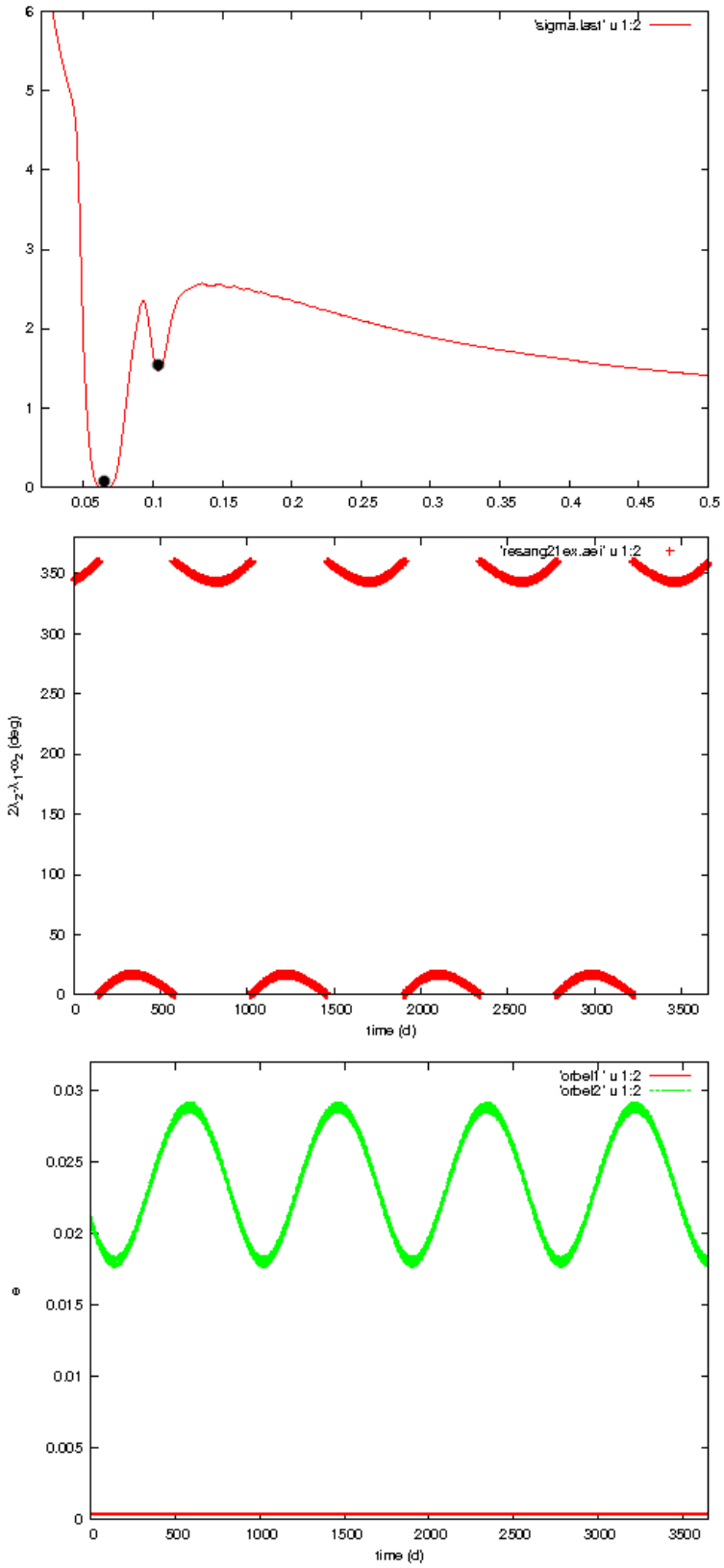

Figure 7.14: The evolution of the system for Model 35. Top: Surface density profile at the end of the computation, the planets are represented by black circles and are located in PC. Centre: Evolution of the librating resonant angle ψ_{ext}. Bottom: Evolution of the orbital eccentricities e_1 (smallest) and e_2 (largest).

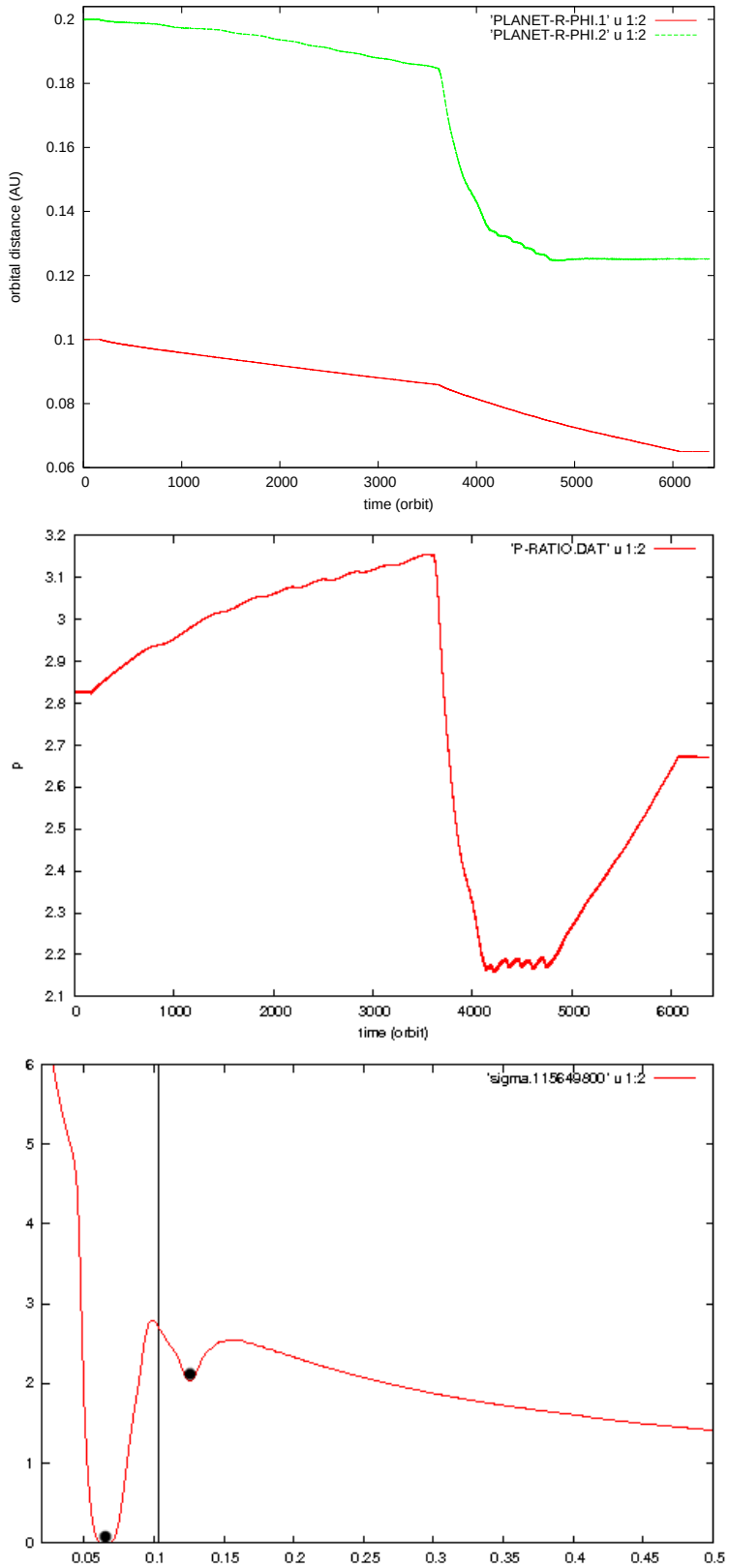

Figure 7.15: The evolution of the system for Model 36. Top: Evolution of the orbital distances for both planets. The inner planet stops at 0.065 AU while the outer planet arrives at 0.125 AU. Centre: Evolution of the period ratio, final value is around 2.67. Bottom: Surface density profile at the end of the computation. Here the planets are represented by black circles and the vertical line denotes the location of the PC.

outputted by the code with a time step of 1000 s. These coordinates are converted in Keplerian elements implementing the same routine part of *MERCURY*. Using the routine already presented in Section 4.5, the TTV curves and RMS TTV (equation 4.4.4) are then calculated over 137.95 days (the observational window considered by Steffen et al. [2012b]), 3.5 years (roughly the length of continued observation available with *Kepler* so far, [e.g. Nesvorny et al., 2013]) and 10 years (as for comparison with Veras et al. [2011]). Findings are outlined in Table 7.3.

Overall, the strongest signals are seen to be created by planets in resonance with higher-amplitude librations and by smaller planet-planet mass-ratios. Veras et al. [2011] considered a detectability threshold for TTV signal of 10 s, Boué et al. [2012] estimated it to be between 10 s and 1 min, while in their observational work Steffen et al. [2012b] confirmed it to be between 0.1 and 15 min with a median of 70 s. I make a rough estimate of how many companions would be detected among the studied configurations. Over the observational window of 137.95 days (0.38 y), supposing a threshold of 10 s: 21 companions, most of the size of Neptune[3] would be detectable; considering a threshold of 70 s: 6 planets would be detectable, three of them are companions to sub-Jupiter transiting bodies and the other three are in pair with a Jupiter-like object.

In agreement with what was pointed out by Veras et al. [2011], the variation of TTV signal as function of the number N of transits is found to be not necessarily monotonic. Here I summarised the apparent trends:

1. Cases not in resonance: TTV signal has no significant amplitude. On a small time scale the algorithm can experience difficulties in estimating P and t_0 (see Section 4.5) because of the small number of data points, with more observations estimates can be improved and the RMS TTV decreases accordingly. For instance, Models 1 and 19 show this trend and are represented in Figure 7.16. In both cases the period of TTV signal is about 120 d.

2. Cases in MMR with TTV signal already well defined on a short time scale: the RMS TTV does not change considerably. For example, the TTV signals of Models 13 and 14 are constituted by two components, the planet anticipates the transit first and postpones it at the following passage. The periods of TTV signals are 1.1 y and 0.7 y, respectively. However, because of the characteristics of the signal, its full amplitude is already deducible on a narrow observational window (see Figure 7.17).

3. Cases in MMR with TTV signal of period longer than the smallest observational window. On a longer time scale, the amplitude gets better defined and it is possible to achieve a better estimate of RMS TTV. For instance, in Figure 7.18 are represented Models 6, 17, 21 and 25 which show this trend. The periods of TTV

[3] $m_{Nep} = 17.1 m_{\oplus}$

Table 7.3: The TTV signal produced by the considered planetary pairs. All the performed simulations with different planetary masses and disc parameters are here summarised. The first column shows the model number, the second the mass of the gas giant, the third the disc aspect ratio, the fourth the mass of the low-mass planet, the fifth the final period ratio p, the sixth the librating resonant angle ψ_{ext} for cases in-PC, the seventh the RMS TTV ζ calculated over 10 y of observations, the eighth the RMS TTV η calculated over 3.5 y of observations, the ninth the RMS TTV ξ calculated over 137.95 d.

Model	$m_1(m_{Jup})$	H/R	$m_2(m_\oplus)$	p	ψ_{ext}	ζ (s)	η (s)	ξ (s)
1	1	0.05	20	2.11		28.4	28.2	33.1
2	1	0.05	10	2.15		13.8	16.4	12.2
3	1	0.05	5	2.15		6.8	8.0	6.2
4	1	0.05	3	2.23		4.8	4.2	4.0
5	1	0.03	20	2.00	$0° \pm 19°$	508.9	427.5	109.8
6	1	0.03	10	2.00	$0° \pm 10°$	74.0	68.2	22.2
7	1	0.03	5	2.15		8.8	7.5	6.6
8	1	0.03	3	2.16		5.3	5.1	4.5
9	1	0.02	20	2.00	$0° \pm 45°$	1368.7	1359.7	390.2
10	1	0.02	10	2.00	$0° \pm 110°$	1870.0	1599.8	324.3
11	1	0.02	5	2.38		6.5	5.9	6.1
12	1	0.02	3	2.56		3.5	3.5	3.4
13	0.5	0.05	20	2.00	$0° \pm 4°$	41.9	35.1	38.3
14	0.5	0.05	10	2.04	$0° \pm 8°$	17.5	17.0	18.6
15	0.5	0.05	5	2.00	$0° \pm 7°$	10.9	9.9	9.4
16	0.5	0.05	3	2.00	$0° \pm 4°$	5.7	5.8	4.3
17	0.5	0.03	20	2.00	$0° \pm 34°$	1977.6	1874.5	225.9
18	0.5	0.03	10	2.00	$0° \pm 7°$	131.5	131.1	15.4
19	0.5	0.03	5	2.09		7.2	8.5	8.7
20	0.5	0.03	3	2.10		4.6	4.5	5.6
21	0.5	0.02	20	2.00	$0° \pm 43°$	2856.5	3030.3	361.5
22	0.5	0.02	10	2.00	$0° \pm 75°$	2720.0	2752.5	46.9
23	0.5	0.02	5	2.00	$0° \pm 39°$	442.6	557.6	33.5
24	0.5	0.02	3	2.32		3.5	3.9	4.0
25	0.2	0.05	20	2.00	$0° \pm 4°$	526.9	474.0	30.4
26	0.2	0.05	10	2.00	$0° \pm 9°$	369.9	406.9	9.9
27	0.2	0.05	5	2.00	$0° \pm 14°$	399.3	506.2	7.4
28	0.2	0.05	3	2.00	$0° \pm 23°$	481.8	623.5	12.8
29	0.2	0.03	20	2.00	$0° \pm 51°$	8527.2	8300.9	356.5
30	0.2	0.03	10	2.00	$0° \pm 12°$	742.5	814.7	19.4
31	0.2	0.03	5	2.00	$0° \pm 15°$	354.4	445.8	15.2
32	0.2	0.03	3	2.00	$0° \pm 60°$	363.0	344.9	21.9
33	0.2	0.02	20	5.44		9.6	9.3	8.8
34	0.2	0.02	10	2.00	$0° \pm 15°$	959.0	1198.6	25.1
35	0.2	0.02	5	2.00	$0° \pm 18°$	328.9	366.3	12.4
36	0.2	0.02	3	2.67		2.9	3.1	3.2

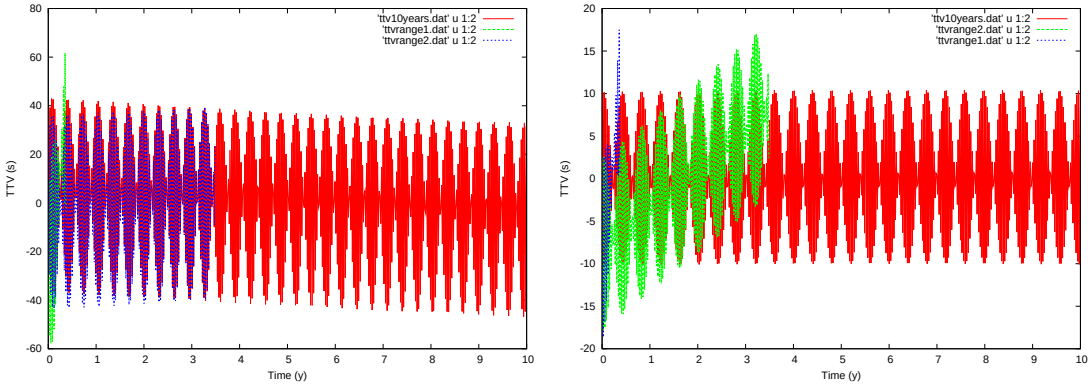

Figure 7.16: The TTV signal over observational windows of 137.95 days, 3.5 years and 10 years for cases not in resonance. Left: Model 1. Right: Model 19.

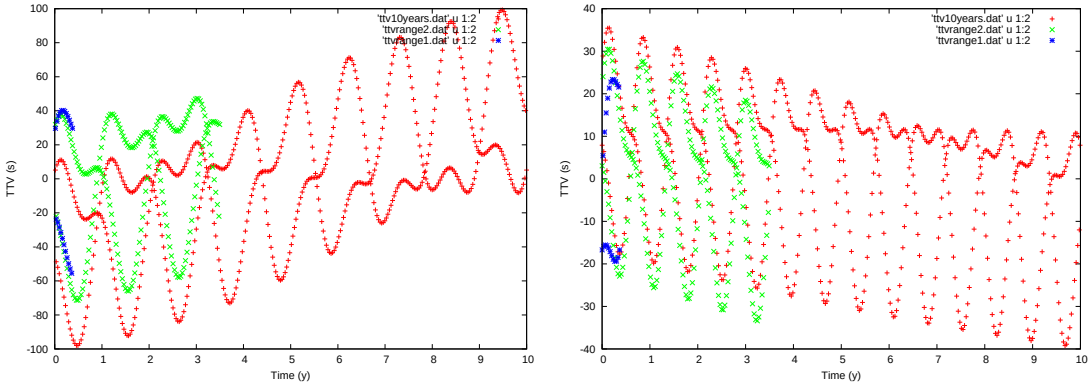

Figure 7.17: The TTV signal over observational windows of 137.95 days, 3.5 years and 10 years for cases in MMR. The signal is already well defined on a short time scale. Left: Model 13. Right: Model 14.

signals are 0.85 y, 1.4 y, 1.4 y and 2.25 y, respectively.

I now focus on low-mass terrestrial objects, the ones with $m_2 \lesssim 5m_\oplus$ which would be detectable only through the TTV method. Figure 7.1 confirms that, over a 10-year period, an RMS TTV of the order of hundreds of seconds can be expected for a 5 $m_\oplus$ planet in 2:1 PC. From the analysis of the RMS TTV over the longest time span of 10 years in Table 7.3, I observe that:

1. With $m_1 = 1m_{Jup}$, no 2:1 PC are present so the TTV amplitude is small. Observationally, this means that the absence of a TTV signal does not imply the absence of a companion planet.

2. With $m_1 = 0.5m_{Jup}$, Models 15 and 16 are in the 2:1 MMR, the resonant angles ψ_{ext} have low-amplitude librations and their RMS TTV are small; Model 23 is in MMR, ψ_{ext} has higher-amplitude libration and its RMS TTV is big; all other runs produce pairs not in 2:1 PC.

3. With $m_1 = 0.2m_{Jup}$, Model 36 is not in 2:1 PC so the TTV produced has a low

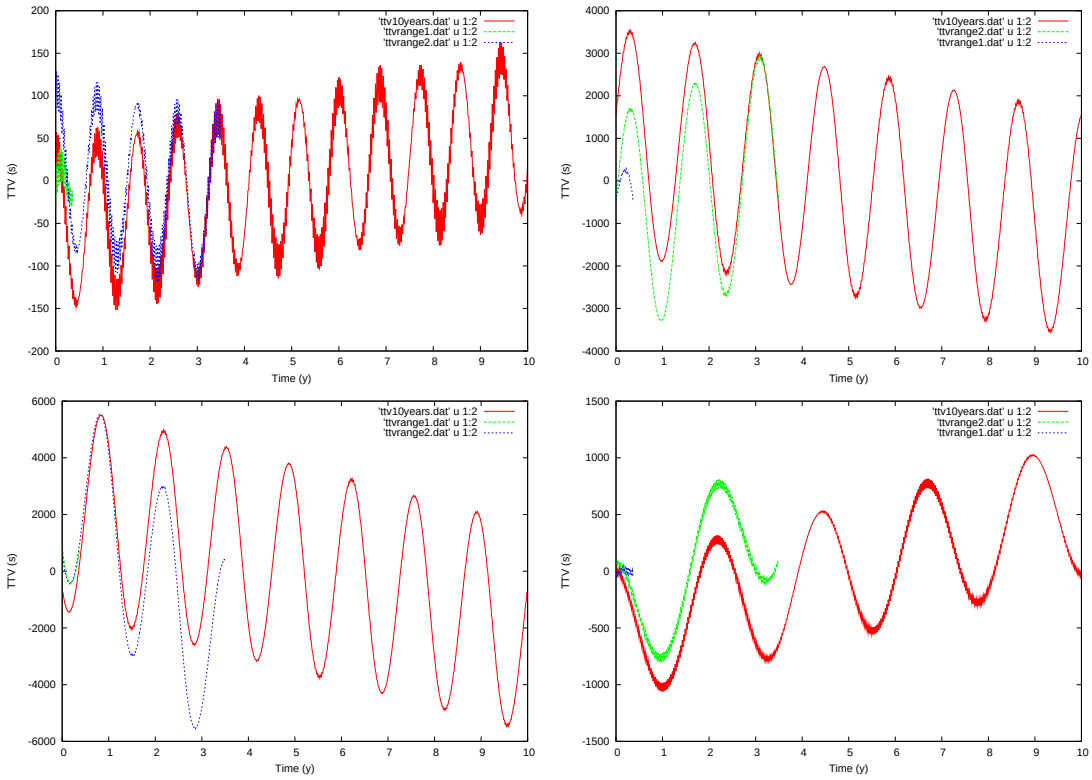

Figure 7.18: The TTV signal over observational windows of 137.95 days, 3.5 years and 10 years for cases in resonance. The signal has a period longer than the narrower observational window. Top-Left: Model 6. Top-Right: Model 17. Bottom-Left: Model 21. Bottom-Right: Model 25.

amplitude; all other cases get into the 2:1 MMR with resonant angles having amplitude of at least 14 degrees and their RMS TTV are significant.

A small amplitude of the resonant angle implies a deep locking into resonance, Boué et al. [2012] confirmed that TTV signal produced by a case in MMR is function of the amplitude of libration. This is confirmed by the simulations presented here, a libration semi-amplitude of at least 10-14 degrees is necessary for RMS TTV to be significant. The importance of resonant amplitude to create stronger TTV signals is supported by Models 26, 27 and 28. In fact, for these runs the RMS TTV does not increase with the planetary mass m_2, they show a libration amplitude higher for smaller planets so that to the highest amplitudes correspond the strongest signals.

The estimate of *P* The TTV plots of Figures 7.16, 7.17 and 7.18 show a long term linear drift in some cases. In this paragraph I aim to explain the reason for that.

In Section 4.5, it was indicated how I estimate $\hat{P}$ and $\hat{t}_0$ as arithmetic means considering all the recorded transits. t_0 is just an off-set which is subtracted from all $\delta t(n)$, therefore is not relevant in this issue and I continue this argumentation considering just P.

I realise that the arithmetic mean is not the best estimator of P. The physical reason is that the TTV curve may exhibit both short- and long-term variations and so for a set of transits not chosen *a priori* these variations may not cancel exactly with the arithmetic mean. This argument is strengthened by the fact that such curve is sampled only during the transits.

Agol et al. [2005], Payne et al. [2010], Boué et al. [2012] determine $\hat{P}$ by linear least squares minimisation of $\sum_n (\delta t(n))^2$, I now introduce the statistical reason to prefer such approach.

In its simplest case, a TTV curve is given by the $\delta t(i) = t_i - i \times \hat{P}$. We want to implement a linear regression model for the relationship: $t_i = i \times P + \delta t(i)$, where $\delta t(i)$ is a random variable and the model fit is

$$\hat{t_i} = i \times \hat{P}, \tag{7.6.1}$$

t_i is the observable and therefore it has a measurement uncertainty, i is the explanatory variable and P is the slope coefficient.

On the basis of the Gauss-Markov theorem [e.g. Plackett, 1950] the best estimator of the coefficient P is given by its linear least squares estimator. This estimator [e.g. Kenney and Keeping, 1954] minimizes the sum of squares of the random variable $\delta t(i)$. The arithmetical mean is a worse estimate of P, therefore a small error builds up because of the term $i \times P$ and generates the tiny drift shown in the residual plot for this fit (i.e. our TTV curve).

Although the implemented estimator is lower order, it is adequate for the problem, since evaluations of the RMS TTVs from the amplitudes of the TTV curves shown in this Section, confirm that the results reported in Table 7.3 are good guesses of the magnitude of the signals. General findings here presented are not modified if, to be conservative, the already arbitrary detectability thresholds are increased by a 10 %, to take into account the fact that the recorded RMS TTVs are upper limits. In future work, the least squares minimization can be implemented to get the TTV curves.

7.7 Discussion

In this Chapter I have investigated the detectability of non-transiting terrestrial planets neighbouring short-period giants, so far no such a detection has been made. From TTV surveys of *Kepler*'s candidates, companions are excluded to hot Jupiters and warm Jupiter, while hot Neptune-size candidates exhibit TTV signatures of companions in three cases, two of which are transiting Neptune-size bodies.

Strong TTV signals are expected to be generated by terrestrial planets in 2:1 MMR with a transiting giant. The possibility of having these objects trapped into resonance has been previously discussed [e.g. Pierens and Nelson, 2008, Podlewska and Szuszkiewicz, 2009]. I have considered a broad range of planetary masses and disc parameters in order to study the outcome of planetary migration for different pairs of a giant plus a low-mass planet. In these runs, the migration of the inner body is halted once a location typical for hot giants is reached, this gives the chance to analyse the final destination of the outer companion.

During its migration in the protoplanetary disc, the outer low-mass planet can be halted at the outer edge of the gap opened by the gas giant or reach the 2:1 MMR if the gap opened is narrower. The studies available in the literature have been confirmed here (Section 7.5); overall, trapping into the 2:1 MMR is seen to be more probable for pairs with a smaller giant and for cases which have evolved into thinner discs. Migration of the outer planet was described to be halted when the Lindblad torque is counterbalanced by the corotation torque produced by a steep and positive surface density gradient in the radial profile of the disc. Here, another mode to stop planetary migration is suggested by some runs with terrestrial low mass planets in thin discs: they are seen to be able to create a shallow gap, but the presence of a disc of material trapped between the two planets does not allow them to approach the inner companion any further. A future study can investigate the issue of varying the disc mass for computational convenience: by defining the computational domain properly, the disc mass can be set to a constant value so that the results presented in this Chapter can be confirmed with another approach and integrated further with more configurations.

The cases where the companion does not end up in PC and the sets where the compan-

ion is trapped in MMR, do not produce substantially different RMS TTV if the amplitude of the resonant angle is less than 10-14 degrees. Migration mechanisms are ascertained to favour a deep trapping into MMR with a low-amplitude resonant libration, this was confirmed by Raymond et al. [2008]. The strongest TTV signals are generated by planets in resonance with higher-amplitude librations and by smaller planet-planet mass-ratios as previously indicated by Veras et al. [2011] and Boué et al. [2012], companions to Neptune-size objects and in thinner discs are here seen to produce the largest amplitudes among the considered cases. Therefore, for these reasons it is deductible that companions to Neptune-class bodies are more probable to be detected, this is in agreement with the observations [Steffen et al., 2012b]. Terrestrial planets in 2:1 MMR with sub-giant bodies can present resonant angles with high amplitude, so that they are likely to be detected on a longer observational window. Planet-planet scattering produces 2:1 MMR configurations with high-amplitude resonant librations in roughly 5% of cases [Raymond et al., 2008], shortage of detected companions may be indication that 2:1 MMR pairs are more probable to be generated through planetary migration rather than scattering. Also, due to the results it can be argued that planets are less likely to form in very thin discs. Although the disc driven migration scenario cannot be ruled out on the basis of there being no companions detected via TTVs, lack of detected companions to hot Jupiters can still be due to dynamical perturbations which would have scattered out them during the gas giant's dynamical evolution [Rasio and Ford, 1996, Fabrycky and Tremaine, 2007].

CHAPTER 8

Conclusions

Just two decades ago, only the planets of the Solar system were known and observed. Therefore, since antiquity the question about the existence of other worlds had been predominately a philosophical topic because of the lack of scientific proofs. Suddenly, a new and revolutionary astronomical branch was born: the study of planetary systems beyond our own with a proliferation of discoveries in recent years which sum up to more than 850 exoplanets confirmed so far. In particular, the detection of more than 130 multiple planet systems offers a broader range of properties than are shown by our Solar system making them the ideal test bed for planetary formation and evolution theories.

The aim of this thesis has been to discuss some characteristic dynamical features presented by the vast pool of catalogued planetary systems. Specifically, I have addressed the following questions:

1. How is it possible to give reasonable constrains on the orbital elements of poorly sampled planets using stability analysis?
2. Which dynamical mechanisms and evolutionary histories are plausible to have generated the peculiar characteristics currently observed for some extrasolar planetary systems?
3. What are the most common configurations of extrasolar system with terrestrial planets and what will be detected by present and future observational programmes?

The rich history of exoplanet detection and characterisation along with their diversity is examined in Chapter 1. The most interesting features are: giant planets in short period orbits, the wide eccentricity distribution of exoplanets and the relatively common detection of mean motion resonances in multiple planet systems.

I have presented the laws of planetary motion and the Radial Velocity discovery technique in Chapter 2. In order to investigate the orbital architectures of planetary systems and constrain their evolutionary histories, measured orbital parameters as accurate as

possible are required. Unfortunately, the accuracy of such measurements are limited due to uncertainties and degeneracies inherent to the RV method. Moreover, a narrow observational window, only partially covering a long orbital period, can lead to solutions representing unrealistic scenarios. Taking into account the *dynamical stability* as an additional observable while interpreting the RV data, it is possible analyse the phase space in a neighbourhood of the statistically best-fit solution and derive dynamically stable configurations that reproduce the observed RV signal. In fact, I have described some special dynamical states as the orbital resonances which, in some circumstances, are able to stabilise a planetary system.

The analysis of the dynamical evolution of a planetary system can be undertaken by means of the Laplace-Lagrange Apsidal Precession Model. With this theory is possible to obtain an analytical solution to the N-body problem by considering the purely secular effects. In fact, in Chapter 3 I have introduced the secular perturbations theory in the generalised form which takes also in consideration the effects produced by general relativity and by a non-spherical central mass. I have applied the model to find analytic approximations of the long-term behaviour for some planetary systems such as the Solar system, μ Araæ, 55 Cancri and HD 125612. Then, I have presented the sweeping of secular resonances: a dynamical mechanism that can be fundamental in explaining some peculiar orbital characteristics and that can be modelled using the secular theory. Moreover, I have discussed how the eccentricity is excited due to the passage of a secular resonance and I have derived the rate of eccentricity forcing in the case in which the passage is due to stellar spin-down. I have continued by presenting another important dynamical mechanism: the planet-planet gravitational scattering. This process is found to naturally create both high-eccentricity orbits and MMRs with large libration amplitudes [Chatterjee et al., 2008, Raymond et al., 2008]. The Chapter is concluded introducing the numerical recipe that I have used to study the sweeping of secular resonances due to stellar spin-down and the planet-planet scattering, including both GR and J_2 effects.

The geometry of a planetary transit and the present state of transit detections is discussed in Chapter 4. Special focus has been addressed to *Kepler*, a discovery-class mission which has more than 130 planet detections confirmed. It was also shown how, is some cases, with spectroscopic follow up observations it is possible to confirm the genuine detection of a transiting planet and obtain its actual mass.

By observing variations in the timing of a transit new planets can be detected. The theory of transit timing effects was presented in Section 4.4. Furthermore, I discussed the numerical recipe implemented to estimate transit timing variations. Also reported were the detections of non-transiting gaseous planets made with *Kepler* and the predictions conceived about the strength of the TTV method of discovering, in particular, terrestrial planets which would be outside the grasp of Radial Velocity surveys. The detection of non-transiting Earth and even super-Earth class planets through the TTV

method will likely remain extremely challenging, given the intricacies of interpreting the TTV signal and the low amplitudes produced by some configurations [e.g. Veras et al., 2011]. Obtaining RV datasets of precision necessary to confirm those discoveries is likely not feasible. Stars in the Kepler sample are typically too faint and active for the kind of RV precision advocated. However, in some circumstances, RV datasets may aid in excluding massive planets in higher-order resonances from the list of possible configurations. Dynamical stability considerations, in the case of putative massive perturbers, will also help to rule out unstable, degenerate solutions.

The three-planet extrasolar system of HD 181433 has been detected with HARPS. The best-fit solution, announced by the discovery team, describes a highly unstable, self-disrupting configuration. Therefore, I have implemented the *dynamical stability* method in Chapter 5, where I have analysed the phase space in the neighbourhood of the statistical best-fit and, by studying the long-term stability of the system, I have been able to reduce the uncertainty on the location of the outer planet HD 181433 *d* to the narrow band where the 5:2 MMR is possible with the other giant HD 181433 *c*. My Newtonian stable best-fit model is capable of surviving for at least 250 Myrs. This MMR does not allow close encounters even in case of highly eccentric orbits. Besides, it is noted that planets *c* and *d* are located in regions spanned by many other strong low-order MMRs. I have study the dynamics of some plausible scenarios and I have illustrate the behaviours caused by secular apsidal resonances and mean motion resonances. Furthermore, I have argued that the existence of a planet between *b* and *c* would fill an empty gap in the system, supporting the 'packed planetary systems' hypothesis [Barnes and Raymond, 2004]. Additional observations are required to investigate on the presence of a terrestrial body in the aforementioned zone of HD 181433, as in the published data this signal would be at the noise level.

In Chapter 6, I have applied the introduced theory to analyse the dynamics of the stellar system of HD 181433. This system consists of two gas giant planets (bodies *c* and *d*) with $m \sin i = 0.65$ M_{Jup} and 0.53 M_{Jup} orbiting with periods 975 and 2468 days, respectively. The two planets appear to be in a 5:2 mean motion resonance as evaluated in Chapter 5, as this is required for the system to be dynamically stable. The third planet with mass $m_b \sin i = 0.023$ M_{Jup} orbits close to the star with an orbital period of 9.37 days. Analysis of the possible tidal evolution of the innermost planet HD 181433 b has suggested that it should be considered as a hot- Neptune rather than a short-period super-Earth. This is because the orbit of a terrestrial planet would have been circularised in a time scale much shorter than any reasonable estimate for the age of the system.

Each planet orbit is significantly eccentric, with current values estimated to be $e_b = 0.39$, $e_c = 0.27$ and $e_d = 0.47$. I have assessed different scenarios that may explain the origin of these eccentric orbits after depletion of the protoplanetary disk, with particular focus on the innermost body, noting that the large eccentricity of planet *b* cannot be

explained through secular interaction with the outer pair. I have considered a scenario in which the system previously contained an additional giant planet that was ejected during a period of dynamical instability among the planets. N-body simulations are presented that demonstrate that during scattering and ejection among the outer planets a close encounter between a giant and the inner body can raise e_b to its observed value. Such an outcome occurs with a frequency of a few %. I have also demonstrated, however, that obtaining the required value of e_b and having the two surviving outer planets land in 5:2 resonance is a rare outcome, therefore I have considered alternative scenarios involving secular resonances. I have considered the possibility that an undetected planet in the system causes planet b to be in a secular resonance, but I have found that the resulting values of forced eccentricity are not large enough. I have also examined a scenario in which the spin-down of the central star causes the system to pass through secular resonance. In its simplest form this latter scenario fails to produce the system observed today, with the mode of failure depending sensitively on the rate of stellar spin-down. For spin-down rates above a critical value, planet b passes through the resonance too quickly, and the forced eccentricity only reaches maximum values $e_b \simeq 0.25$. Spin-down rates below the critical value lead to long-term capture of planet b in secular resonance, driving the eccentricity towards unity. If additional short-period low mass planets are present in the system, however, I have found that mutual scattering can release planet b from the secular resonance, leading to a system with orbital parameters similar to those observed today. This would require a stellar spin period $\lesssim 20$ hours for resonant capture to occur which is well plausible [Baxter et al., 2008]. It is deducible that additional low mass planets between b and c are relevant to support the "packed planetary systems" hypothesis but also the scenario which predicts the generation of the significant orbital eccentricity e_b via sweeping of the secular resonance during the early stage of evolution of HD 181433a.

Because a terrestrial planet in 2:1 MMR should produce a large detectable TTV signal and since no low-mass planet has been detected with the TTV method yet, in Chapter 7 I have investigated the detectability of non-transiting terrestrial bodies neighbouring short-period giants. Looking for TTV signals among the Kepler's candidates, hot and warm Jupiters are seen not to host companions in 2:1 MMR, while hot Neptune-size candidates exhibit TTV signatures of companions in three cases, two of which are transiting Neptune-size bodies. Therefore, because the observed architecture of planetary systems might be the outcome of the large-scale orbital migration induced by disc-planet interactions, I have looked for differences in the formation and dynamical history among the classes of giant-size bodies migrating with low-mass planets.

I have started with presenting a study showing the effects of mass, semi-major axis and mean anomaly of a perturbing planet on the TTV signal produced by a transiting planet. I have confirmed that resonances tend to increase significantly the signal and I have pointed out that, in MMR, the TTV RMS is smaller at the exact centre and big-

ger at the separatrices. I have moved to present the arguments necessary to study the dynamical evolution of two planets embedded into a protoplanetary disc: I have introduced planetary migration mechanisms and I have discussed some preliminary findings available in the literature concerning the evolution of terrestrial planets evolving with giants in a gaseous disc. Moreover, I have shown the characteristics of the model implemented to undertake this study. I have considered a broad range of disc settings and planetary masses. Also, in the simulations the migration of the inner planet was halted once a location typical for hot giants was reached, this gave the possibility to study the final outcome of the process even for those runs which was showing a divergent migration. Trapping into the 2:1 MMR was seen to be more probable for pairs with a smaller giant and for cases which have evolved into thinner discs. As expected, some outer planets were trapped not in resonance at the edge of the gap formed by the inner giant; while some terrestrial low mass planets in thin discs were seen to create a shallow gap, but were halted during their migration by the presence of a disc of material trapped between the two planets making impossible reaching the location of the 2:1 MMR.

To conclude, I have estimated the amplitude of the TTV signal for all the considered runs. It was found that the strongest TTV signals were indeed produced by higher-amplitude librations and by smaller planet-planet mass-ratios, so that companions to Neptune-class objects are more probable to be detected, in agreement with the observations. Terrestrial planets in 2:1 MMR with sub-giant bodies are produced by planetary migration and, in these cases, they can also have a high-amplitude libration angle. Therefore, with a broader observational window they are likely to be detected. Future work can extend the results here presented by considering a wider parameter space and more complex configurations.

This is a time in which a great variety of planetary systems are discovered, theories are called for explain the formation and evolution of such a large zoo which present characteristics very different from the ones shown by our Solar system. New observations can confirm these theories and give new insights on dynamical mechanisms experienced by planetary systems designed by nature.

References

F. C. Adams and G. Laughlin. Long-Term Evolution of Close Planets Including the Effects of Secular Interactions. *ApJ*, 649:1004–1009, Oct. 2006a. doi: 10.1086/506145.

F. C. Adams and G. Laughlin. Effects of Secular Interactions in Extrasolar Planetary Systems. *ApJ*, 649:992–1003, Oct. 2006b. doi: 10.1086/506142.

C. B. Agnor and D. N. C. Lin. On the Migration of Jupiter and Saturn: Constraints from Linear Models of Secular Resonant Coupling with the Terrestrial Planets. *ApJ*, 745: 143, Feb. 2012a. doi: 10.1088/0004-637X/745/2/143.

C. B. Agnor and D. N. C. Lin. System Coupling and the Evolution of Short Period Planets. In *European Planetary Science Congress 2012*, page 946, Sept. 2012b.

E. Agol and J. H. Steffen. A limit on the presence of Earth-mass planets around a Sun-like star. *MNRAS*, 374:941–948, Jan. 2007. doi: 10.1111/j.1365-2966.2006.11213.x.

E. Agol, J. Steffen, R. Sari, and W. Clarkson. On detecting terrestrial planets with timing of giant planet transits. *MNRAS*, 359:567–579, May 2005. doi: 10.1111/j.1365-2966.2005.08922.x.

G. Anglada-Escudé, M. López-Morales, and J. E. Chambers. How Eccentric Orbital Solutions Can Hide Planetary Systems in 2:1 Resonant Orbits. *ApJ*, 709:168–178, Jan. 2010. doi: 10.1088/0004-637X/709/1/168.

P. J. Armitage. Massive Planet Migration: Theoretical Predictions and Comparison with Observations. *ApJ*, 665:1381–1390, Aug. 2007. doi: 10.1086/519921.

P. J. Armitage. Dynamics of Protoplanetary Disks. *ARA&A* , 49:195–236, Sept. 2011. doi: 10.1146/annurev-astro-081710-102521.

A. Baglin, M. Auvergne, P. Barge, J.-T. Buey, C. Catala, E. Michel, W. Weiss, and COROT Team. COROT: asteroseismology and planet finding. In B. Battrick, F. Favata, I. W. Roxburgh, and D. Galadi, editors, *Stellar Structure and Habitable Planet Finding*, volume 485 of *ESA Special Publication*, pages 17–24, Jan. 2002.

S. Ballard, D. Fabrycky, F. Fressin, D. Charbonneau, J.-M. Desert, G. Torres, G. Marcy, C. J. Burke, H. Isaacson, C. Henze, J. H. Steffen, D. R. Ciardi, S. B. Howell, W. D.

Cochran, M. Endl, S. T. Bryson, J. F. Rowe, M. J. Holman, J. J. Lissauer, J. M. Jenkins, M. Still, E. B. Ford, J. L. Christiansen, C. K. Middour, M. R. Haas, J. Li, J. R. Hall, S. McCauliff, N. M. Batalha, D. G. Koch, and W. J. Borucki. The Kepler-19 System: A Transiting 2.2 R Ł Planet and a Second Planet Detected via Transit Timing Variations. *ApJ*, 743:200, Dec. 2011. doi: 10.1088/0004-637X/743/2/200.

T. Barclay, J. F. Rowe, J. J. Lissauer, D. Huber, F. Fressin, S. B. Howell, S. T. Bryson, W. J. Chaplin, J.-M. Désert, E. D. Lopez, G. W. Marcy, F. Mullally, D. Ragozzine, G. Torres, E. R. Adams, E. Agol, D. Barrado, S. Basu, T. R. Bedding, L. A. Buchhave, D. Charbonneau, J. L. Christiansen, J. Christensen-Dalsgaard, D. Ciardi, W. D. Cochran, A. K. Dupree, Y. Elsworth, M. Everett, D. A. Fischer, E. B. Ford, J. J. Fortney, J. C. Geary, M. R. Haas, R. Handberg, S. Hekker, C. E. Henze, E. Horch, A. W. Howard, R. C. Hunter, H. Isaacson, J. M. Jenkins, C. Karoff, S. D. Kawaler, H. Kjeldsen, T. C. Klaus, D. W. Latham, J. Li, J. Lillo-Box, M. N. Lund, M. Lundkvist, T. S. Metcalfe, A. Miglio, R. L. Morris, E. V. Quintana, D. Stello, J. C. Smith, M. Still, and S. E. Thompson. A sub-Mercury-sized exoplanet. *Nature*, 494:452–454, Feb. 2013. doi: 10.1038/nature11914.

A. J. Barker and G. I. Ogilvie. On the tidal evolution of Hot Jupiters on inclined orbits. *MNRAS*, 395:2268–2287, June 2009. doi: 10.1111/j.1365-2966.2009.14694.x.

R. Barnes and R. Greenberg. Stability Limits in Resonant Planetary Systems. *ApJL*, 665: L67–L70, Aug. 2007. doi: 10.1086/521144.

R. Barnes and T. Quinn. The (In)stability of Planetary Systems. *ApJ*, 611:494–516, Aug. 2004. doi: 10.1086/421321.

R. Barnes and S. N. Raymond. Predicting Planets in Known Extrasolar Planetary Systems. I. Test Particle Simulations. *ApJ*, 617:569–574, Dec. 2004. doi: 10.1086/423419.

R. Barnes, R. Greenberg, T. R. Quinn, B. E. McArthur, and G. F. Benedict. Origin and Dynamics of the Mutually Inclined Orbits of Andromedae c and d. *ApJ*, 726:71, Jan. 2011. doi: 10.1088/0004-637X/726/2/71.

E. Baxter, L. Corrales, R. Yamada, and A. A. Esin. Modeling the Rotational Evolution of Young T Tauri Stars. *ApJ*, 689:308–315, Dec. 2008. doi: 10.1086/592315.

J.-P. Beaulieu, D. P. Bennett, P. Fouqué, A. Williams, M. Dominik, U. G. Jørgensen, D. Kubas, A. Cassan, C. Coutures, J. Greenhill, K. Hill, J. Menzies, P. D. Sackett, M. Albrow, S. Brillant, J. A. R. Caldwell, J. J. Calitz, K. H. Cook, E. Corrales, M. Desort, S. Dieters, D. Dominis, J. Donatowicz, M. Hoffman, S. Kane, J.-B. Marquette, R. Martin, P. Meintjes, K. Pollard, K. Sahu, C. Vinter, J. Wambsganss, K. Woller, K. Horne, I. Steele, D. M. Bramich, M. Burgdorf, C. Snodgrass, M. Bode, A. Udalski, M. K. Szymański, M. Kubiak, T. Więckowski, G. Pietrzyński, I. Soszyński, O. Szewczyk, Ł. Wyrzykowski, B. Paczyński, F. Abe, I. A. Bond, T. R. Britton, A. C.

Gilmore, J. B. Hearnshaw, Y. Itow, K. Kamiya, P. M. Kilmartin, A. V. Korpela, K. Masuda, Y. Matsubara, M. Motomura, Y. Muraki, S. Nakamura, C. Okada, K. Ohnishi, N. J. Rattenbury, T. Sako, S. Sato, M. Sasaki, T. Sekiguchi, D. J. Sullivan, P. J. Tristram, P. C. M. Yock, and T. Yoshioka. Discovery of a cool planet of 5.5 Earth masses through gravitational microlensing. *Nature*, 439:437–440, Jan. 2006. doi: 10.1038/nature04441.

G. F. Benedict, B. E. McArthur, T. Forveille, X. Delfosse, E. Nelan, R. P. Butler, W. Spiesman, G. Marcy, B. Goldman, C. Perrier, W. H. Jefferys, and M. Mayor. A Mass for the Extrasolar Planet Gliese 876b Determined from Hubble Space Telescope Fine Guidance Sensor 3 Astrometry and High-Precision Radial Velocities. *ApJL*, 581:L115–L118, Dec. 2002. doi: 10.1086/346073.

G. F. Benedict, B. E. McArthur, G. Gatewood, E. Nelan, W. D. Cochran, A. Hatzes, M. Endl, R. Wittenmyer, S. L. Baliunas, G. A. H. Walker, S. Yang, M. Kürster, S. Els, and D. B. Paulson. The Extrasolar Planet ϵ Eridani b: Orbit and Mass. *AJ*, 132:2206–2218, Nov. 2006. doi: 10.1086/508323.

W. Benz, W. L. Slattery, and A. G. W. Cameron. Collisional stripping of Mercury's mantle. , 74:516–528, June 1988. doi: 10.1016/0019-1035(88)90118-2.

P. R. Bevington and D. K. Robinson. *Data reduction and error analysis for the physical sciences*. 1992.

W. J. Borucki, D. Koch, G. Basri, T. Brown, D. Caldwell, E. Devore, E. Dunham, T. Gautier, J. Geary, R. Gilliland, A. Gould, S. Howell, and J. Jenkins. Kepler Mission: a mission to find Earth-size planets in the habitable zone. In M. Fridlund, T. Henning, and H. Lacoste, editors, *Earths: DARWIN/TPF and the Search for Extrasolar Terrestrial Planets*, volume 539 of *ESA Special Publication*, pages 69–81, Oct. 2003.

W. J. Borucki, D. Koch, G. Basri, T. Brown, D. Caldwell, E. Devore, E. Dunham, T. Gautier, J. Geary, R. Gilliland, A. Gould, S. Howell, J. Jenkins, and D. Latham. The Kepler Mission: Design, expected science results, opportunities to participate. In M. Livio, K. Sahu, and J. Valenti, editors, *A Decade of Extrasolar Planets around Normal Stars Proceedings of the Space Telescope Science Institute Symposium, held in Baltimore, Maryland May 2-5, 2005. Edited by Mario Livio, Kailash Sahu and Jeff Valenti, Space Telescope Science Institute, Baltimore Series: Space Telescope Science Institute Symposium Series (No. 19) ISBN: 9780521897846 Publication date: June 2008, 196 pages, pp.36-49*, pages 36–49, June 2008.

W. J. Borucki, D. G. Koch, T. M. Brown, G. Basri, N. M. Batalha, D. A. Caldwell, W. D. Cochran, E. W. Dunham, T. N. Gautier, III, J. C. Geary, R. L. Gilliland, S. B. Howell, J. M. Jenkins, D. W. Latham, J. J. Lissauer, G. W. Marcy, D. Monet, J. F. Rowe, and D. Sasselov. Kepler-4b: A Hot Neptune-like Planet of a G0 Star Near Main-sequence Turnoff. *ApJL*, 713:L126, Apr. 2010. doi: 10.1088/2041-8205/713/2/L126.

W. J. Borucki, D. G. Koch, G. Basri, N. Batalha, T. M. Brown, S. T. Bryson, D. Caldwell, J. Christensen-Dalsgaard, W. D. Cochran, E. DeVore, E. W. Dunham, T. N. Gautier, III, J. C. Geary, R. Gilliland, A. Gould, S. B. Howell, J. M. Jenkins, D. W. Latham, J. J. Lissauer, G. W. Marcy, J. Rowe, D. Sasselov, A. Boss, D. Charbonneau, D. Ciardi, L. Doyle, A. K. Dupree, E. B. Ford, J. Fortney, M. J. Holman, S. Seager, J. H. Steffen, J. Tarter, W. F. Welsh, C. Allen, L. A. Buchhave, J. L. Christiansen, B. D. Clarke, S. Das, J.-M. Désert, M. Endl, D. Fabrycky, F. Fressin, M. Haas, E. Horch, A. Howard, H. Isaacson, H. Kjeldsen, J. Kolodziejczak, C. Kulesa, J. Li, P. W. Lucas, P. Machalek, D. McCarthy, P. MacQueen, S. Meibom, T. Miquel, A. Prsa, S. N. Quinn, E. V. Quintana, D. Ragozzine, W. Sherry, A. Shporer, P. Tenenbaum, G. Torres, J. D. Twicken, J. Van Cleve, L. Walkowicz, F. C. Witteborn, and M. Still. Characteristics of Planetary Candidates Observed by Kepler. II. Analysis of the First Four Months of Data. *ApJ*, 736:19, July 2011. doi: 10.1088/0004-637X/736/1/19.

W. J. Borucki, E. Agol, F. Fressin, L. Kaltenegger, J. Rowe, H. Isaacson, D. Fischer, N. Batalha, J. J. Lissauer, G. W. Marcy, D. Fabrycky, J.-M. DÃl'sert, S. T. Bryson, T. Barclay, F. Bastien, A. Boss, E. Brugamyer, L. A. Buchhave, C. Burke, D. A. Caldwell, J. Carter, D. Charbonneau, J. R. Crepp, J. Christensen-Dalsgaard, J. L. Christiansen, D. Ciardi, W. D. Cochran, E. DeVore, L. Doyle, A. K. Dupree, M. Endl, M. E. Everett, E. B. Ford, J. Fortney, T. N. Gautier, J. C. Geary, A. Gould, M. Haas, C. Henze, A. W. Howard, S. B. Howell, D. Huber, J. M. Jenkins, H. Kjeldsen, R. Kolbl, J. Kolodziejczak, D. W. Latham, B. L. Lee, E. Lopez, F. Mullally, J. A. Orosz, A. Prsa, E. V. Quintana, R. Sanchis-Ojeda, D. Sasselov, S. Seader, A. Shporer, J. H. Steffen, M. Still, P. Tenenbaum, S. E. Thompson, G. Torres, J. D. Twicken, W. F. Welsh, and J. N. Winn. Kepler-62: A five-planet system with planets of 1.4 and 1.6 earth radii in the habitable zone. *Science*, 340(6132):587–590, 2013. doi: 10.1126/science.1234702. URL `http://www.sciencemag.org/content/340/6132/587.abstract`.

F. Bouchy, M. Mayor, C. Lovis, S. Udry, W. Benz, J.-L. Bertaux, X. Delfosse, C. Mordasini, F. Pepe, D. Queloz, and D. Segransan. The HARPS search for southern extra-solar planets. XVII. Super-Earth and Neptune-mass planets in multiple planet systems HD 47 186 and HD 181 433. *A&A*, 496:527–531, Mar. 2009. doi: 10.1051/0004-6361:200810669.

G. Boué, M. Oshagh, M. Montalto, and N. C. Santos. Degeneracy in the characterization of non-transiting planets from transit timing variations. *MNRAS*, 422:L57, May 2012. doi: 10.1111/j.1745-3933.2012.01236.x.

D. Brouwer and A. van Woerkom. *The secular variations of the orbital elements of the principal planets*. Astronomical papers prepared for the use of the American ephemeris and nautical almanac. U.S. Govt. Print. Off., 1950. URL `http://books.google.co.uk/books?id=z8xEAAAAIAAJ`.

T. M. Brown, D. Charbonneau, R. L. Gilliland, R. W. Noyes, and A. Burrows. Hubble Space Telescope Time-Series Photometry of the Transiting Planet of HD 209458. *ApJ*, 552:699–709, May 2001. doi: 10.1086/320580.

R. P. Butler and G. W. Marcy. A Planet Orbiting 47 Ursae Majoris. *ApJL*, 464:L153, June 1996. doi: 10.1086/310102.

R. P. Butler, G. W. Marcy, E. Williams, H. Hauser, and P. Shirts. Three New "51 Pegasi–Type" Planets. *ApJL*, 474:L115, Jan. 1997. doi: 10.1086/310444.

R. P. Butler, G. W. Marcy, D. A. Fischer, T. M. Brown, A. R. Contos, S. G. Korzennik, P. Nisenson, and R. W. Noyes. Evidence for Multiple Companions to Andromedae. *ApJ*, 526:916–927, Dec. 1999. doi: 10.1086/308035.

R. P. Butler, J. T. Wright, G. W. Marcy, D. A. Fischer, S. S. Vogt, C. G. Tinney, H. R. A. Jones, B. D. Carter, J. A. Johnson, C. McCarthy, and A. J. Penny. Catalog of Nearby Exoplanets. *ApJ*, 646:505–522, July 2006. doi: 10.1086/504701.

G. Campanella. Treating dynamical stability as an observable: a 5:2 mean motion resonance configuration for the extrasolar system HD 181433. *MNRAS*, 418:1028–1038, Dec. 2011. doi: 10.1111/j.1365-2966.2011.19553.x.

G. Campanella, R. P. Nelson, and C. B. Agnor. Possible scenarios for eccentricity evolution in the extrasolar planetary system HD 181433. *ArXiv e-prints*, May 2013.

B. Campbell and G. A. H. Walker. Precision radial velocities with an absorption cell. *PASP*, 91:540–545, Aug. 1979. doi: 10.1086/130535.

B. Campbell, G. A. H. Walker, and S. Yang. A search for substellar companions to solar-type stars. *ApJ*, 331:902–921, Aug. 1988. doi: 10.1086/166608.

J. A. Carter, J. C. Yee, J. Eastman, B. S. Gaudi, and J. N. Winn. Analytic Approximations for Transit Light-Curve Observables, Uncertainties, and Covariances. *ApJ*, 689:499–512, Dec. 2008. doi: 10.1086/592321.

J. E. Chambers. A hybrid symplectic integrator that permits close encounters between massive bodies. *MNRAS*, 304:793–799, Apr. 1999. doi: 10.1046/j.1365-8711.1999.02379.x.

D. Charbonneau, T. M. Brown, D. W. Latham, and M. Mayor. Detection of Planetary Transits Across a Sun-like Star. *ApJL*, 529:L45–L48, Jan. 2000. doi: 10.1086/312457.

S. Chatterjee, E. B. Ford, S. Matsumura, and F. A. Rasio. Dynamical Outcomes of Planet-Planet Scattering. *ApJ*, 686:580–602, Oct. 2008. doi: 10.1086/590227.

G. Chauvin, A.-M. Lagrange, C. Dumas, B. Zuckerman, D. Mouillet, I. Song, J.-L. Beuzit, and P. Lowrance. Giant planet companion to 2MASSW J1207334-393254. *A&A*, 438:L25–L28, Aug. 2005. doi: 10.1051/0004-6361:200500116.

W. D. Cochran, D. C. Fabrycky, G. Torres, F. Fressin, J.-M. Désert, D. Ragozzine, D. Sasselov, J. J. Fortney, J. F. Rowe, E. J. Brugamyer, S. T. Bryson, J. A. Carter, D. R. Ciardi, S. B. Howell, J. H. Steffen, W. J. Borucki, D. G. Koch, J. N. Winn, W. F. Welsh, K. Uddin, P. Tenenbaum, M. Still, S. Seager, S. N. Quinn, F. Mullally, N. Miller, G. W. Marcy, P. J. MacQueen, P. Lucas, J. J. Lissauer, D. W. Latham, H. Knutson, K. Kinemuchi, J. A. Johnson, J. M. Jenkins, H. Isaacson, A. Howard, E. Horch, M. J. Holman, C. E. Henze, M. R. Haas, R. L. Gilliland, T. N. Gautier, III, E. B. Ford, D. A. Fischer, M. Everett, M. Endl, B.-O. Demory, D. Deming, D. Charbonneau, D. Caldwell, L. Buchhave, T. M. Brown, and N. Batalha. Kepler-18b, c, and d: A System of Three Planets Confirmed by Transit Timing Variations, Light Curve Validation, Warm-Spitzer Photometry, and Radial Velocity Measurements. *ApJS*, 197:7, Nov. 2011. doi: 10.1088/0067-0049/197/1/7.

A. C. M. Correia, S. Udry, M. Mayor, J. Laskar, D. Naef, F. Pepe, D. Queloz, and N. C. Santos. The CORALIE survey for southern extra-solar planets. XIII. A pair of planets around HD202206 or a circumbinary planet? *A&A*, 440:751–758, Sept. 2005. doi: 10.1051/0004-6361:20042376.

A. C. M. Correia, J. Couetdic, J. Laskar, X. Bonfils, M. Mayor, J.-L. Bertaux, F. Bouchy, X. Delfosse, T. Forveille, C. Lovis, F. Pepe, C. Perrier, D. Queloz, and S. Udry. The HARPS search for southern extra-solar planets. XIX. Characterization and dynamics of the GJ 876 planetary system. *A&A*, 511:A21, Feb. 2010. doi: 10.1051/0004-6361/200912700.

J. L. Coughlin, G. S. Stringfellow, A. C. Becker, M. López-Morales, F. Mezzalira, and T. Krajci. New Observations and a Possible Detection of Parameter Variations in the Transits of Gliese 436b. *ApJL*, 689:L149–L152, Dec. 2008. doi: 10.1086/595822.

A. Crida, Z. Sándor, and W. Kley. Influence of an inner disc on the orbital evolution of massive planets migrating in resonance. *A&A*, 483:325–337, May 2008. doi: 10.1051/0004-6361:20079291.

S. Csizmadia, S. Renner, P. Barge, E. Agol, S. Aigrain, R. Alonso, J.-M. Almenara, A. S. Bonomo, P. Bordé, F. Bouchy, J. Cabrera, H. J. Deeg, R. de La Reza, M. Deleuil, R. Dvorak, A. Erikson, E. W. Guenther, M. Fridlund, P. Gondoin, T. Guillot, A. Hatzes, L. Jorda, H. Lammer, C. Lázaro, A. Léger, A. Llebaria, P. Magain, C. Moutou, M. Ollivier, M. Pätzold, D. Queloz, H. Rauer, D. Rouan, J. Schneider, G. Wuchterl, and D. Gandolfi. Transit timing analysis of CoRoT-1b. *A&A*, 510:A94, Feb. 2010. doi: 10.1051/0004-6361/200912052.

A. Cumming. Detectability of extrasolar planets in radial velocity surveys. *MNRAS*, 354:1165–1176, Nov. 2004. doi: 10.1111/j.1365-2966.2004.08275.x.

A. Cumming, R. P. Butler, G. W. Marcy, S. S. Vogt, J. T. Wright, and D. A. Fischer. The Keck Planet Search: Detectability and the Minimum Mass and Orbital Period Distribution of Extrasolar Planets. *PASP*, 120:531–554, May 2008. doi: 10.1086/588487.

S. Curiel, J. Cantó, L. Georgiev, C. E. Chávez, and A. Poveda. A fourth planet orbiting Andromedae. *A&A*, 525:A78, Jan. 2011. doi: 10.1051/0004-6361/201015693.

J. M. A. Danby. *Fundamentals of celestial mechanics*. 1988.

T. J. Deeming. Fourier Analysis with Unequally-Spaced Data. , 36:137–158, Aug. 1975. doi: 10.1007/BF00681947.

D. Deming, J. Harrington, G. Laughlin, S. Seager, S. B. Navarro, W. C. Bowman, and K. Horning. Spitzer Transit and Secondary Eclipse Photometry of GJ 436b. *ApJL*, 667: L199–L202, Oct. 2007. doi: 10.1086/522496.

R. F. Díaz, P. Rojo, M. Melita, S. Hoyer, D. Minniti, P. J. D. Mauas, and M. T. Ruíz. Detection of Period Variations in Extrasolar Transiting Planet OGLE-TR-111b. *ApJL*, 682:L49–L52, July 2008. doi: 10.1086/590907.

X. Dumusque, F. Pepe, C. Lovis, D. Ségransan, J. Sahlmann, W. Benz, F. Bouchy, M. Mayor, D. Queloz, N. Santos, and S. Udry. An Earth-mass planet orbiting α Centauri B. *Nature*, 491:207–211, Nov. 2012. doi: 10.1038/nature11572.

R. G. Edgar. Giant Planet Migration in Viscous Power-Law Disks. *ApJ*, 663:1325–1334, July 2007. doi: 10.1086/518591.

D. Fabrycky and S. Tremaine. Shrinking Binary and Planetary Orbits by Kozai Cycles with Tidal Friction. *ApJ*, 669:1298–1315, Nov. 2007. doi: 10.1086/521702.

D. C. Fabrycky, E. B. Ford, J. H. Steffen, J. F. Rowe, J. A. Carter, A. V. Moorhead, N. M. Batalha, W. J. Borucki, S. Bryson, L. A. Buchhave, J. L. Christiansen, D. R. Ciardi, W. D. Cochran, M. Endl, M. N. Fanelli, D. Fischer, F. Fressin, J. Geary, M. R. Haas, J. R. Hall, M. J. Holman, J. M. Jenkins, D. G. Koch, D. W. Latham, J. Li, J. J. Lissauer, P. Lucas, G. W. Marcy, T. Mazeh, S. McCauliff, S. Quinn, D. Ragozzine, D. Sasselov, and A. Shporer. Transit Timing Observations from Kepler. IV. Confirmation of Four Multiple-planet Systems by Simple Physical Models. *ApJ*, 750:114, May 2012a. doi: 10.1088/0004-637X/750/2/114.

D. C. Fabrycky, J. J. Lissauer, D. Ragozzine, J. F. Rowe, E. Agol, T. Barclay, N. Batalha, W. Borucki, D. R. Ciardi, E. B. Ford, J. C. Geary, M. J. Holman, J. M. Jenkins, J. Li, R. C. Morehead, A. Shporer, J. C. Smith, J. H. Steffen, and M. Still. Architecture of Kepler's Multi-transiting Systems: II. New investigations with twice as many candidates. *ArXiv e-prints*, Feb. 2012b.

D. A. Fischer, G. W. Marcy, R. P. Butler, S. S. Vogt, G. Laughlin, G. W. Henry, D. Abouav, K. M. G. Peek, J. T. Wright, J. A. Johnson, C. McCarthy, and H. Isaacson. Five Planets Orbiting 55 Cancri. *ApJ*, 675:790–801, Mar. 2008. doi: 10.1086/525512.

M. J. Fogg and R. P. Nelson. The effect of type I migration on the formation of terrestrial planets in hot-Jupiter systems. *A&A*, 472:1003–1015, Sept. 2007. doi: 10.1051/0004-6361:20077950.

E. B. Ford and M. J. Holman. Using Transit Timing Observations to Search for Trojans of Transiting Extrasolar Planets. *ApJL*, 664:L51–L54, July 2007. doi: 10.1086/520579.

E. B. Ford and F. A. Rasio. Origins of Eccentric Extrasolar Planets: Testing the Planet-Planet Scattering Model. *ApJ*, 686:621–636, Oct. 2008. doi: 10.1086/590926.

E. B. Ford, J. F. Rowe, D. C. Fabrycky, J. A. Carter, M. J. Holman, J. J. Lissauer, D. Ragozzine, J. H. Steffen, N. M. Batalha, W. J. Borucki, S. Bryson, D. A. Caldwell, E. W. Dunham, T. N. Gautier, III, J. M. Jenkins, D. G. Koch, J. Li, P. Lucas, G. W. Marcy, S. McCauliff, F. R. Mullally, E. Quintana, M. Still, P. Tenenbaum, S. E. Thompson, and J. D. Twicken. Transit Timing Observations from Kepler. I. Statistical Analysis of the First Four Months. *ApJS*, 197:2, Nov. 2011. doi: 10.1088/0067-0049/197/1/2.

E. B. Ford, D. C. Fabrycky, J. H. Steffen, J. A. Carter, F. Fressin, M. J. Holman, J. J. Lissauer, A. V. Moorhead, R. C. Morehead, D. Ragozzine, J. F. Rowe, W. F. Welsh, C. Allen, N. M. Batalha, W. J. Borucki, S. T. Bryson, L. A. Buchhave, C. J. Burke, D. A. Caldwell, D. Charbonneau, B. D. Clarke, W. D. Cochran, J.-M. Désert, M. Endl, M. E. Everett, D. A. Fischer, T. N. Gautier, III, R. L. Gilliland, J. M. Jenkins, M. R. Haas, E. Horch, S. B. Howell, K. A. Ibrahim, H. Isaacson, D. G. Koch, D. W. Latham, J. Li, P. Lucas, P. J. MacQueen, G. W. Marcy, S. McCauliff, F. R. Mullally, S. N. Quinn, E. Quintana, A. Shporer, M. Still, P. Tenenbaum, S. E. Thompson, G. Torres, J. D. Twicken, B. Wohler, and Kepler Science Team. Transit Timing Observations from Kepler. II. Confirmation of Two Multiplanet Systems via a Non-parametric Correlation Analysis. *ApJ*, 750:113, May 2012. doi: 10.1088/0004-637X/750/2/113.

T. N. Gautier, III, D. Charbonneau, J. F. Rowe, G. W. Marcy, H. Isaacson, G. Torres, F. Fressin, L. A. Rogers, J.-M. Désert, L. A. Buchhave, D. W. Latham, S. N. Quinn, D. R. Ciardi, D. C. Fabrycky, E. B. Ford, R. L. Gilliland, L. M. Walkowicz, S. T. Bryson, W. D. Cochran, M. Endl, D. A. Fischer, S. B. Howell, E. P. Horch, T. Barclay, N. Batalha, W. J. Borucki, J. L. Christiansen, J. C. Geary, C. E. Henze, M. J. Holman, K. Ibrahim, J. M. Jenkins, K. Kinemuchi, D. G. Koch, J. J. Lissauer, D. T. Sanderfer, D. D. Sasselov, S. Seager, K. Silverio, J. C. Smith, M. Still, M. C. Stumpe, P. Tenenbaum, and J. Van Cleve. Kepler-20: A Sun-like Star with Three Sub-Neptune Exoplanets and Two Earth-size Candidates. *ApJ*, 749:15, Apr. 2012. doi: 10.1088/0004-637X/749/1/15.

R. L. Gilliland and S. L. Baliunas. Objective characterization of stellar activity cycles. I - Methods and solar cycle analyses. *ApJ*, 314:766–781, Mar. 1987. doi: 10.1086/165103.

R. L. Gilliland, W. J. Chaplin, E. W. Dunham, V. S. Argabright, W. J. Borucki, G. Basri, S. T. Bryson, D. L. Buzasi, D. A. Caldwell, Y. P. Elsworth, J. M. Jenkins, D. G. Koch, J. Kolodziejczak, A. Miglio, J. van Cleve, L. M. Walkowicz, and W. F. Welsh. Kepler Mission Stellar and Instrument Noise Properties. *ApJS*, 197:6, Nov. 2011. doi: 10.1088/0067-0049/197/1/6.

R. L. Gilliland, G. W. Marcy, J. F. Rowe, L. Rogers, G. Torres, F. Fressin, E. D. Lopez, L. A. Buchhave, J. Christensen-Dalsgaard, J.-M. Désert, C. E. Henze, H. Isaacson, J. M. Jenkins, J. J. Lissauer, W. J. Chaplin, S. Basu, T. S. Metcalfe, Y. Elsworth, R. Handberg, S. Hekker, D. Huber, C. Karoff, H. Kjeldsen, M. N. Lund, M. Lundkvist, A. Miglio, D. Charbonneau, E. B. Ford, J. J. Fortney, M. R. Haas, A. W. Howard, S. B. Howell, D. Ragozzine, and S. E. Thompson. Kepler-68: Three Planets, One with a Density between that of Earth and Ice Giants. *ApJ*, 766:40, Mar. 2013. doi: 10.1088/0004-637X/766/1/40.

P. Goldreich and S. Soter. Q in the Solar System. , 5:375–389, 1966. doi: 10.1016/0019-1035(66)90051-0.

P. Goldreich and S. Tremaine. Disk-satellite interactions. *ApJ*, 241:425–441, Oct. 1980. doi: 10.1086/158356.

K. Goździewski and C. Migaszewski. Is the HR8799 extrasolar system destined for planetary scattering? *MNRAS*, 397:L16–L20, July 2009. doi: 10.1111/j.1745-3933.2009.00674.x.

K. Goździewski, M. Konacki, and A. J. Maciejewski. Where is the Second Planet in the HD 160691 Planetary System? *ApJ*, 594:1019–1032, Sept. 2003. doi: 10.1086/376969.

K. Goździewski, M. Konacki, and A. J. Maciejewski. Orbital Configurations and Dynamical Stability of Multiplanet Systems around Sun-like Stars HD 202206, 14 Herculis, HD 37124, and HD 108874. *ApJ*, 645:688–703, July 2006. doi: 10.1086/504030.

K. Goździewski, C. Migaszewski, and A. Musieliński. Stability constraints in modeling of multi-planet extrasolar systems. In Y.-S. Sun, S. Ferraz-Mello, and J.-L. Zhou, editors, *IAU Symposium*, volume 249 of *IAU Symposium*, pages 447–460, May 2008. doi: 10.1017/S1743921308016967.

P.-G. Gu, D. N. C. Lin, and P. H. Bodenheimer. The Effect of Tidal Inflation Instability on the Mass and Dynamical Evolution of Extrasolar Planets with Ultrashort Periods. *ApJ*, 588:509–534, May 2003. doi: 10.1086/373920.

T. Guillot, A. Burrows, W. B. Hubbard, J. I. Lunine, and D. Saumon. Giant Planets at Small Orbital Distances. *ApJL*, 459:L35, Mar. 1996. doi: 10.1086/309935.

J. D. Hartman, G. Bakos, K. Z. Stanek, and R. W. Noyes. HATNET Variability Survey in the High Stellar Density "Kepler Field" with Millimagnitude Image Subtraction Photometry. *AJ*, 128:1761–1783, Oct. 2004. doi: 10.1086/423920.

A. P. Hatzes, W. D. Cochran, M. Endl, B. McArthur, D. B. Paulson, G. A. H. Walker, B. Campbell, and S. Yang. A Planetary Companion to γ Cephei A. *ApJ*, 599:1383–1394, Dec. 2003. doi: 10.1086/379281.

G. W. Henry, G. W. Marcy, R. P. Butler, and S. S. Vogt. A Transiting "51 Peg-like" Planet. *ApJL*, 529:L41–L44, Jan. 2000. doi: 10.1086/312458.

W. Herbst, C. A. L. Bailer-Jones, R. Mundt, K. Meisenheimer, and R. Wackermann. Stellar rotation and variability in the Orion Nebula Cluster. *A&A*, 396:513–532, Dec. 2002. doi: 10.1051/0004-6361:20021362.

M. J. Holman and N. W. Murray. The Use of Transit Timing to Detect Terrestrial-Mass Extrasolar Planets. *Science*, 307:1288–1291, Feb. 2005. doi: 10.1126/science.1107822.

M. J. Holman, D. C. Fabrycky, D. Ragozzine, E. B. Ford, J. H. Steffen, W. F. Welsh, J. J. Lissauer, D. W. Latham, G. W. Marcy, L. M. Walkowicz, N. M. Batalha, J. M. Jenkins, J. F. Rowe, W. D. Cochran, F. Fressin, G. Torres, L. A. Buchhave, D. D. Sasselov, W. J. Borucki, D. G. Koch, G. Basri, T. M. Brown, D. A. Caldwell, D. Charbonneau, E. W. Dunham, T. N. Gautier, J. C. Geary, R. L. Gilliland, M. R. Haas, S. B. Howell, D. R. Ciardi, M. Endl, D. Fischer, G. Fürész, J. D. Hartman, H. Isaacson, J. A. Johnson, P. J. MacQueen, A. V. Moorhead, R. C. Morehead, and J. A. Orosz. Kepler-9: A System of Multiple Planets Transiting a Sun-Like Star, Confirmed by Timing Variations. *Science*, 330:51–, Oct. 2010. doi: 10.1126/science.1195778.

P. Hut, J. Makino, and S. McMillan. Building a better leapfrog. *ApJL*, 443:L93–L96, Apr. 1995. doi: 10.1086/187844.

L. Ibgui and A. Burrows. Coupled Evolution with Tides of the Radius and Orbit of Transiting Giant Planets: General Results. *ApJ*, 700:1921–1932, Aug. 2009. doi: 10.1088/0004-637X/700/2/1921.

S. Ida and D. N. C. Lin. Toward a Deterministic Model of Planetary Formation. I. A Desert in the Mass and Semimajor Axis Distributions of Extrasolar Planets. *ApJ*, 604:388–413, Mar. 2004. doi: 10.1086/381724.

L. Iorio. On the possibility of measuring the solar oblateness and some relativistic effects from planetary ranging. *A&A*, 433:385–393, Apr. 2005. doi: 10.1051/0004-6361:20047155.

B. Jackson, R. Greenberg, and R. Barnes. Tidal Evolution of Close-in Extrasolar Planets. *ApJ*, 678:1396–1406, May 2008. doi: 10.1086/529187.

B. Jackson, N. Miller, R. Barnes, S. N. Raymond, J. J. Fortney, and R. Greenberg. The roles of tidal evolution and evaporative mass loss in the origin of CoRoT-7 b. *MNRAS*, 407:910–922, Sept. 2010. doi: 10.1111/j.1365-2966.2010.17012.x.

M. Jurić and S. Tremaine. Dynamical Origin of Extrasolar Planet Eccentricity Distribution. *ApJ*, 686:603–620, Oct. 2008. doi: 10.1086/590047.

J. Kenney and E. Keeping. *Mathematics of statistics*. Number v. 1 in Mathematics of Statistics. Van Nostrand company, 1954. URL `http://books.google.co.uk/books?id=hBnvAAAAMAAJ`.

J. A. Ketchum, F. C. Adams, and A. M. Bloch. Effects of Turbulence, Eccentricity Damping, and Migration Rate on the Capture of Planets into Mean Motion Resonance. *ApJ*, 726:53, Jan. 2011. doi: 10.1088/0004-637X/726/1/53.

J. A. Ketchum, F. C. Adams, and A. M. Bloch. Mean Motion Resonances in Exoplanet Systems: An Investigation Into Nodding Behavior. *ArXiv e-prints*, Nov. 2012.

D. Kipping and G. Bakos. Analysis of Kepler's Short-cadence Photometry for TrES-2b. *ApJ*, 733:36, May 2011. doi: 10.1088/0004-637X/733/1/36.

D. M. Kipping. Transiting planets - light-curve analysis for eccentric orbits. *MNRAS*, 389:1383–1390, Sept. 2008. doi: 10.1111/j.1365-2966.2008.13658.x.

D. M. Kipping. Transit timing effects due to an exomoon. *MNRAS*, 392:181–189, Jan. 2009a. doi: 10.1111/j.1365-2966.2008.13999.x.

D. M. Kipping. Transit timing effects due to an exomoon - II. *MNRAS*, 396:1797–1804, July 2009b. doi: 10.1111/j.1365-2966.2009.14869.x.

D. M. Kipping, S. J. Fossey, and G. Campanella. On the detectability of habitable exomoons with Kepler-class photometry. *MNRAS*, 400:398–405, Nov. 2009. doi: 10.1111/j.1365-2966.2009.15472.x.

Y. Kozai. Secular perturbations of asteroids with high inclination and eccentricity. *AJ*, 67:591, Nov. 1962. doi: 10.1086/108790.

J. Laskar and A. C. M. Correia. HD 60532, a planetary system in a 3:1 mean motion resonance. *A&A*, 496:L5–L8, Mar. 2009. doi: 10.1051/0004-6361/200911689.

D. W. Latham, R. P. Stefanik, T. Mazeh, M. Mayor, and G. Burki. The unseen companion of HD114762 - A probable brown dwarf. *Nature*, 339:38–40, May 1989. doi: 10.1038/339038a0.

P. Lawson, W. Traub, S. Unwin, U. S. N. Aeronautics, S. Administration, and J. P. L. (U.S.). *Exoplanet Community Report*. JPL publication. Jet Propulsion Laboratory, California Institute of Technology, 2009. URL `http://books.google.co.uk/books?id=NOMUYAAACAAJ`.

M. H. Lee and S. J. Peale. Dynamics and Origin of the 2:1 Orbital Resonances of the GJ 876 Planets. *ApJ*, 567:596–609, Mar. 2002. doi: 10.1086/338504.

M. H. Lee and S. J. Peale. Secular Evolution of Hierarchical Planetary Systems. *ApJ*, 592:1201–1216, Aug. 2003. doi: 10.1086/375857.

A. Léger, D. Rouan, J. Schneider, P. Barge, M. Fridlund, B. Samuel, M. Ollivier, E. Guenther, M. Deleuil, H. J. Deeg, M. Auvergne, R. Alonso, S. Aigrain, A. Alapini, J. M. Almenara, A. Baglin, M. Barbieri, H. Bruntt, P. Bordé, F. Bouchy, J. Cabrera, C. Catala, L. Carone, S. Carpano, S. Csizmadia, R. Dvorak, A. Erikson, S. Ferraz-Mello, B. Foing, F. Fressin, D. Gandolfi, M. Gillon, P. Gondoin, O. Grasset, T. Guillot, A. Hatzes, G. Hébrard, L. Jorda, H. Lammer, A. Llebaria, B. Loeillet, M. Mayor, T. Mazeh, C. Moutou, M. Pätzold, F. Pont, D. Queloz, H. Rauer, S. Renner, R. Samadi, A. Shporer, C. Sotin, B. Tingley, G. Wuchterl, M. Adda, P. Agogu, T. Appourchaux, H. Ballans, P. Baron, T. Beaufort, R. Bellenger, R. Berlin, P. Bernardi, D. Blouin, F. Baudin, P. Bodin, L. Boisnard, L. Boit, F. Bonneau, S. Borzeix, R. Briet, J.-T. Buey, B. Butler, D. Cailleau, R. Cautain, P.-Y. Chabaud, S. Chaintreuil, F. Chiavassa, V. Costes, V. Cuna Parrho, F. de Oliveira Fialho, M. Decaudin, J.-M. Defise, S. Djalal, G. Epstein, G.-E. Exil, C. Fauré, T. Fenouillet, A. Gaboriaud, A. Gallic, P. Gamet, P. Gavalda, E. Grolleau, R. Gruneisen, L. Gueguen, V. Guis, V. Guivarc'h, P. Guterman, D. Hallouard, J. Hasiba, F. Heuripeau, G. Huntzinger, H. Hustaix, C. Imad, C. Imbert, B. Johlander, M. Jouret, P. Journoud, F. Karioty, L. Kerjean, V. Lafaille, L. Lafond, T. Lam-Trong, P. Landiech, V. Lapeyrere, T. Larqué, P. Laudet, N. Lautier, H. Lecann, L. Lefevre, B. Leruyet, P. Levacher, A. Magnan, E. Mazy, F. Mertens, J.-M. Mesnager, J.-C. Meunier, J.-P. Michel, W. Monjoin, D. Naudet, K. Nguyen-Kim, J.-L. Orcesi, H. Ottacher, R. Perez, G. Peter, P. Plasson, J.-Y. Plesseria, B. Pontet, A. Pradines, C. Quentin, J.-L. Reynaud, G. Rolland, F. Rollenhagen, R. Romagnan, N. Russ, R. Schmidt, N. Schwartz, I. Sebbag, G. Sedes, H. Smit, M. B. Steller, W. Sunter, C. Surace, M. Tello, D. Tiphène, P. Toulouse, B. Ulmer, O. Vandermarcq, E. Vergnault, A. Vuillemin, and P. Zanatta. Transiting exoplanets from the CoRoT space mission. VIII. CoRoT-7b: the first super-Earth with measured radius. *A&A*, 506:287–302, Oct. 2009. doi: 10.1051/0004-6361/200911933.

H. F. Levison and M. J. Duncan. The long-term dynamical behavior of short-period comets. , 108:18–36, Mar. 1994. doi: 10.1006/icar.1994.1039.

A.-S. Libert and S. Renner. Detection of Laplace-resonant three-planet systems from transit timing variations. *MNRAS*, 430:1369–1375, Apr. 2013. doi: 10.1093/mnras/sts722.

A.-S. Libert and K. Tsiganis. Kozai resonance in extrasolar systems. *A&A*, 493:677–686, Jan. 2009. doi: 10.1051/0004-6361:200810843.

R. Ligi, D. Mourard, A. M. Lagrange, K. Perraut, T. Boyajian, P. Bério, N. Nardetto, I. Tallon-Bosc, H. McAlister, T. ten Brummelaar, S. Ridgway, J. Sturmann, L. Sturmann, N. Turner, C. Farrington, and P. J. Goldfinger. A new interferometric study of four exoplanet host stars: Cygni, 14 Andromedae, Andromedae and 42 Draconis. *A&A*, 545:A5, Sept. 2012. doi: 10.1051/0004-6361/201219467.

D. N. C. Lin and J. Papaloizou. On the tidal interaction between protoplanets and the protoplanetary disk. III - Orbital migration of protoplanets. *ApJ*, 309:846–857, Oct. 1986. doi: 10.1086/164653.

D. N. C. Lin, P. Bodenheimer, and D. C. Richardson. Orbital migration of the planetary companion of 51 Pegasi to its present location. *Nature*, 380:606–607, Apr. 1996. doi: 10.1038/380606a0.

M.-K. Lin and J. C. B. Papaloizou. Type III migration in a low-viscosity disc. *MNRAS*, 405:1473–1490, July 2010. doi: 10.1111/j.1365-2966.2010.16560.x.

J. J. Lissauer, D. C. Fabrycky, E. B. Ford, W. J. Borucki, F. Fressin, G. W. Marcy, J. A. Orosz, J. F. Rowe, G. Torres, W. F. Welsh, N. M. Batalha, S. T. Bryson, L. A. Buchhave, D. A. Caldwell, J. A. Carter, D. Charbonneau, J. L. Christiansen, W. D. Cochran, J.-M. Desert, E. W. Dunham, M. N. Fanelli, J. J. Fortney, T. N. Gautier, III, J. C. Geary, R. L. Gilliland, M. R. Haas, J. R. Hall, M. J. Holman, D. G. Koch, D. W. Latham, E. Lopez, S. McCauliff, N. Miller, R. C. Morehead, E. V. Quintana, D. Ragozzine, D. Sasselov, D. R. Short, and J. H. Steffen. A closely packed system of low-mass, low-density planets transiting Kepler-11. *Nature*, 470:53–58, Feb. 2011a. doi: 10.1038/nature09760.

J. J. Lissauer, D. Ragozzine, D. C. Fabrycky, J. H. Steffen, E. B. Ford, J. M. Jenkins, A. Shporer, M. J. Holman, J. F. Rowe, E. V. Quintana, N. M. Batalha, W. J. Borucki, S. T. Bryson, D. A. Caldwell, J. A. Carter, D. Ciardi, E. W. Dunham, J. J. Fortney, T. N. Gautier, III, S. B. Howell, D. G. Koch, D. W. Latham, G. W. Marcy, R. C. Morehead, and D. Sasselov. Architecture and Dynamics of Kepler's Candidate Multiple Transiting Planet Systems. *ApJS*, 197:8, Nov. 2011b. doi: 10.1088/0067-0049/197/1/8.

J. J. Lissauer, D. Jontof-Hutter, J. F. Rowe, D. C. Fabrycky, E. D. Lopez, E. Agol, G. W. Marcy, K. M. Deck, D. A. Fischer, J. J. Fortney, S. B. Howell, H. Isaacson, J. M. Jenkins, R. Kolbl, D. Sasselov, D. R. Short, and W. F. Welsh. All Six Planets Known to Orbit Kepler-11 Have Low Densities. *ApJ*, 770:131, June 2013. doi: 10.1088/0004-637X/770/2/131.

G. Lo Curto, M. Mayor, W. Benz, F. Bouchy, C. Lovis, C. Moutou, D. Naef, F. Pepe, D. Queloz, N. C. Santos, D. Segransan, and S. Udry. The HARPS search for southern extra-solar planets . XXII. Multiple planet systems from the HARPS volume limited sample. *A&A*, 512:A48, Mar. 2010. doi: 10.1051/0004-6361/200913523.

N. R. Lomb. Least-squares frequency analysis of unequally spaced data. , 39:447–462, Feb. 1976. doi: 10.1007/BF00648343.

C. Lovis, M. Mayor, F. Pepe, Y. Alibert, W. Benz, F. Bouchy, A. C. M. Correia, J. Laskar, C. Mordasini, D. Queloz, N. C. Santos, S. Udry, J.-L. Bertaux, and J.-P. Sivan. An extrasolar planetary system with three Neptune-mass planets. *Nature*, 441:305–309, May 2006. doi: 10.1038/nature04828.

C. Lovis, D. Ségransan, M. Mayor, S. Udry, W. Benz, J.-L. Bertaux, F. Bouchy, A. C. M. Correia, J. Laskar, G. Lo Curto, C. Mordasini, F. Pepe, D. Queloz, and N. C. Santos. The HARPS search for southern extra-solar planets. XXVIII. Up to seven planets orbiting HD 10180: probing the architecture of low-mass planetary systems. *A&A*, 528: A112, Apr. 2011. doi: 10.1051/0004-6361/201015577.

G. Maciejewski, D. Dimitrov, R. Neuhäuser, N. Tetzlaff, A. Niedzielski, S. Raetz, W. P. Chen, F. Walter, C. Marka, S. Baar, T. Krejcová, J. Budaj, V. Krushevska, K. Tachihara, H. Takahashi, and M. Mugrauer. Transit timing variation and activity in the WASP-10 planetary system. *MNRAS*, 411:1204–1212, Feb. 2011. doi: 10.1111/j.1365-2966.2010.17753.x.

R. Malhotra. Orbital Resonances and Chaos in the Solar System. In D. Lazzaro, R. Vieira Martins, S. Ferraz-Mello, and J. Fernandez, editors, *Solar System Formation and Evolution*, volume 149 of *Astronomical Society of the Pacific Conference Series*, page 37, 1998.

R. Malhotra, K. Fox, C. D. Murray, and P. D. Nicholson. Secular perturbations of the Uranian satellites - Theory and practice. *A&A*, 221:348–358, Sept. 1989.

A. M. Mandell and S. Sigurdsson. Survival of Terrestrial Planets in the Presence of Giant Planet Migration. *ApJL*, 599:L111–L114, Dec. 2003. doi: 10.1086/381245.

C. Marchal and G. Bozis. Hill Stability and Distance Curves for the General Three-Body Problem. *Celestial Mechanics*, 26:311–333, Mar. 1982. doi: 10.1007/BF01230725.

G. W. Marcy and R. P. Butler. A Planetary Companion to 70 Virginis. *ApJL*, 464:L147, June 1996. doi: 10.1086/310096.

G. W. Marcy, R. P. Butler, S. S. Vogt, D. Fischer, and J. J. Lissauer. A Planetary Companion to a Nearby M4 Dwarf, Gliese 876. *ApJL*, 505:L147–L149, Oct. 1998. doi: 10.1086/311623.

G. W. Marcy, R. P. Butler, D. Fischer, S. S. Vogt, J. J. Lissauer, and E. J. Rivera. A Pair of Resonant Planets Orbiting GJ 876. *ApJ*, 556:296–301, July 2001. doi: 10.1086/321552.

G. W. Marcy, R. P. Butler, S. S. Vogt, D. A. Fischer, G. W. Henry, G. Laughlin, J. T. Wright, and J. A. Johnson. Five New Extrasolar Planets. *ApJ*, 619:570–584, Jan. 2005. doi: 10.1086/426384.

R. A. Mardling and D. N. C. Lin. On the Survival of Short-Period Terrestrial Planets. *ApJ*, 614:955–959, Oct. 2004. doi: 10.1086/423794.

C. Marois, B. Macintosh, T. Barman, B. Zuckerman, I. Song, J. Patience, D. Lafrenière, and R. Doyon. Direct Imaging of Multiple Planets Orbiting the Star HR 8799. *Science*, 322:1348–, Nov. 2008. doi: 10.1126/science.1166585.

F. S. Masset and J. C. B. Papaloizou. Runaway Migration and the Formation of Hot Jupiters. *ApJ*, 588:494–508, May 2003. doi: 10.1086/373892.

F. S. Masset, A. Morbidelli, A. Crida, and J. Ferreira. Disk Surface Density Transitions as Protoplanet Traps. *ApJ*, 642:478–487, May 2006. doi: 10.1086/500967.

M. Mayor and D. Queloz. A Jupiter-mass companion to a solar-type star. *Nature*, 378: 355–359, Nov. 1995. doi: 10.1038/378355a0.

M. Mayor, X. Bonfils, T. Forveille, X. Delfosse, S. Udry, J.-L. Bertaux, H. Beust, F. Bouchy, C. Lovis, F. Pepe, C. Perrier, D. Queloz, and N. C. Santos. The HARPS search for southern extra-solar planets. XVIII. An Earth-mass planet in the GJ 581 planetary system. *A&A*, 507:487–494, Nov. 2009a. doi: 10.1051/0004-6361/200912172.

M. Mayor, S. Udry, C. Lovis, F. Pepe, D. Queloz, W. Benz, J.-L. Bertaux, F. Bouchy, C. Mordasini, and D. Segransan. The HARPS search for southern extra-solar planets. XIII. A planetary system with 3 super-Earths (4.2, 6.9, and 9.2 $M_{\L}$). *A&A*, 493:639–644, Jan. 2009b. doi: 10.1051/0004-6361:200810451.

B. E. McArthur, M. Endl, W. D. Cochran, G. F. Benedict, D. A. Fischer, G. W. Marcy, R. P. Butler, D. Naef, M. Mayor, D. Queloz, S. Udry, and T. E. Harrison. Detection of a Neptune-Mass Planet in the ρ^1 Cancri System Using the Hobby-Eberly Telescope. *ApJL*, 614:L81–L84, Oct. 2004. doi: 10.1086/425561.

S. Meschiari and G. P. Laughlin. Systemic: A Testbed for Characterizing the Detection of Extrasolar Planets. II. Numerical Approaches to the Transit Timing Inverse Problem. *ApJ*, 718:543–550, July 2010. doi: 10.1088/0004-637X/718/1/543.

S. Meschiari, A. S. Wolf, E. Rivera, G. Laughlin, S. Vogt, and P. Butler. Systemic: A Testbed for Characterizing the Detection of Extrasolar Planets. I. The Systemic Console Package. *PASP*, 121:1016–1027, Sept. 2009. doi: 10.1086/605730.

S. Meschiari, G. Laughlin, S. S. Vogt, R. P. Butler, E. J. Rivera, N. Haghighipour, and P. Jalowiczor. The Lick-Carnegie Survey: Four New Exoplanet Candidates. *ApJ*, 727: 117, Feb. 2011. doi: 10.1088/0004-637X/727/2/117.

A. Milani and A. M. Nobili. On topological stability in the general three-body problem. *Celestial Mechanics*, 31:213–240, Nov. 1983. doi: 10.1007/BF01844226.

N. Miller, J. J. Fortney, and B. Jackson. Inflating and Deflating Hot Jupiters: Coupled Tidal and Thermal Evolution of Known Transiting Planets. *ApJ*, 702:1413–1427, Sept. 2009. doi: 10.1088/0004-637X/702/2/1413.

E. Miller-Ricci, J. F. Rowe, D. Sasselov, J. M. Matthews, R. Kuschnig, B. Croll, D. B. Guenther, A. F. J. Moffat, S. M. Rucinski, G. A. H. Walker, and W. W. Weiss. MOST Space-based Photometry of the Transiting Exoplanet System HD 189733: Precise Timing Measurements for Transits across an Active Star. *ApJ*, 682:593–601, July 2008. doi: 10.1086/587634.

J. Miralda-Escudé. Orbital Perturbations of Transiting Planets: A Possible Method to Measure Stellar Quadrupoles and to Detect Earth-Mass Planets. *ApJ*, 564:1019–1023, Jan. 2002. doi: 10.1086/324279.

A. V. Moorhead and F. C. Adams. Giant planet migration through the action of disk torques and planet planet scattering. , 178:517–539, Nov. 2005. doi: 10.1016/j.icarus.2005.05.005.

C. Moutou and F. Pont. Detection and characterization of extrasolar planets: the transit method. *Ecole de Goutelas*, 28:55–79, Mar. 2006.

C. D. Murray and A. C. M. Correia. *Keplerian Orbits and Dynamics of Exoplanets*, pages 15–23. 2011.

C. D. Murray and S. F. Dermott. *Solar system dynamics*. 1999.

N. Murray and M. Holman. The role of chaotic resonances in the Solar System. *Nature*, 410:773–779, Apr. 2001.

M. Nagasawa and D. N. C. Lin. The Dynamical Evolution of the Short-Period Extrasolar Planet around Andromedae in the Pre-Main-Sequence Stage. *ApJ*, 632:1140–1156, Oct. 2005. doi: 10.1086/433162.

M. Nagasawa, D. N. C. Lin, and E. Thommes. Dynamical Shake-up of Planetary Systems. I. Embryo Trapping and Induced Collisions by the Sweeping Secular Resonance and Embryo-Disk Tidal Interaction. *ApJ*, 635:578–598, Dec. 2005. doi: 10.1086/497386.

R. Narayan, A. Cumming, and D. N. C. Lin. Radial Velocity Detectability of Low-Mass Extrasolar Planets in Close Orbits. *ApJ*, 620:1002–1009, Feb. 2005. doi: 10.1086/426380.

V. Nascimbeni, G. Piotto, L. R. Bedin, M. Damasso, L. Malavolta, and L. Borsato. TASTE II. A new observational study of transit time variations in HAT-P-13b. *A&A*, 532:A24, Aug. 2011. doi: 10.1051/0004-6361/201116830.

J. A. Nelder and R. Mead. A simplex method for function minimization. *Computer Journal*, 7:308–313, 1965.

R. P. Nelson and J. C. B. Papaloizou. Possible commensurabilities among pairs of extrasolar planets. *MNRAS*, 333:L26–L30, June 2002. doi: 10.1046/j.1365-8711.2002.05506.x.

R. P. Nelson, J. C. B. Papaloizou, F. Masset, and W. Kley. The migration and growth of protoplanets in protostellar discs. *MNRAS*, 318:18–36, Oct. 2000. doi: 10.1046/j.1365-8711.2000.03605.x.

D. Nesvorný. Transit Timing Variations for Eccentric and Inclined Exoplanets. *ApJ*, 701:1116–1122, Aug. 2009. doi: 10.1088/0004-637X/701/2/1116.

D. Nesvorný and A. Morbidelli. Mass and Orbit Determination from Transit Timing Variations of Exoplanets. *ApJ*, 688:636–646, Nov. 2008. doi: 10.1086/592230.

D. Nesvorný, D. M. Kipping, L. A. Buchhave, G. Á. Bakos, J. Hartman, and A. R. Schmitt. The Detection and Characterization of a Nontransiting Planet by Transit Timing Variations. *Science*, 336:1133–, June 2012. doi: 10.1126/science.1221141.

D. Nesvorny, D. Kipping, D. Terrell, J. Hartman, G. A. Bakos, and L. A. Buchhave. KOI-142, the King of Transit Variations, is a Pair of Planets near the 2:1 Resonance. *ArXiv e-prints*, Apr. 2013.

A. Ofir and S. Dreizler. An Independent Planet Search In The Kepler Dataset. I. A hundred new candidates and revised KOIs. *ArXiv e-prints*, June 2012.

G. I. Ogilvie and D. N. C. Lin. Tidal Dissipation in Rotating Giant Planets. *ApJ*, 610:477–509, July 2004. doi: 10.1086/421454.

J. C. B. Papaloizou. Protoplanet magnetosphere interactions. *A&A*, 463:775–781, Feb. 2007. doi: 10.1051/0004-6361:20065414.

J. C. B. Papaloizou and R. P. Nelson. Models of accreting gas giant protoplanets in protostellar disks. *A&A*, 433:247–265, Apr. 2005. doi: 10.1051/0004-6361:20042029.

J. C. B. Papaloizou, R. P. Nelson, and F. Masset. Orbital eccentricity growth through disc-companion tidal interaction. *A&A*, 366:263–275, Jan. 2001. doi: 10.1051/0004-6361:20000011.

M. J. Payne, E. B. Ford, and D. Veras. Transit Timing Variations for Inclined and Retrograde Exoplanetary Systems. *ApJL*, 712:L86–L92, Mar. 2010. doi: 10.1088/2041-8205/712/1/L86.

F. Pepe, F. Bouchy, D. Queloz, and M. Mayor. From CORALIE to HARPS: Towards 1 Meter/Sec RV Precision. In D. Deming and S. Seager, editors, *Scientific Frontiers in Research on Extrasolar Planets*, volume 294 of *Astronomical Society of the Pacific Conference Series*, pages 39–42, 2003.

F. Pepe, A. C. M. Correia, M. Mayor, O. Tamuz, J. Couetdic, W. Benz, J.-L. Bertaux, F. Bouchy, J. Laskar, C. Lovis, D. Naef, D. Queloz, N. C. Santos, J.-P. Sivan, D. Sosnowska, and S. Udry. The HARPS search for southern extra-solar planets. VIII. <ASTROBJ>μ Arae</ASTROBJ>, a system with four planets. *A&A*, 462:769–776, Feb. 2007. doi: 10.1051/0004-6361:20066194.

F. A. Pepe and C. Lovis. From HARPS to CODEX: exploring the limits of Doppler measurements. *Physica Scripta Volume T*, 130(1):014007, Aug. 2008. doi: 10.1088/0031-8949/2008/T130/014007.

A. Pierens and R. P. Nelson. Constraints on resonant-trapping for two planets embedded in a protoplanetary disc. *A&A*, 482:333–340, Apr. 2008. doi: 10.1051/0004-6361:20079062.

R. L. Plackett. Some theorems in least squares. *Biometrika*, 37(1-2):149–157, 1950. doi: 10.1093/biomet/37.1-2.149. URL `http://biomet.oxfordjournals.org/content/37/1-2/149.short`.

E. Podlewska and E. Szuszkiewicz. A Super-Earth caught in a trap. *MNRAS*, 397:1995–2003, Aug. 2009. doi: 10.1111/j.1365-2966.2009.15107.x.

D. L. Pollacco, I. Skillen, A. Collier Cameron, D. J. Christian, C. Hellier, J. Irwin, T. A. Lister, R. A. Street, R. G. West, D. Anderson, W. I. Clarkson, H. Deeg, B. Enoch, A. Evans, A. Fitzsimmons, C. A. Haswell, S. Hodgkin, K. Horne, S. R. Kane, F. P. Keenan, P. F. L. Maxted, A. J. Norton, J. Osborne, N. R. Parley, R. S. I. Ryans, B. Smalley, P. J. Wheatley, and D. M. Wilson. The WASP Project and the SuperWASP Cameras. *PASP*, 118:1407–1418, Oct. 2006. doi: 10.1086/508556.

J. B. Pollack, O. Hubickyj, P. Bodenheimer, J. J. Lissauer, M. Podolak, and Y. Greenzweig. Formation of the Giant Planets by Concurrent Accretion of Solids and Gas. , 124:62–85, Nov. 1996. doi: 10.1006/icar.1996.0190.

W. H. Press, S. A. Teukolsky, W. T. Vetterling, and B. P. Flannery. *Numerical recipes in C. The art of scientific computing*. 1992.

D. Queloz, F. Bouchy, C. Moutou, A. Hatzes, G. Hébrard, R. Alonso, M. Auvergne, A. Baglin, M. Barbieri, P. Barge, W. Benz, P. Bordé, H. J. Deeg, M. Deleuil, R. Dvorak, A. Erikson, S. Ferraz Mello, M. Fridlund, D. Gandolfi, M. Gillon, E. Guenther, T. Guillot, L. Jorda, M. Hartmann, H. Lammer, A. Léger, A. Llebaria, C. Lovis, P. Magain, M. Mayor, T. Mazeh, M. Ollivier, M. Pätzold, F. Pepe, H. Rauer,

D. Rouan, J. Schneider, D. Segransan, S. Udry, and G. Wuchterl. The CoRoT-7 planetary system: two orbiting super-Earths. *A&A*, 506:303–319, Oct. 2009. doi: 10.1051/0004-6361/200913096.

A. C. Quillen. Reducing the probability of capture into resonance. *MNRAS*, 365:1367–1382, Feb. 2006. doi: 10.1111/j.1365-2966.2005.09826.x.

T. R. Quinn, S. Tremaine, and M. Duncan. A three million year integration of the earth's orbit. *AJ*, 101:2287–2305, June 1991. doi: 10.1086/115850.

F. A. Rasio and E. B. Ford. Dynamical instabilities and the formation of extrasolar planetary systems. *Science*, 274:954–956, Nov. 1996. doi: 10.1126/science.274.5289.954.

S. N. Raymond, A. M. Mandell, and S. Sigurdsson. Exotic Earths: Forming Habitable Worlds with Giant Planet Migration. *Science*, 313:1413–1416, Sept. 2006. doi: 10.1126/science.1130461.

S. N. Raymond, R. Barnes, P. J. Armitage, and N. Gorelick. Mean Motion Resonances from Planet-Planet Scattering. *ApJL*, 687:L107–L110, Nov. 2008. doi: 10.1086/593301.

E. J. Rivera, J. J. Lissauer, R. P. Butler, G. W. Marcy, S. S. Vogt, D. A. Fischer, T. M. Brown, G. Laughlin, and G. W. Henry. A ˜7.5 M_L Planet Orbiting the Nearby Star, GJ 876. *ApJ*, 634:625–640, Nov. 2005. doi: 10.1086/491669.

P. Robutel and J. Laskar. Frequency Map and Global Dynamics in the Solar System I. Short Period Dynamics of Massless Particles. , 152:4–28, July 2001. doi: 10.1006/icar.2000.6576.

J. P. Rozelot, S. Godier, and S. Lefebvre. On the theory of the oblateness of the Sun. , 198:223–240, Feb. 2001. doi: 10.1023/A:1005238718479.

A. Santerne, R. F. Díaz, C. Moutou, F. Bouchy, G. Hébrard, J.-M. Almenara, A. S. Bonomo, M. Deleuil, and N. C. Santos. SOPHIE velocimetry of Kepler transit candidates. VII. A false-positive rate of 35% for Kepler close-in giant candidates. *A&A*, 545:A76, Sept. 2012. doi: 10.1051/0004-6361/201219608.

J. D. Scargle. Studies in astronomical time series analysis. II - Statistical aspects of spectral analysis of unevenly spaced data. *ApJ*, 263:835–853, Dec. 1982. doi: 10.1086/160554.

S. Seager and G. Mallén-Ornelas. A Unique Solution of Planet and Star Parameters from an Extrasolar Planet Transit Light Curve. *ApJ*, 585:1038–1055, Mar. 2003. doi: 10.1086/346105.

N. I. Shakura and R. A. Sunyaev. Black holes in binary systems. Observational appearance. *A&A*, 24:337–355, 1973.

S. Singer and J. Nelder. Nelder-mead algorithm. 4(2):2928, 2009.

A. Skumanich. Time Scales for CA II Emission Decay, Rotational Braking, and Lithium Depletion. *ApJ*, 171:565, Feb. 1972. doi: 10.1086/151310.

M. D. Snellgrove, J. C. B. Papaloizou, and R. P. Nelson. On disc driven inward migration of resonantly coupled planets with application to the system around GJ876. *A&A*, 374:1092–1099, Aug. 2001. doi: 10.1051/0004-6361:20010779.

R. H. Soja, W. J. Baggaley, P. Brown, and D. P. Hamilton. Dynamical resonant structures in meteoroid stream orbits. *MNRAS*, 414:1059–1076, June 2011. doi: 10.1111/j.1365-2966.2011.18442.x.

S. G. Sousa, N. C. Santos, M. Mayor, S. Udry, L. Casagrande, G. Israelian, F. Pepe, D. Queloz, and M. J. P. F. G. Monteiro. Spectroscopic parameters for 451 stars in the HARPS GTO planet search program. Stellar [Fe/H] and the frequency of exo-Neptunes. *A&A*, 487:373–381, Aug. 2008. doi: 10.1051/0004-6361:200809698.

J. H. Steffen and E. Agol. An analysis of the transit times of TrES-1b. *MNRAS*, 364: L96–L100, Nov. 2005. doi: 10.1111/j.1745-3933.2005.00113.x.

J. H. Steffen and E. Agol. Developments in Planet Detection using Transit Timing Variations. In C. Afonso, D. Weldrake, and T. Henning, editors, *Transiting Extrapolar Planets Workshop*, volume 366 of *Astronomical Society of the Pacific Conference Series*, page 158, July 2007.

J. H. Steffen, D. C. Fabrycky, E. B. Ford, J. A. Carter, J.-M. Désert, F. Fressin, M. J. Holman, J. J. Lissauer, A. V. Moorhead, J. F. Rowe, D. Ragozzine, W. F. Welsh, N. M. Batalha, W. J. Borucki, L. A. Buchhave, S. Bryson, D. A. Caldwell, D. Charbonneau, D. R. Ciardi, W. D. Cochran, M. Endl, M. E. Everett, T. N. Gautier, R. L. Gilliland, F. R. Girouard, J. M. Jenkins, E. Horch, S. B. Howell, H. Isaacson, T. C. Klaus, D. G. Koch, D. W. Latham, J. Li, P. Lucas, P. J. MacQueen, G. W. Marcy, S. McCauliff, C. K. Middour, R. L. Morris, F. R. Mullally, S. N. Quinn, E. V. Quintana, A. Shporer, M. Still, P. Tenenbaum, S. E. Thompson, J. D. Twicken, and J. Van Cleve. Transit timing observations from Kepler - III. Confirmation of four multiple planet systems by a Fourier-domain study of anticorrelated transit timing variations. *MNRAS*, 421:2342–2354, Apr. 2012a. doi: 10.1111/j.1365-2966.2012.20467.x.

J. H. Steffen, D. Ragozzine, D. C. Fabrycky, J. A. Carter, E. B. Ford, M. J. Holman, J. F. Rowe, W. F. Welsh, W. J. Borucki, A. P. Boss, D. R. Ciardi, and S. N. Quinn. Kepler constraints on planets near hot Jupiters. *Proceedings of the National Academy of Science*, 109:7982–7987, May 2012b. doi: 10.1073/pnas.1120970109.

J. H. Steffen, D. C. Fabrycky, E. Agol, E. B. Ford, R. C. Morehead, W. D. Cochran, J. J. Lissauer, E. R. Adams, W. J. Borucki, S. Bryson, D. A. Caldwell, A. Dupree, J. M.

Jenkins, P. Robertson, J. F. Rowe, S. Seader, S. Thompson, and J. D. Twicken. Transit timing observations from Kepler - VII. Confirmation of 27 planets in 13 multiplanet systems via transit timing variations and orbital stability. *MNRAS*, 428:1077–1087, Jan. 2013. doi: 10.1093/mnras/sts090.

G. Takeda and F. A. Rasio. High Orbital Eccentricities of Extrasolar Planets Induced by the Kozai Mechanism. *ApJ*, 627:1001–1010, July 2005. doi: 10.1086/430467.

H. Tanaka, T. Takeuchi, and W. R. Ward. Three-Dimensional Interaction between a Planet and an Isothermal Gaseous Disk. I. Corotation and Lindblad Torques and Planet Migration. *ApJ*, 565:1257–1274, Feb. 2002. doi: 10.1086/324713.

B. Tingley and P. D. Sackett. A Photometric Diagnostic to Aid in the Identification of Transiting Extrasolar Planets. *ApJ*, 627:1011–1018, July 2005. doi: 10.1086/430494.

G. Torres, D. M. Gelino, K. von Braun, and E. Forum 2008 Radial Velocity Committee. Exoplanet Community Report on Radial Velocities. In *American Astronomical Society Meeting Abstracts #213*, volume 41 of *Bulletin of the American Astronomical Society*, page 310.06, Jan. 2009.

G. Torres, J. Andersen, and A. Giménez. Accurate masses and radii of normal stars: modern results and applications. *A&A. Rev*, 18:67–126, Feb. 2010. doi: 10.1007/s00159-009-0025-1.

J. Tregloan-Reed and J. Southworth. An extremely high photometric precision in ground-based observations of two transits in the WASP-50 planetary system. *MNRAS*, Mar. 2013. doi: 10.1093/mnras/stt227.

M. Trevisan, B. Barbuy, K. Eriksson, B. Gustafsson, M. Grenon, and L. Pompéia. Analysis of old very metal rich stars in the solar neighbourhood. *A&A*, 535:A42, Nov. 2011. doi: 10.1051/0004-6361/201016056.

D. E. Trilling, W. Benz, T. Guillot, J. I. Lunine, W. B. Hubbard, and A. Burrows. Orbital Evolution and Migration of Giant Planets: Modeling Extrasolar Planets. *ApJ*, 500:428, June 1998. doi: 10.1086/305711.

M. Tuomi. Evidence for nine planets in the HD 10180 system. *A&A*, 543:A52, July 2012. doi: 10.1051/0004-6361/201118518.

S. Udry, X. Bonfils, X. Delfosse, T. Forveille, M. Mayor, C. Perrier, F. Bouchy, C. Lovis, F. Pepe, D. Queloz, and J.-L. Bertaux. The HARPS search for southern extrasolar planets. XI. Super-Earths (5 and 8 M$\{\oplus\}$)$ina3 - planetsystem. A\&A, 469 : L43 - -L47, July2007. doi$:10.1051/0004-6361:20077612.

G. B. Valsecchi, A. Carusi, and A. E. Roy. The effect of orbital eccentricities on the shape of the Hill-type analytical stability surfaces in the general three-body problem. *Celestial Mechanics*, 32:217–230, Mar. 1984. 10.1007/BF01236601.

P. van de Kamp. Astrometric study of Barnard's star from plates taken with the 24-inch Sproul refractor. *AJ*, 68:515–521, Sept. 1963. 10.1086/109001.

D. Veras and P. J. Armitage. The dynamics of two massive planets on inclined orbits. , 172:349–371, Dec. 2004. 10.1016/j.icarus.2004.06.012.

D. Veras and P. J. Armitage. Extrasolar Planetary Dynamics with a Generalized Planar Laplace-Lagrange Secular Theory. *ApJ*, 661:1311–1322, June 2007. 10.1086/516726.

D. Veras and E. B. Ford. Secular Orbital Dynamics of Hierarchical Two-planet Systems. *ApJ*, 715:803–822, June 2010. 10.1088/0004-637X/715/2/803.

D. Veras, E. B. Ford, and M. J. Payne. Quantifying the Challenges of Detecting Unseen Planetary Companions with Transit Timing Variations. *ApJ*, 727:74, Feb. 2011. 10.1088/0004-637X/727/2/74.

S. S. Vogt, S. L. Allen, B. C. Bigelow, L. Bresee, B. Brown, T. Cantrall, A. Conrad, M. Couture, C. Delaney, H. W. Epps, D. Hilyard, D. F. Hilyard, E. Horn, N. Jern, D. Kanto, M. J. Keane, R. I. Kibrick, J. W. Lewis, J. Osborne, G. H. Pardeilhan, T. Pfister, T. Ricketts, L. B. Robinson, R. J. Stover, D. Tucker, J. Ward, and M. Z. Wei. HIRES: the high-resolution echelle spectrometer on the Keck 10-m Telescope. In D. L. Crawford and E. R. Craine, editors, *Society of Photo-Optical Instrumentation Engineers (SPIE) Conference Series*, volume 2198 of *Society of Photo-Optical Instrumentation Engineers (SPIE) Conference Series*, page 362, June 1994.

S. S. Vogt, R. P. Butler, E. J. Rivera, N. Haghighipour, G. W. Henry, and M. H. Williamson. The Lick-Carnegie Exoplanet Survey: A 3.1 M $_{\L}$ Planet in the Habitable Zone of the Nearby M3V Star Gliese 581. *ApJ*, 723:954–965, Nov. 2010a. 10.1088/0004-637X/723/1/954.

S. S. Vogt, R. A. Wittenmyer, R. P. Butler, S. O'Toole, G. W. Henry, E. J. Rivera, S. Meschiari, G. Laughlin, C. G. Tinney, H. R. A. Jones, J. Bailey, B. D. Carter, and K. Batygin. A Super-Earth and Two Neptunes Orbiting the Nearby Sun-like Star 61 Virginis. *ApJ*, 708:1366–1375, Jan. 2010b. 10.1088/0004-637X/708/2/1366.

G. A. H. Walker, D. A. Bohlender, A. R. Walker, A. W. Irwin, S. L. S. Yang, and A. Larson. Gamma Cephei - Rotation or planetary companion? *ApJL*, 396:L91–L94, Sept. 1992. 10.1086/186524.

W. R. Ward. Protoplanet Migration by Nebula Tides. , 126:261–281, Apr. 1997. 10.1006/icar.1996.5647.

W. R. Ward, G. Colombo, and F. A. Franklin. Secular resonance, solar spin down, and the orbit of Mercury. , 28:441–452, Aug. 1976. 10.1016/0019-1035(76)90117-2.

J. N. Winn, D. Fabrycky, S. Albrecht, and J. A. Johnson. Hot Stars with Hot Jupiters Have High Obliquities. *ApJL*, 718:L145–L149, Aug. 2010. 10.1088/2041-8205/718/2/L145.

J. Wisdom and M. Holman. Symplectic maps for the n-body problem. *AJ*, 102:1528–1538, Oct. 1991. 10.1086/115978.

A. Wolszczan and D. A. Frail. A planetary system around the millisecond pulsar PSR1257 + 12. *Nature*, 355:145–147, Jan. 1992. 10.1038/355145a0.

J. T. Wright, S. Upadhyay, G. W. Marcy, D. A. Fischer, E. B. Ford, and J. A. Johnson. Ten New and Updated Multiplanet Systems and a Survey of Exoplanetary Systems. *ApJ*, 693:1084–1099, Mar. 2009. 10.1088/0004-637X/693/2/1084.

U. Ziegler. NIRVANA$^+$: An adaptive mesh refinement code for gas dynamics and MHD. *Comput. Phys. Commun.*, 109(2-3):111–134, 1998. 10.1016/S0010-4655(98)00022-8.